Development of robotic volumetric PIV with applications in sports aerodynamics

Jux, C.

DOI
10.4233/uuid:643a6936-ce92-4c3e-af0f-5c251a50abbe

Publication date
2022

Document Version
Final published version

Citation (APA)
Jux, C. (2022). *Development of robotic volumetric PIV: with applications in sports aerodynamics*. [Dissertation (TU Delft), Delft University of Technology]. https://doi.org/10.4233/uuid:643a6936-ce92-4c3e-af0f-5c251a50abbe

Development of robotic volumetric PIV

with applications in sports aerodynamics

C. Jux

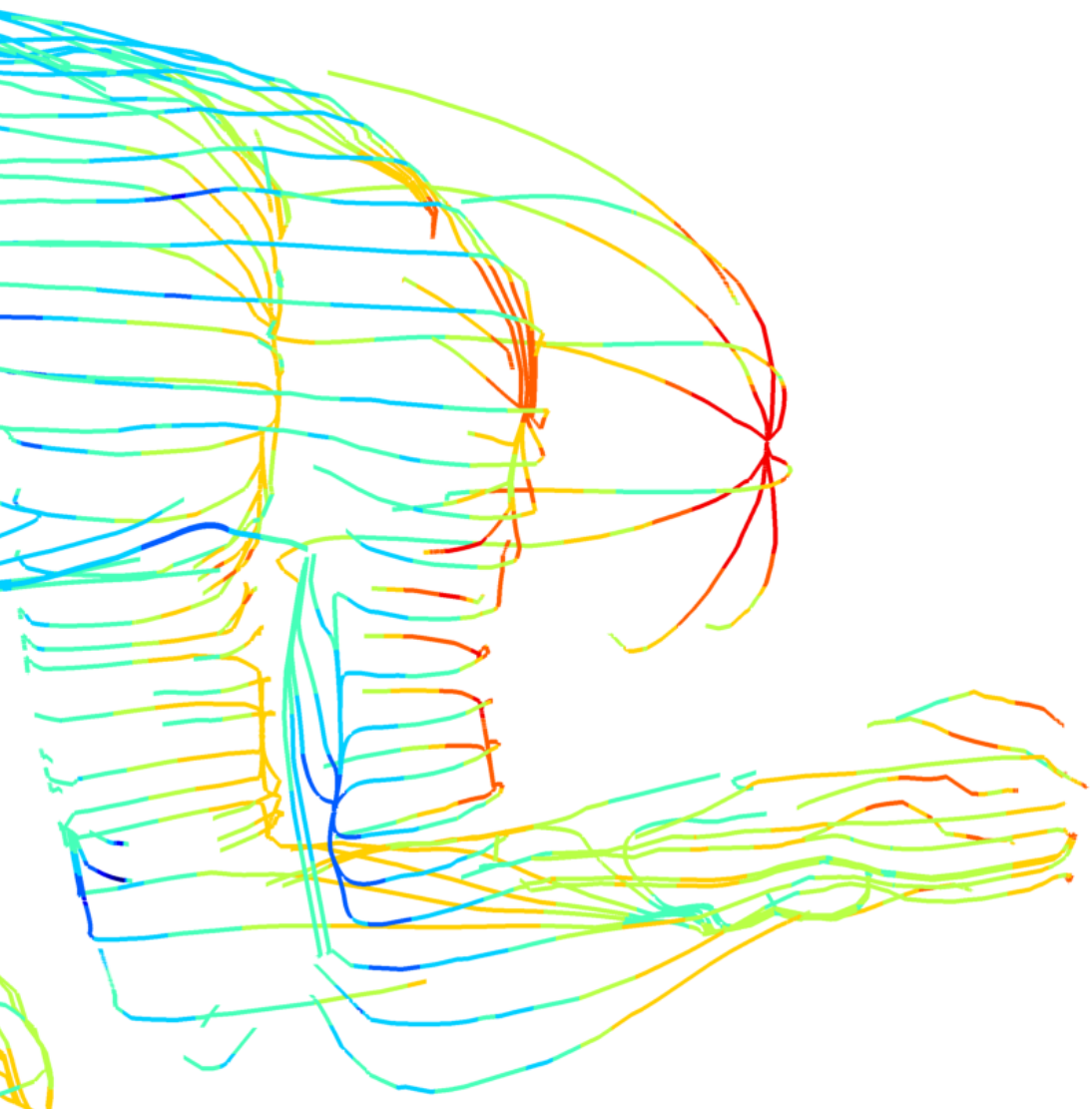

Propositions

accompanying the dissertation

Development of robotic volumetric PIV

with applications in sports aerodynamics

by

Constantin Jux

1. A 3D imaging system with universal calibration is instrumental for large-scale flow analysis by robotic volumetric PIV. (*chapter 3*)
2. The PIV-based surface pressure measurement on a 3D object gains accuracy if the specification of boundary conditions on the object surface is avoided. (*chapter 5*)
3. The 3D PTV study of a fluid flow past a solid object suffices for the shape reconstruction of the fluid-solid interface. (*chapter 6*)
4. Road bicycle tires triggering laminar-to-turbulent boundary layer transition maximize a bicycle wheel's stall angle in yaw, and thus, minimize the wheel's wind-averaged drag coefficient. (*chapter 8*)
5. Excellent research and knowledge creation are not enough to leave a mark in science. Instead, excelling at knowledge communication is instrumental.
6. Elite sports is an excellent driver and communicator for scientific progress.
7. The pursuit of scientifically sound data-processing methods restricts the deployment of pragmatic engineering solutions.
8. Genuine long-term and future-oriented politics are prevented by excluding the youngest generations from democratic elections.
9. A country's happiness index (in Europe) correlates with the share of residents using the bicycle as their primary means of transport. Incentivising cycling will therefore yield a happy nation.
10. A plant grows as tall as the pot it is planted in. Further research is required to understand if potted plants serve as a valid model for junior scientists.

These propositions are regarded as opposable and defendable, and have been approved as such by the promotor Prof. dr. F. Scarano.

Development of robotic volumetric PIV

with applications in sports aerodynamics

Development of robotic volumetric PIV

with applications in sports aerodynamics

Dissertation

for the purpose of obtaining the degree of doctor
at Delft University of Technology
by the authority of the Rector Magnificus Prof.dr.ir. T.H.J.J. van der Hagen;
Chair of the Board for Doctorates
to be defended publicly on
Wednesday, 16th March 2022 at 17:30 o'clock

by

Constantin JUX

Master of Science in Aerospace Engineering
Delft University of Technology, The Netherlands
born in Bergisch Gladbach, Germany.

This dissertation has been approved by the *promotor* and *copromotor*.

Composition of the doctoral committee:

Rector Magnificus,	chairperson
Prof.dr. F. Scarano,	TU Delft, *promotor*
Dr. A. Sciacchitano,	TU Delft, *copromotor*

Independent members:

Prof.dr.ing. S. Kallweit,	FH Aachen, Germany
Prof.dr.ir. C.J. Simão Ferreira,	TU Delft
Dr. X. Liu,	San Diego State University, USA
Dr. F. di Felice,	INM, Italy
Dr. B. Wieneke,	LaVision GmbH, Germany

Reserve member:

Prof.dr.ir. L.L.M. Veldhuis,	TU Delft

Keywords: Quantitative flow visualization, Particle image velocimetry, Pressure measurement, low-speed aerodynamics

Printed by: Proefschriftenprinten.nl

Front & Back: Skin-friction lines on a time-trialling cyclist

ISBN 978-94-6366-519-3

An electronic version of this dissertation is available at
http://repository.tudelft.nl/.

Contents

Summary

Particle image velocimetry (PIV) is the state of the art for quantitative, full-field, 3D flow diagnostics. Despite the maturity of the technique, two bottlenecks are identified which are addressed in this thesis: the achievable measurement volume size, and the optical access to geometrically complex objects. Both aspects are well illustrated when considering the human body in sports action. Characterising the aerodynamic flow topology around an athlete demands measurement volumes on the cubic-meter scale, whereas the simultaneous illumination and imaging of the flow near the athlete's body is challenged by the geometric complexity of the human body and the sports equipment. Focusing on sport performance, especially in timed disciplines, it is recognized that due to the shape of the human body, the aerodynamic resistance is often dominated by pressure drag. Therefore, a third element addressed in this thesis is the PIV-based pressure evaluation in the flow and on an object surface.

To overcome the identified measurement constraints, a PIV system for the 3D diagnostics of large-scale and low-speed flows has been developed, synthesizing advancements in PIV imaging and illumination hardware, automation technology, tracer particle generation, and particle tracking algorithms. The so called *robotic volumetric PIV* concept is proposed in Part I of this thesis, along with dedicated data analysis methods to retrieve the shape of the test object, the total pressure in the fluid flow, and the aerodynamic pressure on the object surface. Part II features applications of the proposed tools in the context of sport aerodynamics, with specific examples in cycling and swimming.

Robotic volumetric PIV is an approach that makes a partition of a large measurement domain into a series of sub-volumes, scanned in rapid succession by a compact 3D velocimetry probe mounted on a robotic arm. The measurement probe merges imagers and light source in one unit, maintaining the relative position of its components at all times. Thus, the system features a universal calibration, established prior to the first measurement. This enables the efficient time-average analysis of volumes on the cubic-meter scale.

The introduced system is utilized for PIV-based pressure analysis. It is demonstrated that robotic volumetric PIV presents a viable alternative to total-pressure wake-surveys using intrusive probes. Drawing advantage of the enhanced optical access, a second technique to evaluate the static pressure on generic 3D test geometries is proposed. The method integrates the pressure gradient in the domain of rotational flow, applying Bernoulli's principle elsewhere. This avoids the challenging specification of boundary conditions on the model surface, while minimizing the integration paths, and thus, the accumulation of measurement error.

An element often overlooked in experimental flow studies is the accurate identification of the test model geometry. The latter is mandatory if evaluating surface

flow properties. An algorithm for the identification of the fluid-solid interface, working on the spatial distribution of PIV tracers is developed. The model geometry is reconstructed within the resolution of the flow measurement by this approach.

The study of a full-scale cyclist model demonstrates the suitability of robotic volumetric PIV for flow analysis in a 2 m^2 domain. Dominant vortex structures in the cyclist's wake are identified. The pressure distribution and the near-surface flow pinpoint regions of flow separation which are linked to high pressure drag.

The PIV analysis near an isolated bicycle wheel in cross-wind shows that the wheel works like a sail: the wheel's resistance at non-zero yaw angle reduces until the flow separates. The stall angle depends highly on the tire surface texture. A tire triggering laminar-to-turbulent boundary layer transition maximizes the stall angle.

The hydrodynamic effect of thumb position on the flow past a swimmer's hand has been studied. The arm's wake features two main recirculation zones: a rolling vortex downstream of the hand, fed by the flow between the fingers; and a cylinder-like wake behind the forearm. A third vortex forms if the thumb is abducted from the index finger. Thumb abduction reduces the stagnation pressure on the index finger base, signalling a loss in propulsive force.

Samenvatting

Een PIV (Particle Image Velocimetry) systeem voor de 3D-diagnostiek van grootschalige stromingen en stromingen met lage snelheid werd ontwikkeld, waarbij vooruitgang in PIV beeldvormingshardware, tracer deeltjes-technologie, en deeltjes tracking algoritmen gecombineerd werden. Het zogenaamde *gerobotiseerde volumetrische PIV* concept wordt voorgesteld in Deel I van dit proefschrift, samen met specifieke data-analysemethodes voor geïntegreerde aerodynamische metingen. Deel II beschrijft toepassingen van de voorgestelde instrumenten in de context van sport-aerodynamica.

Gerobotiseerde volumetrische PIV verdeelt grote domeinen in een reeks subvolumes, die snel na elkaar worden gescand door een 3D velocimetrische sonde gemonteerd op een robotarm. De meetsonde voegt cameras en lichtbron samen in één eenheid, waarbij de relatieve positie van de componenten te allen tijde behouden blijft. Het systeem beschikt dus over een universele ijking, die vóór de eerste meting wordt uitgevoerd. Dit maakt een efficiënte tijd-gemiddelde analyse van volumes op kubieke-meterschaal mogelijk.

Het geïntroduceerde systeem wordt gebruikt voor drukanalyse door middel van PIV. Aangetoond wordt dat gerobotiseerde volumetrische PIV een haalbaar alternatief vormt voor totale-druk zog-onderzoeken met behulp van indringende sondes. Gebruikmakend van de verbeterde optische toegang, wordt een tweede techniek voorgesteld om de statische druk te evalueren op generische 3D test geometrieën. De methode integreert de drukgradiënt in het domein van de rotatiestroming en past elders het principe van Bernoulli toe. Dit vermijdt de uitdagende specificatie van randvoorwaarden op het modeloppervlak, terwijl de integratiewegen, en dus de accumulatie van meetfouten, geminimaliseerd worden.

Een element dat vaak over het hoofd wordt gezien bij experimentele stromingsstudies is de nauwkeurige identificatie van de geometrie van het testmodel. Dit laatste is verplicht bij het evalueren van oppervlakte stromingseigenschappen. Een algoritme voor de identificatie van het vloeistof-vaste stof grensvlak, dat werkt op de ruimtelijke verdeling van PIV tracers, is ontwikkeld. De modelgeometrie wordt door deze aanpak gereconstrueerd binnen de resolutie van de stromingsmeting.

De studie van een wielrenner model op ware grootte toont de geschiktheid aan van volumetrische PIV met robots voor stromingsanalyse in een domein van 2 m^2. Dominante vortex structuren in het zog van de fietser worden geïdentificeerd. De drukverdeling en de stroming nabij het oppervlak geven gebieden aan waar de stroming los laat en die in verband staan met hoge drukweerstand.

De PIV analyse in de buurt van een geïsoleerd fietswiel in zijwind toont aan dat het wiel werkt als een zeil: de weerstand van het wiel bij een yaw hoek van niet nul vermindert tot de stroming los laat. De overtrekhoek hangt sterk af van de textuur

van het bandoppervlak. Een band die de overgang van laminaire naar turbulente grenslaag triggert, maximaliseert de overtrekhoek.

Het hydrodynamisch effect van de positie van de duim op de stroming langs de hand van een zwemmer is onderzocht. Het zog van de arm vertoont twee belangrijke recirculatiezones: een rollende draaikolk stroomafwaarts van de hand, gevoed door de stroming tussen de vingers; en een cilindervormig zog achter de onderarm. Een derde draaikolk ontstaat als de duim van de wijsvinger wordt weg bewogen. Het spreiden van de duim vermindert de stagnatiedruk op de basis van de wijsvinger, wat een verlies aan voortstuwingskracht betekent.

Acknowledgements

This book marks a closing point for my academic career at TU Delft. My journey in Delft started in 2011 as a freshmen in Aerospace Engineering. If I was to compare this period to a bicycle race, it would need to be a long and tricky one: starting in a big peloton, the bunch quickly reduced early into the event. Riding and enjoying the race together with a select group of companions, we safely navigated through the many twists and turns of the course. While the route took me to a handful of other unique destinations, it ultimately returned to Delft again and again. Now I am entering the final, with the Doctorate in sight at the finish line.

Surely, I am only in a position to finish this ride thanks to my excellent coaching team: firstly, I need to express my gratitude to Prof. Dr. Fulvio Scarano, who convinced me to pursue the PhD. His experience, enthusiasm and dedication were truly inspirational, and I am glad that I could rely on him as a coach and promotor. Secondly, I need to thank Dr. Andrea Sciacchitano, for providing his expertise, for stimulating the knowledge exchange within the infamous large-scale PIV group, and for magically being almost always available despite the size of the team he is managing. Thirdly, I need to thank Dr. Bernd Wieneke and Dirk Michaelis on behalf of LaVision GmbH. Your contributions to the project, especially the realization of the first CVV prototype, but also posing the right questions, and providing honest feedback were invaluable.

Even the best team of athletes, coaches and sponsors cannot function without its supporting staff. Therefore, I thank Colette Russo for mastering all administrative requests, organizing PhD days, and sharing the latest department news. Likewise, I thank Frits Donker Duyvis for all sorts of technical support, including high-precision alignment of lasers and designing several HFSB seeding generators; Dennis Bruikman for his technical support with a fine attention to detail, including the production of our first in-house FSU, as well as the speed controller for the wheel experiments; Nico van Beek for maintaining robustness with our IT and server systems; and lastly, Peter Duyndam deserves a huge Kudos, for his excellent technical craftsmanship in the workshop, and equally for his great sportsmanship and discussions on the latest training runs and rides.

Team tactics can only be executed to plan with the best team mates. In this respect, I express my gratitude towards my collaborators who supported me on the way approaching the finish line. Thank you David Ordóñez, and Joris van den Berg for letting me be part of your masters thesis projects. I also need to thank Prof. Dr. Willem van de Water, for his engagement, diplomacy, and initiative in the swimmer's hand project. A special thanks goes to Dr. Jan Schneiders, who supervised me during my masters thesis, providing a perfect lead-out into the PhD, and kindly offering me his desk at the window-side.

A good bicycle race also demands the right amount of competitors and spectators. I am grateful for my colleagues in the office (and behind the screens in times of the pandemic), who cheered me up, endured my complaints, provided feedback where needed, and discussed the weirdest and most ingenious ideas during lunch and coffee hours. Thank you and Chapeau to the generation that already finished their PhDs: Dr. Beppe Caridi, Dr. Tiago Pestana, Dr. David E. Faleiros, Dr. Haohua Zong, Dr. Weibo Hu, Dr. Jacopo Serpieri, Dr. Zeno Belligoli and Dr. Yi Zhang – it was great to work with and alongside you. A special acknowledgement must go to the cycling-doctorates, Dr. Wouter Terra and (*bijna Dr.*) Alexander Spoelstra. The working experience would not have been the same without discussing the best equipment investments, training plans, technological advancements, race predictions and results in the field of cycling with you. I am equally grateful for the current and younger generation of colleagues in the office. I had the luxury of relying on the expertise of my experimental colleagues at all times: thank you Edoardo Saredi, Christoph Mertens, Gabriel Gonzalez, Alessandro D'Aguanno, Kushal Kempaiah, Sagar Adatrao, Ming Huang, Beto R. Vidales, Ilda Hysa and Jane Bulut. Likewise, I am grateful for the interaction with my colleagues from the parallel universe of numerical flow simulations: Luis Laguarda, Varun Jain, Jordi Casacuberta, Mohamad Fahti, Xiaodong Li and Martin Schmelzer, it was a pleasure to work with you. Apologies to the names I missed, and best of luck to the younger colleagues.

Any sports event demands an organizer and a jury. The TU Delft and Aerospace Engineering Graduate School made for a unique experience, allowing all PhD candidates to foster relevant personal and professional skills in parallel to the core research activities. Regarding the jury, I appreciate the interest of the committee members who have taken their precious time for evaluating this dissertation, providing feedback, and challenging me at the thesis defence.

Since starting in Delft I was blessed to meet and connect with marvellous people, many of which I can now call my friends. David Jimenez-Lluva, Arwin Khoshnewiszadeh, Marco Pfahler, Lukas Klespe, Bastian Telgen, Felix Lindemann, Max Hirsch, and Dr. Max Opgenoord – thank you for enriching the bachelors experience. A special appreciation goes to Matthieu Rhomberg, who proved invaluable in mastering the masters together. Additionally, there was the triathlon chapter: starting somewhere in the masters and continuing to date. The countless swims, bike-rides, and runs with Max Hirsch, (*bijna Dr.*) Alexander Spoelstra (2 × again), and Dr. Martin Sand, along with the conversation before, during and after, were priceless for managing not only the Ironman but also the PhD.

Last but not least, it is time to thank my family for their continuous support and encouragement. All together, you have ensured I maintained my balance, and you have pointed me in the right direction if I went off track. To Franzi, my parents, my brother and my grandparents: you have been the greatest asset in completing this journey.

Constantin Jux
Delft, March 2022

Prologue

1

Introduction

Every accomplishment starts with the decision to try.

John F. Kennedy

1

Citius, Altius, Fortius – the Olympic motto in Latin, translating to *faster, higher, stronger* represents a creed of many athletes, professional and amateur alike, who follow a desire to be faster, reach higher, and go further. Succeeding in this desire demands physical and mental strength. The latter, alone, does not suffice in many sports where aerodynamics plays a major role, especially in timed disciplines. The athlete's motion through the air causes an interaction of human body and equipment with the airflow, which ultimately results in an aerodynamic force being exerted on the athlete that opposes the motion and dissipates energy.

Performance optimization in (speed) sports requires an understanding and quantification of the relevant aerodynamic forces. Accurately determining these forces in the field remains challenging, and therefore, wind tunnel experiments are conducted to quantify the aerodynamic characteristics of athlete and equipment, as illustrated in Figure 1.1(a). Classical approaches, such as balance measurements provide a reliable quantification of the aerodynamic forces and moments. Such force quantification is of paramount importance, yet it only contains information on the resulting loads without providing insight into the underlying flow mechanisms.

Nowadays, computational fluid dynamics (CFD) simulations allow for the detailed scrutiny of flow topology and forces in parametric studies. The simultaneous analysis of flow structures and load data enables informed decision making in an attempt to optimize aerodynamic performance. An exemplary flow field computation of a drafting marathon runner is illustrated in Figure 1.1(b). If instead only the forces are measured experimentally, i.e. a quantification or visualization of the flow field is not afforded, aerodynamic optimization certainly remains possible, but it demands experience and good intuition from the experimentalist.

(a) Simultaneous wind tunnel testing of a triathlete and a car, with smoke visualisation of the flow over the vehicle. Image reproduced from Mercedes-Benz AG (2019).

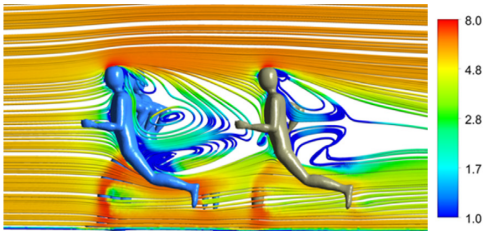

(b) CFD simulation of a drafting marathon runner. Colorbar indicating flow velocity in m/s. Figure reproduced from Polidori et al. (2020).

Figure 1.1: Examples of wind tunnel measurements and CFD in sports aerodynamics.

Wind tunnel experiments often remain limited to the aforementioned load measurements, along with qualitative flow visualisations, and local, point-wise flow measurements, such as smoke flow visualisations and pressure probes, respectively. A rigorous flow topology analysis is enabled if quantitative, full-field flow visualisations are acquired. An established technique in this respect is particle image velocimetry (PIV).

PIV is an optical and non-intrusive method that quantifies the velocity distribution in a fluid flow by measuring the displacement of tracer particles dispersed in that flow. Since its introduction by Adrian (1984), PIV has matured into a versatile technique that enables the measurement of the three-dimensional (3D) and three-component (3C) velocity field in a fluid flow, as demonstrated in the review article from Discetti and Coletti (2018).

However, PIV carries its own limitations. The general setup complexity of a PIV system is high, exemplified by the stereoscopic PIV system for automotive applications shown in Figure 1.2. For 3D measurements at least one additional camera is compulsory, further increasing the setup complexity. The system requirements necessitate a tedious calibration process, and the optical access to geometrically intricate models is challenged by the large aperture angle between the cameras.

In the context of aerodynamics, due to the use of microscopic droplets as tracers, the achievable measurement volumes are small, typically on the order of a few cubic centimetres only. A substantial step towards large-scale, 3D PIV measurements was granted by the introduction of millimetre-scale, neutrally buoyant tracer particles such as helium filled soap bubbles (HFSB, Bosbach et al., 2009; Scarano et al., 2015, among others). The latter enabled volumetric PIV measurements in unconfined flows in domains of several litres. This constraint, nonetheless, clashes with the need to study the flow around the human body, demanding observation volumes on the cubic-meter scale. Likewise, the desired measurement volumes in industrial applications are often significantly larger, consider e.g. the cases of the cyclist and the car in Figure 1.1(a). These limitations have, to date, prevented a greater dissemination of 3D PIV systems in sports aerodynamics and industrial facilities.

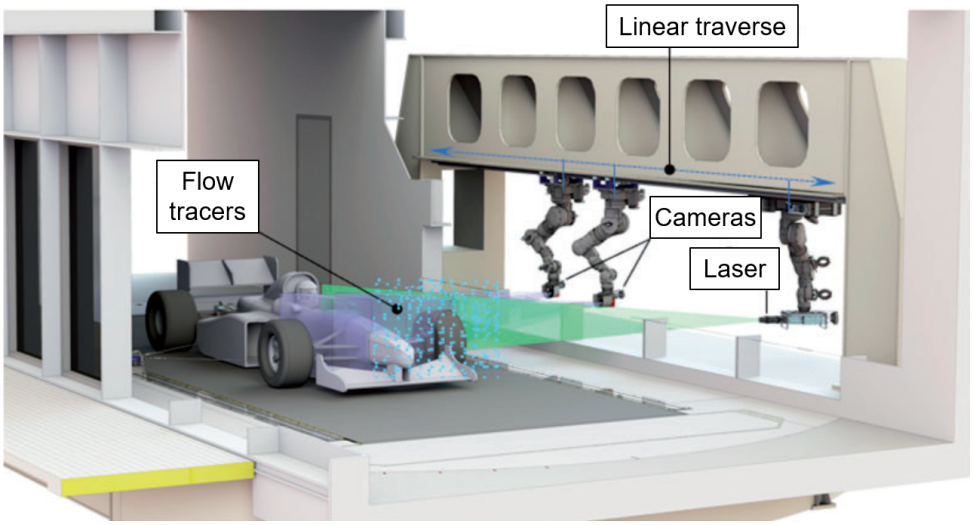

Figure 1.2: Illustration of a steroscopic PIV system for automotive wind tunnels. Figure reproduced from Senft and Gillan (2019).

To mitigate the identified bottlenecks, this dissertation aims to assess and advance the feasibility of PIV-based, 3D flow diagnostics at large scale. The first step in this assessment addresses two major constraints of state-of-the-art 3D PIV systems: namely, the insufficient measurement volume size and the poor optical access. The centrepiece of this thesis is the novel robotic volumetric PIV system, which overcomes such limitations (Chapter 3).

Focusing on the human body in sports action, enhancement of aerodynamic performance is often associated with reduction of aerodynamic drag. Due to the nature of the human body, which could be characterised as an agglomeration of bluff body segments, the aerodynamic drag on the athlete is often dominated by pressure rather than skin-friction, as the flow separates from the athlete's body. Evaluation of the aerodynamic pressure, in the flow field and on an object surface, therefore presents a main pillar in the present research.

Pressure measurements in aerodynamics are typically conducted via intrusive probes in the flow, or small orifices integrated in the test model surface. Pressure sensing on full-scale, human-sized models yields complex models with multitudes of tubing; whereas scanning the wake pressure on large domains is time consuming. Following the introduction of the robotic volumetric PIV system, the thesis goes on to consider methods for the PIV-based pressure analysis, accounting for the characteristics of the proposed measurement instrument in Chapters 4 and 5.

An issue that arises is the treatment of boundary conditions, in particular on the object surface. This has inspired the advancement of a method that can reconstruct its geometry based on the surrounding fluid flow measurement (Chapter 6).

Part I (Chapters 3 to 6) constitutes the advancements in the field of measurement technology made over the course of this doctoral thesis. Subsequently, the proposed tools and methods are applied in selected sport applications in Part II (Chapters 7 to 9). Lastly, the current impact of the presented developments is demonstrated by a survey of applications in Chapter 10. The latter provides an overview of measurements utilizing the proposed robotic volumetric PIV concept, conducted by fellow researches in aerodynamics. Conclusions and directions for further research are provided in Chapter 11.

2

Background: particle image velocimetry

This dissertation proposes a novel particle image velocimetry (PIV) system for volumetric flow measurements at large-scale—robotic volumetric PIV. To justify the developments presented in Part I of this thesis, it is on one hand essential to establish the working principles and state of the art of the underlying PIV technique. On the other hand, it is important to focus on current challenges in PIV technology, especially in the context of large-scale flow diagnostics in aerodynamics. Lastly, the potential of velocimetry techniques stretches far beyond the measurement of flow velocity. Other flow properties, such as the pressure distribution can be derived from the measured velocity field and are of great interest in several engineering problems.

This chapter provides a foundation for Part I of this thesis which discusses the technological advancements made over the course of this research project. Working principles of PIV are laid out in Section 2.1. Focusing on large-scale flows and industrial applications, Section 2.2 highlights technological challenges arising upon scaling of the measurement domain. Section 2.3 shifts the focus from system considerations to aspects of data acquisition and processing techniques, that are necessary for an intuitive analysis of the experimental observations. This discussion lays the groundwork for extended PIV data analysis, such as investigation of the pressure distribution in Section 2.4, and the detection of solid surfaces in the measurement domain in Section 2.5.

2.1. Working principles

Particle image velocimetry (PIV) as a measurement technique for fluid dynamics was first explored in the late 1980s and has rapidly developed from a laboratory and research based tool to an industrial-scale measurement technique. The underlying principle is simple: to see the fluid flow, it is seeded with tracer particles. Subsequently, the motion of these tracers is tracked in time. Observing the tracers displacement over a known time separation yields the flow velocity.

To illustrate the principle, imagine standing on a river-bridge and throwing a stick into the water stream. Following the stick's trajectory in the water will allow you to make a first estimate of the local flow velocity and direction. Of course one does not use sticks in water in a laboratory environment; instead, one seeds the flow with many tracer particles that are known to follow the fluid closely. Snapshots of the particle positions are then recorded with digital cameras.

The layout of a PIV setup is provided in Figure 2.1. Relevant items and processes for this dissertation are elaborated in the remainder of this section. For further details of the specific working principles the reader is referred to literature, for instance the books by Raffel et al. (2018) or Adrian and Westerweel (2011).

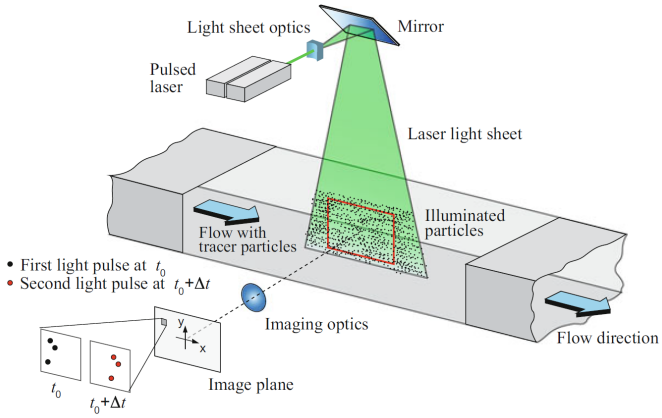

Figure 2.1: Schematic of a planar (2-dimension, 2-component; 2D2C) PIV setup. Illustration reproduced from Raffel et al. (2018).

The advantages of PIV over alternative velocimetry techniques, such as Laser-Doppler anemometry (LDV, LDA) and hot-wire probes (HWA), are its potential to provide instantaneous field measurements instead of single point observations and its non-intrusiveness. In its initial stages PIV has been devised as a planar (2D) technique measuring the in-plane velocity components (2C) in a thin light sheet through recordings from a single camera. The light sheet is in most cases generated using a pulsed laser light source. For volumetric (3D) flow measurements, the use of pulsed LEDs for illumination is gaining popularity, see e.g. Huhn et al. (2018), Mertens et al. (2021b) or Schröder et al. (2021). Illuminated tracer particles in the flow scatter the light, which is then recorded by a camera. Evaluating the particle

position at two subsequent time instants separated by a finite time interval, yields their velocity.

Current PIV systems are suitable to capture more than "just" the planar (2D) two-component (2C) velocity field. A schematic classification of PIV systems and configurations as proposed in literature is outlined in Figure 2.2.

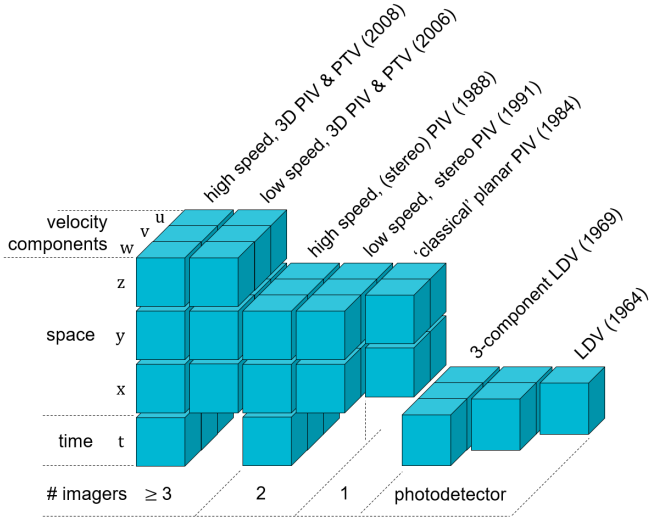

Figure 2.2: Characterisation of PIV and LDV systems by means of measurement dimensionality, resolved velocity components and minimum number of required imagers. Time references in parenthesis indicating first scientific publications of a technique, listed here in order of appearance. LDV: Yeh and Cummins (1964), 3C-LDV: Huffaker et al. (1969), 2D2C-PIV: Adrian (1984), TR-2D2C-PIV: Vogel and Lauterborn (1988), 2D3C-PIV: Arroyo and Greated (1991), 3D3C-PIV: Elsinga et al. (2006), TR-3D3C-PIV: Schröder et al. (2008). Illustration adapted from Hinsch (1995) and Scarano (2012).

Adding a second camera to a PIV system enables to make a stereoscopic setup, where all three velocity components can be measured in a plane. Utilising such 2D systems to slice volumes in depth, scanning PIV provides 3D measurements by multiple planar samples (e.g. Brücker, 1995).

The breakthrough to fully volumetric measurements can be seen in the development of tomographic PIV by Elsinga et al. (2006). Using three or more cameras the particle distribution in a volume is reconstructed from its two-dimensional images in a tomographic reconstruction problem, such that the motion analysis is carried out in a three-dimensional (3D) space. A schematic 3D PIV setup is sketched in Figure 2.3. While tomographic PIV is regarded as the state-of-the-art volumetric PIV technique, it still possesses a number of challenges, including:

1. The maximum achievable measurement volume
2. The setup complexity and strict calibration requirements
3. The optical access on geometrically complex test objects
4. The necessary processing time and computer memory requirements

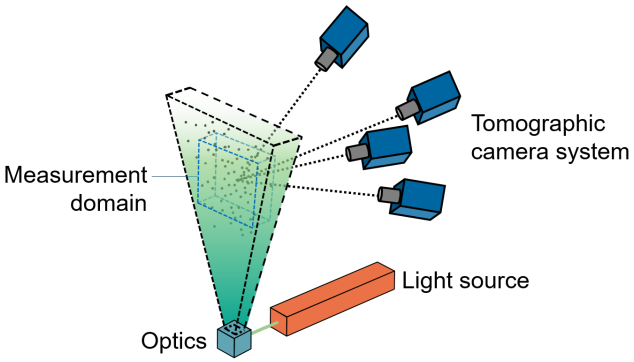

Figure 2.3: A generic tomographic (3D3C) PIV setup. Illustration adapted from Elsinga et al. (2006).

Measurement volume

The first challenge, the measurement domain size, stems from the requirement to illuminate the full measurement volume such that the tracer particles scatter enough light into the cameras. The specific role of tracer particles in PIV at large scale is discussed in Section 2.2.3.

Setup complexity and system calibration

The second challenge stems from the interaction of the PIV system components. A tomographic type PIV setup consists of a minimum of three cameras, a high-power light source, and a suitable seeding generator for the tracer particles. Installation and alignment of the aforementioned systems is demanding. Relevant examples of complex PIV systems are given in Section 2.2.1.

Optical access

The third point, concerning optical access on geometrically complex objects, can be ascribed to the system complexity too. A limiting factor is the tomographic aperture angle β spanned between the cameras. The tomographic particle reconstruction accuracy is found to be accurate if $\beta \geq 40°$ (Scarano, 2012). Reducing the aperture angle instead yields an increased reconstruction error. The latter is illustrated in Figure 2.4. The subject of optical access in PIV, and its relation to the tomographic aperture angle are elaborated in more detail in Section 3.1, with specific attention to low aperture imaging systems.

Computational requirements

The fourth challenge, the computational cost of 3D PIV data processing, has been greatly mitigated by the introduction of particle-based 3D reconstruction algorithms as compared to previous tomographic reconstruction methods working with light intensity distributions in voxelized domains. Two pertinent works in this respect are the invention of the iterative particle reconstruction algorithm (IPR, Wieneke, 2012), and the Lagrangian particle tracking algorithm Shake-The-Box (STB, Schanz et al., 2016). These inventions have initiated a trend that current studies employing

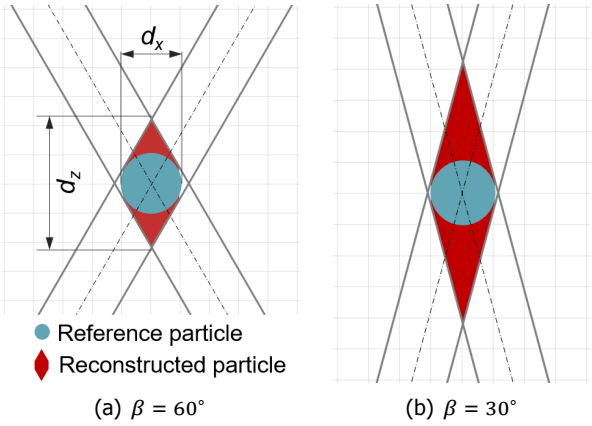

Figure 2.4: Particle reconstruction error versus aperture angle β. Figure adapted from Scarano (2012).

volumetric velocimetry techniques in low speed flows rely on tracking of individual particles, rather than spatial cross-correlation approaches that track small ensembles of tracer particles. The distinction between the velocity evaluation approaches is discussed further in Section 2.3.

2.2. Challenges at large scale

Since its introduction, particle image velocimetry has advanced into a versatile technique for aerodynamics research. Although PIV is predominantly used in research laboratories, its application in industrial wind tunnel facilities is broadly documented as indicated in Table 2.1.

Noticeably, all but one of the listed studies (Casper et al., 2016) consider planar two-component or stereoscopic PIV configurations, of which the illumination and imaging systems are installed on independent traversing systems. Some studies repeat 2D measurements in several planes to gather knowledge across a volumetric domain: Nakagawa et al. (2015) slice the volume downstream of a 28%-scale car model with several horizontal PIV planes. Similarly, Mead et al. (2015) employ repeated stereoscopic PIV measurements in the validation of noise prediction models, scanning a coaxial jet flow. The concept of scanning a large or 3D domain by several planar measurements is elaborated upon in Section 2.2.2.

The industry preference for multiple planar measurements instead of a fully volumetric approach may be twofold: (1) the system complexity and data processing burden make the deployment of tomographic PIV at industrial level unlikely in its present form. Specific examples indicated in Table 2.1 are discussed in Section 2.2.1. More importantly, (2) achievable measurement volumes in tomographic PIV remain fairly limited, as indicated in Section 2.1. The full-scale car study of Wendt and Forll (2001) shows that even for stereoscopic measurements, multiple FOVs are required to capture the desired domain. One key to lift the measurement

Table 2.1: Experiments conducted in industrial or large-scale aerodynamic testing facilities with PIV.

	Research application & group	Configuration	Facility	Domain size
Aviation	Aircraft half-model Pengel et al. (1997)	Planar	DNW (LLF) Marknesse (NL)	$300 \times 300\,\mathrm{mm}^2$ $0.09\,\mathrm{m}^2$
	Aircraft half-model Coustols et al. (2004)	10 camera system with purpose built support	ONERA (B10) Lille (FR)	$1390 \times 920\,\mathrm{mm}^2$ $1.28\,\mathrm{m}^2$
	Rotor trailing vortices Raffel et al. (2004)	Stereoscopic 4-axis traverse	DNW (LLF) Marknesse (NL)	$460 \times 360\,\mathrm{mm}^2$ $0.17\,\mathrm{m}^2$
	Helicopter rotor wake Jenkins et al. (2009)	Stereoscopic	NASA (14×22) Langley (USA)	$1524 \times 914\,\mathrm{mm}^2$ $1.39\,\mathrm{m}^2$
	Coaxial jet flow, Aero-acoustics Mead et al. (2015)	Stereoscopic Purpose made traversing system	QinetiQ (NTF) Farnborough (GB)	$350 \times 200\,\mathrm{mm}^2$ $(10\times)\ 0.07\,\mathrm{m}^2$
	Tiltrotor aircraft model Faleiros (2021)	Stereoscopic HFSB tracers	DNW (LLF) Marknesse (NL)	$1.1 \times 1.1\,\mathrm{m}^2$ $(7\times)\ 1.21\,\mathrm{m}^2$
Automotive	Full-scale car model Wendt and Forll (2001)	Stereoscopic In-plane traverse	Audi Ingolstadt (DE)	$540 \times 1600\,\mathrm{mm}^2$ $(3\times)\ 0.86\,\mathrm{m}^2$
	Full-scale car testing Cardano et al. (2008)	Stereoscopic Traversing system	Pininfarina wind tunnel, Turin (IT)	$\mathcal{O}\left(1\,\mathrm{m}^2\right)$
	28%-scale car wake Nakagawa et al. (2015)	Planar	Toyota R&D Aichi (JPN)	$540 \times 405\,\mathrm{mm}^2$ $(16\times)\ 0.22\,\mathrm{m}^2$
	Full-scale car wake Casper et al. (2016)	Tomographic PIV HFSB tracers	Volkswagen Wolfsburg (DE)	$2.0 \times 1.6 \times 0.2\,\mathrm{m}^3$ $0.12\,\mathrm{m}^3$
	Automotive motorsports TMG (2017)	Stereoscopic Traversing system	TMG Cologne (DE)	$350 \times 350\,\mathrm{mm}^2$ $0.12\,\mathrm{m}^2$

volume lies in the tracer particles, which is demonstrated in Section 2.2.3.

Whereas this thesis is focused on the aerodynamic flow analysis, the above trends can also be observed in the wider range of fluid-dynamic studies. A detailed review of concepts and applications in hydrodynamic facilities is avoided for sake of conciseness. The interested reader will find selected examples in the field of hydrodynamics for instance in the work of Di Felice and Pereira (2007), while some specific PIV concepts from hydrodynamic applications are discussed in Section 2.2.2.

2.2.1. System complexity

The complexity of 3D PIV measurements stems from the setup of a multitude of cameras, in combination with an appropriate illumination source. The calibration of the optical path from the image space to the measurement region in physical space requires high precision for a successful tomographic reconstruction (Scarano, 2012; Wieneke, 2008). The time and care needed to precisely install the imaging and illumination devices and to re-calibrate them, makes it unfeasible to repeat multiple 3D PIV measurements of adjacent sub-volumes. To date, to the best of the author's knowledge, no work is reported in the literature where tomographic PIV is performed on a multitude of regions for the purpose of covering a complex three-dimensional domain of interest.

Already for stereoscopic PIV configurations the system complexity can be high. The helicopter rotor wake study by Raffel et al. (2004) involves five cameras and three double pulsed Nd:YAG lasers on a 10 m long and 15 m high traversing system. The measurements of Mead et al. (2015) required a purpose-built gantry to enable the desired multi-plane PIV acquisitions in the coaxial jet flow.

The PIV community feeds the industry demand by supplying dedicated and partially automated PIV systems, as already illustrated in Chapter 1 (Figure 1.2). Details on a particular stereoscopic PIV system which is known to be popular in automotive, motorsport wind tunnels are presented by Michaux et al. (2018). The so-called RoboPIV system, which is discussed further in the subsequent section, combines three robot arms on a linear traverse. Two robots each carry a PIV camera, the third one holds the laser head. In this way a stereoscopic PIV system with fast repositioning capabilities is realised, that also comprises the stringent alignment requirements of focusing, Scheimpflug condition and stereoscopic calibration.

2.2.2. Scanning PIV principle

The measurement examples provided in Table 2.1 revealed that the concept of scanning either a 3D domain, or a planar section in excess of the measurable cross-section for a given 2D PIV system, is commonly employed. As this concept of *domain partitioning* is vital for the work presented in this thesis, in particular the robotic volumetric PIV principle proposed in Chapter 3, let us consider some of the seminal works utilizing such scanning principle.

In the discussion of scanning PIV systems one must distinguish between rapid scanning approaches that yield temporally correlated and resolved measurements; and "slow", temporally uncorrelated scanning of the domain of interest. The former approach was first introduced by Brücker (1995), who demonstrated the potential of time resolved scanning PIV on a finite cylinder in a water channel at a Reynolds number of 300. The difficulty in this approach is to maintain a sufficiently small distance between neighbouring scanning planes for maintaining spatial resolution, while still scanning sufficiently fast to maintain temporal resolution. Another example of this type of scanning approach is the work of Burgmann et al. (2006), in which the laminar separation bubble over a 20 cm airfoil in a water tunnel is studied at Reynolds numbers ranging from $20,000 - 60,000$. The latter study required ten individually controlled laser diodes to manage a temporally resolved acquisition, which goes to show that this approach becomes unfeasible when scaling up experiments to larger domains and faster flows.

When temporal resolution is not a concern, the scanning PIV approach can be used to slice a 3D domain of interest with several 2D measurements, or to compose a large 2D measurement area by several sub-domain measurements. Examples such as the studies of Nakagawa et al. (2015) and Mead et al. (2015) have been introduced with Table 2.1 already. Tescione et al. (2014) demonstrate this principle in the phase-locked measurement of a vertical axis wind turbine (VAWT) wake. By installing a planar and a stereoscopic PIV system on a two-axis (streamwise-spanwise) traversing mechanism, Tescione et al. (2014) capture the wake flow up to three diameters ($D = 1$ m) downstream of the turbine, whereas each individual

measurement images an area of $37 \times 43\,\mathrm{cm}^2$ only. An illustration of the setup, along with an exemplary flow measurement is provided in Figure 2.5.

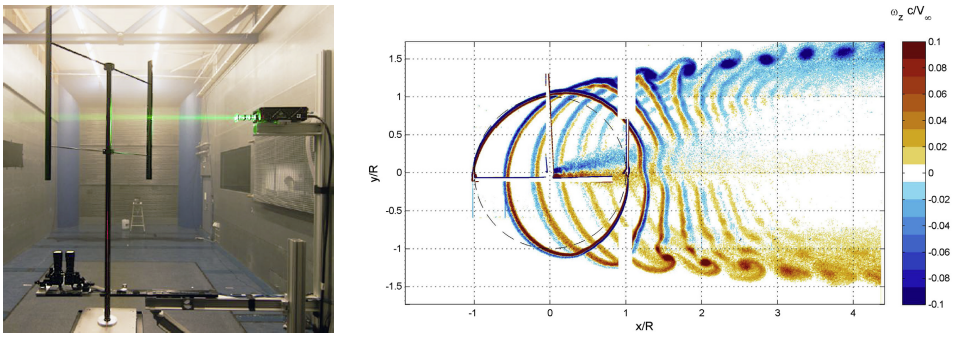

(a) Planar PIV setup

(b) Phase-locked vorticity in the VAWT wake

Figure 2.5: Scanning PIV in the wake of a VAWT, reproduced from Tescione et al. (2014).

The scanning PIV setup shown in Figure 2.5(a) indicates that even for a 2D-2C PIV measurement the construction to support the measurement equipment becomes increasingly complex. To counteract the increase in setup complexity, compact PIV systems have been developed in which cameras and light source are united in one body that can be translated with, or relative to, the test model. One such example is the so-called *PF 3D PIV Probe* by Cardano et al. (2008). The referenced probe comprises two PIV cameras and a laser in an L-shaped frame, capable of stereoscopic (2D-3C) flow measurements. An illustration of the probe, along with its use in the Pininfarina aerodynamics laboratories is shown in Figure 2.6. When mounted on a traverse, as shown in Figure 2.6(b), the probe is easily moved around the test model, to capture the flow field in several planes of interest.

Compact probes similar to the one shown in Figure 2.6 have proven particularly beneficial in applications where the model moves through the fluid, as opposed to classical wind tunnel applications where the fluid moves past the model. The former type of testing is common for hydrodynamic towing tank facilities, in which test models are towed through a larger water tank. An example of PIV testing in such facility is presented by Falchi et al. (2014), where a stereoscopic PIV system is integrated in a torpedo-like structure as illustrated in Figure 2.7. Dragging the probe along with the test model allows to capture the flow evolution in a fixed position relative to the test model. In the specific case studied by Falchi et al. (2014) the flow past a catamaran model is analysed.

If a compact PIV probe like the ones shown in Figures 2.6 and 2.7 is mounted on a traverse mechanism that can be moved relative to the test model, large domains can be scanned by successive PIV measurements without the need to recalibrate the PIV system. An example of such measurement is presented by Di Felice and Pereira (2007), and illustrated in Figure 2.8. The latter work combines 18 sub-domain measurements to compose a measurement cross section in excess of $0.8\,\mathrm{m}^2$.

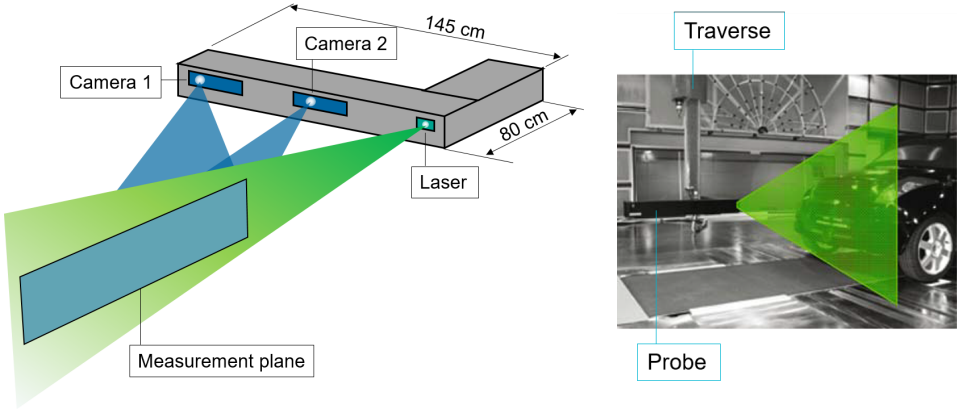

(a) Probe layout (b) Probe in full-scale car testing.

Figure 2.6: Layout and application of the stereoscopic Pinifarina 3D PIV probe. Illustrations adopted from Cardano et al. (2008).

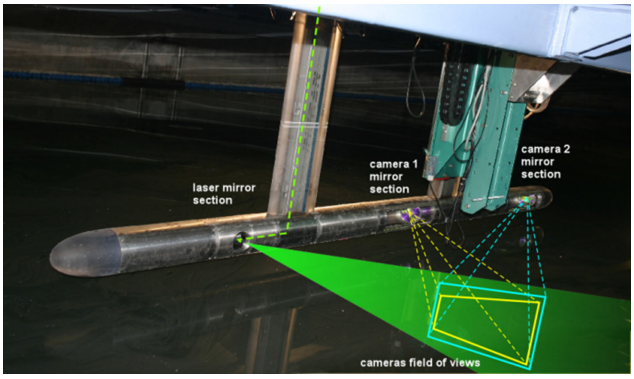

Figure 2.7: Submersible, torpedo-like stereo PIV system for towing tanks by Falchi et al. (2014).

The above studies demonstrate the advantages of using a compact PIV probe and manipulating it by a traverse mechanism to compose the desired measurement domain. A dominant advantage is that the relative position of the imagers and the light sheet is fixed, and therefore, the calibration does not need to be repeated after changing the PIV probe position.

More recently, an alternative approach was presented by Michaux et al. (2018), in which two PIV cameras and a laser including light sheet optics are separately supported by one robotic arm each. The seven-axis robots are mounted on linear traverses which allow large translations in the streamwise direction. Such configuration provides more freedom to align the individual components, e.g. when optical access is limited. Yet, it demands a precise positioning from the robotic manipulators, as a change in the relative position between the PIV system components may

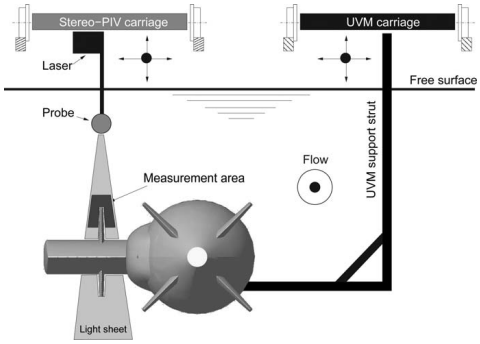

(a) Towing tank setup

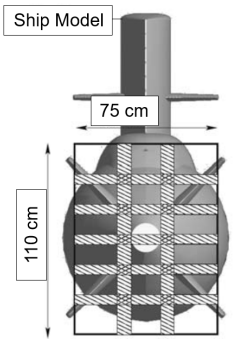

(b) Composition of the domain

Figure 2.8: Scanning PIV on a submersible ship model. Images reproduced from Di Felice et al. (2007).

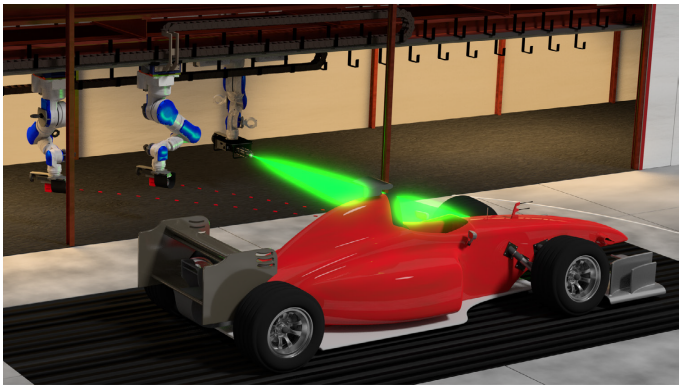

(a) RoboPIV in a motorsports wind tunnel

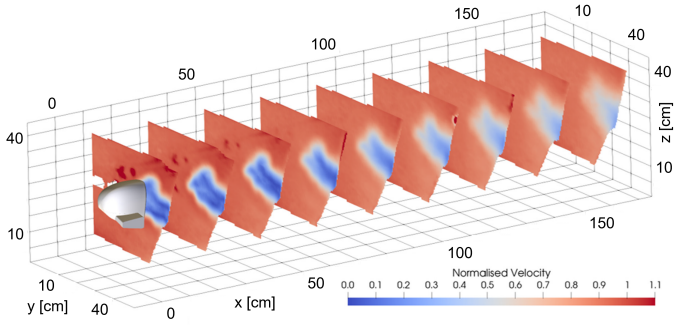

(b) Wake flow measurement downstream of a wing mirror

Figure 2.9: The stereoscopic RoboPIV system developed by Michaux et al. (2018). Images reproduced from Michaux et al. (2018).

impact the flow measurement capability. While a similar system was already presented in Figure 1.2, Figure 2.9 shows another illustration of this state-of-the-art, so-called *RoboPIV*, system along with an exemplary measurement of the wake flow downstream of a car mirror.

The few examples illustrated in this section provide a brief overview of available scanning PIV systems, and it has illustrated the benefits of compact PIV probes in such scanning concepts. This is only a glimpse of the examples available in the literature. Nonetheless, in particular the last example shown in Figure 2.9(b) demonstrates how a 3D flow measurement can be constructed by multiple 2D-3C measurements. In this thesis, Chapter 3 investigates the option to accomplish a fully volumetric (3D-3C) measurement approach by a similar volume scanning principle.

2.2.3. Tracer particles

Returning to the more general challenges of PIV at large scale, one finds that the appropriate selection of tracer particles is fundamental to any PIV measurement. Assessing the fluid velocity through quantification of particle displacements in images implies that the disparity between the particles and the fluid motion is negligible. In other terms, the particle velocity must adapt rapidly to any change in the fluid velocity, which is quantified by the particle response time τ_p (Raffel et al., 2018). For a small spherical tracer, the response time reads

$$\tau_p = \frac{d_p^2}{18} \frac{(\rho_p - \rho_f)}{\mu} \tag{2.1}$$

Where ρ_p and ρ_f represent tracer particle and fluid density, respectively. The above equation is derived from the Stokes drag which assumes the particle-fluid interaction is dominated by viscous forces and therefore, it is only valid for small particles. The fluid kinematic viscosity, in terms of density ρ_f and dynamic viscosity μ, is a given property of the fluid of interest, meaning that the only parameters that can be varied are the particle diameter d_p and density ρ_p. Consequently, the response time in Equation (2.1) is minimised by selecting small particles (reducing d_p), or by choosing neutrally buoyant tracers with particle density approaching that of the fluid ($\rho_p \approx \rho_f$). Commonly, the response time is considered acceptable if the Stokes number Stk is below 0.1.

$$Stk = \frac{\tau_p}{\tau_f} \tag{2.2}$$

where τ_f is the relevant flow time scale.

Intuitively, the tracer size will affect the light scattering properties of the particles. The smaller the tracer, the less light will be scattered and vice versa. The amount of light scattered increases proportional to the scattering cross-section which scales with the square of the particle diameter. An in depth study of tracer particle scattering characteristics for PIV was carried out by Melling (1997).

For volumetric particle velocimetry scattering efficient tracers are essential, as the illumination intensity rapidly decays if the light is expanded over a large cross section. Additionally, to image tracer particles in focus, the focal depth δz must be greater than or equal to the illuminated measurement volume depth Δz. Focal

depth is proportional to $f_\#^2$, with $f_\#$ being the f-number (or f-stop), indicating the ratio of focal length f to lens aperture diameter D. Thus, for a given focal length, the amount of light passing through the lens scales with $f_\#^{-2}$, further lowering the light intensity captured on the camera sensor. Lastly, when the particle image is diffraction limited, the particle image diameter d_τ is directly proportional to $f_\#$. A larger particle image diameter yields a reduced peak particle intensity I_p.

The combination of the above factors, namely the light expansion into a volume, the necessary focal depth, and the increase in diffraction, presents a real challenge for large-scale 3D PIV measurements. To illustrate, let us consider a domain with a fixed field of view and a given volume depth Δz. From the outlined relations it follows that peak particle intensity scales with $I_p \propto \Delta z^{-3}$. Thus, doubling the measurement depth, results in an order of magnitude decrease in the particle intensity. Therefore, scattering-efficient tracers with relatively large diameter but density equivalent to the fluid density are the preferred choice for large-volume measurements.

For applications in air flows, helium filled soap bubbles (HFSB) have emerged as neutrally buoyant particles. Caridi et al. (2016) demonstrate that the HFSB tracers scatter approximately $10,000$ times more light compared to conventional micron-sized PIV tracers. The response time of a nominal $300\,\mu$m diameter HFSB tracer is reported within $10-30\,\mu$s by Scarano et al. (2015). Likewise, Faleiros et al. (2018) reports slightly larger HFSB of $550\,\mu$m diameter with a similar response time of $30 \pm 20\,\mu$s based on a particle density of $1.1 \pm 0.05\,\mathrm{kg/m^3}$. The latter observation supports the assumption of neutral buoyancy ($\rho_p \approx \rho_f$) for such HFSB tracers, when used in atmospheric conditions. A more detailed analysis of the HFSB production regimes and its effect on bubble size, weight and response time is found in the work of Faleiros et al. (2019).

Using HFSB seeding technology, measurement volumes of several litres are reported, e.g. by Caridi et al. (2016) who analysed the tip vortex on a vertical axis wind turbine in a $40\times20\times15\,\mathrm{cm^3}$ volume, and Schanz et al. (2016) who realised 4D flow data on a $0.5\,\mathrm{m^3}$ domain in a confined vessel. In stereoscopic studies, HFSB tracers have enabled on-site and outdoor flow measurements for the aerodynamic analysis of athletes, as demonstrated by Spoelstra et al. (2019) who completed wake measurements on professional cyclists, and lately also on speed skaters as shown in Figure 2.10.

HFSB are typically generated by coaxial, orifice-type nozzles following the initial design of Bosbach et al. (2009). An illustration of the generator architecture along with a shadowgraph of the bubble production is shown in Figure 2.11.

A fluid supply unit controls the flow rates of air, helium and soap solution (BFS) provided to the bubble generator. Faleiros et al. (2019) studied the impact of the relative flow rates on the bubble characteristics, in terms of size, production rate and buoyancy. Depending on the operating conditions and nozzle design $10,000-70,000$ tracers/second are produced by one nozzle. Such high production rates are necessary for seeding of relevant measurement volumes. In fact, single nozzles are often insufficient to seed the desired measurement volume and consequently, rakes housing multiple nozzles are designed to enhance the tracer particle concentration.

Figure 2.10: On-site aerodynamic study of a speed skater with HFSB tracers for stereoscopic PIV measurements. Image reproduced from TU Delft (2021).

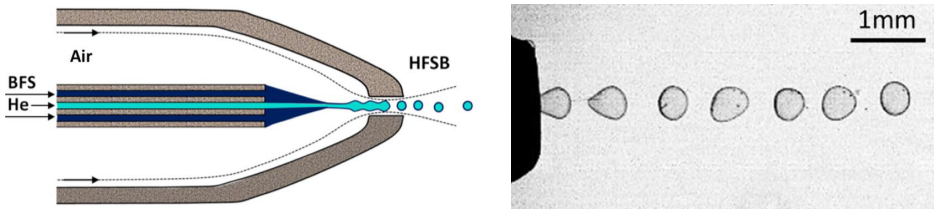

(a) Coaxial HFSB nozzle architecture (b) Shadowgraph of bubble production

Figure 2.11: HFSB nozzle design and operation. Figures reproduced from Faleiros et al. (2018).

Faleiros (2021) recently presented a 400-nozzle, 3×3 m^2 cross section HFSB seeding system for operations in the Large Low-Speed Facility (LLF) of the DNW laboratories, whereas Gibeau and Ghaemi (2018) suggest placing the HFSB nozzles in-line to enhance the local seeding concentration.

2.3. Measurement chain: from images to velocity

The general principle of PIV has been established earlier in this chapter. The details of PIV image acquisition, analysis, and subsequent processing of the velocity data are discussed in this section.

2.3.1. Image acquisition strategies

PIV images can be recorded in a variety of modes, changing the number of frames and light exposures per frame. If we disregard single-frame and multi-exposure techniques, two modes of acquisition remain: double-frame (single-exposure), and

multi-frame (single-exposure) imaging (Raffel et al., 2018, chapter 3). A schematic timing diagram for the two modes is provided in Figure 2.12.

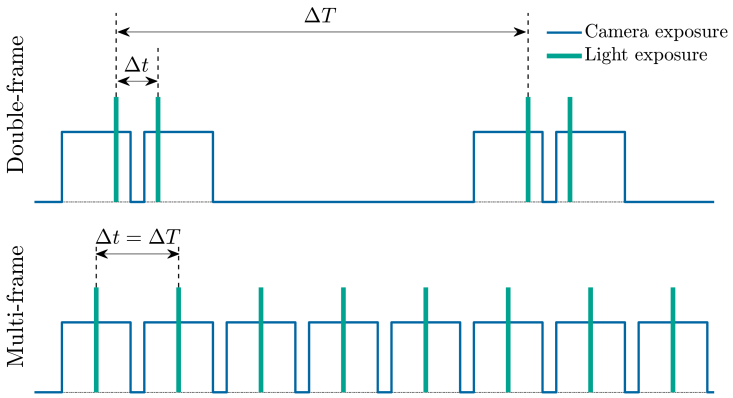

Figure 2.12: Timing of camera and light source in double-frame (top) and multi-frame (bottom) acquisition. Figure adapted from Caridi (2018).

In double-frame mode, two image frames are taken in rapid succession. One light pulse in each of the frames, separated by a time interval Δt, captures the instantaneous position of the tracer particles in the image. After one image pair is recorded, it takes relatively long to read out the images and to recharge the light source, such that the subsequent image pair will be taken at an interval ΔT, where $\Delta T \gg \Delta t$. Consequently, image pairs in double-frame mode are usually uncorrelated with respect to the integral flow scales.

In multi-frame imaging, instead, images are taken at a continuous time separation Δt. The latter must be sufficiently small to correlate particles in one frame with those in the subsequent frame. Thus, multi-frame acquisitions are also referred to as time-resolved. Time-resolution is sometimes stated as the fourth measurement dimension, adding to the three spatial axes, as indicated in Figure 2.2. Multi-frame PIV requires high-speed cameras and lasers (or LEDs), which limits image quality and light intensity. On the positive side, one can take advantage from the available temporal information, as will be shown in the following section.

2.3.2. Image analysis: PIV or PTV?

Similar to the image acquisition modes, also the image analysis techniques can be categorized into two classes: correlation-based methods, and tracking of individual particles. The latter is also often referred to as particle tracking velocimetry (PTV), or Lagrangian particle tracking (LPT). Irrespective of the chosen approach, both methods rely on particle images and therefore, they are equally referred to as particle image velocimetry (PIV) techniques in this document.

In correlation-based image analysis, particle images are sectioned into windows, such that each window contains $\mathcal{O}(10)$ tracer particles. Each so-called interrogation window is then cross-correlated with the same window in the subsequent frame.

The peak of the cross-correlation map indicates the mean particle displacement for that window, which upon division by Δt yields the velocity measurement. The process is schematically illustrated in Figure 2.13.

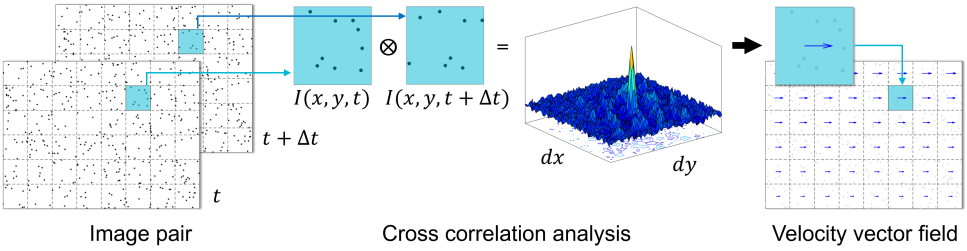

Figure 2.13: Principle of correlation-based PIV image analysis.

In today's practice cross-correlation analysis is normally executed in an iterative manner, with a successive reduction (and deformation) of the interrogation window size (Scarano, 2001). For volumetric measurements the analysis is extended to 3D interrogation volumes. To maintain a robust signal in the cross-correlation, a window (or volume) shall contain at least five particles (Scarano, 2012). The minimum interrogation window size, which presents a limit for the achievable spatial resolution, is therefore dictated by the tracer particle seeding concentration. The latter can, however, not be increased arbitrarily. At excessive seeding concentration, the particle image density in particles per pixel (ppp) exceeds the limits that can be handled by the tomographic reconstruction and particle triangulation algorithms when considering volumetric flow analysis. Above this limit the number of falsely reconstructed, so called ghost particles (Maas et al., 1993), corrupts the velocimetry analysis.

The spatial resolution is raised beyond that of the correlation-based analysis if individual particles are tracked, yielding one velocity vector per tracer rather than one per interrogation volume. The pitfall in this reasoning is that the particle image density requirements for particle tracking tends to be more stringent, given that any particle pairing with a ghost particle yields a false velocity measurement.

To quantify the PIV measurement resolution, it is good practise to use the dynamic spatial and velocity range, DSR and DVR. The dynamic ranges describe the ratio of the largest- to smallest resolvable length and velocity scales, respectively (Adrian, 1997).

$$DSR = \frac{L_x}{l_v} \tag{2.3a}$$

$$\overline{DVR} = \frac{\overline{u}_{max}}{\overline{u}_{min}} \tag{2.3b}$$

Classically, DSR and DVR are defined for instantaneous data, but the velocity range can analogously be specified for time-averaged analysis as shown in Equation (2.3b). For the spatial range, L_x presents the characteristic length of the mea-

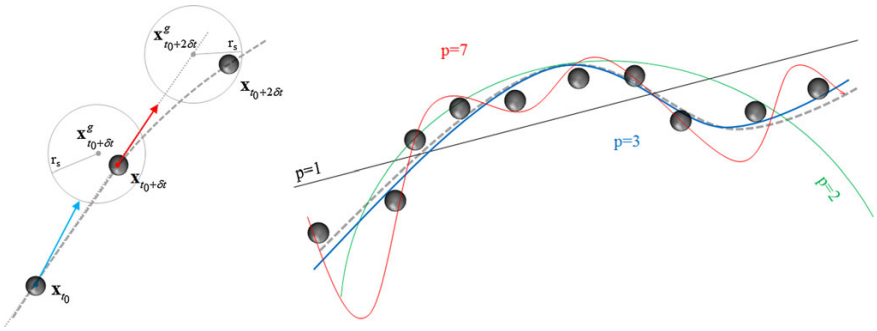

Figure 2.14: Schematics of Lagrangian particle tracking in time-resolved acquisitions. Principle of particle tracking with predictor (left), and polynomial trajectory fitting (right). Figure reproduced from Novara and Scarano (2013).

surement domain, and l_v is a measure of the smallest resolvable spatial scale, usually defined by the linear interrogation window (or volume) size in cross-correlation based analysis, or the mean inter-particle distance in particle tracking approaches.

Only recently, robust 3D particle reconstruction and tracking methods have been introduced that lift the acceptable ppp to the equivalent level of correlation based analysis (Schanz et al., 2016; Wieneke, 2012). Both methods, the iterative particle reconstruction (IPR, Wieneke, 2012) and Shake-The-Box (STB, Schanz et al., 2016), work directly on the 3D particle positions rather than the intensity distribution in voxelized 3D volumes common to tomographic reconstruction algorithms.

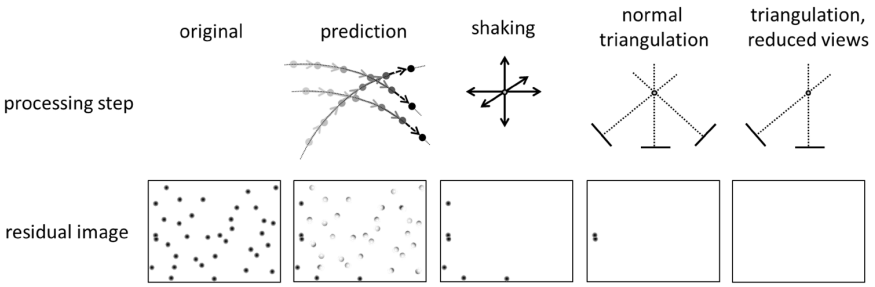

Figure 2.15: Working principle of the *Shake-The-Box* algorithm, with prediction of particle positions. Image reproduced from Schanz et al. (2016).

The STB algorithm takes the iterative particle reconstruction one step further by predicting the particle positions in the subsequent image, based on the particles trajectories tracked in the previous (time-resolved) images. The principle is illustrated in Figure 2.15.The Lagrangian tracking approach carries two key advantages: on one hand, the method is computationally efficient. On the other hand, the particle tracks can be regularized, e.g. by fitting of low-order polynomial functions, as indicated in Figure 2.14. In this way, the tracking accuracy is enhanced, and non-physical tracks that result from ghost particles are effectively filtered, be-

cause ghost particles do not produce coherent tracks across multiple images. Thus, the STB algorithm allows to track individual particles in 3D space at high seeding concentration.

Focusing on the data structure of correlation- and tracking-based 3D velocimetry samples, the two differ critically: whereas the interrogation windows and volumes provide a structured grid for the 3D velocity data, the particle tracks are dispersed at the tracers positions in 3D space. A meaningful analysis of such dispersed data is challenging. Therefore, particle track data is often mapped onto structured grids. An example of a jet flow measurement by Novara et al. (2018), containing a particle track visualization as well as the corresponding averaged velocity field is given in Figure 2.16. Regularization of disperse velocity measurements is addressed in the subsequent section.

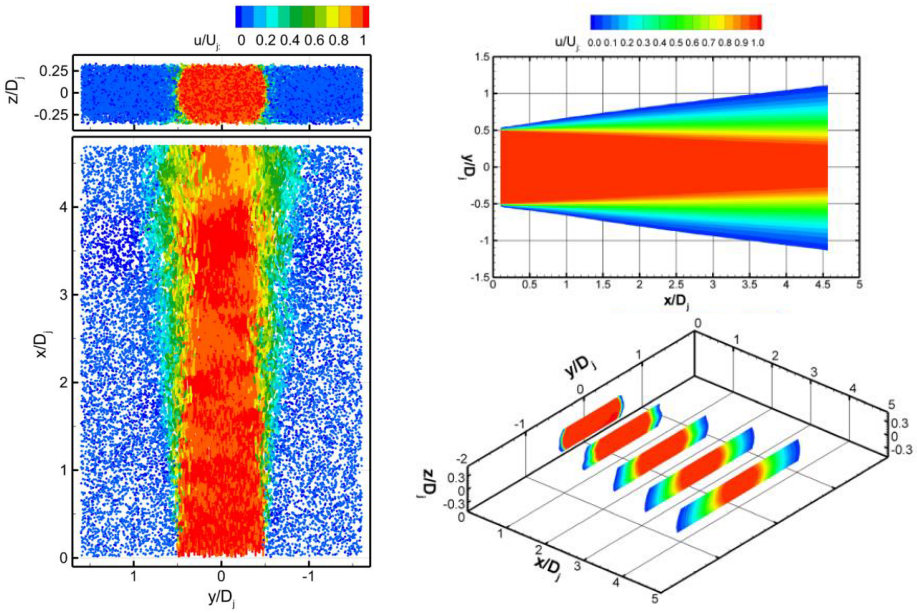

(a) Instantaneous LPT tracks

(b) Ensemble averaged velocity field

Figure 2.16: Visualization of LPT data and corresponding averaged velocity field. Figure reproduced from Novara et al. (2018).

2.3.3. Mean flow analysis by ensemble averaging

This section discusses the conversion of unstructured particle track data onto a structured grid. In this data reduction exercise, one must distinguish between the evaluation of instantaneous and time-averaged velocity fields. For densely seeded, unsteady flows the experimentalist is often interested in the analysis of the instantaneous flow data. The conversion of instantaneous particle tracks to structured formats has been tackled in various ways (e.g., Agüí and Jimenez, 1987; Casa and

Krueger, 2013; Gesemann et al., 2016; Jeon et al., 2018a; Schneiders and Scarano, 2016; Vedula and Adrian, 2005, among others). In this thesis, the focus instead lies on the evaluation of the time-average flow field.

For the time-average analysis of particle track data, the velocity information belonging to an ensemble of particles is averaged in both, space and time. Hence, the process is frequently referred to as a spatio-temporal ensemble averaging. The common strategy that is pursued in this thesis works on the following basis:

1. The measurement domain is discretised into small, equally shaped and spaced sub-volumes. Each of these volumes, also referred to as cells or bins, will represent one velocity measurement at its centre.
2. The particle tracks are assigned to the cells, based on their spatial position. This step leads to an ensemble of particle velocity readings for each cell.
3. The velocity readings are averaged per cell, yielding the mean velocity field on the Cartesian grid defined by the cells. Averaging schemes range from an arithmetic mean to fitting of distribution functions and beyond.
4. Once the mean velocity for a cell is computed, also a statistical analysis in terms of velocity fluctuations can be performed, e.g., evaluation of the root-mean-square (rms) velocity fluctuations.

A detailed description on this type of ensemble averaging procedure, specifically for 3D PTV data is presented by Agüera et al. (2016). The authors compare different averaging approaches of the particle track data, including the arithmetic mean, also referred to as the top-hat average, computed through

$$\overline{\mathbf{u}} = \frac{1}{N}\sum_{i=1}^{N}\mathbf{u}_i \tag{2.4}$$

where N is the number of particles in a bin, recorded over the full course of the acquisition period T_{aq}. The arithmetic mean must be regarded as the most simple mean computation. To account for the distance between a particle and the cell centre, weighting functions can be used giving more importance to particle readings close to the cell centre. Perhaps the most common in this respect is the application of Gaussian weighting functions. The averaging calculation then reads,

$$\overline{\mathbf{u}} = \frac{\sum_{i=1}^{N} w_i \mathbf{u}_i}{\sum_{i=1}^{N} w_i} \tag{2.5}$$

Where w_i are the cell-centre distance based weights. Whereas this approach may provide a more accurate estimation of the cell centred mean velocity, it cannot account for spatial velocity gradients. The latter is achieved by fitting a polynomial function for each cell. For the most simple case of a linear distribution function, the mean velocity is then given by,

$$\overline{\mathbf{u}} = a_0 + a_1\Delta x + a_2\Delta y + a_3\Delta z \tag{2.6}$$

Where $\Delta\mathbf{x}$ is the (particles) distance to the cell centre, and the coefficients a_i are determined through least-squares regression. The advantage of fitting a distribution function is twofold: as indicated, velocity gradients inside a cell can be captured. In fact, for the linear model in Equation (2.6) the coefficients a_i directly provide the spatial velocity gradients $\nabla\overline{\mathbf{u}}$. Because the velocity distribution inside a cell is described through a function, the particles velocity fluctuations can be evaluated as a function of the local mean, rather than the cell centred mean which otherwise tends to overestimate average velocity fluctuations. The work by Agüera et al. (2016) suggests to use second order polynomials to fit the velocity distribution inside a fluid cell, as indicated in the visualization of the three above averaging approaches in Figure 2.17. Higher order models have the potential to increase accuracy, at the risk of being susceptible to measurement noise.

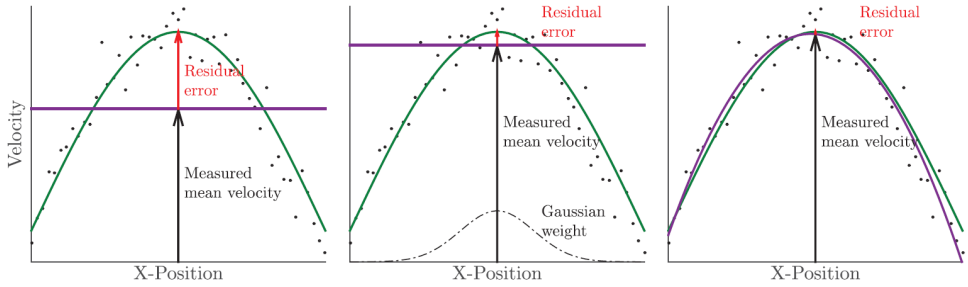

(a) Arithmetic mean (b) Gaussian weighting (c) Polynomial fit

Figure 2.17: Comparison of ensemble averaging schemes. Exact (parabolic) velocity distribution in green, black dots indicating particle velocity measurements, and purple curve shows filtered mean. Figure reproduced from Agüera et al. (2016).

Recent literature features further advancements in the field of ensemble averaging for 3D particle track data. One example thereof is the adaptive ensemble averaging presented by Raiola et al. (2020) which attempts to enhance spatial resolution by stretching the averaging cells along the direction of maximum curvature of the velocity fields. An alternative approach to enhance spatial resolution is presented by Godbersen and Schröder (2020). The latter work integrates the full particle trajectories, approximated by a polynomial fit, rather than considering only the discrete particle positions corresponding with the PIV frames. Doing so, averaging cells can be decreased in size, enhancing spatial resolution at the expense of increased computational burden. Despite the potential of these approaches, they have not been implemented for the content of this thesis, and instead, the simpler yet robust methods outlined above are chosen.

2.4. Beyond velocity: pressure from PIV

Particle image velocimetry systems are designed to measure a fluid flow velocity in a 2D or 3D domain. The previous sections detailed the principles and methods

relevant to this thesis, with focus on the evaluation of the time-average, 3D velocity field based on particle track data. The recorded velocity field can now be analysed to compute further flow variables. One of the most studied items in aerodynamics is the flow pressure, given that next to shear friction it is the only mechanism that can exert a force onto a body moving through a fluid (Anderson, 2011). PIV based pressure evaluations have gained popularity over the past two decades, and for a topical review the reader is referred to the work of van Oudheusden (2013).

2.4.1. Governing equations

By definition, pressure is a normal force per unit area. In aerodynamics one distinguishes between total, static and dynamic pressure. For incompressible and irrotational flow, the three quantities are related by Bernoulli's equation:

$$p_0 = p + \frac{1}{2}\rho\,(\mathbf{u}\cdot\mathbf{u}) \tag{2.7}$$

where p_0 is the total, p the static, and $q_\infty = \frac{1}{2}\rho\,(\mathbf{u}\cdot\mathbf{u})$ the dynamic pressure. ρ is the fluid density, and $|u|$ is the velocity magnitude. If referring only to a flow pressure in aerodynamics, by default it is assumed to relate to the static pressure.

The key to derive pressure from a velocity measurement is knowledge of the governing equations, in this case the conservation of momentum. The latter balances any change in fluid momentum to the forces acting on the fluid, those being pressure forces, viscous shear stresses, and body forces. For an incompressible flow ($\nabla\cdot\mathbf{u} = 0$), the momentum equation reads,

$$\rho\frac{D\mathbf{u}}{Dt} = -\nabla p + \mu\nabla^2\mathbf{u} + \mathbf{f} \tag{2.8}$$

with the spatial pressure gradient ∇p, the viscosity μ, body forces $\mathbf{f}$ and the material derivative of the velocity $\frac{D\mathbf{u}}{Dt}$. Expressing the material derivative in an Eulerian framework yields,

$$\frac{D\mathbf{u}}{Dt} = \frac{\partial\mathbf{u}}{\partial t} + \mathbf{u}\cdot\nabla\mathbf{u} \tag{2.9}$$

where determination of the material acceleration is only necessary for evaluation of the instantaneous pressure field. If dealing with time-average data, as is the focus in this dissertation, the local time derivative of the velocity (the Eulerian acceleration) $\frac{\partial\mathbf{u}}{\partial t}$ is zero, simplifying the PIV based evaluation of Equation (2.9). For the time-average analysis, Reynolds averaging is applied to the momentum equation (Equation (2.8)). Rearranging to isolate the time-average pressure gradient, and assuming absence of body forces yields,

$$\nabla\overline{p} = -\rho\left(\overline{\mathbf{u}}\cdot\nabla\right)\overline{\mathbf{u}} - \rho\nabla\cdot\overline{\mathbf{u}'\mathbf{u}'} + \mu\nabla^2\overline{\mathbf{u}} \tag{2.10}$$

which now includes the Reynolds shear stress term ($\overline{\mathbf{u}'\mathbf{u}'}$). Note that the above equation contains all three velocity components of $\mathbf{u}$ as well as their spatial derivatives in all three axis directions; calling for fully volumetric velocimetry measurements. Integration of Equation (2.10) finally provides the sought pressure field.

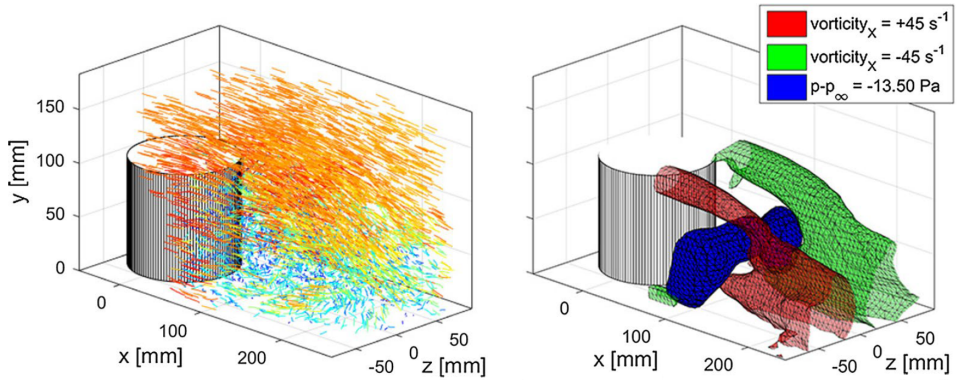

(a) 3D particle distribution, with particles colored by velocity magnitude.

(b) Time-averaged isosurfaces of pressure and vorticity in the cylinder wake.

Figure 2.18: Large-scale, tomographic PTV-based pressure measurement downstream of a truncated cylinder. Figures reproduced from Schneiders et al. (2016).

Literature on PIV based pressure evaluation converges to two main methods for the task of integrating the pressure gradient: direct spatial (marching) integration of the mean pressure gradient (e.g. Liu and Katz, 2006), and the Poisson approach (e.g., Gurka et al., 1999) which solves the divergence of the pressure gradient equation in a global approach. Limitations and advantages of the two methods in the context of this work are elaborated in Chapters 4 and 5. Chapter 4 addresses the pressure distribution in the wake of a truncated cylinder, similar to the case studied by Schneiders et al. (2016) who present pressure evaluations in a 6 L volume based on tomographic PTV measurements as illustrated in Figure 2.18. Subsequently, Chapter 5 focuses on the pressure measurement on a test model surface.

2.4.2. Boundary conditions

No matter if choosing the Poisson, or spatial integration solution for pressure evaluation, both methods require the specification of boundary conditions. Commonly, Neumann conditions ($dp/d\mathbf{n}$, the pressure gradient in the direction of the surface normal $\mathbf{n}$ is specified) are specified on most boundaries, given that the pressure field is not known yet. If specifying Neumann boundary conditions exclusively, the pressure field may, however, only be solved up to an integration constant. The issue is solved by specifying a Dirichlet boundary condition (p is specified) through measurement of a reference pressure in at least one point. The latter can be circumvented if a Dirichlet condition is specified based on reasonable flow assumptions, such as irrotational flow condition.

Appropriate boundary condition specification is crucial, as any error propagates into the pressure field. In terms of error propagation, the spatial integration of the pressure gradient approach is prone to accumulation of local measurement errors along the integration path and such errors vary along different paths to the same

point, yielding a path dependency. On the other hand, the method can be tailored such that the regions of largest error (often the solid boundaries) are reached only at the end of the path (e.g., Dabiri et al., 2014). The Poisson approach provides a global solution and solves the previous problem of sensitivity to the integration path. The method, however, propagates errors arising from the boundaries in the entire domain, let them be Neumann or Dirichlet condition. Figure 2.19 indicates the type of boundary conditions to be specified for the two approaches.

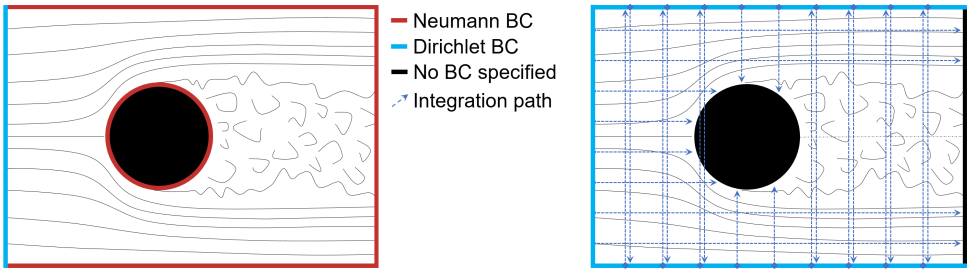

(a) Poisson. (b) Path integration.

Figure 2.19: Schematic of boundary conditions (BC) for the pressure field evaluation on a 2D cylinder flow, using a Poisson approach and a spatial integration scheme.

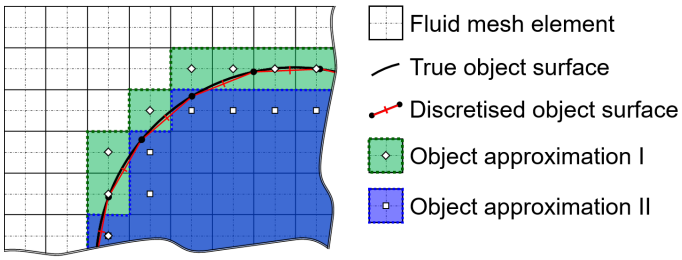

Figure 2.20: Representation of a curved object on a uniform Cartesian grid. Modelling the 'true' curved surface by grid elements with cell centres inside the geometry results in the blue-shaded body (boundary cell-centres indicated by hollow squares), whereas considering all grid elements which penetrate the object yields the green-shaded shape (boundary cell-centres indicated with diamonds).

In the study of immersed objects, an additional difficulty arises from the mismatch at the fluid-solid interface between the two systems of coordinates (fluid & surface mesh), which results into uncertainties for specifying the boundary conditions for the Poisson problem. This is illustrated in Figure 2.20 for the case of a generic curved fluid-solid interface.

The illustration shows the effect of a coarse discretization introducing an uncertainty in the boundary condition specification and compromising the pressure field evaluation. Some effects of error propagation through incorrect boundary condition specifications in PIV-based pressure field calculations are discussed in the work of Pan et al. (2016). The treatment of boundary conditions, especially those on the

model surface, takes a special role when discussing the evaluation of surface pressure measurements based on 3D PIV data in Chapter 5.

2.5. From fluid to solid: surface detection in PIV

PIV is designed for the accurate velocity measurement of fluid flows. Many engineering studies focus on the flow around objects immersed in the fluid stream. For meaningful data interpretation, determination of the object surface position and orientation is deemed essential, especially if one is interested in surface flow properties such as pressure or even skin friction.

The object geometry may be known a-priori, e.g. by a computer-aided design (CAD) model, and determining a small number of reference points on its surface may sound a trivial solution. This approach, however, does not account for several sources of uncertainty: production and assembly tolerances, model deformations due to mechanical and aerodynamic loads or thermal stresses. The latter justifies the need for in-situ measurements of the fluid-solid interface.

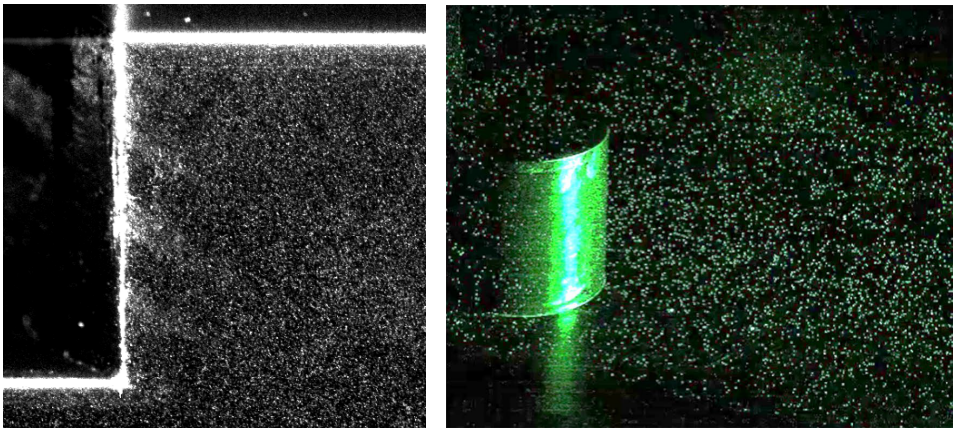

(a) 2D PIV image from a cavity flow experiment, reproduced from Adatrao et al. (2019).

(b) 3D PIV image from a truncated cylinder flow experiment, reproduced from Schneiders et al. (2016).

Figure 2.21: Example images of light reflections on immersed objects in 2D and 3D PIV imaging.

For 2D PIV studies, the fluid-solid interface can be retrieved through the sharp light reflection resulting from the light sheet striking the object. An example is provided in Figure 2.21(a). A range of image-based feature and edge detection methods is available to identify the model silhouette from such reflections; more details are discussed in Chapter 6. In 3D PIV studies the problem of fluid-solid interface detection is challenged by the diffuse illumination, which does not produce the characteristic sharp reflection on the object surface, as seen in the example provided in Figure 2.21(b). Therefore the object shape must be retrieved in a different way in volumetric studies.

An alternative approach to accurately determine the object surface is the intro-

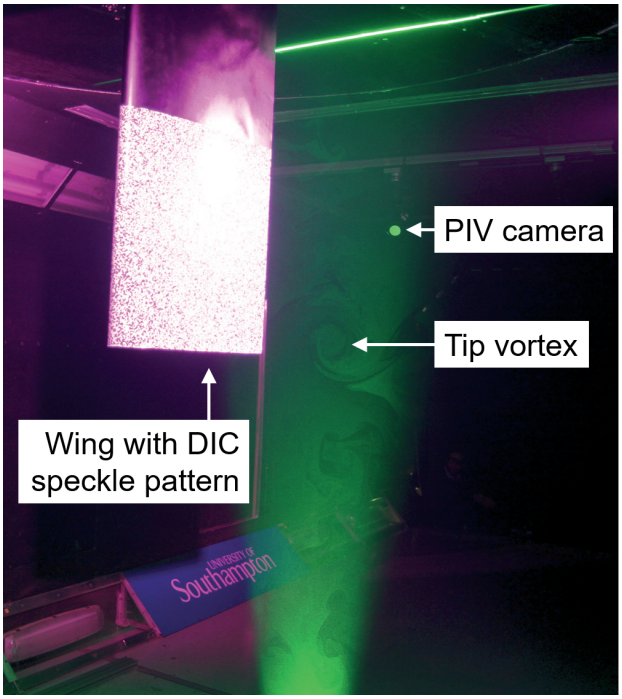

Figure 2.22: Simultaneous DIC and PIV measurement. Figure reproduced from Giovannetti et al. (2015).

duction of an independent measurement system. Photogrammetry software and 3D scanning systems for 3D object reconstructions are commercially available, however, these approaches rely either on some level of surface texture or the reflection of a light pattern projected onto the object. PIV models, instead, are usually painted black to avoid light reflections. Thus, the application of the aforementioned techniques is unpromising, unless the model surface can be treated accordingly.

Such dual-measurements are still seen in fluid-structure-interaction (FSI) studies, which feature the fluid flow analysis e.g. by PIV, combined with the study of the model's structural response e.g. by digital image correlation (DIC). The latter does require to distribute markers on the model surface, as indicated in Figure 2.22.

Two recent examples of such approach are presented by Zhang et al. (2019) on a flexible cantilever plate in a water current, and by Acher et al. (2019) who studied the deformation of a flexible wing with a synchronized DIC and tomographic PIV measurement. In some cases, operating two separate systems may not be affordable, motivating the development of FSI methods in which the flow imaging system simultaneously captures the structural deformation. Such approaches typically rely on image separation strategies to distinguish between the flow tracers, and a marker pattern on the object surface. Examples include the works of Jeon and Sung (2012) and Im et al. (2015) on the flow around arbitrarily moving bodies, the studies of Mitrotta et al. (2019) and Mertens et al. (2021a) on a plate and a wing

under gust loading, and the investigation of Saiz et al. (2021) on a flexible panel in a cylinder wake. This type of approach, however, carries two disadvantages:

1. It may not be feasible, e.g. when the model surface cannot be treated.
2. It increases the information density on the imaging system, usually quantified in particles per pixel (ppp), which can hamper the achievable spatial resolution in the flow measurement.

These observations motivate the interest in interface detection approaches solely based on the fluid flow tracer measurements, as obtained by PIV techniques.

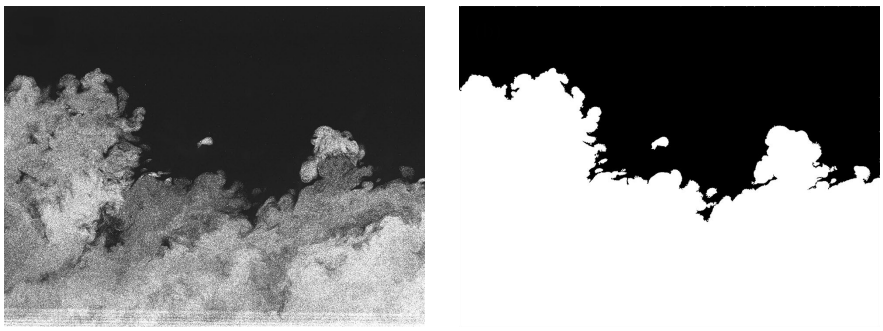

(a) Raw image (b) Separated and binarized image

Figure 2.23: PIV image of a turbulent flow with a seeded and a non-seeded phase. The particle presence provides a means to separate the two phases. Images reproduced from Reuther and Kähler (2018).

Flow measurement based 3D surface reconstruction techniques are the focus in Chapter 6. The fact that tracer particles do not enter the solid body can be exploited by discriminating a void phase corresponding to the solid body from a seeded phase pertaining to the fluid flow. This principle is likewise suitable for identification of fluid-fluid interfaces, e.g. in multi-phase flows where only one phase carries tracer particles as indicated in Figure 2.23. Chapter 6 proposes a new method to identify the fluid-solid interface based on such discrimination of void and seeded phase.

Part I

Measurement Technology and Instrumentation

3

Robotic volumetric PIV

The literature study in Chapter 2 revealed two main limitations that prevent greater dissemination of 3D PIV systems in industrial facilities and sports aerodynamics: first, the general system complexity; and second, the small volumes achievable with state-of-the-art PIV instrumentation. Therefore, alternative PIV concepts are necessary to overcome these challenges. This chapter proposes the novel robotic volumetric PIV system, which integrates developments from different disciplines in order to realize a compact measurement device suitable for the study of large flow domains.

The chapter contains three parts. Robotic volumetric PIV builds on the concept of coaxial volumetric velocimetry (CVV), which is discussed in Section 3.1. The key potential of a CVV probe lies in its compactness, which enables rapid repositioning of the probe without demanding a new calibration. Consequently, coupling a CVV probe with robotic arm manipulation ensures an efficient volume scanning process. This approach is presented in Section 3.2. Subsequently, the proposed measurement concept is demonstrated in Section 3.3, where the flow around a 15 cm diameter sphere is studied. In Part II of this thesis, the approach will be applied to selected examples in the field of sports aerodynamics.

Schneiders JFG, Scarano F, Jux C and Sciacchitano A. Coaxial volumetric velocimetry, *Meas. Sci. Technol.* **29**, 065201 (2018)

Jux C, Sciacchitano A, Schneiders JFG and Scarano F. Robotic volumetric PIV of a full-scale cyclist, *Exp. Fluids* **59**, 74 (2018)

3.1. Coaxial volumetric velocimetry

The coaxial volumetric velocimeter (CVV), recently introduced by Schneiders et al. (2018), is a compact measurement device that has the potential to exploit the full advantage of robotic manipulation. The literature survey in Chapter 2 revealed that large-scale PIV measurements around complex objects require the superposition of a multitude of observation domains along different directions. The latter can only be approached by the operation of a three-dimensional measurement system that does not require calibration after repositioning of the measurement probe. Such characteristics are found in the CVV system, which is described in this section.

3.1.1. Working principle

The working principle of CVV is akin to tomographic PIV (Elsinga et al., 2006). Alignment of the imaging and illumination axes with four cameras at considerably lower tomographic aperture (see Figure 3.1) as compared to the setup used in tomographic PIV experiments yields unique imaging characteristics.

The measurement volume depth resulting from the CVV arrangement typically exceeds the volume width and height, as opposed to the situation encountered with thin or thick sheet measurements in tomographic PIV. The depth of field (DOF) may reach well up to 1 m and implies considerable variations of the particle imaging properties along the depth direction (z).

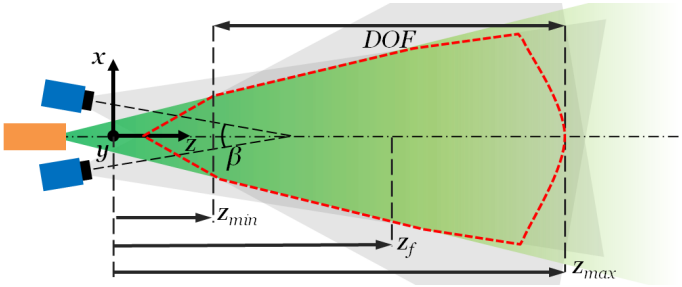

Figure 3.1: 2D illustration of coaxial volumetric velocimetry including reference frame definition, reproduced from Schneiders et al. (2018). Cameras (blue) at tomographic aperture angle β in a coaxial arrangement with the laser light source (orange). Illumination volume indicated in green, whereas field of view is grey. The overlap of the latter defines the measurement region outlined in dashed red.

Particle detection and tracking probability is maximized when particle images are formed in focus. This condition requires a depth of field encompassing the full depth of the measurement domain. It follows that for a large depth of field, a high $f_\#$ (low numerical aperture) is necessary,

$$DOF \propto f_\#^2 \tag{3.1}$$

which limits the amount of light received by the camera.

The particle image displacement of a tracer at velocity u is inversely proportional to the distance z. The variation is due to the optical magnification M being inversely proportional to the object distance z ($M \times z = constant$). It is noted that in

the nominal working range, particle images recorded in the CVV configuration are diffraction limited.

In the above conditions the particle image intensity of the coaxial imaging and illumination arrangement obeys an inverse fourth order relation with object distance:

$$I_p \propto z^{-4} \tag{3.2}$$

It follows that the maximum measurement distance z_{max} is limited by the relative particle image intensity with respect to the detector noise level. Furthermore, classical micron sized PIV seeding particles do not scatter enough light to achieve a volumetric measurement by the CVV principle. Therefore, larger tracing particles such as helium filled soap bubbles (HFSB, Section 2.2.3) with a typical tracer diameter of $300 - 500\,\mu$m (Scarano et al., 2015) are required to attain large-scale 3D measurement volumes in a coaxial arrangement. Conversely, the closest distance where measurements are still valid (z_{min}) is limited by the aerodynamic interference between the coaxial velocimeter head, also referred to as the CVV probe, and the airflow. The latter is studied in Section 3.1.4.

3.1.2. Measurement uncertainty

The low tomographic aperture angle in CVV affects the positional uncertainty in the 3D particle reconstruction. Schneiders et al. (2018) shows that the in-plane uncertainty (ϵ_x, ϵ_y) must be distinguished from the uncertainty in the viewing direction (ϵ_z). The former is, analogous to conventional (planar) PIV systems, proportional to the particle image size d_τ (Adrian, 1984), whereas the latter is dominated by the aperture angle β.

$$\epsilon_x = \epsilon_y = \frac{c_\tau d_\tau}{M} \tag{3.3a}$$

$$\epsilon_z = \frac{2\epsilon_x}{\beta} \tag{3.3b}$$

The coefficient c_τ describes the uncertainty in locating the particle centroid in the image, and it typically lies in a range of $0.1 - 0.2$ (Adrian and Westerweel, 2011). It is important to realise that the angle β reduces with the imaging distance z,

$$\beta = \frac{\beta_0 z_0}{z} \tag{3.4}$$

where β_0 is the aperture angle at a reference distance z_0. For the specific system considered in this chapter the aperture angle is $\beta_0 = 8°$ at a distance of $z_0 = 40$ cm. Consequently, the particle positional uncertainty in the viewing direction (z) is one order of magnitude larger than the equivalent uncertainty in the in-plane direction (x, y). The difference in positional uncertainty will be reflected in the uncertainty of the velocity measurement.

3.1.3. Optical access

Alignment of imaging and illumination axes in the CVV concept yields an imaging system that is characterised by a single line of sight. The topic of optical access is

barely discussed in the literature, as each experiment poses its specific challenges. A general observation is, that the access by PIV to a fluid domain close to and all around complex, non-transparent geometries requires multiple illumination and imaging directions. This is often achieved partitioning the fluid domain, composing the desired region of interest from several subsequent measurements. For flow data acquisition near curved models, a limiting factor is identified: the angle spanned between the imaging and the illumination system, hereafter referred to as α.

To understand the characteristic differences between a coaxial imaging and illumination configuration and a conventional large-aperture imaging setup in terms of optical access, let us consider a simple two-dimensional example: assume we are interested in the flow around a circular cylinder, aiming to measure the velocity field in vicinity to the object surface around the whole cylinder ($360°$). To simplify the analysis, it is assumed that there are no constraints on placing the imaging equipment, e.g. due to aerodynamic intrusiveness or similar. Additionally, we assume that the object is sufficiently small to be captured by a single view, i.e. the diameter is smaller than the instantaneous field of view. A further simplification of parallel imaging and illumination is introduced, implying that a camera can view exactly one half of the cylinder surface; the same applies to the light illumination.

Following these assumptions, the coverage of the cylinder surface, in this context expressed by the angle γ, can be determined as a function of the tomographic aperture angle β, and the relative angle α between imaging and illumination axis. The definition of angles for a generic imaging setup is illustrated in Figure 3.2.

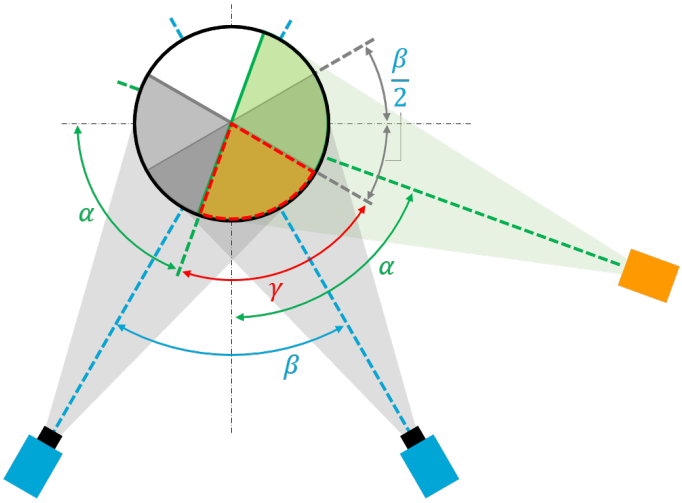

Figure 3.2: 2D schematic of large-aperture imaging setup with definition of characteristic angles. Cameras illustrated in blue, light source in orange, effective coverage angle γ indicated in red.

In the following, it is assumed that α can vary between $0°$ and $90°$. Within this range two regimes can be defined: the sideward illumination regime (typical of planar and stereoscopic PIV in 2D, respectively tomographic PIV in volumetric imaging), for which $\alpha > 0.5\beta$; and the coaxial illumination regime, whereby the light

source is located within the aperture angle spanned by the cameras, $\alpha \leq 0.5\beta$. In the coaxial regime, the coverage γ depends solely on the tomographic aperture angle β, and it is given by,

$$\gamma = 180° - \beta \tag{3.5}$$

This case is visualised for a typical CVV arrangement in Figure 3.3(a), where the illumination axis is aligned with the main imaging axis, and the aperture angle β spanned by the imagers is small, resulting in a coverage angle γ approaching $180°$.

Considering instead a classical large-aperture setup with perpendicular illumination ($\alpha = 90°$, Figure 3.3(b)), the coverage angle γ in this sideward imaging regime is governed by,

$$\gamma = 180 - \left(\alpha + \frac{\beta}{2}\right) \tag{3.6}$$

which in the simplified case of a purely orthogonal setup may not exceed $\gamma = 90°$. For a typical stereoscopic (or tomographic in 3D) arrangement γ will be even smaller, as seen for the case shown in Figure 3.3(b). In conclusion, the coaxial approach yields 2 – 3 times larger surface coverage for a single view, in this 2D example.

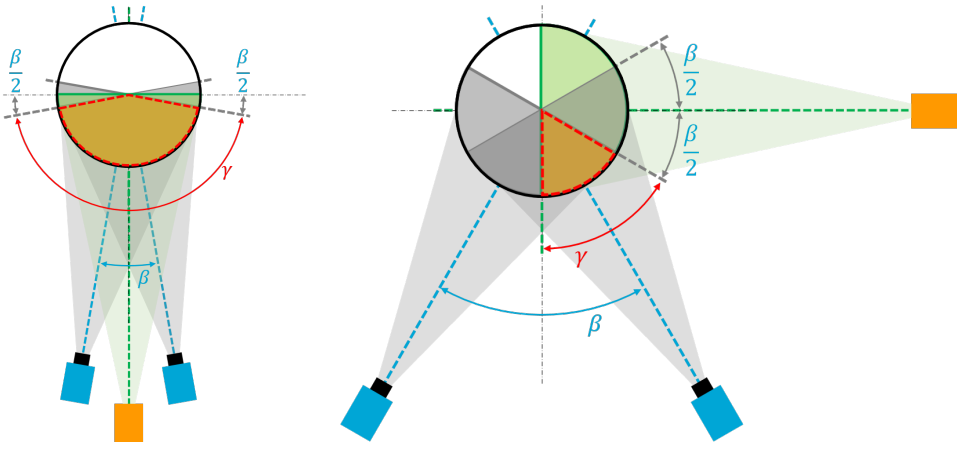

(a) Coaxial configuration. (b) Classical arrangement.

Figure 3.3: 2D schematics for classical large-aperture imaging setup and a coaxial imaging system.

An extension to a 3D case is omitted for conciseness. Yet, it is noted that a compact CVV system can be easily repositioned without need for re-calibration, which is elaborated in more detail in Section 3.2.4; whereas a large aperture system will require a new calibration for each new orientation, unless the full imaging and illumination system can be mounted on a rigid frame which can then be re-positioned all-together. Such setup realization has to date, however, only been demonstrated for planar and stereoscopic PIV setups (see e.g., Cardano et al., 2008; Falchi et al., 2014; Grizzi et al., 2010), whereas a likewise configuration for

volumetric PIV systems with three or more cameras and simultaneous illumination is not known to the best of the author's knowledge. Therefore, if domain partitioning is desired, significant time must be spent on calibration procedures, especially considering volumetric imaging systems with a minimum of three cameras. Given the higher complexity in setting up the tomographic imaging systems and the associated calibration procedure (volume self-calibration, Wieneke, 2008), performing tomographic PIV measurements along different views is rarely pursued in view of time and complexity of the measurements. The example discussed here emphasizes the key advantage of a coaxial illumination system in the context of surface flow investigations, and flow measurements around geometrically complex objects, as it allows for a significantly faster data acquisition process.

3.1.4. Aerodynamic interference

Recalling the discussion on particle image intensity in a coaxial imaging and illumination configuration in Section 3.1.1, it was concluded that the maximum measurement distance z_{max} is limited by the achievable intensity I_P relative to the image noise level. Conversely, the nearest measurement distance z_{min} is determined by analysis of the aerodynamic interference stemming from the CVV probe immersed in the flow. The latter is the focus of this section.

Modelling the velocimeter as a sphere and seeking the 3D potential flow solution as a first approximation of aerodynamic interference provides justification for a minimum distance z_{min}, below which velocity measurements shall not be considered valid. Defining a freestream V_∞ in spherical coordinates

$$V_{r_0} = V_\infty \cos(\theta) \tag{3.7a}$$

$$V_{\theta_0} = -V_\infty \sin(\theta) \tag{3.7b}$$

$$V_{\phi_0} = 0 \tag{3.7c}$$

and adding a doublet to model the flow around a sphere of radius R, the potential velocity field around the sphere is described by (e.g., Anderson, 2011, chapter 6)

$$V_r = V_\infty \left(1 - \frac{R^3}{r^3}\right) \cos(\theta) \tag{3.8a}$$

$$V_\theta = -V_\infty \left(1 + \frac{R^3}{2r^3}\right) \sin(\theta) \tag{3.8b}$$

$$V_\phi = 0 \tag{3.8c}$$

where r is the radial distance to the sphere centre. Comparing Equations (3.8a) and (3.8b), it is observed that the disturbance of both radial and tangential velocity component decays with r^{-3}. Quantifying the velocity deviation induced by the sphere as

$$\epsilon_V = \frac{\sqrt{\left(V_r - V_{r_0}\right)^2 + \left(V_\theta - V_{\theta_0}\right)^2}}{V_\infty} \tag{3.9}$$

results in elliptical iso-lines of induced velocity error ϵ_V with the major axis aligned with the freestream, as shown in Figure 3.4. In the assumption that the probe is not directly upstream of the region of interest ($\theta > \pi/2$), the velocity perturbation is least significant along the y-axis ($\theta = \pi/2$). For a given radial distance r, the error ϵ_V increases with increasing θ beyond $\theta = \pi/2$.

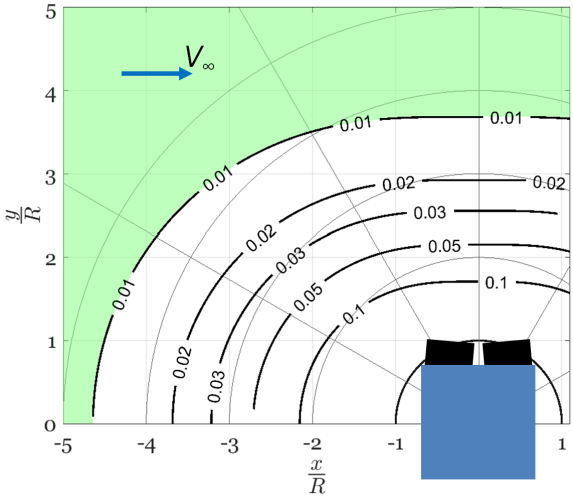

Figure 3.4: Contours of ϵ_V induced by the presence of a sphere with radius R, assuming a potential flow solution. Freestream V_∞ as defined in Equation (3.7) with $x = r\cos(\theta)$ and $y = r\sin(\theta)$. Green area indicating valid measurement region for $\epsilon_V < 1\,\%$.

Considering a nominal working range of $\pi/2 < \theta < 5\pi/6$, in the best case scenario ($\theta = \pi/2$) the error ϵ_V stays below $1\,\%$ for $r > 3.7\,R$. In the worst case ($\theta = 5\pi/6$), it can be shown that for a given r, the relative error ϵ_V is 1.8 times higher. Along this viewing direction the $1\,\%$ mark is reached at $r = 4.5\,R$.

In the work presented in this thesis two different coaxial velocimeters have been used, the MiniShaker S and the MiniShaker Aero, which will be introduced in Section 3.1.5. The former probe is modelled by a sphere of 10 to $12.4\,$cm diameter ($R = 5$ to $6.2\,$cm) based on cross sectional equivalence of its side faces. Allowing for a maximum velocity disturbance of $1\,\%$, a minimum measurement distance of $z_{min} = 17.5$ to $21.7\,$cm must be respected. For the MiniShaker Aero, the cross sectional area is in fact larger; however, the connection point to the robot arm is further to the back of the cameras and thus, it minimizes the interference of the robotic arm. Its cross-section in side-view ($\theta = \pi/2$) is approximated by a sphere of $8\,$cm radius, yielding a minimum distance of $z_{min} = 28\,$cm.

The first order prediction of flow disturbance based on potential flow theory is compared with the freestream measurements conducted in side viewing condition ($\theta = \pi/2$, Figure 3.4). The results show an acceptable agreement in terms of flow deflection and acceleration caused by the measurement probe.

3.1.5. Hardware: CVV probe

The data presented in this thesis has been acquired with two different CVV probes. In the initial studies the *MiniShaker S* prototype with a square camera arrangement was used. More recent works are based on measurements with the *MiniShaker Aero*, which features a diamond camera arrangement. Both velocimeters are made by *LaVision GmbH*, and contain four CMOS camears each. Images of the two devices are shown in Figure 3.5, whereas relevant technical data is tabulated in Table 3.1.

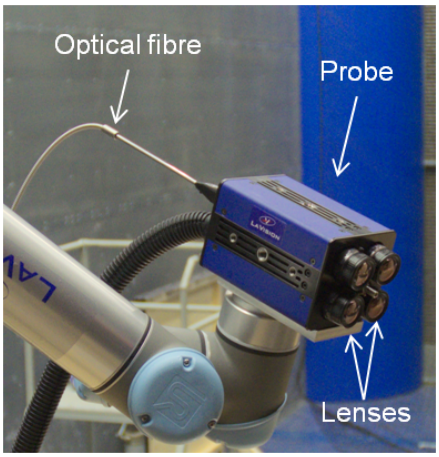

(a) MiniShaker S

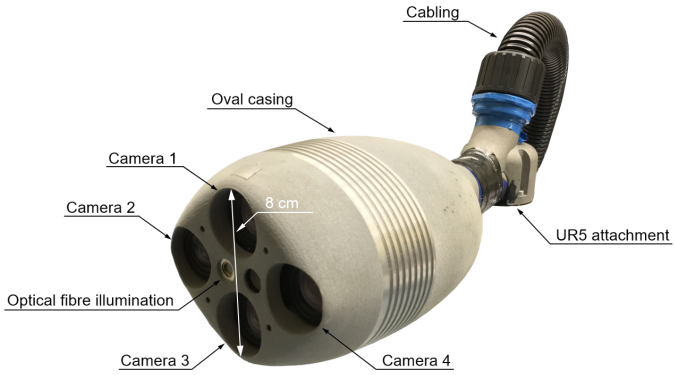

(b) MiniShaker Aero.

Figure 3.5: The two velocimetry probes by *LaVision GmbH* utilized in the experiments for this thesis.

Illumination is provided by a *Quantronix Darwin Duo* Nd:YLF laser[1], coupled with a spherical, converging 20 mm lens to direct the light beam into an optical

[1]This laser was used in all studies presented in this dissertation, but any other high-speed laser with similar power output may be coupled with the CVV system.

Table 3.1: Technical specifications of the coaxial volumetric velocimetry probes.

			MiniShaker S	MiniShaker Aero
Housing	Size	$w \times h \times d$	$131 \times 90 \times 83\,\text{mm}^3$	$300 \times 110 \times 130\,\text{mm}^3$
Optics	Focal length	f_i	4 mm	4 mm
	Numerical aperture	$f_\#$	8	11
Imaging	Tomographic aperture at $z_0 = 40$ cm	β_0	4°	8° horizontal, 4° vertical
	Active sensor	$S_x \times S_y$	$640 \times 476\,\text{px}^2$	$640 \times 476\,\text{px}^2$
	Pixel pitch	Δ_{px}	4.8 μm	4.8 μm
	Bit depth	b	10 bits	10 bits
	Acquisition frequency	f	758 Hz	821 Hz
Illumination	Pulse energy	E_p	$\mathcal{O}$ (25 mJ)	$\mathcal{O}$ (25 mJ)
	Wavelength	λ	527 nm	527 nm

fibre. Another 4 mm spherical, diverging lens is attached at the fibre end to obtain the desired light spreading angle.

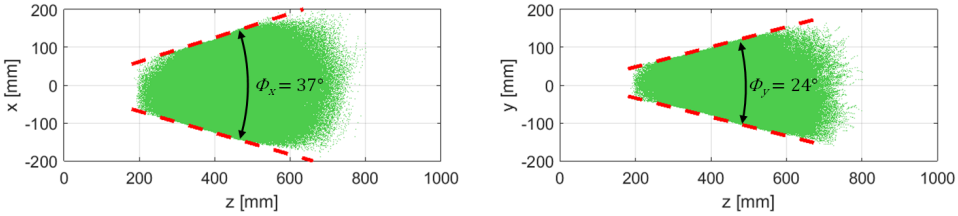

Figure 3.6: Particle tracks recorded in 5000 time frames with the CVV probe shown in Figure 3.5(a).

The measurable volume, assuming absence of objects and sufficient seeding, is bound within the region where the camera views overlap in lateral and vertical direction, whereas the maximum depth is constrained by the relative particle light intensity with respect to the image noise level. For the *MiniShaker S*, at a measurement distance of $z = 20$ cm, the field of view (FOV) attains $8 \times 13\,\text{cm}^2$ which extends to $25 \times 40\,\text{cm}^2$ at $z = 60$ cm. In a separate experiment, the maximum measurement depth is recorded at $z_{max} = 75$ cm. Figure 3.6 shows particle tracks recorded in the sample measurement. It follows that the achievable measurement volume in this configuration is on the order of 20 L.

3.2. Volume scanning by robotic manipulation

The coaxial volumetric velocimetry probe introduced in the previous section is suitable for the velocity measurement in volumes on the order of 20 L. To further enhance the size of the measurement domain, this section investigates the option to analyse large volumes through a scanning process in which the CVV probe is manipulated by a robotic system. Robotic handling is suited for controlled and rapid coverage of large measurement volumes by partitioning the domain of interest into

a number of local 3D measurements.

Section 3.2.1 opens the discussion by considering the requirements of a robotic system that is intended to be used for PIV measurements. Subsequently, the specifics of the robot selected for the work presented in this thesis are detailed in Section 3.2.2, followed by the robot and data positioning details in Section 3.2.3. The calibration procedure coupling the PIV with the robotic system is presented in Section 3.2.4, followed by the data acquisition principle (Section 3.2.5) and the resulting data properties in terms of dynamic ranges in Section 3.2.6.

3.2.1. Manipulator requirements and considerations

Requirements for robotic systems suitable for PIV applications have been postulated by Michaux et al. (2018). The latter work suggests four primary selection criteria, those being

1. Sufficient workspace and degrees of motion of the robotic system for adequate positioning of the PIV system;
2. Payload capability to support the PIV hardware weight;
3. Positioning accuracy and repeatability; and
4. Compact size for wind tunnel integration.

It follows from these criteria, that the "right" robot selection depends not only on the intended measurement purpose, e.g. the desired measurement volume and the test model shape, but also on the PIV equipment and the wind tunnel facility that is going to be used. For the current work only one robot is required, because the CVV probe unites all imagers together with the optical fibre illumination in a compact body. Instead, the referenced work by Michaux et al. (2018) utilizes three robots to support two cameras and the laser optics independently, similar to the illustration provided earlier in Figure 1.2. Such configuration differences directly impact the above requirement on positioning accuracy and repeatability. In the CVV approach, the flow measurement capability is not affected by the robot positioning accuracy (except for a potential positioning error in the flow measurement), whereas in the referenced multi-robot case, uncertainties in the robot positioning are prone to translate into the measurement capability of the PIV system.

Adding to the four points above, further requirements for the current work are placed relating to,

5. Robot accessibility in terms of cost; and
6. Usability, e.g. in terms of safety considerations, when operating in an educational environment.

The last requirement motivates the utilization of collaborative robots, i.e. robotic devices that manipulate objects in collaboration with a human operator (Colgate et al., 1996).

Robotic manipulators can be classified into *parallel* and *serial* kinematics, and hybrid systems combining the two types of kinematics (e.g., Khalil and Dombre,

2002). On an abstract level, serial manipulators provide greater motion flexibility and attain a bigger workspace for a given robot size, whereas a parallel kinematic carries advantages in terms of stiffness, payload capacity for a given size, and accuracy. Schematics of the two types are provided in Figure 3.7.

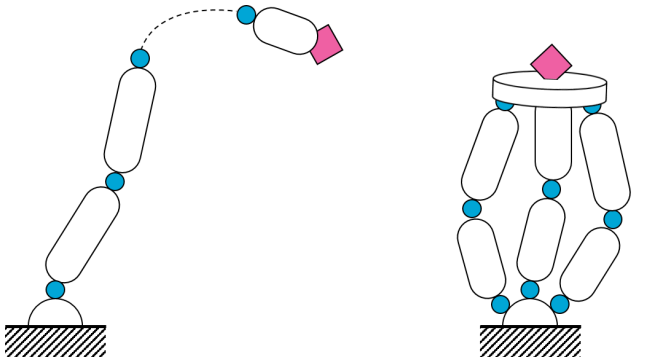

(a) Serial kinematic (b) Parallel kinematic

Figure 3.7: Schematic illustration of serial and parallel robot kinematics with end effector (pink diamond) connecting to base via chains of structural members (black/white ovals) and joints (blue circles). Sketches adapted from Khalil and Dombre (2002).

3.2.2. Hardware selection: collaborative robotic arm

Based on the requirements formulated in the previous section, the *Universal Robots - UR5* emerged as a suitable candidate to execute the desired manipulation of the velocimetry probe for the proposed robotic volumetric PIV concept. The UR5 is a collaborative robotic arm, providing motion with six degrees of freedom, similar to the movement range of a human arm, see Figure 3.8. The robot base features a single degree of freedom joint, which connects to the so-called shoulder joint, providing the second degree of freedom. The third joint connects the two robot arms in analogy to an elbow. Three more rotation axes at the end of the second arm mimic the articulation of a wrist. The latter connects to the support flange, herein referred to as the robot hand, which holds the CVV probe. The maximum reach of the UR5 stretches 85 cm in radius around its base.

In the remainder, the concept of robotic volumetric PIV is discussed based on the robot selection made here. The principle of volume scanning by manipulating a coaxial volumetric velocimetry probe with a robotic system maintains its validity, of course, also for a different robot selection. The interested reader will find a number of suitable candidates in the seminal work of Michaux et al. (2018).

3.2.3. Probe and data positioning

The position and direction of the CVV probe is set by moving the robot manually aiming at a target point specified either on a digital display belonging to the UR5, or in a robot control software such as *RoboDK*. The position repeatability for the spe-

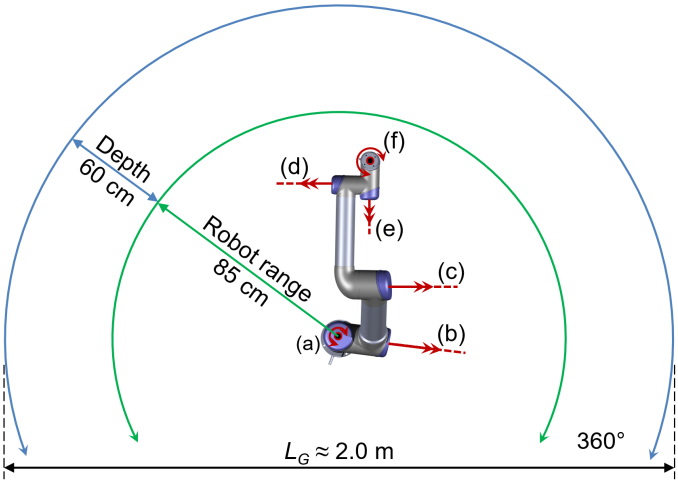

Figure 3.8: Robot arm with indication of its range. Robot joints labelled as: (a) base, (b) shoulder, (c) elbow and (d-f) wrist. Degrees of freedom indicated in red. The CVV measurement range extends the robot's range by its measurement depth. Drawing not to scale.

cific robot used herein is reported as 0.1 mm by the manufacturer (Universal Robots, A/S, 2017). The absolute accuracy of the robot, i.e. its maximum positioning error with respect to a target position defined in Cartesian space (e.g., Greenway, 2000), is not reported and the repeatability uncertainty may only serve as a lower bound for the absolute accuracy. Assuming an order of magnitude difference between relative and absolute uncertainty, yields an absolute positioning error of 1 mm, which is still considered small relative to the typical linear averaging cell size for the fluid measurements which is $l_v = \mathcal{O}(10\,\text{mm})$. A first order estimate of the positioning error is provided in Section 3.2.4.

It is noted that the positioning error of the robot does not affect the measurement capabilities of the CVV probe. However, a robot positioning error will translate into a positioning error of the velocity measurement after the data pertaining to the CVV reference frame has been mapped to the targeted measurement frame, where the latter typically pertains to the wind-tunnel. The effect of such error on the combined velocity measurement will be most noticeable in the presence of velocity gradients, e.g. near object surfaces, separated shear layers and vortex flows.

Focusing on the data positioning of the flow measurement in the proposed robotic volumetric PIV approach, let us recall the function of the robotic arm: the robot tool end, herein referred to as the robot hand, holds the CVV probe and controls its position and orientation. At each position, the 3D PIV measurement obtained by the CVV probe yields the time averaged velocity field in the "robot hand reference frame" ($\mathbf{x}_{rh}$). Note that the latter corresponds to the reference frame of the velocimeter ("c") indicated in Figure 3.1, offset by a known distance $\mathbf{x}_{cor}$ ($\mathbf{x}_{rh} = \mathbf{x}_c - \mathbf{x}_{cor}$). Translating ($\mathbf{x}_t$) and rotating the robot hand along roll, pitch and yaw (α, β, γ) allows selecting different regions of the flow to be in-

spected, or to observe the same region from a different viewing direction in case of obstructed view or unwanted reflections. The probe position is controlled with respect to the robot's base position, indicated by the point P_b in Figure 3.9.

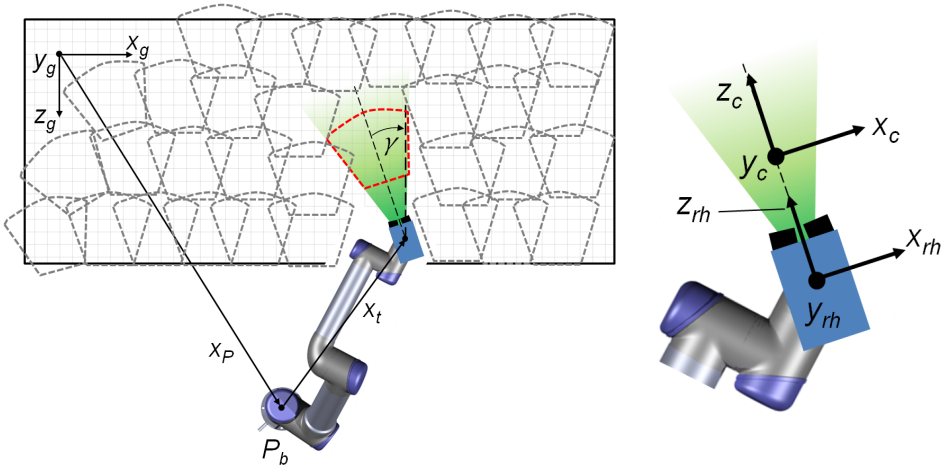

(a) Global reference frame with arbitrary region of interest. Potential measurement volumes outlined to illustrate concept of domain partitioning.

(b) Robot hand holding the CVV probe with indication of reference frames.

Figure 3.9: Illustration of reference frames and volume scanning approach.

The robot provides the required information of the probe translations and rotations relative to its base. The distance $\mathbf{x}_{cor}$ is determined a priori. This provides the necessary information to map the measurement data onto a global ("g") frame of reference related to the object or the wind tunnel. Then,

$$M_x = \begin{bmatrix} 1 & 0 & 0 \\ 0 & \cos(\beta) & \sin(\beta) \\ 0 & -\sin(\beta) & \cos(\beta) \end{bmatrix} \tag{3.10a}$$

$$M_y = \begin{bmatrix} \cos(\gamma) & 0 & -\sin(\gamma) \\ 0 & 1 & 0 \\ \sin(\gamma) & 0 & \cos(\gamma) \end{bmatrix} \tag{3.10b}$$

$$M_z = \begin{bmatrix} \cos(\alpha) & \sin(\alpha) & 0 \\ -\sin(\alpha) & \cos(\alpha) & 0 \\ 0 & 0 & 1 \end{bmatrix} \tag{3.10c}$$

$$\mathbf{x}_g = (\mathbf{x}_{rh})\left(M_x M_z M_y\right) + \mathbf{x}_p + \mathbf{x}_t \tag{3.11}$$

$$\mathbf{u}_g = \left(M_y M_z M_x\right)\mathbf{u}_{rh} \tag{3.12}$$

Where M_i represent the rotation matrices around the i-axes and $\mathbf{x}_g$ respectively $\mathbf{u}_g$ are the position and velocity in the global reference frame. A simplified view of the layout is shown in Figure 3.9.

3.2.4. System calibration

The intrinsic calibration of the CVV probe follows the same procedure as that for tomographic PIV, consisting of a geometric calibration (Soloff et al., 1997) followed by a volume self-calibration (Wieneke, 2008), with the additional requirement that the optical response function is experimentally determined (OTF calibration, Schanz et al., 2012). The latter is necessary to employ the Shake-the-Box algorithm for tracers motion analysis (Schanz et al., 2016). Once performed, the calibration pertains to the CVV system and does not need to be repeated (universal calibration). Furthermore, transforming the velocity measurements from the individual volumetric domains towards the global coordinate system requires the coefficients appearing in Equations (3.10) to (3.12) to be determined.

A calibration procedure determines the relative distance between the robot hand and the origin of the measurement domain ($\mathbf{x}_{cor}$). Such calibration is performed imaging and reconstructing known targets from different views, and iteratively determining the offset distance that minimizes the positional error of the reconstructed markers after mapping them into a common reference frame. The variation in the reconstructed and mapped target positions provides an initial estimate of the robot positioning accuracy, in the assumption that the positioning error is significantly larger than the reconstruction error from the imaging system. For the experiments presented in this thesis, the root-mean-square error of the reconstructed particle positions after mapping to a common reference frame is on the order of 2 to 5 mm. For an independent assessment of the robot positioning accuracy, its position must be measured with an external device. This has not been done, as the observed uncertainties were deemed acceptable compared to the large scale of the test models and measurement volumes.

Lastly, the position of the robot hand in the global coordinate system is evaluated by imaging a marker in the origin of the latter coordinate system.

3.2.5. Data acquisition

The motion of the particle tracers is evaluated using the Shake the Box (STB) algorithm (Schanz et al., 2016) implemented in the *LaVision DaVis* software. The Lagrangian particle tracking procedure is computationally efficient, while allowing for reliable tracking even in densely seeded flows, yielding advantages in computational time and velocity dynamic range, when compared to tomographic PIV. For each tracer particle, the position $\mathbf{x}_{rh}$ along a trajectory is sampled several times, yielding its velocity vector $\mathbf{u}_{rh}$ at a given time step t_i.

For the robotic CVV system used in the present experiment, the particle tracks are first reconstructed within the reference system of the local measurement ($\mathbf{x}_{rh}$). The spatially randomly distributed particle data is expressed through coordinates transformation in the global system of reference, where the ensemble statistics are evaluated.

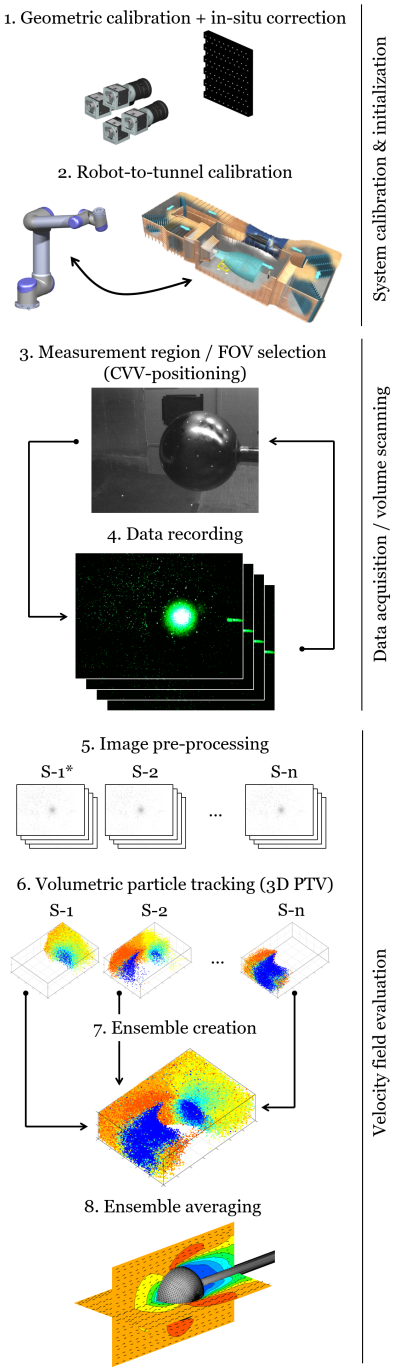

Figure 3.10: Workflow for robotic volumetric PIV data acquisition process. *Labels S-i in steps (5 & 6) indicating the data sets resulting from the volume scanning process (3 & 4).

Data within a finite time interval and spatial range is included in an averaging cell, where the results are temporally and spatially averaged. The topic of ensemble averaging is discussed in Section 2.3. Within this thesis, ensemble statistics are always computed on a structured Cartesian grid, yielding the time-averaged 3D-3C velocity field on that grid, which is also referred to as the fluid mesh.

The sequence of system calibration, data acquisition and velocity field evaluation in the proposed robotic volumetric PIV approach is graphically illustrated in Figure 3.10.

3.2.6. Dynamic spatial and velocity range

Following the outlined volume scanning process above, large measurement domains composed by multiple sub-volumes can be analysed. As introduced in Section 2.3.2 the dynamic spatial and velocity range (DSR and DVR) describe the ratio of the largest- over the smallest resolvable length and velocity scales, respectively. For the system at hand, the largest resolvable spatial scale is L_x is defined by the characteristic length of the measurement domain, and the smallest scale l_v is given by the linear cell size of a fluid mesh element. For a CVV measurement L_x is limited by the depth of the measurement volume, which was shown to be on the order of 50 cm in Section 3.1. In the proposed robotic measurement approach, the maximum domain size is instead limited by the reach of the robotic arm. For the specific robotic arm considered in this thesis, L_x can approach up to 2 m. The linear cell size is not affected, and is for CVV and robotic volumetric PIV typically on the order of 1 cm. This results in a DSR of 50 for a typical CVV measurement, which can be extended up to 200 if the CVV probe is coupled with a robotic arm.

For the dynamic velocity range, the maximum velocity that can be recorded is determined by the maximum particle displacement that can be afforded by the tracking algorithm. The latter is typically on the same order of magnitude as the anticipated freestream velocity u_∞. Contrary, the minimum resolvable velocity $\overline{u}_{min}$ is determined by the uncertainty in the mean velocity measurement $\epsilon_{\overline{u}}$. The latter is commonly estimated through the turbulent fluctuations $\sigma_{\overline{u}}$ and the number of uncorrelated samples inside the averaging ensemble (N).

$$\epsilon_{\overline{u}} = \frac{k\sigma_{\overline{u}}}{\sqrt{N}} \tag{3.13}$$

The confidence interval is accounted for by the coverage factor k (Coleman and Steele, 2009). For a generic flow with 10 % turbulence intensity, and an ensemble of $N = 100$ samples, the CVV and robotic PIV approach return a dynamic range of $\overline{DVR} = 100$

3.3. Assessment on the flow around a sphere

The principles of coaxial volumetric velocimetry and robotic volumetric PIV are illustrated by application to the flow around a 15 cm diameter sphere in this section. Applications in the field of sports engineering are included in Part II.

The wind tunnel facility and the experimental apparatus are introduced in Section 3.3.1. Subsequently, the measurement results are discussed in Section 3.3.2.

3.3.1. Experimental apparatus and procedures

The sphere flow experiments described in this chapter were conducted at TU Delft's Open Jet Facility (OJF). The OJF is an atmospheric, closed-loop, open-jet wind tunnel with a contraction ratio of $3:1$ and an octagonal exit section of $2.85 \times 2.85\,\mathrm{m}^2$. The fan controlling the flow speed is driven by a $500\,\mathrm{kW}$ electrical motor. The wind speed ranges from 4 to $35\,\mathrm{m/s}$. The jet stream is bounded by shear layers spreading with a semi-angle of $4.7°$ (Lignarolo et al., 2014). During the measurements, the wind speed is held constant at $10\,\mathrm{m/s}$. A heat exchanger downstream of the test section maintains a constant air temperature independent of the flow speed. The turbulence intensity of the free stream is reported to be $0.5\,\%$ (Lignarolo et al., 2014). The latter does not include the aerodynamic effects of the seeding generator that produces the PIV tracer particles. The seeding rake raises the turbulence intensity in the test section, which is addressed later in this section.

The robotic PIV system comprises three major components: the HFSB seeding generator which is described hereafter, the coaxial volumetric velocimeter including the illumination unit described in Section 3.1.5, and further the robotic arm as discussed in Section 3.2.2.

HFSB tracer particle generation

Tracer particles are generated by a 10-wing, 200-nozzle HFSB seeding rake installed in the settling chamber, downstream of the turbulence meshes. For this seeder, an individual nozzle in nominal working conditions produces $20,000$ to $60,000$ bubbles per second of 300 to $500\,\mu$m diameter (Faleiros et al., 2018; Scarano et al., 2015). Nozzles are spaced $5\,\mathrm{cm}$ apart, yielding a seeded streamtube of $0.5 \times 1.0\,\mathrm{m}^2$ cross section. The seeding rake is shown in Figure 3.11. A fluid supply unit (FSU) from *LaVision GmbH* controls the supply of air, helium, and soap to the generators.

In the assumption of straight flow through the seeding generator, each nozzle seeds a cross section of $25\,\mathrm{cm}^2$ based on the nozzle pitch. At a freestream velocity of $10.0\,\mathrm{m/s}$ in the test section (corresponding to $3.33\,\mathrm{m/s}$ in the settling chamber) the seeding concentration of the undisturbed flow (C_{HFSB}) can be estimated as (Caridi et al., 2016):

$$C_{HFSB} = \frac{\dot{N}}{\dot{V}} = \frac{40,000\,\frac{tracers}{s}}{25\,cm^2 \times 3,333\,\frac{cm}{s}} = 0.48\frac{tracers}{cm^3} \tag{3.14}$$

where $\dot{N}$ is the production rate of an individual generator and $\dot{V}$ is the volume flow rate across the area delimited by neighbouring generators. The aerodynamic invasiveness of the seeding generator is studied by means of a freestream measurement $2\,\mathrm{m}$ downstream of the contraction exit using the robotic PIV system. With the seeding rake installed inside the settling chamber, the recorded turbulence intensity remains within $1.5\,\%$.

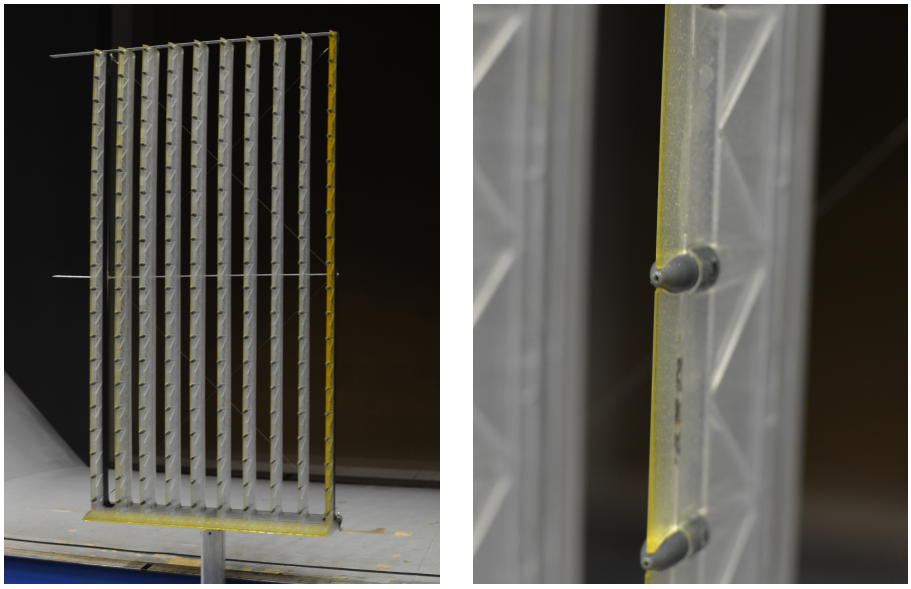

(a) HFSB seeding rake (b) Nozzle integration in aerodynamic rake

Figure 3.11: HFSB seeding rake with 200 nozzles distributed over ten wings.

Robotic volumetric PIV system

The *LaVision MiniShaker Aero* coaxial volumetric velocimeter is installed on a *Universal Robots - UR5* collaborative robotic arm to form the robotic volumetric PIV system. As discussed in Section 3.1.5 the CVV probe comprises four CMOS imagers in a diamond arrangement, integrated with an optical fibre for light transmission in the centre. A *Quantronix Darwin-Duo* Nd:YLF laser (2×25 mJ nominal pulse energy at 1 kHz) serves as a light source for illumination ($\lambda = 527$ nm). The cameras feature an active sensor of 640×476 pixels each, acquiring image quadruplets at a rate of 821 Hz.

Test model

The above systems are used to observe the airflow around a 3D printed sphere of diameter $D = 15$ cm at 10 m/s free-stream velocity. The corresponding Reynolds number $Re_D = 9.9 \times 10^4$, obeys the sub-critical flow regime (Achenbach, 1972), where the boundary layer remains laminar until flow separation. Additionally, the sphere is equipped with 15 static pressure taps in the vertical symmetry plane, between -10° and 130° azimuth at an equidistant spacing of 10°. The orifices feature 1 mm diameter. The surface pressure measurements are discussed in more detail in Chapter 5.

The sphere is supported from behind by a 30 mm diameter, circular, stainless steel tube. A vertical beam holds the support from 1.2 m downstream. The sphere sits 1 m above the ground. The experimental apparatus is shown in Figure 3.12.

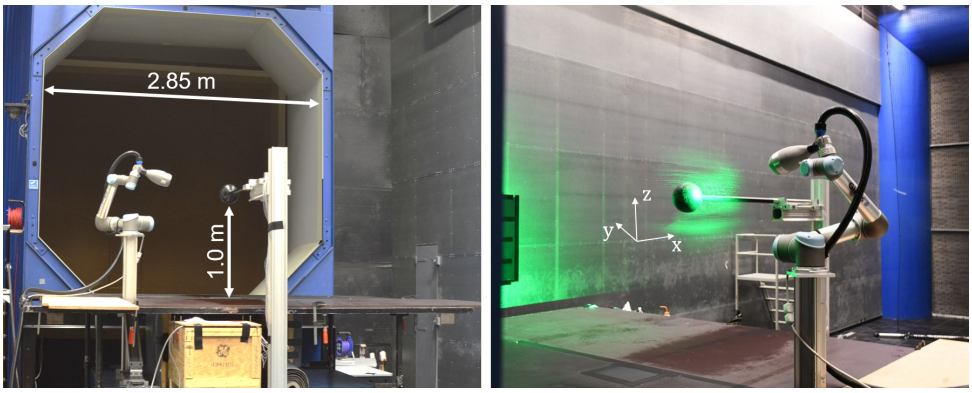

Figure 3.12: Experimental setup for the sphere flow experiment in OJF.

Data acquisition and processing

During acquisitions, the CVV probe is oriented normal to the free-stream direction, at approximately 40 cm distance to the sphere centre. Streamwise translations of the probe yield data acquisitions up- and downstream of the sphere. Each view contains $10,000$ images ($T_{aq} = 12.1$ s). The total measurement volume, combining multiple acquisitions, exceeds 50 L.

For the selected free-stream velocity and acquisition frequency, a particle tracer displaces by 12.2 mm in the free-stream, respectively 23 px on the camera sensors (at a nominal distance of $z_0 = 40$ cm). Figure 3.13 shows a typical recording of particle images, with a particle image density of approximately $N_p = 0.01$ ppp in the image centre. Background illumination is eliminated by image pre-processing with a high-pass frequency filter (Sciacchitano and Scarano, 2014) and a subsequent mean subtraction, which eliminates any residual background noise.

The particle images are analysed with the procedure outlined in Section 3.2, con-

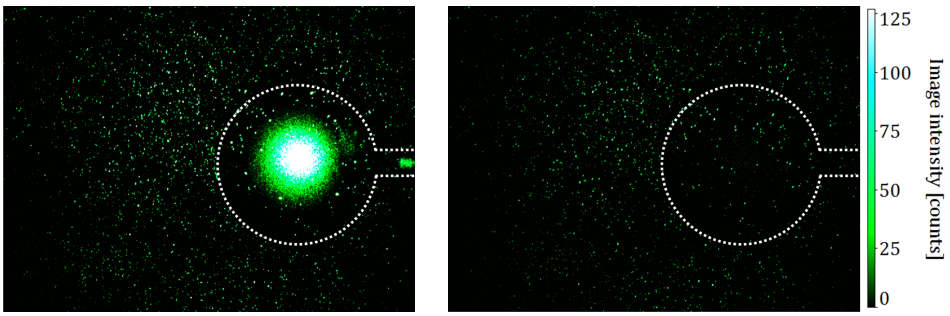

(a) Raw image (b) Pre-processed image

Figure 3.13: Instantaneous particle image recording. Approximate sphere-model position outlined by white-dashed line.

sisting of particle tracking in 3D using the Shake-The-Box algorithm implemented in *LaVision DaVis*, the data mapping based on the robot arm position, and subsequent ensemble averaging to yield the 3D-3C mean velocity field on a Cartesian grid.

For the given setup, a characteristic flow frequency of 67 Hz is estimated from the sphere diameter D and the free-stream velocity u_∞. An acquisition of $T_{aq} = 12.1$ s therefore results in approximately $N = 800$ statistically uncorrelated samples. Further assuming a maximum fluctuation level in the sphere wake of the order of 30 % with respect to the free-stream velocity (Terra et al., 2017), the 95 % confidence level uncertainty in the ensemble averaged mean velocity is about 2 % (0.2 m/s).

3.3.2. Results and discussion

Prior to analysis of the complete measurement volume, Figure 3.14(a) shows a subset of particles that is recorded from a single CVV position (also referred to as a *view* in the remainder) corresponding to the raw image shown in Figure 3.13. The particles are coloured by velocity magnitude, and data that extends beyond the sphere's centre plane is hidden for clarity of the visualisation. This illustration indicates distinct flow features including a deceleration towards the stagnation point, a flow acceleration around the sphere, as well as the onset of a low-velocity region downstream of the sphere which corresponds to the separated wake.

The measurement domain of the single CVV view shown in Figure 3.14(a) is extended by applying the volume scanning procedure described in Section 3.2. The combined data captures a 50 L volume of the flow around the sphere. Figure 3.14(b) illustrates a subset of particles in the robotic volumetric PIV measurement volume.

The scattered PTV data shown in Figures 3.14(a) and 3.14(b) is ensemble averaged, yielding the time-averaged 3D-3C velocity field on a structured grid. The ensemble averaged data in the vertical median plane is illustrated in Figure 3.15. Upstream of the sphere, the measured flow data is compared to the potential flow solution which is a valid reference in this part of the domain (Anderson, 2011).

Comparison of the measured velocity contour with the potential flow solution in Figure 3.15 indicates a good agreement in the region of decelerated flow upstream of the sphere. For the accelerated flow past the sphere, the velocity field is affected by the separated flow downstream of the object. Therefore, the comparison to the potential flow solution is not valid here.

Figure 3.16 contains a more detailed comparison of the measured velocity to the potential flow solution along the stagnation line. Additionally, the analysis compares two ensemble averaging schemes for varying spatial resolution: the simple arithmetic mean, sometimes also referred to as the tophat average; and the fit of a linear distribution function inside the averaging cell. Spatial resolution is quantified in terms of linear cell size l_v for the iso-tropic cells used in this study.

The stagnation line data in Figure 3.16 confirms the agreement of the solutions beyond two radii upstream of the sphere centre. In this region the low resolution data (large cell size l_v) agrees best with the potential flow solution, because the random error is minimized as a result of the larger ensemble size in the bigger cells.

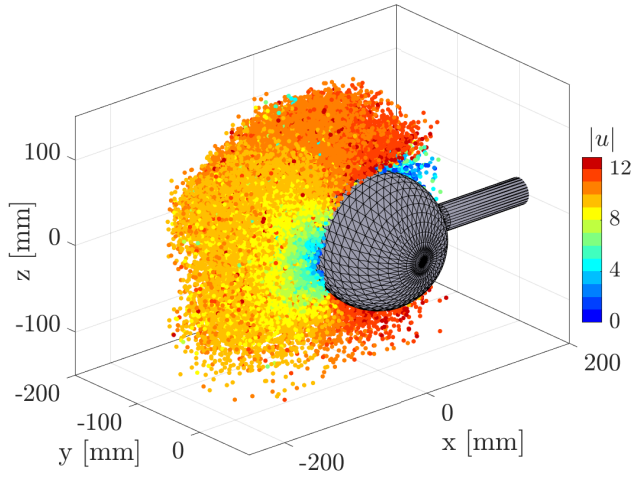

(a) Subset of particle tracks obtained from a single CVV position.

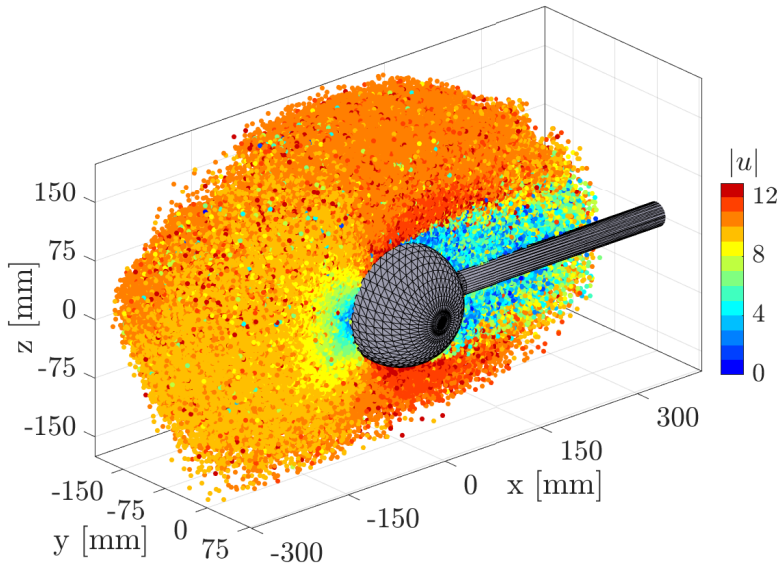

(b) Subset of particle tracks obtained by robotic volumetric PIV. Data consists of 11 CVV views acquired in a volume scanning process.

Figure 3.14: 3D particle tracks recorded with the CVV probe around the sphere model. Data beyond the zx-plane ($y \leq 0$) is hidden for clarity.

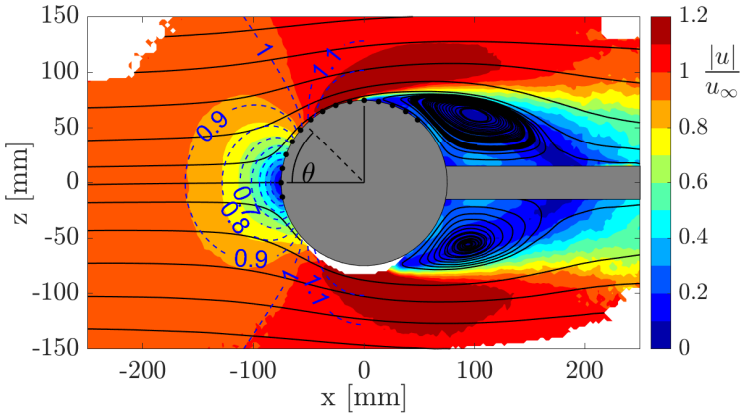

Figure 3.15: Velocity magnitude contour in the sphere's symmetry plane ($y = 0$), along with surface streamlines in the contour plane. Dashed-blue contours corresponding to potential flow solution.

Closer to the sphere, around $x^* = -1.5$ the measured velocity falls below the anticipated value from potential flow theory. The mismatch is within $2.5\,\%$ of the freestream velocity, and it does not indicate a significant dependency on spatial resolution.

The largest discrepancies are observed at the stagnation point $x^* = -1$. Comparing the error between the arithmetic mean and the linear fit highlights that the simple average cannot account for the large velocity gradient close to the stagnation point. Consequently, the mean velocity is biased and over-predicts the true velocity. The modulation is stronger as the cell size increases. The data obtained through the linear fit shows a similar behaviour, but with a reduced error magnitude. The first order function reduces the velocity error approximately by a factor $2\times$ with respect to the arithmetic mean. For the intermediate cell sizes of $l_v = 10 - 20\,\text{mm}$ the maximum error in the stagnation point is within $5\,\%$ of the freestream velocity, if the linear fit of the velocity measurement is considered.

The level of velocity fluctuations recorded by the robotic volumetric PIV system well upstream of the sphere provides an indication of the uncertainty in the velocity measurement. Computing the velocity fluctuations $\mathbf{u}'_{rms}$ when considering a cell size of $l_v = 10\,\text{mm}$ and ensemble averaging by fitting a linear polynomial, yields in-plane fluctuations (u'_{rms}, w'_{rms}) of up to $1.5\,\%$. Because the CVV measurements were taken predominantly from the side of the sphere, the out-of-plane component features a significantly larger velocity fluctuation of $v'_{rms} = 8.8\,\%$. This difference is ascribed to the low tomographic aperture angle in the coaxial arrangement. Whereas the in-plane fluctuations correspond approximately with the expected turbulence intensity level of the wind-tunnel with the HFSB seeding system installed, the out-of-plane fluctuations are an artefact of the coaxial camera and illumination arrangement. Nonetheless, considering that the mean velocity value is computed

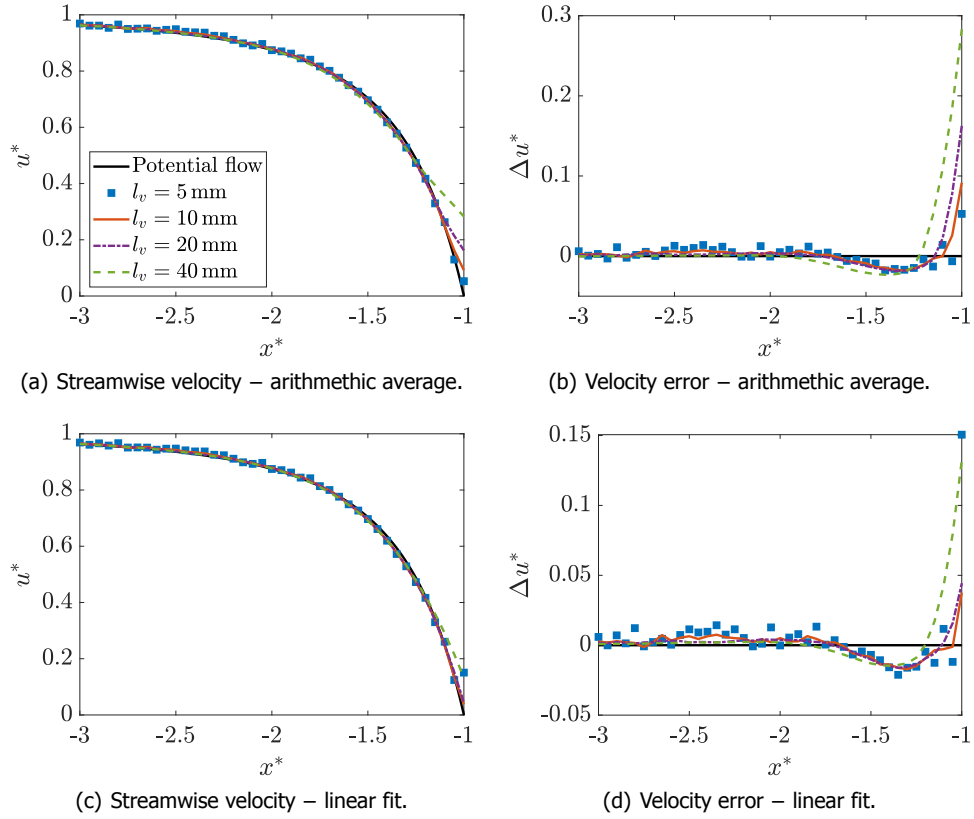

(a) Streamwise velocity – arithmethic average.

(b) Velocity error – arithmethic average.

(c) Streamwise velocity – linear fit.

(d) Velocity error – linear fit.

Figure 3.16: Streamwise velocity profile along stagnation line and corresponding error based on potential flow solution for varying spatial resolution and ensemble averaging scheme. ($x^* = x/R$)

from an ensemble that typically counts well over 100 instantaneous samples in each cell, the uncertainty of the mean velocity measurement becomes an order of magnitude smaller than the stated velocity fluctuations.

The dynamic spatial and velocity range discussed in Section 3.2.6 for the sphere experiment is estimated based on the above results. For the spatial range, a cell size of $l_v = 10\,\mathrm{mm}$ is considered which provides a balance of random and truncation errors. The measurement domain spans $50\,\mathrm{cm}$ in the streamwise direction which yields a DSR of 50. For the dynamic velocity range, the out-of-plane velocity fluctuations are the limiting factor. Those were estimated with $8.8\,\%$. Considering an order of magnitude decrease for the mean velocity estimate, and a maximum velocity of the same order of magnitude as the freestream velocity yields a $\overline{DVR}$ of 100. The latter is limited by the acquisition frequency that can be achieved with the CVV cameras and the high uncertainty in the viewing direction. The spatial range can however be extended further as will be shown in Part II, which also includes more detailed 3D flow analyses on larger and intricate geometries.

3.4. Conclusion

A novel approach for measuring large-scale complex aerodynamic flows has been proposed and assessed on the aerodynamic flow over a 15 cm diameter sphere. The approach is based on the combination of coaxial volumetric velocimetry and robotics. The compact CVV technology provides improved optical access and it eliminates the need for re-calibration following a probe movement. The combination with a collaborative robot arm yields the capability to rapidly partition a large fluid domain into multiple adjacent sub-volume measurements.

A first order estimate of the probe's aerodynamic intrusiveness is provided based on potential flow theory. For future applications where the robotic volumetric PIV system is immersed in the flow, it will be beneficial to assess its aerodynamic impact on the flow through the measurement domain using a higher fidelity model, also accounting for the presence of the robot arm.

Measurement volumes of up to 20 L are obtained in a single CVV measurement. The volume is rapidly enlarged when scanning the domain of interest with assistance of a robotic arm. For the case of the sphere, a volume of 50 L is realized for proof of concept.

The flow topology upstream of the sphere is compared to potential flow theory. Good agreement of the velocity data is observed, and maximum deviations are found at the stagnation point, where the velocity gradient is most pronounced. Comparison of the mean velocity computed with a simple arithmetic mean, and by fitting a first order polynomial shows that near stagnation the measurement error can be reduced by approximately 50 % if a first order fit is afforded in the ensemble averaging of the scattered PTV data. In the latter case the measurement error in the stagnation point is bound within 5 % when the averaging cell spans $10-20$ mm.

The analysis of velocity fluctuations in the freestream confirms that the measurement uncertainty of the coaxial arrangement is amplified in the viewing direction. The latter stems from the low tomographic aperture of the CVV system. The out-of-plane fluctuations were quantified with 8.8 % whereas the in-plane fluctuations were found to be within 1.5 %, and thus, close to the expected wind tunnel turbulence intensity with a HFSB seeding system installed.

4

Total pressure wake survey

It's impossible to move, to live, to operate at any level without leaving traces, bits, seemingly meaningless fragments of personal information.

William Ford Gibson

Irrespective of the advancements in velocimetry techniques, the measurement of flow pressure in aerodynamics remains highly relevant. Measuring the total pressure provides a means to quantify the amount of energy in the fluid flow. Classically, the aerodynamic pressure is recorded through mechanical probes in the flow. If instead the flow pressure is retrieved through PIV, the pressure is obtained in a non-intrusive manner. In the specific context of pressure evaluation through robotic volumetric PIV the question arises, whether existing PIV-based pressure evaluation strategies suffice, or if dedicated methods are required that handle the large but coarse velocimetry data. This chapter focuses specifically on total pressure wake surveys, providing a comparative assessment of the pressure fields obtained by robotic volumetric PIV and a traversing Kiel probe.

The chapter starts with a brief literature review on wake surveys in aerodynamics in Section 4.1. Subsequently, Section 4.2 details the method of evaluating total pressure through 3D PIV data, which is then applied to the flow past a truncated and surface-mounted cylinder in Section 4.3.

Jux C, Ordóñez D, Sciacchitano A and Scarano F. Total pressure wake survey by robotic volumetric PIV, *in preparation for Exp. Fluids*.

4.1. Wake surveys in aerodynamics

Wake surveys in fluid dynamics present a long-established means to study the flow past an object immersed in a fluid stream and the resulting aerodynamic loads. In its original form, the profile drag of a 2D airfoil is deduced through measurement of the total pressure deficit in the object wake, where the total pressure distribution is recorded by a Pitot-tube rake (e.g. Jones, 1936). Ever since, variations of the method and the more general control volume approach (e.g. Anderson, 2011) are brought forward, including extensions to three-dimensional objects (e.g. Brune, 1994), measurement of time-dependent forces (e.g. Noca et al., 1999), data acquisition through optical instruments such as laser Doppler velocimetry (LDV, e.g. McAlister et al., 1995), or particle image velocimetry (e.g. van Oudheusden et al., 2006).

Despite these developments, recording the total pressure distribution in an object wake using intrusive pressure probes remains common practice in aerodynamic testing up to date. An example thereof is the motorsport industry, commonly using wake-rakes on track and inside wind-tunnels to verify correlation between the scaled wind tunnel models and the actual race car (Senft and Gillan, 2019). Such applications in unsteady wake flows require care in selecting and positioning the pressure probes, due to the limited directional sensitivity of typical Kiel- and multi-hole probes (see e.g. Tropea et al., 2007). Further, the experimentalist needs to trade off the intrusiveness of a multi-probe pressure rake, against the time-consuming alternative of scanning the wake by traversing a single probe, or a small probe array through the domain of interest.

For the analysis of large-scale and three-dimensional flows, the wake pressure evaluation through PIV data represents an effective alternative. The fields of pressure from PIV and volumetric velocimetry have been extensively studied in recent years, with topical reviews on both subjects available by van Oudheusden (2013), and Discetti and Coletti (2018), respectively. It is noted that the bulk of literature on pressure from PIV discusses predominantly the evaluation of static pressure. Moreover, the study of large-scale and 3D flows by PIV remains limited by the achievable measurement volume size. The latter is addressed in the work of Schneiders et al. (2016), featuring the time-resolved pressure reconstruction in a 6 litre (L) volume downstream of a truncated cylinder through tomographic PIV. The measurement domain can be further augmented to the cubic-meter scale by implementing a volume scanning approach, such as the robotic volumetric PIV concept introduced in Chapter 3. On this scale, PIV-based pressure measurements attain feasibility for industrial applications, e.g. in the automotive or aerospace industry, albeit only allowing for the study of the time-averaged flow field. Upon the aforementioned trends and developments, this chapter aims at the feasibility assessment of large-scale, time-average total pressure wake surveys by robotic volumetric PIV.

4.2. PIV-based total pressure analysis

Bernoulli's equation defines the total pressure as the sum of static and dynamic pressure. The time-averaged static pressure is evaluated through the Poisson equation

for pressure (see e.g. van Oudheusden, 2013),

$$\nabla^2 \overline{p} = -\rho \nabla \cdot \left(\overline{\mathbf{u}} \cdot \nabla\right) \overline{\mathbf{u}} - \rho \nabla \cdot \nabla \cdot \left(\overline{\mathbf{u}'\mathbf{u}'}\right) \tag{4.1}$$

which is solved up to an integration constant with Neumann boundary conditions over the entire domain boundary. Subsequently, a Dirichlet condition based on Bernoulli's equation is specified at a position where irrotational flow conditions can be safely assumed and therefore, total pressure is equal to free-stream conditions. The terms of the velocity gradient in Equation (4.1) are evaluated by a second order central difference scheme on the interior domain and a first order upwind scheme on the domain boundaries. It is important to realize that Equation (4.1) neglects the viscous term in the momentum equation, which is deemed common practice when dealing with high Reynolds number flows ($Re > 10^3$, see van Oudheusden, 2013). Lastly, the total pressure is evaluated through Bernoulli's principle for unsteady flows (de Kat and van Oudheusden, 2012),

$$\overline{p}_{tot} = \overline{p} + \frac{1}{2}\rho \left(\overline{\mathbf{u} \cdot \mathbf{u}}\right) \tag{4.2}$$

where $\overline{p}$ describes the static pressure relative to free-stream conditions p_∞.

4.3. Wake survey on a truncated cylinder

The experimental assessment is based on a flow field similar to that studied by Schneiders et al. (2016): a wall mounted cylinder of 10 cm diameter and height, exposed in a 10 m/s air stream, seeded with helium filled soap bubbles (HFSB, Scarano et al., 2015). The Reynolds number is 6.6×10^4 based on the cylinder diameter. The experiments are conducted in a low-speed, open-jet, wind tunnel featuring a 40×40 cm^2 exit cross section. The boundary layer on the ground plate is tripped 10 cm downstream of the ground plate leading edge, and 50 cm upstream of the cylinder.

4.3.1. Experimental apparatus and procedures

Particle images are acquired by robotic volumetric PIV as described in Chapter 3, consisting of a robotic arm (Universal Robots - UR5) and a coaxial volumetric velocimeter (LaVision - MiniShaker Aero), which records image quadruples of 640×476 px^2 each at a rate of 821 Hz. HFSB tracers are generated by a 0.5×1.0 m^2 seeding generator located in the settling chamber, yielding a tracer particle concentration of approximately 0.25 tracers/cm^3. Particle images are analysed by the Lagrangian particle tracking algorithm Shake-The-Box (STB, Schanz et al., 2016). An illustration of the experimental setup is provided in Figure 4.1.

The velocity field is recorded in a 24 L volume downstream of the cylinder. The measurement is composed of six separate acquisitions of $7,000$ frames, equivalent to an observation period T_{aq} of 8.5 s each. The instantaneous velocity data is ensemble averaged in space and time by a linear approximation of the local velocity distribution within cubic cells of 20 mm width (as introduced in Section 2.3). Cells are overlapped by 75 %, yielding a vector spacing of 5 mm for the resulting velocity

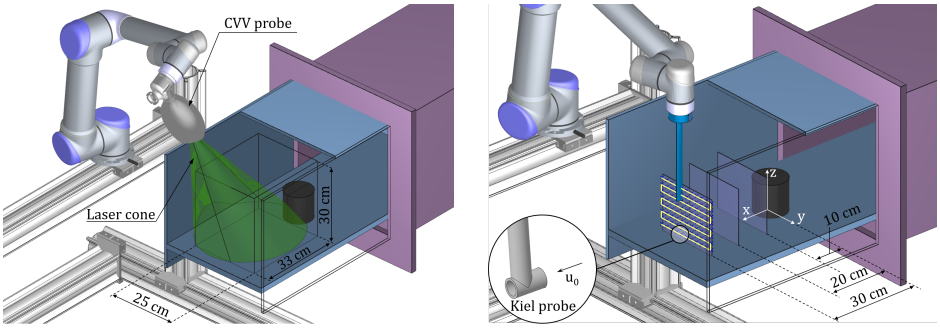

(a) PIV setup including visualisation of the illuminated laser cone, and the total measurement volume.

(b) Kiel probe setup with indication of scanning path for the most downstream assessment plane.

Figure 4.1: Illustration of experimental apparatus for the cylinder experiment.

field. An integral time scale of $T_I = 0.01$ s is estimated by the ratio of cylinder diameter to free-stream velocity, resulting in $N = 850$ statistically uncorrelated samples based on the ratio of T_{aq} over T_I. Given the maximum observed velocity fluctuations u'_{rms} of approximately 3 m/s, the uncertainty on the mean velocity measurement at 95 % confidence is estimated with 0.2 m/s, respectively 2 %.

The PIV-based pressure data is benchmarked against two reference measurements: 20 pressure orifices spaced at 40 mm in spanwise, and 50 mm in streamwise direction, record the static pressure distribution on the ground wall, downstream of the object. Data at intermediate positions is obtained by moving the cylinder position every 20 mm in spanwise, and 12.5 mm in streamwise direction. The resulting measurement yields the wall pressure on a 100×200 mm^2 domain by 102 grid points. The flow total pressure is surveyed using a Kiel probe (United Sensor Corp., KAA-6) that scans the domain at three cross sections (200×140 mm^2) downstream of the object, with a streamwise interval of 100 mm. At each plane, measurement points are spaced 20 mm in both directions. The Kiel probe (KP) is mounted on the robotic arm for an efficient scanning process. Such pressure probes are often employed in automotive wind tunnels, due to their low directional sensitivity which makes them suitable also for unsteady flows. The probe used here enables pressure measurements with an error below 1 % for flow angles within $\pm 52°$ yaw, and $[-40°, +47°]$ pitch. The setup with the probe on the robotic arm is illustrated in Figure 4.1(b). Both pressure systems acquire data at a frequency of $2,000$ Hz. The wall pressure is averaged over 30 s, whereas the KP data is averaged during 20 s at each measurement point. The reference pressure of the differential pressure transducer (p_{ref}) is obtained from the difference between the mean total pressure measured by the KP at the upper domain boundary ($z = 150$ mm) where irrotational flow conditions are assumed, and the free-stream dynamic pressure q_∞.

$$p_{ref} = \overline{p}_{KP}\big|_{\frac{z}{D}=1.5} - q_\infty \tag{4.3}$$

where q_∞ is measured by a Pitot-static tube upstream of the cylinder.

Results are represented in terms of static and total pressure coefficients. The normalization of the measured pressure difference is based upon the free-stream dynamic pressure $q_\infty = 0.5\rho u_\infty^2$.

4.3.2. Results and discussion

The mean flow topology in the cylinder wake is illustrated in Figure 4.2. The velocity contours in Figures 4.2(a) and 4.2(b) indicate the presence of reverse flow. Flow recirculation is also highlighted by the surface streamlines on the velocity contours. Main features, including the counter-rotating tip vortices, the horseshoe vortex, and the secondary vortex are shown in Figure 4.2(c). The measured flow topology agrees well with literature (e.g. Hain et al., 2008; Schneiders et al., 2016; Sumner, 2013).

In the context of a pressure wake survey it is anticipated that the vortex structures connect to regions of low pressure. The high flow angularity and reverse flow exposed by the streamlines in Figures 4.2(a) and 4.2(b) present a challenge for the Kiel probe measurements, necessitating a validation of the local inflow conditions for the probe readings.

Static pressure at the bottom wall

The pressure field calculation based on the PIV measurements is compared against the pressure recorded by the wall orifices downstream of the object. The comparison is based on the left-hand-side ($y \leq 0$) floor pressure only. From the comparison (Figure 4.3(a)) a good agreement can be concluded between the surface pressure distributions obtained by the two instruments. Some discrepancies are noticed in the minimum pressure region, which is more pronounced in the PIV data; and the pressure recovery in the streamwise direction, where the PIV-based pressure suggests a slightly weaker adverse pressure gradient as compared to the transducer data. Absolute differences are within one contour level, corresponding to $0.1\,C_P$ (6 Pa).

The streamwise pressure profile along the median plane ($y/D = 0$) in Figure 4.3(b) allows for a more quantitative comparison. Additionally, the results of Schneiders et al. (2016), who studied the same flow in a closed test-section at half the free-stream velocity, are included for reference. The uncertainty estimate for the pressure tap data is based on the transducer uncertainty of 4 Pa specified by the manufacturer, and the flow stability provided by the wind tunnel estimated with 2.1 Pa, yielding a total uncertainty of 4.5 Pa. The PIV-based floor pressure data lies within the uncertainty band of the pressure tap measurements, thereby confirming the validity of the static pressure field provided by PIV. Largest differences between the instruments are obtained furthest downstream, with PIV predicting a lower pressure, respectively a weaker adverse pressure gradient, as already observed in the analysis of Figure 4.3(a). A fair agreement with the data of Schneiders et al. (2016) is observed too, despite an apparent streamwise shift in the location of the minimum pressure point and the subsequent pressure recovery.

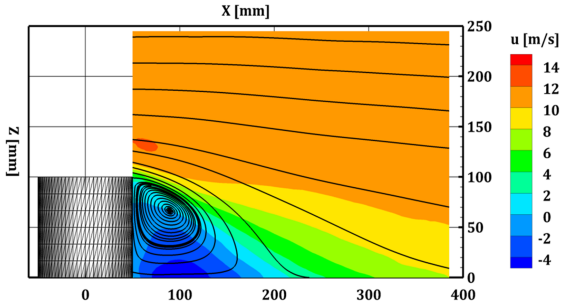

(a) Streamwise velocity u with surface streamlines in the median plane ($y = 0$ mm).

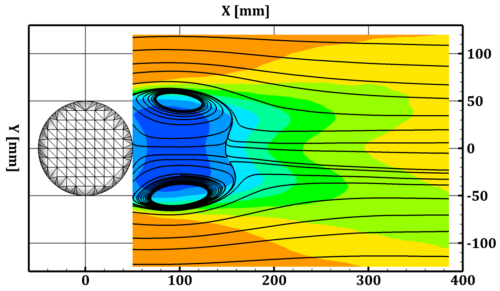

(b) Streamwise velocity u with surface streamlines at $z = 30$ mm.

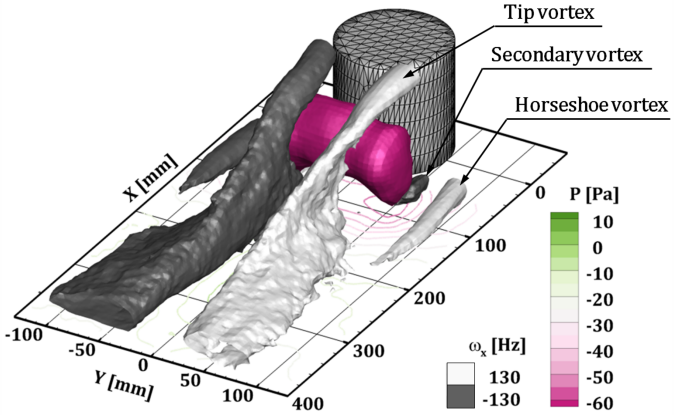

(c) Iso-surfaces of streamwise vorticity $|\omega_x| = 130$ Hz in grey. Magenta pressure iso-surface at $P = -55$ Pa, along with pressure contour on the ground ($z = 0$ mm).

Figure 4.2: Time-averaged flow topology visualization for the truncated cylinder flow.

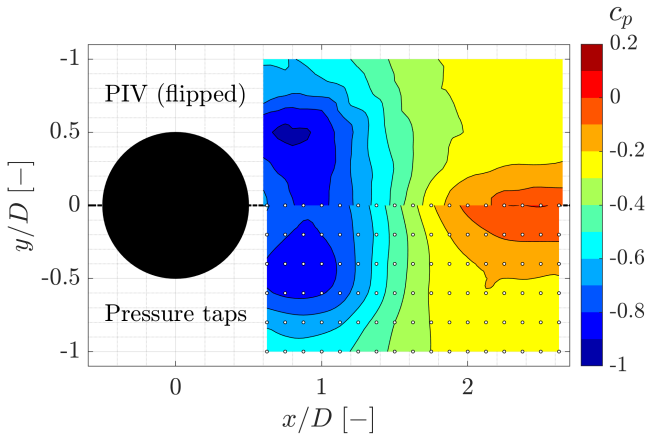

(a) Comparison of PIV-based and direct pressure measurements.

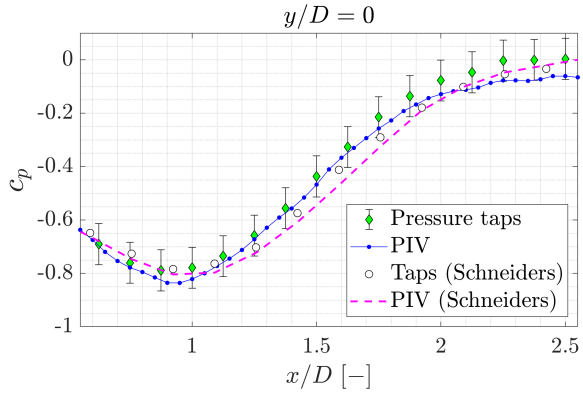

(b) Line profile at $y/D = 0$ including data from Schneiders et al. (2016).

Figure 4.3: Time-averaged floor pressure distribution in the cylinder wake.

Total pressure field

The total pressure field obtained through PIV is compared against the Kiel probe measurements in three downstream planes, perpendicular to the free-stream direction, located at 1, 2, and 3 diameter from the cylinder origin, respectively. The results are shown in Figure 4.4. Despite the relatively wide directional receptivity of the KP, the anticipated range of inflow angles for each measurement target is assessed based on the particle track data acquired within 5 mm radius of the measurement point. If the probability of flow velocity vectors beyond the angular range exceeds 25 %, the KP measurement is considered invalid. Invalid measurements are highlighted in the resulting pressure maps shown in Figure 4.4. It is evident that in the near wake (within one diameter from the object), the KP measurements cannot be considered as a valid reference, as they are affected by a large bias

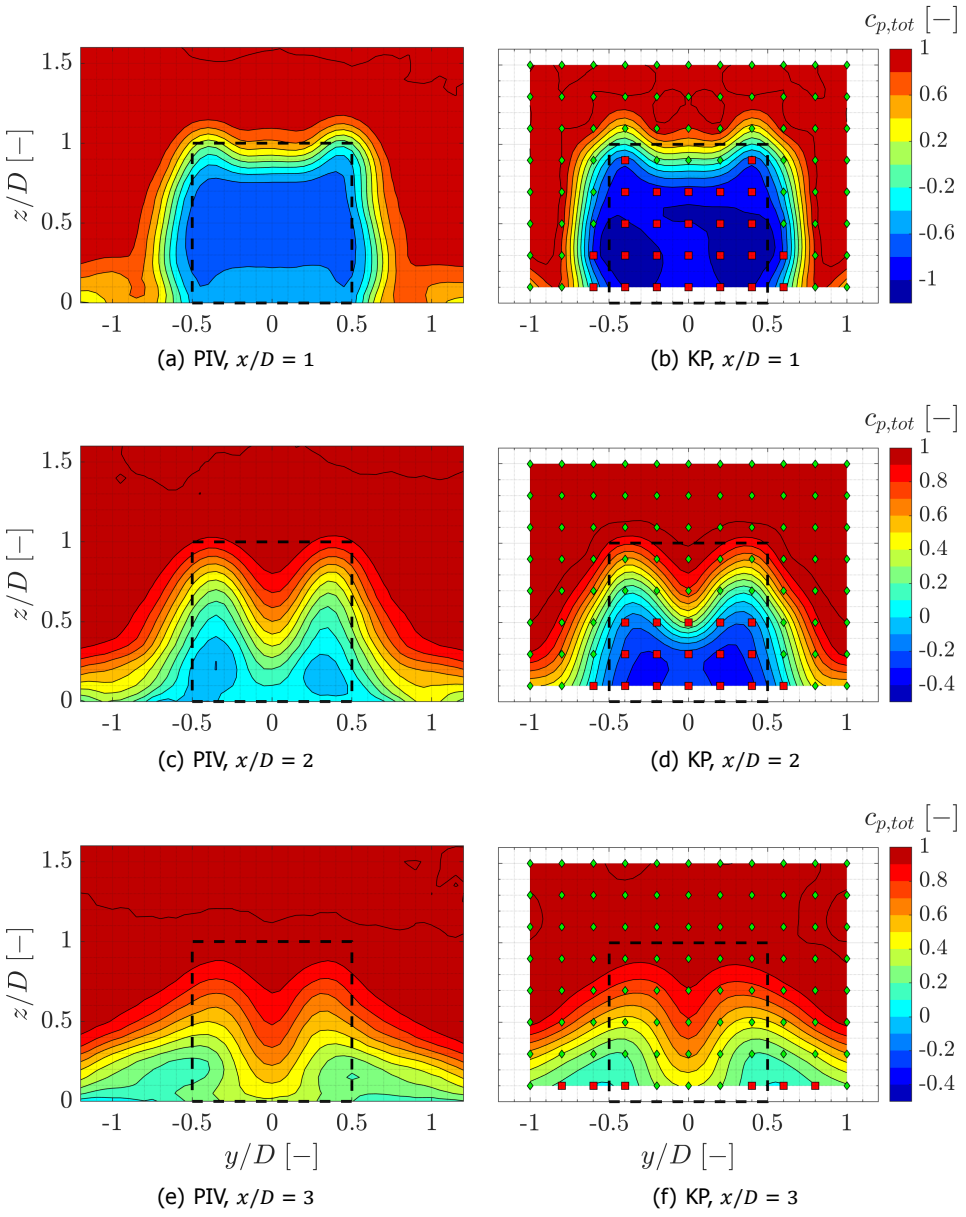

Figure 4.4: Total pressure contours in streamwise planes downstream of the cylinder. Left: PIV data; right: Kiel probe. Valid KP targets labelled by green diamonds, biased points by red squares.

error. At the mid-plane ($x/D = 2$), several measurement points are still affected by large variations of the velocity vector, under the effect of the vortical structures emanating from the object and the unsteady behaviour of the separated region. At the most downstream plane ($x/D = 3$), the conditions for a reliable measurement with the KP are restored in most of the domain.

The most upstream plane ($x/D = 1$) features a broad low pressure region in the cylinder wake, corresponding to the low pressure iso-surface shown in Figure 4.2(c). The intermediate plane ($x/D = 2$) shows two pressure minima, which are linked to the tip vortices. While the pressure minima are observed in both PIV and KP data, direct quantitative comparison should not be afforded, as the local inflow angle exceeds the KP working range. The data in this plane correlates well where the KP measurement is considered valid.

The most downstream plane ($x/D = 3$) still contains two weaker pressure minima along the cores of the counter-rotating vortex pair, whose spanwise location coincides with the projected cylinder edge. Comparison of PIV and KP data here returns a good agreement. For a more quantitative analysis, two pressure profiles are extracted for the two downstream planes: a vertical profile at $y/D = -0.4$, and a spanwise profile at $z/D = 0.2$, as shown in Figure 4.5.

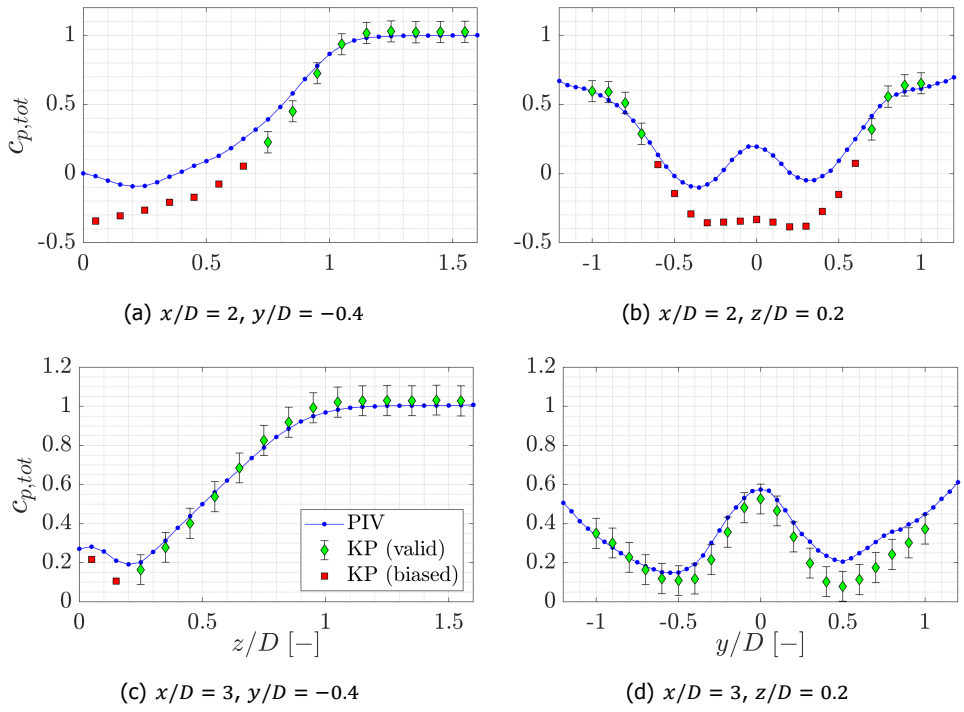

(a) $x/D = 2$, $y/D = -0.4$ (b) $x/D = 2$, $z/D = 0.2$

(c) $x/D = 3$, $y/D = -0.4$ (d) $x/D = 3$, $z/D = 0.2$

Figure 4.5: Total pressure profiles in the cylinder wake.

The pressure profiles in Figure 4.5 confirm the overall agreement in total pressure measurement by PIV and KP, where the KP data is valid. In two areas the PIV pressure exceeds the uncertainty range of the KP measurement however: in the region of maximum pressure gradient in Figure 4.5(a) the pressure is overestimated by PIV. A similar overestimation is observed for the right-hand-side (RHS) in Figure 4.5(d). The former region corresponds with the shear layer of the cylinder wake, whereas the latter is linked to the main RHS vortex as shown in Figure 4.2(c). Discrepancies between PIV and KP data are up to $0.125\,C_P$ (7.5 Pa). The source for this discrepancy is unclear, yet the asymmetry in the PIV data in Figure 4.5(d) points to a locally enhanced measurement error in the PIV measurement. Despite this mismatch, the clear advantage of the PIV based analysis is pinpointed by the profiles in the intermediate plane ($x/D = 2$), in particular by the horizontal profile in Figure 4.5(b): the PIV data features two distinct pressure minima which link well to the main vortex cores where pressure minima are expected. The KP cannot capture this pressure distribution due to the local flow angles exceeding the KP operating range.

4.4. Conclusion

The study in this chapter demonstrates the use of robotic volumetric PIV measurements to obtain time-average total pressure estimates, similar to those otherwise obtained by pressure probes. The approach enables wake surveys in a 3D domain at a relatively large scale.

The case study of the flow past a truncated cylinder at $Re = 6.6 \times 10^4$ compares the data gathered with a Kiel probe with those inferred from PIV. Discrepancies do not exceed $0.125\,C_P$ (7.5 Pa). Interestingly, the PIV analysis excels in the near wake close to the cylinder, where the results are not affected by flow reversal, contrary to the Kiel probe pressure measurements. As such, the PIV wake survey offers a complementary approach, if not alternative, to classical wake surveys by total pressure probes.

5

Surface pressure evaluation by robotic volumetric PIV

The only mechanism nature has for communicating a force to a body moving through a fluid are pressure and shear stress on the body surface.

John D. Anderson

Chapter 4 demonstrated the suitability of robotic volumetric PIV for total pressure wake measurements in large cuboid-shaped domains. Complementary to such wake surveys, the pressure on an object surface is of interest in various fluid dynamic applications; it is often difficult to capture appropriately by means of orifices integrated into the model surface. PIV measurements present an attractive alternative for surface pressure evaluation on generic 3D objects immersed in a flow. However, the analysis in Chapter 4 does not fully account for new challenges that arise, such as the treatment of boundary conditions along a curved fluid-solid interface. Therefore, this chapter proposes a dual-model pressure evaluation strategy, designed to handle the intricacies of PIV-based surface pressure evaluations on large-scale and 3D models immersed in a fluid flow.

The chapter opens with a brief literature review on aerodynamic load assessments by PIV. Subsequently, the methodology of PIV-based surface pressure analysis is discussed, culminating in the introduction of the abovementioned dual-model strategy in Section 5.1. This strategy demands a robust partitioning of the measurement domain, which is the core of Section 5.2. Next, the mapping of the flow pressure onto the model surface is detailed in Section 5.3; Section 5.4 then applies the proposed approach to the flow around a sphere.

Jux C, Sciacchitano A and Scarano F. Flow pressure evaluation on generic surfaces by robotic volumetric PTV, *Meas. Sci. Technol.* **31**, 104001 (2020)

The measurement of surface pressure in aerodynamics is of paramount importance for several engineering problems, from ground transport to aviation and including wind energy. The interest stems from the fact that pressure is, next to skin friction, the only mechanism for aerodynamic forces being exerted to an object immersed in the fluid stream.

For wind tunnel experiments, surface pressure taps are considered the standard approach to instrument scaled models, providing accurate values of the local surface pressure. Installation of pressure taps impacts the design and manufacturing of the models with multitudes of pressure orifices and highways of small tubes towards the transducer unit. In some cases the installation of pressure taps becomes challenging, consider the proximity of sharp edges, flexible objects or when working with animals and humans.

Pressure sensitive paint (PSP, McLachlan and Bell, 1995) offers the ability to map the distributed pressure field on the surface non-intrusively. Most applications of PSP are reported in the compressible flow regime (Bitter et al., 2012; Gregory et al., 2008; Klein et al., 2005, among others), whereas at low speed the small pressure variations exhibited at the surface are not accurately described (see e.g. Tagliabue et al., 2017).

The principle of inferring the flow field pressure from velocity measurements has already been introduced in Section 2.4. A challenge for PIV-based pressure measurements over generic 3D surfaces was identified in the difficulty to simultaneously illuminate a complex curved surface and record images of the flow tracers travelling above the surface. In this context, coaxial volumetric velocimetry (CVV) and its application in a robotic measurement approach have been shown to provide good optical access around curved bodies, see e.g., the discussion in Section 3.1.3 and the applications of robotic volumetric PIV to flows past human body segments in Part II.

An open question in the evaluation of the time-averaged surface pressure on generic geometries by means of robotic volumetric PIV is the treatment of solid boundaries. The topic of boundary conditions in PIV-based pressure measurements has been introduced in Section 2.4. The effect of error propagation originating from spurious or under-resolved data at the surface, however, has not been fully understood. Moreover, it is recognized that the pressure gradient integration is unnecessary within regions where the flow regime is irrotational (e.g. free stream or outer stream), and consequently simpler models (Bernoulli or isentropic flow relations) relating velocity and pressure can suffice. The latter principle has been demonstrated in the work from Ragni et al. (2009) around a 2D airfoil in the transonic flow regime and in the study of Kurtulus et al. (2007) around a square cylinder in the incompressible regime.

This chapter describes an experimental approach to evaluate the time-averaged static surface pressure distribution on generic geometries by means of robotic volumetric PIV measurements. Two key elements are addressed:

1. The method to partition the domain for pressure evaluation into a region where Bernoulli's equation is applied and a second one where spatial integration of the pressure gradient is necessary. This part of the work extends the

study of Jeon et al. (2018b), who partition the PIV measurement domain for a sequential pressure integration based on the local measurement reliability, to generic 3D objects, yet for time-averaged analysis.

2. The problem of pressure discretization on a surface that is not compliant with the Cartesian dataset of the velocity measurements is addressed.

Section 5.1 deals with the PIV-based evaluation of the 3D pressure field around immersed objects. The process of domain partitioning is addressed in Section 5.2, followed by the pressure evaluation procedures in the established domains and on the model surface in Section 5.3. Experiments are presented first in form of proof-of-principle with the measurement around a sphere in Section 5.4. Later, the database pertaining the flow around a full scale cyclist mannequin is examined in Part II. Experimental uncertainties are quantified using conventional surface pressure taps over the sphere model.

5.1. Dual model pressure analysis

The pressure field and surface pressure evaluation process by robotic volumetric PIV may be split into two main components: the first step delivers the time-averaged, three-dimensional (3D), three-component (3C) velocity field and its statistical fluctuations, in terms of root-mean-square fluctuations and Reynolds stress components. Data acquisition and processing procedures for the robotic volumetric PIV system used in this study have been discussed in Section 3.2. The second step pertains the post-processing of the velocity data to yield the static pressure distribution in the measurement domain and on the solid object surface. The foundation for the pressure evaluation, as indicated in Section 2.4, is the computation of the pressure gradient. The pressure field is subsequently obtained by spatial integration of its gradient. Let us recall the time-averaged pressure gradient $\nabla\overline{p}$ discussed in Section 2.4 (Equation (2.10)) for convenience:

$$\nabla\overline{p} = -\rho\left(\overline{\mathbf{u}}\cdot\nabla\right)\overline{\mathbf{u}} - \rho\nabla\cdot\overline{\mathbf{u}'\mathbf{u}'} \tag{5.1}$$

where the viscous term is omitted as it becomes negligible in the high Reynolds number regime ($Re > 10^3$) as demonstrated in previous studies by Ghaemi et al. (2012) and van Oudheusden et al. (2007). The ensemble averaging of the particle track data by a linear fit in isotropic cells provides $\overline{\mathbf{u}}$, its spatial gradient $\nabla\overline{\mathbf{u}}$, and $\overline{\mathbf{u}'\mathbf{u}'}$, whereas the gradient of $\overline{\mathbf{u}'\mathbf{u}'}$ is estimated by central finite-differences. With respect to evaluation of the above pressure gradient, the fit of a distribution function carries two advantages over a simple arithmetic mean:

1. Velocity fluctuations ($\mathbf{u}'$) can be evaluated with respect to the local mean, rather than the cell-centred mean, resulting in an improved estimation of the fluctuations in the presence of a spatial velocity gradient inside a cell.

2. The tangent of the distribution function immediately provides the local velocity gradient, which is required for the computation of the pressure gradient.

Some details of ensemble averaging are discussed in Section 2.3, whereas effects of different averaging schemes onto the mean velocity measurement are compared in Section 3.3.

Integration of the pressure gradient (Equation (5.1)) requires the selection of appropriate boundary conditions, as introduced in Section 2.4. Specifying pressure boundary conditions on solid objects immersed inside a PIV measurement domain is prone to errors as indicated in Section 2.4.2. The propagation of errors from the solid object boundaries is avoided when the values at the boundary do not take part in the pressure integration process. This can be realized by a unidirectional integration procedure (see e.g. Dabiri et al., 2014). In this way, the pressure gradient can be integrated from the outer (fluid-domain) boundary towards the object of interest, as illustrated in Figure 2.19(b).

The spatial integration of the pressure gradient over a long path, however, is prone to error accumulation. To attenuate such effects, a dual-model approach for the evaluation of the static pressure field is envisaged: the measurement domain is partitioned into a region of irrotational flow where Bernoulli's equation returns the pressure from the local velocity, and the remaining region (rotational flow) where the pressure gradient is integrated uni-directionally. The equations used in this approach read as:

$$\overline{p} = \begin{cases} \overline{p}_{ir} = p_0 - \frac{1}{2}\rho\left(\overline{\mathbf{u}\cdot\mathbf{u}}\right) \\ \overline{p}_{rot} = \overline{p}_{ref} + \int\left(-\rho\left(\overline{\mathbf{u}}\cdot\nabla\right)\overline{\mathbf{u}} - \rho\nabla\cdot\overline{\mathbf{u}'\mathbf{u}'}\right)\cdot d\mathbf{s} \end{cases} \tag{5.2}$$

The proposed concept is illustrated schematically in Figure 5.1 and it is discussed in detail hereafter, starting with the criterion that identifies the irrotational flow domain.

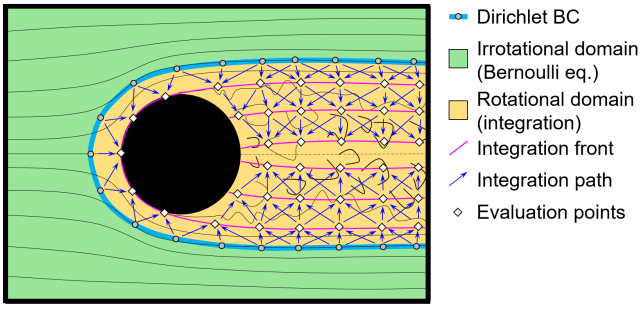

Figure 5.1: Schematic of domain partitioning for dual-model pressure evaluation around a circular object.

5.2. Domain partitioning

The goal of domain partitioning is the robust identification of the sub-region where Bernoulli's equation can be applied accurately. The problem translates into determining the interface between the rotational- and irrotational domain.

Recalling Anderson (2011), a vector field $\mathbf{u}(\mathbf{x})$ is defined irrotational if its curl is zero ($\nabla \times \mathbf{u} = 0$). For the latter, a (scalar) potential φ can be defined such that $\mathbf{u} = \nabla\varphi$. In the assumption of incompressible, inviscid and adiabatic flow, the total pressure remains constant, yielding Bernoulli's principle. The main question arising here is: how can the part of the flow domain with constant total pressure be identified?

In an initial attempt the region of constant total pressure was approximated by geometry- and turbulence-based surrogates (Jux et al., 2019). In this chapter, the principle of domain partitioning and subsequent pressure evaluation is examined on an experimental dataset obtained for the flow around a sphere. The experimental setup and selected results have been presented in Chapter 3. Figure 5.2 illustrates the flow topology in the sphere's centre plane. Further results are discussed in Section 5.4.

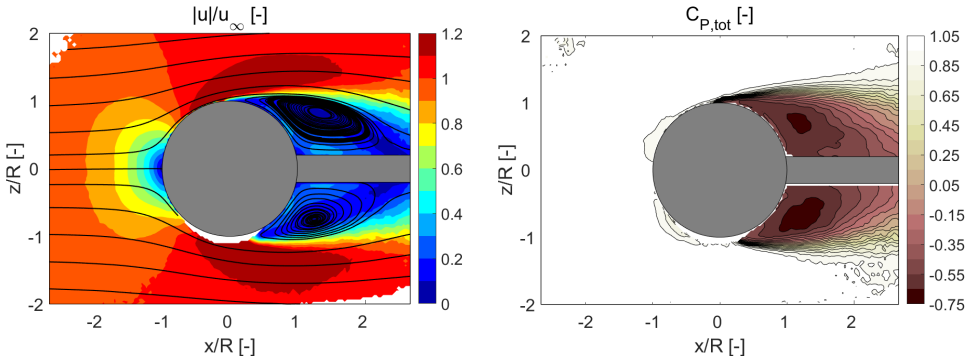

(a) Streamwise velocity magnitude (b) Total pressure coefficient

Figure 5.2: Mean streamwise velocity and total pressure coefficient estimate in the zx-plane ($y = 0$). Total pressure estimate resulting from spatial integration of $\nabla\overline{p}$ assuming free-stream conditions at the upstream boundary ($x/R = -2.67$).

5.2.1. Total pressure approximation

A first approximation of the total pressure field is obtained when the total pressure at the inflow boundary is assumed as constant. The resulting distribution of total pressure coefficient, herein defined as,

$$C_{P,tot} = \frac{\overline{p}_0 - p_\infty}{q_\infty} = \frac{(\overline{p} - p_\infty) + \frac{1}{2}\rho\left(\overline{\mathbf{u}\cdot\mathbf{u}}\right)}{\frac{1}{2}\rho u_\infty^2} \tag{5.3}$$

is computed, based on the measured, time-average velocity magnitude $\overline{\mathbf{u}\cdot\mathbf{u}}$, and the static pressure field $(\overline{p} - p_\infty)$. The latter is obtained by spatial integration of the pressure gradient, following the pressure integration scheme detailed in Section 5.3.2, starting from a constant total pressure boundary condition upstream of the sphere model. The resulting pressure distribution is illustrated in Figure 5.2(b), where $C_{P,tot}$ drops below unity in the wake region.

5.2.2. Definition of irrotational-rotational interface

The first-level estimation of total pressure serves to define the edge of the rotational region as to where $C_{P,tot} < 1$. However, given the finite uncertainty in the determination of $C_{P,tot}$ a threshold needs to be selected for $C_{P,tot}$ below unity, that encompasses such uncertainty. A possible approach to determine the experiment-specific threshold level is based on the analysis of the standard deviation of the total pressure coefficient in the irrotational domain $\sigma_{C_{P,tot}}$, for instance over a region upstream of the model where the condition of constant total pressure can be assumed valid with high confidence. For the present case Figure 5.3 illustrates such choice, along with the resulting $C_{P,tot}$ contour when allowing for a reduction of $3 \times \sigma_{C_{P,tot}}$ below unity.

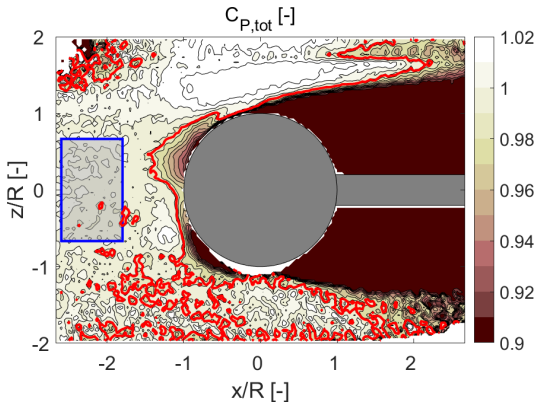

Figure 5.3: Total pressure contour in the zx-plane ($y = 0$), along with the threshold level contour ($\epsilon_{C_{P,tot}} = 0.985$) in red, based on the standard deviation of $C_{P,tot}$ ($\sigma_{C_{P,tot}} = 0.005$) estimated from the region inside the blue contour.

For the case shown here, a threshold of $\epsilon_{C_{P,tot}} = 0.985$ is determined based on a standard deviation of $\sigma_{C_{P,tot}} = 0.5\,\%$. It should be retained in mind that defining the domain interface at any value of $C_{P,tot}$ below unity introduces a systematic underestimation of the total pressure at such interface —a bias error of $1.5\,\%$ in the present case. Such bias error, can be mitigated or eliminated if the rotational domain is dilated, moving the interface towards the irrotational domain, with values of $C_{P,tot}$ closer to unity. The need and extent of such operation may be case-dependent and a detailed discussion is not given here for sake of conciseness. Nevertheless, a comparison of the surface pressure obtained with and without domain partitioning is presented in the results in Section 5.4.2.

5.3. Fluid and surface pressure evaluation

The static pressure distribution in the measurement domain and on the object surface is evaluated making use of two models as outlined before.

5.3.1. Pressure evaluation by Bernoulli's equation

In the steady irrotational fluid domain the relation between velocity and pressure is accurately approximated with Bernoulli's equation, i.e. uniform total pressure. The pressure relative to known free-stream conditions (u_∞, p_∞) is then given by,

$$\overline{p} - p_\infty = \frac{1}{2}\rho\left(u_\infty^2 - \overline{\mathbf{u}\cdot\mathbf{u}}\right) \tag{5.4}$$

where $\overline{\mathbf{u}}$ is the experimentally measured time-averaged velocity. The direct relation between velocity and pressure yields a robust point-wise estimate of the static pressure as it does not depend on boundary conditions, and local errors do not accumulate along a path. Figure 5.4 illustrates the share of the measurement domain that can be evaluated by this approach for the flow around a sphere.

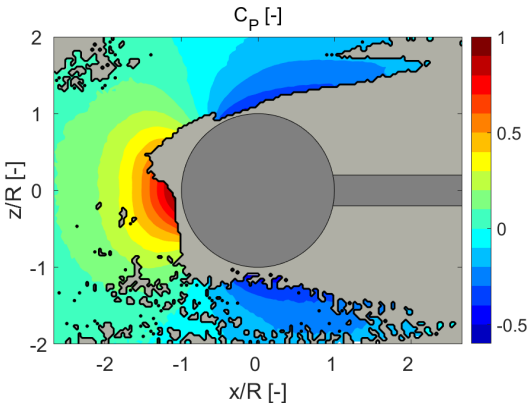

Figure 5.4: Static pressure distribution in the irrotational flow domain, based on Bernoulli's equation. The gray-shaded area surrounding the sphere model requires pressure integration based on Equation (5.5).

5.3.2. Pressure integration

For the rotational flow region the static pressure is obtained through spatial integration of the pressure gradient ($\nabla\overline{p}$, see Equation (5.1)), with the pressure at the edge of the irrotational region providing the necessary Dirichlet boundary condition.

The pressure gradient is integrated with a spatial marching process of the whole interface, intended to enforce consistency among adjacent paths. The boundary of the rotational part of the flow field is eroded, starting from an initial interface with the irrotational domain (Figure 5.4). The pressure is assigned for points in the rotational domain of the fluid mesh with a minimum of 8 neighbour points (N_{min}) with known pressure, considering a $3 \times 3 \times 3$ kernel around the point of interest. Selecting a smaller value of N_{min} results in a faster propagation of the integration front, whereas a larger value adds redundancy, as the local pressure estimate is built from a larger ensemble. Its effect on the pressure integration procedure is discussed for the 2D case in the work of van Oudheusden (2008). For the selected

points, the pressure gradient $\nabla\overline{p}$ is integrated from the available neighbors $\mathbf{x}_i$ to the evaluation point $\mathbf{x}_e$.

$$\overline{p}\,(\mathbf{x}_e) = \frac{1}{N}\sum_{i=1}^{N}\left(\overline{p}\,(\mathbf{x}_i) + \Delta\overline{p}_{i-e}\right) \tag{5.5a}$$

$$\Delta\overline{p}_{i-e} = \frac{1}{2}\left(\nabla\overline{p}_i + \nabla\overline{p}_e\right)\cdot(\mathbf{x}_e - \mathbf{x}_i) \tag{5.5b}$$

With each integration step, the domain of known static pressure is dilated. Conversely, the part of the rotational domain where the pressure has not been integrated yet is eroded.

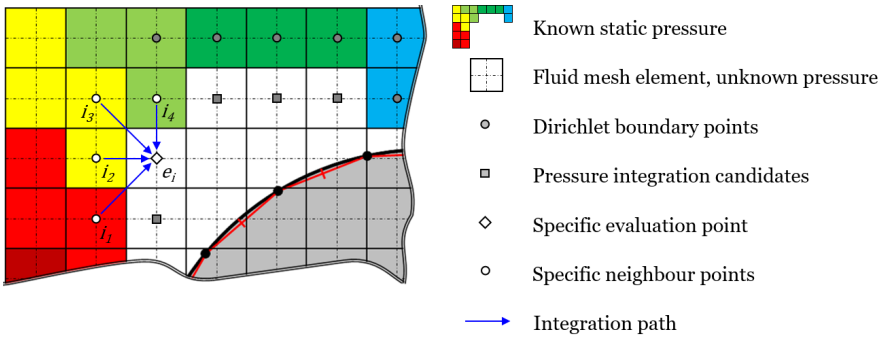

Figure 5.5: Illustration of the spatial marching pressure integration procedure.

A 2D visualization of the spatial marching procedure is given in Figure 5.5. The spatial marching algorithm advances its front until the static pressure is evaluated at all cells, yielding the pressure distribution in the flow field.

5.3.3. Surface pressure mapping

For the evaluation of the pressure at the object surface, few markers are placed on the object that are detected by the measurement system and accurately position the model within the measurement domain. Once the model position is known, its surface is discretised at the desired spatial resolution, yielding a description of the surface by a point cloud $\mathbf{x}_s$. Here, a conventional surface mesh with triangular faces, stored in a stereolithography (.stl) file is considered (see e.g. Kai et al., 1997), but any equivalent type of discrete surface description may be used.

The value of the pressure on each point of the discretized surface $\mathbf{x}_s$ is obtained from its nearest neighbour in the flow field (Cartesian) mesh. The nearest neighbour is determined by considering the geometrical distance (Euclidean). Points within a $3 \times 3 \times 3$ kernel centred around the nearest neighbour point are used to compute the static pressure at the surface node. The latter is determined following a similar approach as outlined in Equation (5.5), namely by integration of the pressure gradient. The principle is schematically outlined in Figure 5.6.

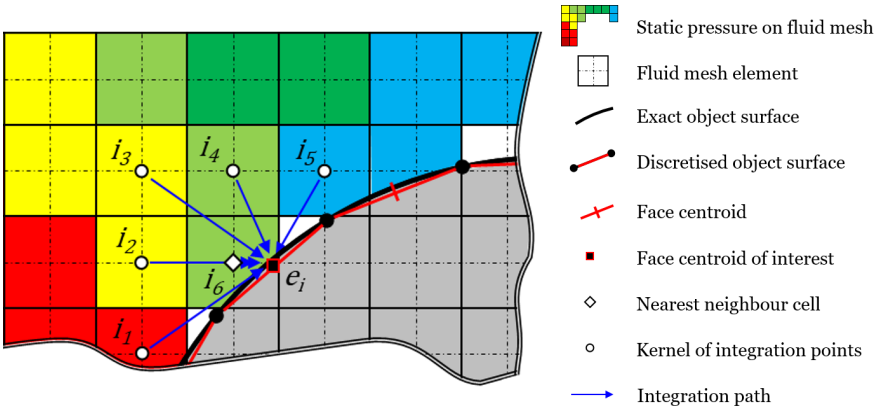

Figure 5.6: 2D schematic of surface pressure mapping principle.

In this last part of the process, the pressure gradient from the nodes is used, rather than using the trapezoidal type integration used in the flow field. Therefore, $\Delta\overline{p}_{i-e}$ from Equation (5.5b) is changed into,

$$\Delta\overline{p}_{i-e} = \nabla\overline{p}_i \cdot (\mathbf{x}_e - \mathbf{x}_i) \tag{5.6}$$

The pressure mapping is carried out for all surface nodes that have neighbouring fluid mesh cells with valid static pressure values, yielding the surface pressure distribution on the object of interest.

5.4. Assessment on the flow around a sphere

The proposed method is applied to the flow around a sphere, and results are compared to surface pressure measurements acquired by pressure taps. Applications to more complex geometries are included in Part II.

5.4.1. Experimental apparatus and procedures

The method is applied to the sphere-flow data presented in Section 3.3. For convenience the essential setup parameters and procedures are summarized here: experiments are conducted in TU Delft's Open Jet Facility (OJF) at 10 m/s freestream velocity, at atmospheric conditions. HFSB tracer particles are generated by a 10-wing, 200-nozzle seeding rake situated downstream of the turbulence meshes in the settling chamber. The seeded streamtube has a cross-section of 0.5 m^2, which reduces by a factor 3 upon passing through the wind tunnel contraction.

The robotic volumetric PIV system consists of a *Universal Robots UR5* collaborative robotic arm and the *LaVision MiniShaker Aero* coaxial volumetric velocimeter. The active camera sensors count 640×476 pixels and image quadruplets are acquired at a rate of 821 Hz.

The above systems are used to observe the airflow around a 3D printed sphere of diameter $d = 15$ cm. The corresponding Reynolds number $Re_D = 9.9{\times}10^4$, obeys

the sub-critical flow regime (Achenbach, 1972), where the boundary layer remains laminar until flow separation. The sphere is equipped with 15 static pressure taps in the vertical symmetry plane, between -10° and 130° azimuth at an equidistant spacing of 10°. The orifices feature 1 mm diameter. The overall setup is presented in Section 3.3. Instead, Figure 5.7 shows some details of the sphere model and its pressure orifices.

(a) Model preparation: installing the pressure tap tubing.

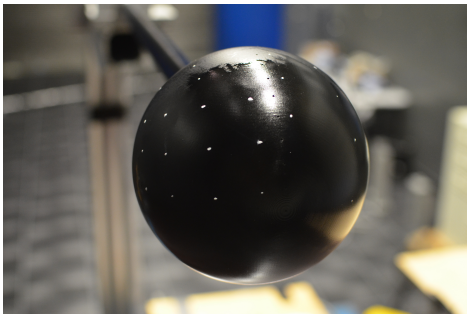

(b) Model with orifices and surface markers installed in OJF.

Figure 5.7: Sphere model with pressure orifices.

The sphere is supported from behind by a 30 mm diameter, circular tube. A vertical beam holds the support from 1.2 m downstream. The sphere sits 1 m above the ground. The pressure tap measurements serve as a reference for the surface-pressure evaluations from the robotic volumetric PIV recordings.

During acquisitions, the CVV probe is oriented normal to the free-stream direction, at approximately 40 cm distance to the sphere centre. Streamwise translations of the probe yield data acquisitions up- and downstream of the sphere. Each view contains $10,000$ images ($T_{aq} = 12.1$ s). The total measurement volume, combining multiple acquisitions, exceeds 50 L. The measurement uncertainty on the mean velocity was estimated with 2 % (0.2 m/s) in Section 3.3.

Particle images are analysed with the procedure outlined in Section 3.2, consisting of particle tracking in 3D and subsequent ensemble averaging.

5.4.2. Results and discussion

The time-averaged velocity field measurement is shown in Figure 5.8(a) in the vertical symmetry plane of the sphere. The corresponding pressure field as obtained by the outlined method is illustrated in Figure 5.8(b).

Flow stagnation in Figure 5.8(a) is corresponded in Figure 5.8(b) with a relative pressure increase of 60 Pa, consistent with the flow dynamic pressure in the free-stream ($q_\infty = 60$ Pa). The flow accelerates around the object up to approximately $\theta = 80^\circ$, where the onset of separation is observed to occur. In the rear region of the sphere, a circulatory motion is established with reverse flow conditions. The inspection of the 3D data returns a toroidal structure for the recirculation, consistent

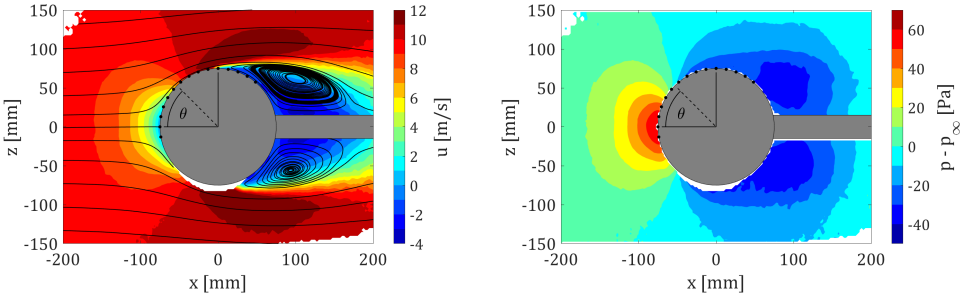

(a) Streamwise velocity (b) Static pressure

Figure 5.8: Time-averaged flow field for a linear bin size of 10 mm in the vertical symmetry plane. Black dots indicate pressure tap locations.

with the axial symmetry of the object geometry. The pressure distribution exhibits little variation past separation, with an annular region of mildly lower pressure ($\Delta p = -30$ Pa) in the separated recirculating flow ($\theta \approx 150°$).

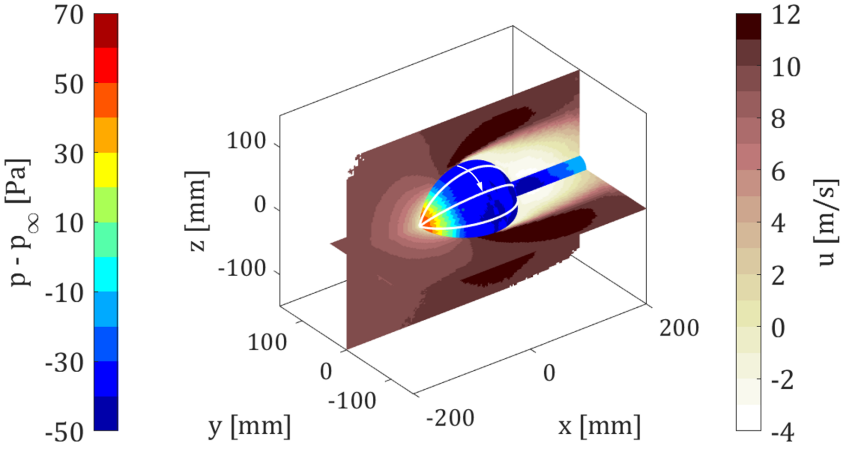

Figure 5.9: Contours of streamwise velocity in horizontal and vertical symmetry plane along with the static pressure distribution on the discretized sphere model. Definition of elevation angle ϕ indicated by white iso-lines at $[15, 45, 75]$ degrees, with $0°$ corresponding to an equivalent line in the zx-plane.

The 3D static surface pressure distribution is shown in Figure 5.9, along with contours of the streamwise velocity field on orthogonal symmetry planes. From a careful analysis of the 3D surface pressure data, it is observed that the flow field is not fully axis-symmetric, but the flow acceleration in the horizontal plane appears to be more dominant as compared to the acceleration in the zx-plane. This translates into a further reduction in surface pressure of up to 7 Pa on the side of the sphere (negative y).

The level of symmetry of the surface pressure data is quantified in Figure 5.10, where the distribution of the pressure coefficient C_P is plotted as function of azimuth angle θ and elevation level ϕ. The data shown in Figure 5.10 exhibit some degree of variation along the elevation, which feature a delayed pressure decrease followed by an increased suction around $\phi = 90°$. The maximum disparity narrowly exceeds one contour level, which corresponds to $10\,\%\,C_P$ for the present data.

Because potential flow theory can be considered as ground truth only in a limited angular range ($\theta \leq 30°$), the accuracy of the surface pressure distribution resulting from the 3D velocimetry data is compared to the direct measurements obtained by pointwise pressure taps. The latter are located in the zx-plane, as indicated in Figure 5.8, corresponding to $\phi = 0°$ elevation.

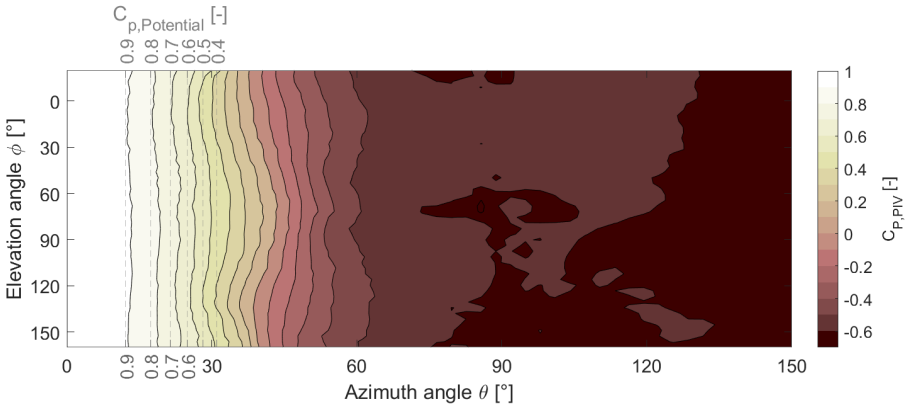

Figure 5.10: Surface pressure coefficient distribution over the sphere as measured by robotic volumetric PIV, compared to potential flow theory for $\theta < 40°$. Definition of angles provided in Figures 5.8 and 5.9.

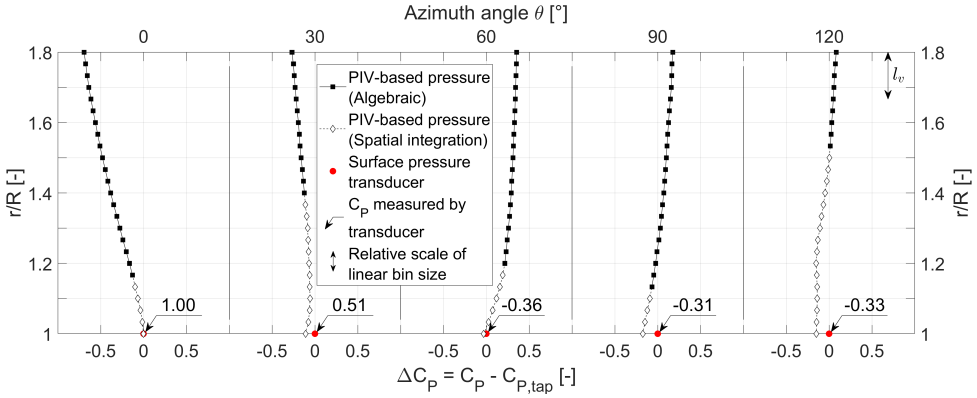

Figure 5.11: Pressure distribution along radial lines in the zx-plane, compared to pressure tap readings at the surface.

The pressure coefficient distribution along radial lines is shown for selected azimuth angles in Figure 5.11, where the value at the sphere surface is compared to the recording from the pressure transducer. For $0°$ and $30°$ azimuth, the static pressure is increasing towards the sphere surface as expected from the flow deceleration. For larger azimuth angles, a reduction of C_P towards the wall is observed instead. For the selected angles, the pressure obtained by robotic volumetric PIV correlates well with the transducer readings for $\theta \leq 60°$, whereas a difference of up to $0.17\ C_P$ is observed approaching flow separation.

Lastly, the effect of spatial resolution in the time-averaged velocity field measurement on the computed surface pressure distribution is assessed. The size of the averaging bin is varied in the range from $l_v = 10$ to 50 mm. An overlap factor between adjacent bins of 75 % is applied. The results are compared to the reference measurements by the wall orifices in Figure 5.12. Two more solutions are included in the comparison:

1. The surface pressure distribution obtained by full spatial integration, starting from a free-stream boundary condition far upstream of the sphere;
2. The surface pressure distribution obtained through solution of the Poisson problem formulation. In this approach, first the pressure Poisson equation is solved. Subsequently, the flow pressure is mapped onto the sphere surface by means of linear extrapolation.

Both of the above are evaluated with a linear bin size of $l_v = 10$ mm.

For the forward part of the sphere ($\theta \leq 30°$) potential flow theory is considered a reliable approximation of the flow, which is plotted (solid black) in Figure 5.12(a) for reference. In this region, the PIV pressure agrees well with both, potential flow theory and surface tap measurements. Differences here are smaller than $0.03\ C_P$ (1.8 Pa) for $\theta < 30°$, even at the coarsest resolution ($l_v = 50$ mm). The Poisson solution instead underestimates the stagnation value by approximately 10 %. The pressure obtained by full integration matches well at stagnation, and shows a gradually increasing error until $\theta = 40°$.

For larger angles, the wall taps provide the reference up to $\theta = 130°$. In the region of $30° \leq \theta \leq 60°$, the azimuthal pressure distribution reaches its maximum gradient. The pressure provided by the PIV measurements is lower and closer to the potential flow solution as compared to the tap readings. A maximum deviation of $0.15\ C_P$ is found at $40°$. Interestingly, there is no clear dependence of the results from the spatial resolution, except for the coarsest bin size (50 mm), with the overall effect of smoothing the surface pressure distribution along the azimuth.

A small region with maximum suction point is located at $\theta = 70°$ according to the orifice measurements, with the PIV data approximately following it. The subsequent mild pressure recovery (adverse pressure gradient) downstream of this point is observed in the transducer data but not well captured by robotic volumetric PIV. Depending on the spatial resolution of the velocity measurement, the resulting difference is approximately 0.15 to $0.21\ C_P$ (9 to 12.6 Pa) in the separated wake region for the data obtained with the proposed method. The data obtained by full spatial integration shows an increasing mismatch in the wake region up to $0.26\ C_P$.

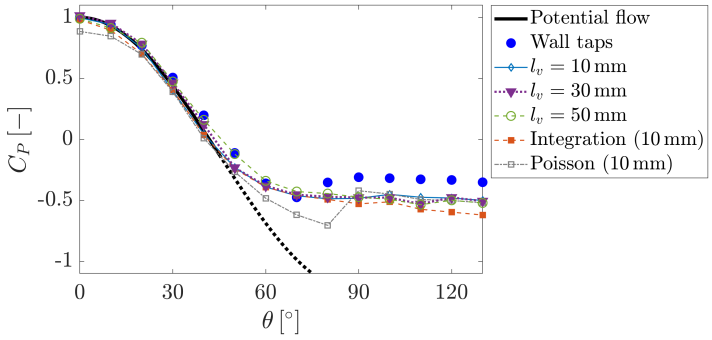

(a) Pressure coefficient

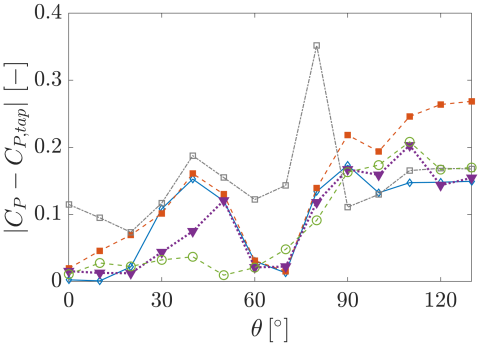

(b) Error relative to pressure tap data

Figure 5.12: Azimuthal pressure distribution for different spatial resolution. Results compared to pressure transducer data, Poisson approach and full spatial integration.

Considering the above, one may conclude that for the measurement of the time-averaged surface pressure distribution, spatial resolution effects are not observed as long as the interrogation bin remains smaller than half the local radius of curvature of the test model. The latter can be regarded as a design criterion for pressure measurements by robotic volumetric PIV.

5.5. Conclusion

A novel pressure-evaluation approach is presented to examine static surface pressure distributions on generic three-dimensional geometries by means of ensemble averaged 3D velocimetry data as obtained by robotic volumetric PIV. The pressure field is retrieved in a dual-model approach, exploiting Bernoulli's equation in the region of constant total pressure, and integrating the mean pressure gradient elsewhere. The uni-directional integration of the pressure gradient avoids the specification of boundary conditions on the fluid-solid interface, which often deteriorates the result following the Poisson approach.

Experiments on a 15 cm diameter sphere model in a 10 m/s airflow return pressure distributions in good agreement with potential flow theory and pressure tap measurements. Differences up to $0.15\ C_P$ are observed in the region of maximum pressure gradient and in the separated wake. It is observed that spatial resolution of the ensemble averaged velocity field appears not to be critical as long as the linear bin size is smaller than half the local radius of curvature.

Measurement accuracy relies on the constant total pressure field hypothesized at the inflow boundary. Secondly a known model geometry and position are also assumed. The former is common practice in wind tunnel experiments, whereas the second assumption may not hold true when using flexible models or bending under the action of the aerodynamic forces is observed.

6

Flow-tracer-based object surface reconstruction

While the previous chapter focused on the pressure evaluation on an object surface, it disregarded the fact that in wind tunnel testing, the precise location of the fluid-solid interface is often unknown. Such uncertainty can stem from elastic deformations under aerodynamic loading, manufacturing tolerances, or loads introduced during model installation. This necessitates the in-situ measurement of the fluid-solid interface for the PIV-based surface pressure evaluation. Rather than acquiring the model shape through a secondary instrument, e.g. a 3D scanning device, this chapter investigates model shape reconstruction through the tracer particle distribution that results from the PIV measurement.

The chapter opens with a brief literature study on conventional model positioning approaches in PIV. Subsequently, the principle of fluid-solid interface detection by analysis of the flow tracer distribution is investigated for the 2D case in Section 6.1. The developed method is then scrutinized on the synthetic particle distribution around a 2D airfoil in Section 6.2. This section includes a parametric study of key quantities, such as the tracer particle concentration. Extending the approach to the 3D case (Section 6.3) allows for an experimental assessment of this method on the flow around a simplified car's side-mirror model in Section 6.4.

Jux C, Sciacchitano A and Scarano F. Object surface reconstruction from flow tracers, *Exp. Fluids* **62**, 42 (2021)

Chapters 3 to 5 have focused on the velocity measurement in fluid flows and the subsequent analysis of the pressure distribution based on the acquired velocity data. Representative for many aerodynamic investigations, all studies in the previous chapters focused on the flow around an object immersed in the fluid stream. When the experimentalist is interested in the near-surface flow properties, such as pressure and even skin-friction, accurate determination of the object surface position and orientation is mandatory.

An overview of the literature returns a disproportionate comparison between methods dedicated to advance the analysis of the flow velocity and those that examine the geometry of the object immersed in the flow. As a result, the problem of object surface determination for applications in fluid flow investigations has only been studied in few works and problem-specific solutions have been proposed. The imbalance is particularly evident in volumetric studies, where the diffuse illumination prevents the object identification by classical edge detection or masking approaches. The latter methods usually suffice in the 2D case, e.g. by tracing the characteristic sharp intensity gradient resulting from the light sheet striking the object. An overview of edge detection approaches is presented by Ziou et al. (1998), including the well-known Sobel operator (e.g. Duda et al., 1973) and the popular algorithm proposed by Canny (1986). Texton-based approaches, such as described in the work of Malik et al. (2001), are also well suited for the feature detection in 2D images. PIV-specific methods have been developed for the purpose of image filtering and mask generation. Examples thereof are the digital masking technique (e.g. Gui et al., 2003), the concept of anisotropic diffusion (e.g. Adatrao and Sciacchitano, 2019), or the recently presented dynamic masking technique by Vennemann and Rösgen (2020) which relies on artificial neural networks. As indicated, these techniques work well in 2D PIV measurements, but they do not apply to surface reconstruction of generic 3D objects in fully volumetric flow investigations, which presents the main target of the work presented in this chapter.

As discussed in Section 2.5, the object geometry may be known a-priori, e.g. by a computer-aided design (CAD) model, and determining a number of reference points on its surface may sound a trivial solution. This approach, however, does not account for several sources of uncertainty: production and assembly tolerances, model deformations due to mechanical and aerodynamic loads or thermal stresses. The latter justifies the need for in-situ measurements of the fluid-solid interface.

The broader topic of interface detection (including fluid-fluid interfaces) within particle imaging techniques has been addressed from several perspectives: Adhikari and Longmire (2012) developed the visual hull method for tomographic particle image velocimetry measurements around moving objects, which automates the process of identification and masking of the solid object, and thereby, suppresses the reconstruction of ghost particles inside the solid. Im et al. (2014) present the reconstruction of a refractively matched nasal cavity model, based on tomographic PIV measurements of the flow through the complex three-dimensional geometry. Also here, a key motivation in the latter study is the suppression of ghost particle reconstruction inside the solid object, ultimately improving the tomographic reconstruction quality in the fluid flow domain. Relevant work has been conducted

in problems dealing with fluid interfaces: Reuther and Kähler (2018) evaluate detection methods for the turbulent/non-turbulent interface of wall-bounded flows through planar PIV measurements. Ebi and Clemens (2016) instead, investigate the simultaneous measurement of a 3D flame front, and its encompassing velocity field by means of tomographic PIV.

This brief survey expresses the multifaceted nature of interface detection in particle imaging. Exception made for the visual hull method, an interesting commonality of the referenced studies above is that they attempt to discriminate a seeded phase where velocimetry measurements are taken, from a void region which is characterized by the absence of tracer particles.

Focusing on fluid-solid interfaces, an alternative approach to accurately determine the object surface is the introduction of an independent measurement system that detects markers distributed along the model geometry. Such dual-measurements are typical for fluid-structure-interaction (FSI) studies, which feature the fluid flow analysis e.g. by PIV, combined with the study of the model's structural response e.g. by digital image correlation (DIC). Two recent examples by Zhang et al. (2019) and Acher et al. (2019) have been introduced in Section 2.5. In some cases, the complexity of operating two separate systems may not be affordable, motivating the development of FSI methods in which the flow imaging system simultaneously captures the structural deformation. A number of studies following such approach is available in the literature, and has been discussed in Section 2.5. Both of the above approaches rely on appropriate treatment of the model surface. This, however, carries two disadvantages:

1. It may not be feasible in some conditions, e.g. when the model surface cannot be treated. Consider the above case of the refractively matched model in the study of Im et al. (2014) for instance.

2. It increases the information density on the imaging system, usually quantified in particles per pixel (ppp), which can hamper the achievable spatial resolution in the flow measurement.

From these observations, stems the interest for interface detection approaches solely based on the fluid flow tracer measurements, as obtained by PIV techniques.

Lastly, it is noted that the studies of Im et al. (2014) and Ebi and Clemens (2016) utilize tomographic particle reconstructions followed by an analysis of the spatial particle distribution in a discretized (voxelized) domain. Similarly, the study of Reuther and Kähler (2018) includes methods that work on correlation based PIV data as well as an approach that analyses discrete pixel intensities in the 2D image. The advancements of particle reconstruction algorithms at high image source densities, such as the iterative particle reconstruction (IPR) method by Wieneke (2012) and the Lagrangian particle tracking algorithm Shake-The-Box (STB) by Schanz et al. (2016) have allowed to efficiently track individual particles at high spatial resolution. However, also within these latter cases, most research works have focused on the tracers motion analysis, leaving the problem of surface detection unexplored.

This chapter addresses the task of object surface detection making use of flow tracer analysis. The resulting method assumes therefore that the position of in-

dividual particle tracers flowing around an object can be detected in the three-dimensional space as done with existing particle tracking or reconstruction algorithms. Summarizing, the goal of the present study is to detect the surface of a solid object immersed in a seeded flow, solely based on the spatial distribution of flow tracers as recorded and reconstructed from a generic particle tracking velocimetry (PTV) measurement.

The working principle of the method investigated here follows the spatial distribution of particle tracers captured within a spherical neighbourhood around the fluid-solid boundary, which separates the seeded and void region. The offset between the centroid of captured tracers and the geometrical centre of the neighbourhood provides the fundamental information for the measurement of the object surface position and orientation.

The working principle is discussed in the following section and demonstrated for the 2D case. A numerical illustration of the problem is presented with synthetically generated data around an airfoil (Section 6.2), before generalizing the developed theory to 3D space (Section 6.3). The interface detection method is assessed on an experimental data set capturing the 3D flow around a wall mounted obstacle in Section 6.4.

6.1. Principle of interface detection in 2D

Let us consider the surface of a solid object immersed in a fluid flow where tracers are dispersed at random positions, up to the solid surface. The task of identifying the model interface translates into detecting the boundary between seeded and void regions. Figure 6.1 illustrates particle tracers randomly distributed above the flat surface of an object. When a circle of radius R is considered (a sphere will later be substituted for the 3D analysis) at a distance h from the wall such that $h > R$, the distribution of particle tracers will feature a centre of mass ξ close to the geometrical centre of the circle (as in case of A). In the hypothesis of high tracer particle concentration c_p (corresponding to a small mean inter-particle distance λ_p), and a uniform particle distribution, the particles centre of mass ξ coincides with the centre of the bounding circle. When the circle approaches and partly intersects the wall (case B) the centroid of the particles distribution ξ is offset in a direction away from the wall, by a vector $\mathbf{x}_n$ from B. In more general terms we define $\mathbf{x}_n$ as the vector between the particles centre of mass ξ and the search area's geometric centre C_i:

$$\mathbf{x}_n = \xi - C_i \tag{6.1}$$

In the specific condition where the circle is centred on the object surface (case C) the centroid offset reaches a specific value. The latter can be associated with the wall position detection. Furthermore, for a circle centred inside the solid ($h < 0$, case D), the distance $|\mathbf{x}_n|$ keeps increasing and tends to become the circle radius when the circle is fully immersed in the solid. In the latter case, the centroid of the particles distribution cannot be defined as no particle is captured inside the circle ($h \leq -R$, case E). The analytical expression of the offset $|\mathbf{x}_n|$ as a function of h is derived and discussed shortly.

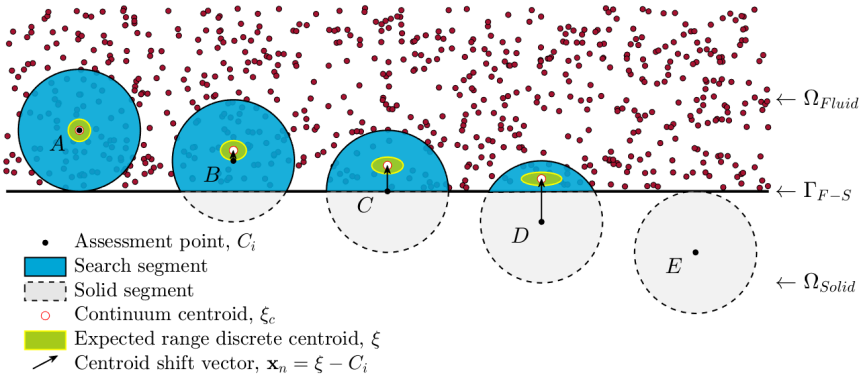

Figure 6.1: Schematic 2D particle distribution near a fluid-solid interface (Γ_{F-S}).

It can be concluded from the above analysis, that the magnitude of the vector $|\mathbf{x}_n|$ spanned between the mean particle position ξ and the geometrical centre C_i of the circular search area (SA) indicates whether C_i lies within the fluid domain or is part of the solid region. Moreover, the direction of $\mathbf{x}_n$ provides an estimate of the normal to the surface.

In the following $|\mathbf{x}_n|$ denotes the centroid shift. The expected centroid shift can be expressed as a function of the elevation h (the wall normal distance of C_i relative to the object interface Γ_{F-S}). Modelling the fluid domain as a continuum, the centroid shift for any point C_i with elevation h smaller than the search radius R, follows from the geometric centre of the search area's segment coinciding with the fluid domain (Ω_{Fluid}). A definition of the key parameters is provided in Figure 6.2.

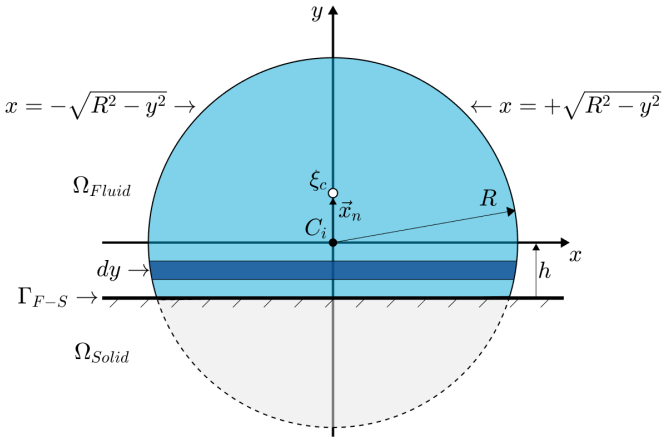

Figure 6.2: Illustration defining key parameters and terminology used in the proposed interface detection concept. Search segment shaded in blue, bounded by the circle of radius R, around the assessment point C_i, located at a wall-normal distance h to the fluid-solid interface Γ_{F-S}. The centroid shift vector $\mathbf{x}_n$ connects C_i with the geometric search segment centre ξ_c.

An analytical expression of the centroid shift $|\mathbf{x}_n|$ as a function of the elevation from the surface h, maintaining a constant search radius R is derived hereafter. The result is presented for the 2D problem and later generalized to 3D space. The validity of the expression is based on the following assumptions:

1. The particles concentration is modelled as a continuous distribution (limit of infinite concentration).
2. The surface is flat and aligned with the x-axis.

Upon these assumptions, it is trivial that the centroid position in wall-parallel direction (x) is located on the symmetry axis ($x = 0$), and only the wall-normal component (y) needs to be considered.

Defining a system of axes with origin at C_i, the centroid shift $|\mathbf{x}_n|$ is identical to the search segment's geometric centre ξ_c (the subscript c denotes the continuum representation). The latter is determined through integration, following the definitions provided in Figure 6.2,

$$\xi_c(h) = \frac{\int_{-h}^{R} y\, f(y)\, dy}{\int_{-h}^{R} f(y)\, dy} \tag{6.2}$$

where $f(y)$ describes the circular arc of radius R.

$$x = \pm f(y) = \pm\sqrt{R^2 - y^2} \tag{6.3}$$

Since the distribution is symmetric over the y-axis, only positive values of x, respectively $f(y)$, are considered here. Substituting Equation (6.3) into Equation (6.2) and solving the integral on the interval $[-h, R]$ yields the analytical solution for the search segment centroid ξ_c dependent on the elevation h,

$$\begin{aligned}
\xi_c(h) &= \frac{\int_{-h}^{R} y\, f(y)\, dy}{\int_{-h}^{R} f(y)\, dy} \\
&= \frac{\left[-\frac{1}{3}\left(R^2 - y^2\right)^{\frac{3}{2}}\right]_{-h}^{R}}{\left[\frac{1}{2}\left(y\sqrt{R^2 - y^2} + R^2 \tan^{-1}\left(\frac{y}{\sqrt{R^2 - y^2}}\right)\right)\right]_{-h}^{R}} \\
&= \frac{\frac{1}{3}\left(R^2 - h^2\right)^{\frac{3}{2}}}{\frac{1}{2}\left(\frac{R^2\pi}{2} - \left(-h\sqrt{R^2 - h^2} + R^2 \tan^{-1}\left(\frac{-h}{\sqrt{R^2 - h^2}}\right)\right)\right)}
\end{aligned} \tag{6.4}$$

Despite the complexity of the resulting algebraic expression, the function $\xi_c(h)$ decreases monotonically in the interval $h = [-R, R]$. In the following, starred labels $(^*)$ are used to indicate normalization by the search radius R. Figure 6.3 displays the dependence of the centroid shift ξ^* upon wall elevation h^*.

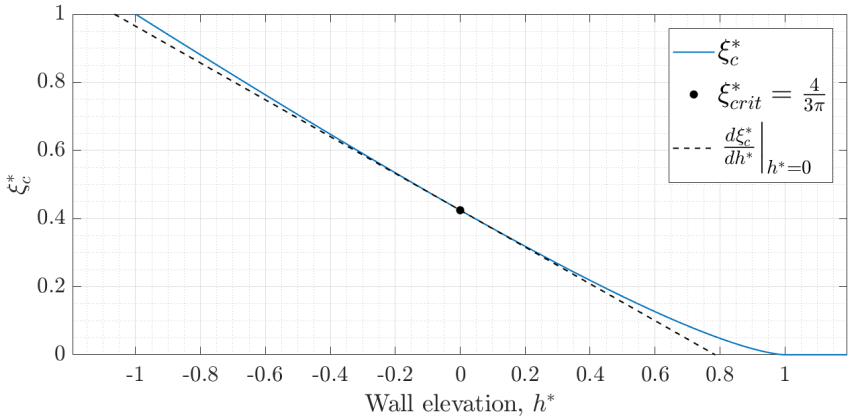

Figure 6.3: Analytical centroid shift magnitude ξ_c^* as function of wall elevation h^*. Starred labels $(^*)$ indicating normalization by search radius R.

As expected, the centroid shift is zero when the search segment does not intersect the interface $(h^* \geq 1)$. As the wall normal distance reduces, the centroid shift gradually increases, reaching a critical value of $\xi_{crit}^* = \frac{4}{3\pi}$ at the interface $(h^* = 0)$. For points inside the object $(h^* < 0)$, the centroid shift keeps increasing up to a maximum value of 1, when $h^* = -1$. Based on this observation, we define a criterion to discriminate whether the point C_i belongs to the fluid or the solid region:

$$\begin{cases} |\mathbf{x}_n^*| < \xi_{crit}^* & \rightarrow C_i \in \Omega_{Fluid} \\ |\mathbf{x}_n^*| = \xi_{crit}^* & \rightarrow C_i \in \Gamma_{F-S} \\ |\mathbf{x}_n^*| > \xi_{crit}^* & \rightarrow C_i \in \Omega_{Solid} \end{cases} \tag{6.5}$$

Additionally, we note that the centroid shift as function of wall elevation h^* as given in Equation (6.4) and illustrated in Figure 6.3, can be classified into three regions:

1. Far away from the interface $(|h^*| > 1)$ the centroid shift is zero;
2. In close proximity to the interface $(|h^*| \leq 0.5)$ the centroid shift is well approximated by a linear trend, indicated by the tangent $\frac{d\xi_c^*}{dh^*}\Big|_{h*=0}$ shown in Figure 6.3;
3. For moderate wall elevations $(0.5 \leq |h^*| \leq 1)$, the centroid shift is accurately described by Equation (6.4) but it follows a non-linear shape, as observed in Figure 6.3.

6.1.1. Discrete problem formulation

When the hypothesis of a continuous distribution of tracers is removed, the effect of a finite number of tracers falling within the SA needs to be considered. The statistical analysis hereafter takes as key parameters the SA radius R and the tracers

spatial concentration c_p. Assuming a tracer particle distribution that is approximately uniform within the local search area, the number N of particles within the circular SA is directly proportional to the area of SA coinciding with the fluid domain. The latter is equal to the denominator of Equations (6.2) and (6.4), and is graphically illustrated in Figure 6.4.

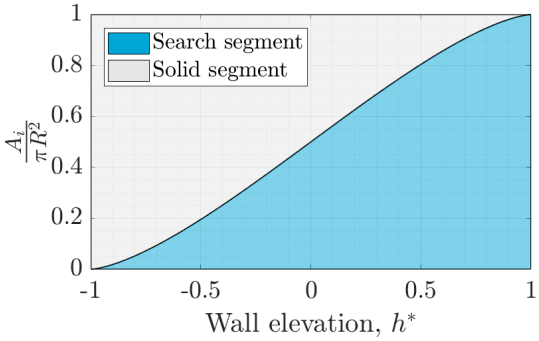

Figure 6.4: Relative share of search- and solid-segment area as function of normalized wall normal distance h^*. The former is directly proportional to the expected ensemble size N for a given particle concentration c_p.

Treating the tracer particle position as a discrete random variable, whose distribution is governed by the shape of the search segment, the expected mean position is identical to the continuum centroid (ξ_c, see Equations (6.2) and (6.4)) and the variance (σ_ξ^2) around the mean position can be estimated as,

$$\sigma_{\xi,y}^2 = \int y^2 \mathrm{pdf}\,(y)\,dy - \xi_y^2 = \frac{\int_{-h}^{R} y^2 f\,(y)\,dy}{\int_{-h}^{R} f\,(y)\,dy} - \xi_c^2 \tag{6.6}$$

which is only shown for the wall-normal y-direction here, but can be analysed in the equivalent manner for the wall-parallel x-direction. The expansion of the integral is omitted here, and only the resulting standard deviation (σ_ξ^*) as function of wall-normal distance h^* is shown in Figure 6.5. Comparison of the standard deviation in the wall-normal ($\sigma_{\xi,y}^*$) and the wall-parallel direction ($\sigma_{\xi,x}^*$) suggests that the variability in the normal direction is significantly smaller, exception made for the limit cases ($|h^*| = 1$), which do not feature any directional sensitivity.

Figure 6.5 illustrates the expected variability for a single data point. For a distribution of N samples, the standard deviation of the mean instead scales with $N^{-\frac{1}{2}}$ based on,

$$\sigma_{\bar{\xi},i}^* = \frac{\sigma_{\xi,i}^*}{\sqrt{N}} \tag{6.7}$$

Upon this observation, the uncertainty for the centroid shift obtained from a discrete distribution of tracers can be estimated as function of the sample size. This is illustrated for a point coinciding with the fluid-solid interface ($h^* = 0$; $\sigma_{\xi,x}^* = 0.5$,

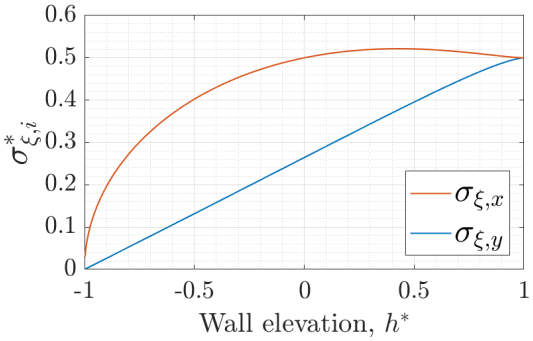

Figure 6.5: Expected standard deviation in interface normal (y) and parallel (x) direction when modelling particle position as random variable inside a search segment defined by h^* and R.

$\sigma^*_{\xi,x} \approx 0.26$) in Figure 6.6. For the specific case of an interrogation point located on the fluid-solid interface (h^* =0), the sample size is denoted by the variable k in the remainder.

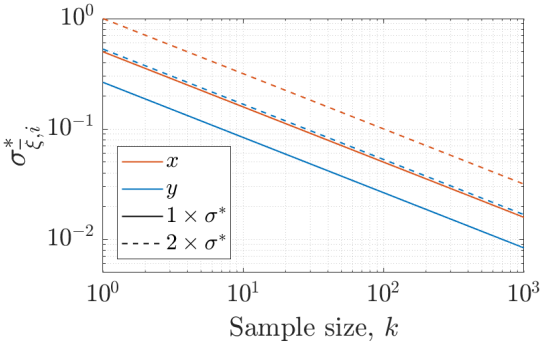

Figure 6.6: Expected standard deviation in interface normal (y) and parallel (x) direction as function of sample size, when modelling particle position as random variable inside a semi-circular search segment of radius R, located at the interface ($h^* = 0$).

Based on this analysis, the necessary sample size k_{min} for a desired confidence and uncertainty level of the discretely calculated centroid shift $|\mathbf{x}^*_n|$ can be determined. In the assumption that the latter is dominated by the wall-normal component, the sample size selection can be based solely on $\sigma^*_{\xi,y}$. Furthermore, assuming a known tracer particle concentration c_p (in particles/m^2), the minimum required search radius is given by,

$$R_{min} = \sqrt{\frac{2k_{min}}{\pi c_p}} \tag{6.8}$$

Similarly, the sample size can also be selected based on a desired directional accuracy of the interface normal estimate $\mathbf{x}_n$. Let us define θ as the angle between $\mathbf{x}_n$

and the wall normal y, with positive values indicating a counter-clockwise rotation of $\mathbf{x}_n$. Assuming the angle θ is dominated by the wall-parallel uncertainty ($\sigma^*_{\bar{\xi},x}$), and further, that the small angle approximation can be applied ($\xi_x \ll \xi_y \cap \sigma_{\bar{\xi},x} \ll \xi_y$), the directional uncertainty for a coverage factor m is estimated as follows,

$$U_\theta \approx \frac{m\sigma^*_{\bar{\xi},x}}{\xi^*_{crit}} \tag{6.9}$$

Let us provide the following example as an illustration: assume for a given tracer particle concentration c_p a search radius R is selected such that for a semi-circular search segment around a point C_i coinciding with the flat interface, $k = 100$ tracer particles are captured within the search area. Prescribing a $95\,\%$ confidence interval ($m = 2$) the discrete centroid shift magnitude is expected to be accurate within $0.05\,R$ based on Equation (6.7), whereas the directional accuracy shall be within $13.5°$ according to Equation (6.9).

6.1.2. Methodical detection of a fluid-solid interface

Prior to application and assessment of the theory outlined up to this point, the above considerations are consolidated, providing a graphical illustration of the interface detection method on a flat interface. Considering a generic 2D tracer particle distribution of concentration c_p, as shown in Figure 6.7(a), the search radius R is chosen such that on average $k = 30$ particles are contained in a semi-circular search segment spanned by R.

To evaluate the distribution characteristics systematically, a uniform grid of assessment points C_i is defined, with a grid spacing of $h_x = h_y = 0.5\,R$ in both axis directions. At each grid node the centroid shift vector $\mathbf{x}_n$ is evaluated based on the nearby tracers within the radius R, following Equation (6.1).

The resulting contour of the centroid shift magnitude $|\mathbf{x}_n|$ is shown in Figure 6.7(b), normalized by the search radius R. The highlighted contour of $|\mathbf{x}_n| = \xi_{crit} = \frac{4R}{3\pi}$ in Figure 6.7(b) does therefore provide the estimate of the fluid-solid interface Γ_{F-S} according to Equation (6.5). Additionally, evaluating the direction of $\mathbf{x}_n$ along the identified contour provides the estimate of the corresponding interface-normal direction as shown in Figure 6.7(c). The individual steps taken in this analysis are summarized in a workflow-diagram describing the proposed flow tracer-based interface detection algorithm in Figure 6.8.

An element which has not been discussed yet is the grid-spacing parameter h_x, defining the distance between the assessment points C_i. Assuming the iso-contour of the critical displacement $|\mathbf{x}_n| = \xi_{crit}$ is approximated by linear interpolation of the discretely evaluated centroid shift vector field $\mathbf{x}_n$ on C_i, results in the requirement that h_x must be sufficiently small, such that the change of $|\mathbf{x}_n|$ across the interval h_x can be considered linear around the location of the interface.

Reconsidering the analytically anticipated centroid shift as function of wall elevation h in Figure 6.3, it was concluded that the assumption of linearity is a good approximation on the interval $[-R/2, R/2]$ around the interface ($h = 0$), providing the condition that the grid spacing h_x shall be smaller than the search radius R. If

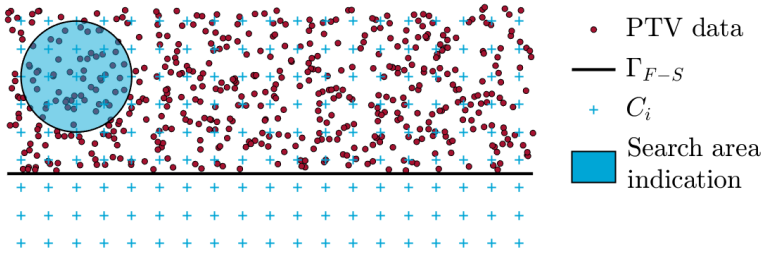

(a) Tracer particle distribution on top of model surface with regular grid of assessment points.

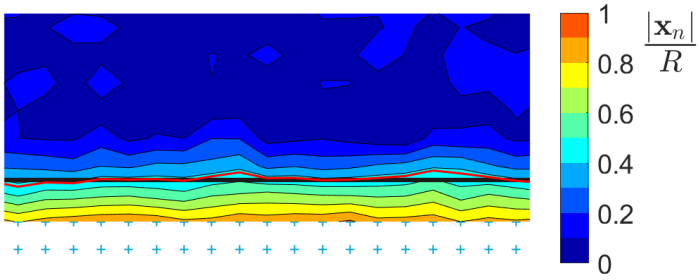

(b) Resulting centroid-shift map, normalized by the search radius R. Iso-contour of critical displacement ξ_{crit} in red provides the reconstructed interface.

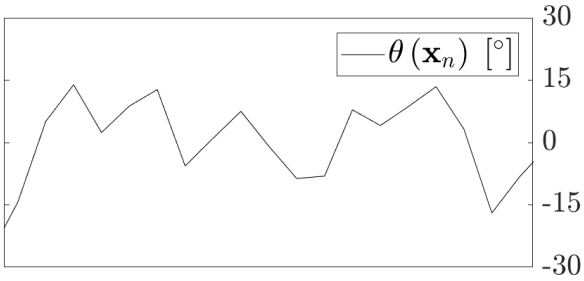

(c) Estimation of the interface-normal based on direction of $\mathbf{x}_n$ along the identified contour. θ defines the angle between $\mathbf{x}_n$ and the y-axis, with positive values indicating a counter-clockwise rotation of $\mathbf{x}_n$.

Figure 6.7: Stepwise illustration of interface detection algorithm.

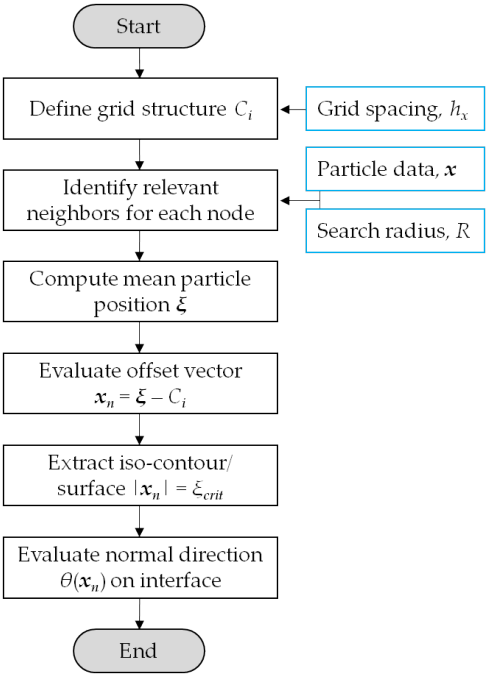

Figure 6.8: Workflow diagram of the interface-detection method.

considering a regularization of the centroid shift map $\mathbf{x}_n$ on C_i however, e.g. by linear regression, the assumption of linearity for $\mathbf{x}_n$ must hold on the full interval over which the regression is applied. Considering a kernel of 3×3 grid points C_i, the linearity assumption must hold across the kernel's diagonal, yielding the criterion that $2\sqrt{2}h_x \leq R$.

6.1.3. Surface curvature

The model developed up to this point assumes solely flat interfaces. As such, application of the proposed method to curved interfaces presents a source of error that is to be understood. To estimate the positional error associated with object curvature, let us consider an interface of constant curvature radius ρ. Further, let us distinguish between concave and convex interfaces, as illustrated in Figure 6.9.

For both, concave and convex interfaces, the search segment's centroid in the continuum assumption is obtained by superposition of the previously derived solution for the centroid of a circular segment (see, Section 6.1, Figure 6.2, Equations (6.2) to (6.4)). To this end the search segment on the curved interface is split into two circular segments along the radical line of the search area of radius R and the curved interface of radius ρ as illustrated in Figure 6.9. The elevation of the radical line (h') is defined by,

$$h' = \frac{l^2 - \rho^2 + R^2}{2l} \tag{6.10}$$

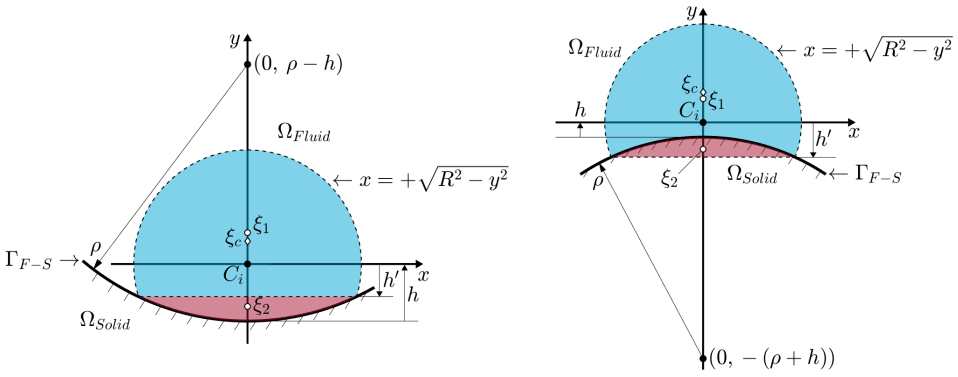

(a) Concave interface

(b) Convex interface

Figure 6.9: Centroid shift analysis on curved interfaces.

where l indicates the position of the centre of curvature with respect to the search area centre C_i. With the origin defined at C_i, l therefore equals the y-coordinate of the centre of curvature, $\rho - h$ and $-(\rho + h)$ for concave and convex case respectively, as indicated in Figure 6.9.

The centroid ξ_1 of the segment bounded by the radical line and the search radius R (blue, with dashed contour in Figure 6.9) is found by adjusting the integration limits in Equation (6.4) to $[h', R]$. The centroid ξ_2 of the segment bounded by the radical line and the interface (shaded in red) is determined in the equivalent manner: the search radius R is substituted by the curvature radius ρ. For the concave interface, the integration is carried out on the interval $[l + h', \rho]$, and the result is mapped by subtracting the integral from the distance l, to match the chosen reference frame with origin at C_i.

$$\xi_2\,(h') = l - \frac{\int_{l+h'}^{\rho} y\sqrt{\rho^2 - y^2}\,dy}{\int_{l+h'}^{\rho} \sqrt{\rho^2 - y^2}\,dy} \tag{6.11}$$

For the convex case, the integration limits are defined by $[|l| - h', \rho]$ and the result is mapped by subtracting the magnitude $|l|$ from the integral.

$$\xi_2\,(h') = \frac{\int_{|l|-h'}^{\rho} y\sqrt{\rho^2 - y^2}\,dy}{\int_{|l|-h'}^{\rho} \sqrt{\rho^2 - y^2}\,dy} - |l| \tag{6.12}$$

Lastly, the joint centroid is found by superposition,

$$\xi_c = \frac{\sum \xi_i A_i}{\sum A_i} \tag{6.13}$$

where A_i indicates the segment area. The resulting centroid estimate for selected curvature radii is plotted in Figure 6.10(a).

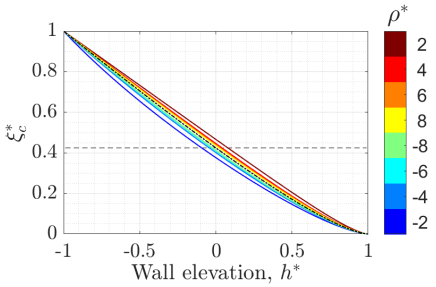

(a) Centroid estimate.

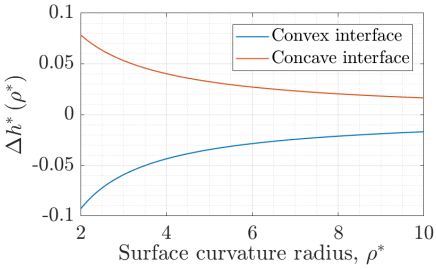

(b) Positional error when adhering to flat interface assumption for the critical centroid shift ξ_{crit}.

Figure 6.10: Effect of surface curvature on interface location estimate for selected curvature radii ρ. Negative values of ρ correspond to a convex surface. Dash-dotted line representing reference for a flat interface, with the dashed horizontal line indicating the corresponding critical centroid shift in the assumption of a flat interface.

6

As expected, the centroid shift is overestimated on concave interfaces, whereas a reduced shift is observed on convex shapes. Adhering to the flat-interface assumption thus causes the reconstructed interface to be dilated on concave boundaries, and to be eroding the true interface on convex shapes. Figure 6.10(b) shows the anticipated positional error as function of curvature radius. It is concluded that the positional error of the detected interface is within 5 % of R when the object's radius of curvature exceeds $4\,R$. In principle, the data in Figure 6.10(b) can be used for a first order correction of the interface reconstruction, after estimating its curvature profile. Such correction, however, is not considered here.

To illustrate the working principle of the proposed concept and to discuss its main parameters, the method is applied to the synthetic particle distribution around a 2D airfoil hereafter.

6.2. Illustration on 2D synthetic airfoil data

The test object for the synthetic study presented in this section is the *DU 91-W2-250* wind turbine dedicated airfoil shown in Figure 6.11 (Timmer and Van Rooij, 2003). Wind turbine blades are often deflecting substantially during operation and wind tunnel testing. The determination of the blade surface during wind tunnel experiments is thus of particular relevance.

The thick and cambered airfoil features a wide range of curvature radii, along with a pointy trailing edge. Applying the curvature analysis from Section 6.1.3 to the specific geometry indicates the reconstruction error that is to be anticipated for a given search radius R, as illustrated in Figure 6.12. It is evident that regions of high curvature, such as the airfoil leading edge, present a specific challenge for reconstruction by the proposed algorithm.

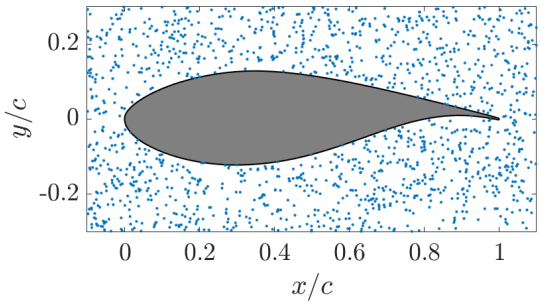

Figure 6.11: Airfoil shape (DU 91-W2-250, Timmer and Van Rooij, 2003) immersed in random particle distribution at the coarsest considered tracer concentration ($\lambda_p = 0.01\,c$).

Key parameters in the interface detection routine are investigated. First, the influence of the sample size —that is, the number of tracers used for calculation of the centroid shift vector —is evaluated (Section 6.2.1), which connects to the previous discussion on expected uncertainties in the discrete centroid estimate. Note that the particle count is expected to vary due to the random nature of the tracer distribution, and a reduction in the search segment area for circles intersecting the solid object. Thus, specifications of the sample size k in the following, refer to the mean number of particles expected in a semi-circular search segment centred at a flat fluid-solid interface, in line with the definition provided in Section 6.1.1. The effect of tracer particle concentration is addressed separately in Section 6.2.2. Lastly, Section 6.2.3 incorporates the application of a regression model to the discretely evaluated centroid shift data.

The quality of the reconstructed interface is quantified in terms of positional accuracy only, which is reported by the maximum and root-mean-square distance of the reconstructed contour normal to the reference geometry, $\epsilon_{x_{max}}$ and $\epsilon_{x_{rms}}$ respectively.

6.2.1. Sample size

Focusing on method specific parameters, the sample size is controlled by specification of the search radius R for a known concentration c_p, respectively mean nearest neighbour distance λ_p. Mean particle distance and concentration in 2D are related as follows (Bansal and Ardell, 1972),

$$\lambda_p = \frac{1}{2\sqrt{c_p}} \tag{6.14}$$

In the analysis of the sample size we limit ourselves to two seeding levels: a coarse tracer distribution ($\lambda_p = 0.01\,c$) which is considered representative of an instantaneous particle image analysis, and a dense case ($\lambda_p = 0.001\,c$) equivalent to the study of multiple (here, 100) particle images acquired on a steady model. The airfoil chord length c is used to normalize λ_p for the specific case of the 2D airfoil. In the

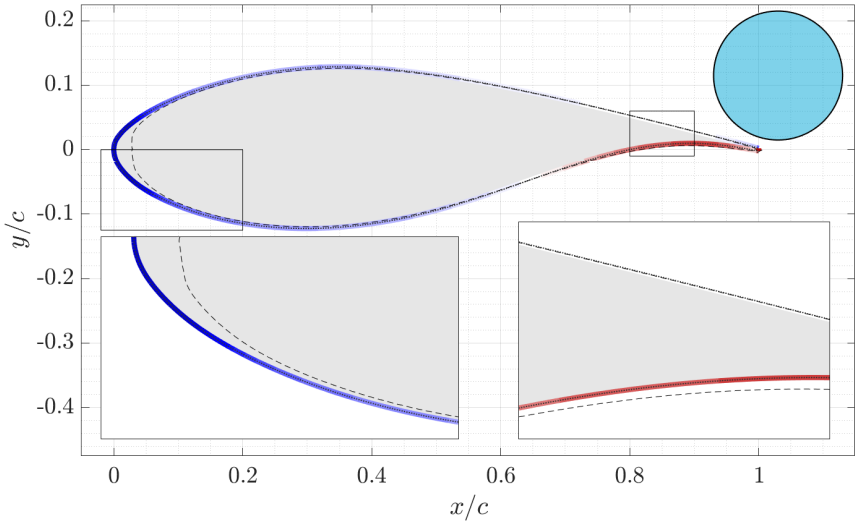

Figure 6.12: Airfoil model with contour coloured by curvature (blue/convex - white/neutral - red/concave), and expected reconstructed shape (dashed black) following error analysis in Section 6.1.3 based on a continuous distribution and assuming a search radius of $R = 0.1\,c$ as indicated in the top right, with c being the airfoil chord.

following, different search radii R are considered, such that the expected average sample size in a semi-circular search segment at a linear interface varies between 4 and 50 particles, based on Equation (6.8). Figure 6.13 shows the corresponding positional reconstruction error as function of sample size.

The data in Figure 6.13 suggests that two types of error can occur in the reconstruction of the airfoil shape:

1. For low values of k (< 10) a steep increase in the positional error is observed. For such small sample sizes a high uncertainty in the centroid estimate is to be expected (see Section 6.1.1, Equation (6.7)), which can lead to false interface detection and consequently, large positional errors. This error is referred to as *random* error.

2. For larger sample sizes, the search radius R increases, which limits the spatial resolution of the reconstruction. As such, a gradual error growth is observed for large values of k (> 20), in particular in the maximum positional error. In this regime, comparison of the maximum positional error and the search radius R, indicates a direct correlation between the quantities.

The latter trend is understood by inspection of a specific case. Figure 6.14(a) details the centroid shift magnitude for the coarse case ($\lambda_p = 0.01\,c$), normalized by the critical centroid shift ξ_{crit}, at a mean sample size of $k = 30$ ($R = 0.09\,c$) along with the resulting interface upon identification of the unity-contour in Figure 6.14(b). The

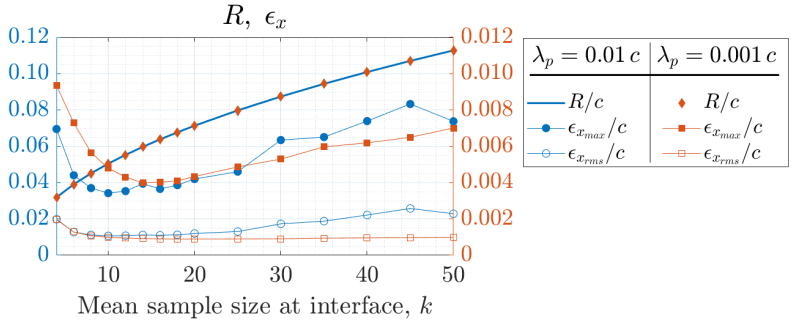

Figure 6.13: Maximum and mean positional error of reconstructed airfoil contour, as function of mean sample size k. Note the scale difference for the y-axes, between the coarse data ($\lambda_p = 0.01\,c$) corresponding to the left axis, and the high resolution data ($\lambda_p = 0.001\,c$) on the right axis. Data shows averaged error from 100 independent synthetic particle distributions.

corresponding positional error is shown in Figure 6.14(c). While the centroid shift magnitude in Figure 6.14(a) indicates a clear increase towards the airfoil model, four peculiarities are observed:

1. Far inside the model ($|h| > R$) the centroid shift cannot be computed as no tracer particles are available here.

2. The thin aft section does not cause a significant increase in the centroid shift magnitude. The airfoil thickness in this section is smaller than the search segment's radius. In such case, search segments in model vicinity capture tracer particles on either side of the model, resulting in a reduced distribution bias. This yields the observed reduction of the centroid shift magnitude, which ultimately results in an eroded interface contour when adhering to the assumption of a flat and infinitely thick solid object.

3. Along the aft airfoil section, at around $x/c = 0.7$, the reconstruction of a secondary interface inside the object is seen. Here, the object thickness is between the search radius and the search diameter. Under this circumstance, approaching the model from either side the centroid shift is expected to behave as demonstrated for the hypothesized flat and infinitely thick solid in Section 6.1. Yet, for assessment points penetrating the model surface the centroid shift magnitude is expected to shrink back to zero again towards the centre of the thick object. In such case, two additional occurrences of the critical centroid shift magnitude must be anticipated, both of which are identified as the presence of a fluid-solid interface despite being located inside the solid. These errors associated with the finite model thickness justify the observation, that the maximum error in Figure 6.13 correlates well with the search radius R, in the assumption that the error due to model thickness is dominant. It further provides a motivation to keep the sample size k low, for minimization of the positional error.

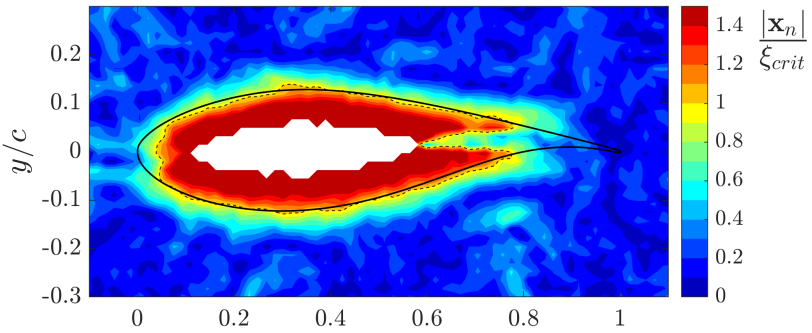

(a) Centroid shift map with airfoil silhouette indicated by solid black line and reconstructed interface by dashed black contour.

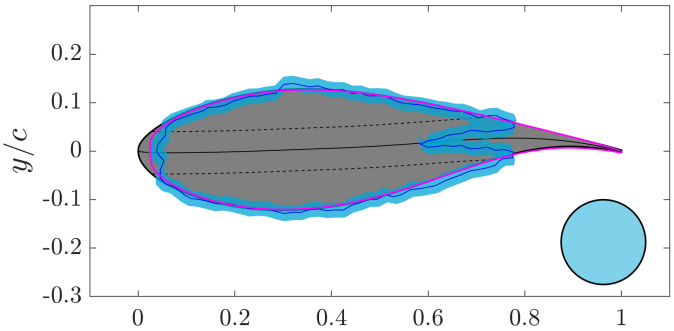

(b) Reconstructed interface (blue) with anticipated error band based on 95 % confidence interval using Equation (6.7). Magenta contour illustrating expected reconstruction accounting for curvature effects. Dashed lines above and below camber line highlighting where model thickness is beyond the search radius R. The search area size is illustrated on the bottom right by a light blue circle.

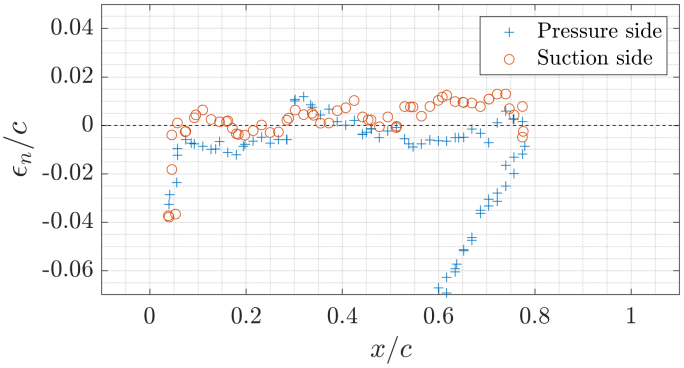

(c) Reconstruction error in terms of wall-normal distance, separated for pressure and suction side, and normalized by airfoil chord c.

Figure 6.14: Application of the proposed method to the synthetic 2D particle distribution around an airfoil of chord c, with mean inter particle distance $\lambda_p = 0.01\,c$.

4. Around the airfoil leading edge, a delayed increase in the centroid shift magnitude is seen. The leading edge geometry is characterized by high curvature (small radius of curvature), violating the assumption of a flat (non-curved) interface. This yields an erosion of the convex, curved leading edge, as seen in Figure 6.14(b) and the increased (negative) error magnitude in Figure 6.14(c). Such behaviour has been foreseen in the discussion in Section 6.1.3.

The analysis of the synthetic distribution examined here indicates that two error types must be considered in the selection of the sample size k:

1. If the sample size is too small, high uncertainties in the centroid estimate negatively affect the surface reconstruction.

2. Large values of k instead yield a loss in resolution, which amplifies the bias errors on curved surfaces and limits the detection of features smaller than the search diameter.

For the particular case studied here, error minimization is achieved for a mean sample size of $10 \leq k \leq 20$ tracers captured inside a semicircle of search radius R, depending on the particle concentration.

6.2.2. Tracer concentration

The sample size assessment indicated that the reconstruction error is dominated by the search radius R. The latter can be reduced for the same sample size, if the tracer particle concentration is high, respectively the mean particle distance is low. In an instantaneous measurement, it is likely that the achievable tracer concentration will dictate the positional error of the interface reconstruction. In a time-averaged study, an abundance of tracers can slow down the particle analysis however. In such case, data sub-sampling to a concentration level that allows for surface reconstruction at a desired positional accuracy is preferable. To this end, the mean particle distance around the airfoil is successively reduced, keeping the mean sample size constant at $k = 50$. The resulting trend is illustrated in Figure 6.15. For the range of mean particle distances considered here, the mean and maximum positional error reduce approximately linearly with mean particle distance.

6.2.3. Data regression

The centroid shift contours shown in Figures 6.7(b) and 6.14(a) indicate how $|\mathbf{x}_n|$ can vary even away from the interface. Such fluctuations are due to the random particle distribution. The reduction of such noise can be achieved by increasing the sample size. For a given particle concentration c_p, the sample size can only be raised by increasing the search area, and thus the search radius R. The latter limits the achievable resolution, which is undesirable following the previous analysis in Section 6.2.1. Instead, data regularization is realized by regression of the centroid shift field. Recalling the centroid shift as function of wall elevation in the continuum assumption (see Figure 6.3), the relation is approximately linear with h, motivating the application of a linear regression model.

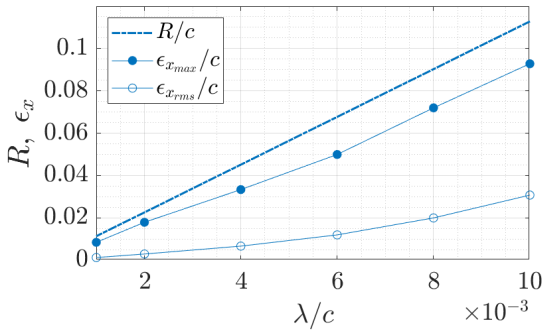

Figure 6.15: Maximum and mean positional error in airfoil reconstruction with change in tracer particle concentration. Error data averaged from 100 independent synthetic particle distributions.

$$\overline{\mathbf{x}}_n = a_1 x + a_2 y + a_3 \tag{6.15}$$

Such regression is applied on a sliding kernel to regularize the centroid shift contour. Because the centroid shift as a function of the wall distance is expected to be linear only within a domain of $\Delta h \leq R$, the kernel width should be smaller than the search radius to avoid truncation. Herein we consider a 5×5 kernel surrounding a grid point C_i on a structured grid of grid spacing $h_x = 0.2\,R$. The resulting centroid shift contour is shown and compared to the original map for one case in Figure 6.17, whereas a comparison of the positional error is provided in Figure 6.16 for varying particle concentration.

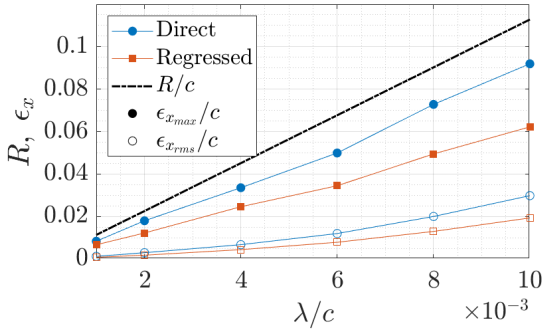

Figure 6.16: Maximum and mean positional error with and without regression of centroid shift field. Linear regression on 5×5 kernel, ($h_x = h_y = 0.2\,R$). Data averaged from 100 synthetic particle distributions.

Comparison of the reconstructed interfaces with and without regression in Figure 6.17 shows the noise reduction effect of the data regularization. For the main airfoil body the regression based interface follows the true profile more closely, and the construction of a secondary interface on the thin airfoil tail is avoided. Yet, the

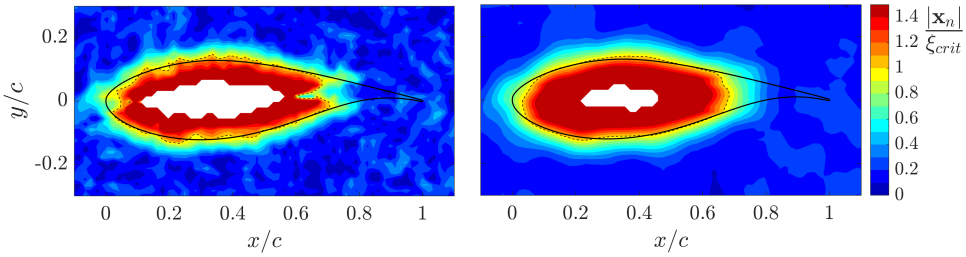

(a) Original centroid shift field. Unity contour in dashed black indicating identified interface.

(b) Linearly regressed centroid shift field, using a sliding kernel of 5×5 points.

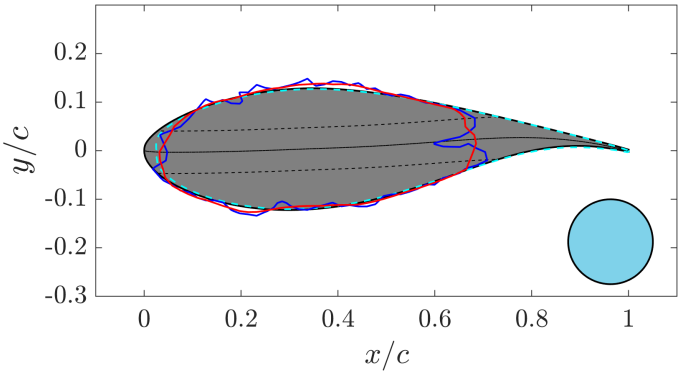

(c) Comparison of reconstructed profiles for direct evaluation (blue) and regressed data (red), along with anticipated shape from curvature analysis (dashed-cyan).

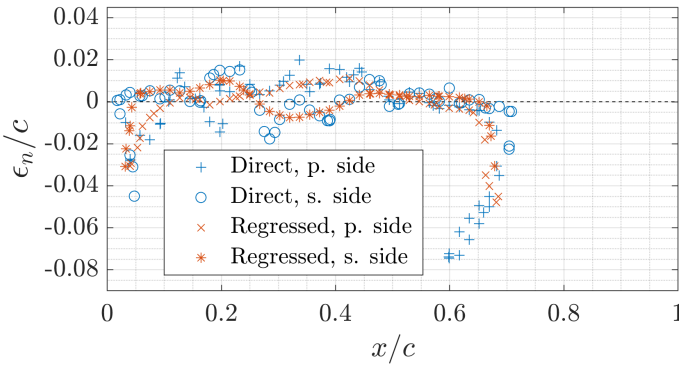

(d) Positional errors, separated for pressure and suction side.

Figure 6.17: Comparison of direct interface identification against evaluation after linear regression of the centroid shift field.

erosion of the curved leading edge as well as the truncation of the thin aft section are amplified on the regressed data. On average, the positional accuracy of the reconstructed interface is improved, as shown in Figure 6.16, where both maximum and mean positional error are approximately $25\,\%$ reduced when regression is applied.

This concludes the study on the synthetic particle distribution surrounding a cambered airfoil in a 2D plane. The study shows that the search radius must satisfy a balance, such that it includes a statistically significant number of samples, yet remains sufficiently small to maintain positional accuracy. For the specific case considered in Section 6.2.1 error minimization is achieved for $10 \leq k \leq 20$, depending on the tracer particle concentration. In applications where the particle concentration is varying significantly across the measurement domain, this can motivate the implementation of a variable search radius approach, which is not considered in this work however. The thin airfoil tail highlights that finite geometry effects must be considered when the search diameter is below the feature thickness of the investigated object. More accurate reconstructions can be obtained when the particle concentration is high, respectively the average inter-particle distance λ_p is low. For the specific data considered here, the maximum reconstruction error is approximately one order of magnitude larger than the average inter-particle distance λ_p. Furthermore, a regularization of the centroid shift field is seen to smooth the interface reconstruction, which helps mitigating random fluctuations, but can amplify smoothing of curved and thin features.

6.3. Extension to 3D space

The interface detection principle has been demonstrated for the 2D problem. For the 3D case, the circular search area for assessment of the local particle distribution changes to a spherical search volume, still bounded by the search radius R. This change affects the distribution characteristics analysed for the 2D case in Section 6.1. Two key points are revisited for the volumetric case:

1. The centroid shift as function of wall normal distance in the continuum limit.
2. The expected variability of the mean position for a discrete distribution.

Considering a planar interface, and modelling the fluid domain as a continuum the centroid shift $\mathbf{x}_n$ as function of wall elevation h is derived in the same way as for the 2D case. Only the distribution function $f(y)$ (Equation (6.3)) changes to,

$$f(z) = \pi\left(R^2 - z^2\right) \tag{6.16}$$

for the spherical case, which describes the cross sectional area of a sphere at an elevation z normal to the interface. The search segment centroid is then given by,

$$\xi_c = \frac{\int_{-h}^{R} z f(z)\,dz}{\int_{-h}^{R} f(z)\,dz} = \frac{\pi\left[\frac{R^2 z^2}{2} - \frac{z^4}{4}\right]_{-h}^{R}}{\pi\left[R^2 z - \frac{z^3}{3}\right]_{-h}^{R}} = \frac{\frac{1}{4}\left(R^4 - 2R^2h^2 + h^4\right)}{\frac{1}{3}\left(2R^3 - h^3 + 3R^2h\right)} \tag{6.17}$$

The critical centroid displacement at zero elevation is consequently equal to,

$$\xi_{crit} = \frac{3R}{8} \tag{6.18}$$

The centroid displacement is graphically illustrated as function of wall elevation in Figure 6.18.

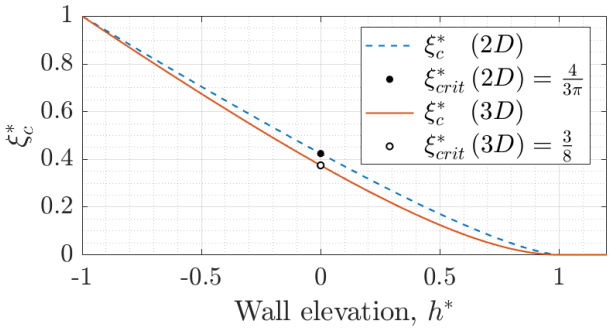

Figure 6.18: Centroid shift magnitude versus wall elevation h^*, assuming a continuous fluid domain along a planar interface for circular and spherical search areas (volumes) in 2D and 3D, respectively.

To predict the uncertainty of the mean particle position resulting from a discrete tracer particle distribution, the variance is evaluated for the limit case of zero elevation ($h = 0$, hemi-spherical search volume), similar to the 2D case (see, Equation (6.6)). As for the 2D case, in the volumetric study the variability parallel to the interface

$$\sigma_{\xi,x}^* = \sigma_{\xi,y}^* = 5^{-\frac{1}{2}} \approx 0.45$$

is significantly larger as compared to the wall normal direction,

$$\sigma_{\xi,z}^* = \left(\frac{19}{320}\right)^{\frac{1}{2}} \approx 0.24$$

whereas the magnitudes are similar for 2D and 3D situation. Therefore, for both cases uncertainties in the discretely computed centroid shift $\mathbf{x}_n$ behave similarly.

Specific scrutiny of curvature and finite geometry effects is not provided for the 3D case. The qualitative behaviour is expected to be equivalent to the 2D case shown in Section 6.1.3. Instead the working principles and limitations are demonstrated on the particle distribution surrounding a surface mounted test object in the following section.

6.4. Experimental assessment

The test object studied here is a simplified car side-mirror model, consisting of a wall-mounted cylindrical profile of semi-circular cross-section ($d = 2r = h =$

10 cm), rounded off with a quarter sphere ($d = 2r = 10$ cm), as illustrated in Figure 6.19. The data was kindly provided by Saredi et al. (2021) who utilized the velocimetry data for advancing data assimilation schemes. Few more details can be found in Chapter 10. Following common PIV practice, the model is painted black to limit surface reflections in the particle images. The experiment is conducted in a low-speed, open-jet wind tunnel, featuring a $60 \times 60\,\text{cm}^2$ exit cross section which is run at 12 m/s free-stream velocity.

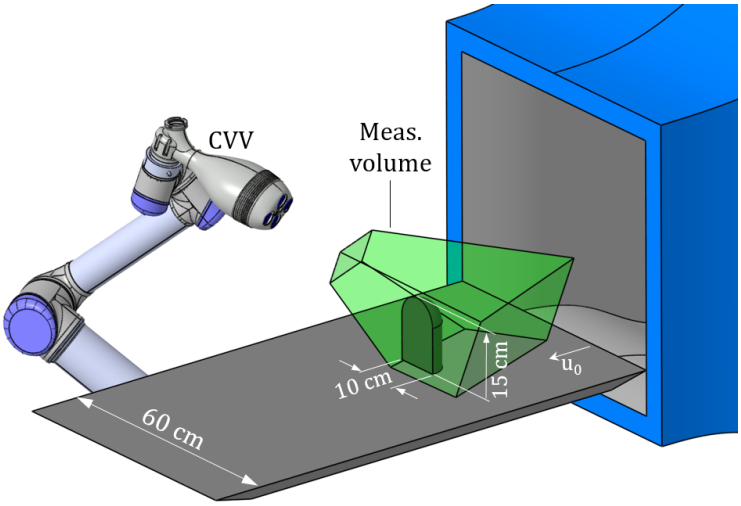

Figure 6.19: Experimental setup by Saredi et al. (2021), with wall-mounted side-mirror model.

Experiments are conducted by robotic volumetric PIV (Chapter 3), in which particle images are acquired by a coaxial volumetric velocimeter. $10,000$ image quadruples of $640 \times 452\,\text{px}^2$ are recorded at a rate of 858 Hz. Helium filled soap bubbles (HFSB) serve as tracer particles which are supplied by a $0.5 \times 1.0\,\text{m}^2$ seeding system located in the wind-tunnel settling chamber. Individual tracers are located and tracked in time by the Lagrangian particle tracking algorithm Shake-The-Box (STB Schanz et al., 2016). On average, about 320 particles are reconstructed and tracked in each image (0.001 ppp). The measurement volume is approximately 16 L, resulting in an average particle concentration of 200 particles/cm^3 for the data ensemble. In this condition, the proposed method can only be used for reconstruction of stationary objects, whereas the application to moving bodies demands a significantly higher instantaneous tracer particle concentration.

The CVV is positioned above, and to the left of the test object, capturing the planar, downstream face of the side-mirror model and most of the upstream-facing, curved, left-half of the model. Raw images as shown in Figure 6.20(a) are preprocessed with a high-pass frequency filter (Sciacchitano and Scarano, 2014), removing the majority of background noise and model reflections, see Figure 6.20(b). Some reflections, stemming from soap contamination on the model, are unsteady in time and are not efficiently filtered, resulting in a small share of ghost parti-

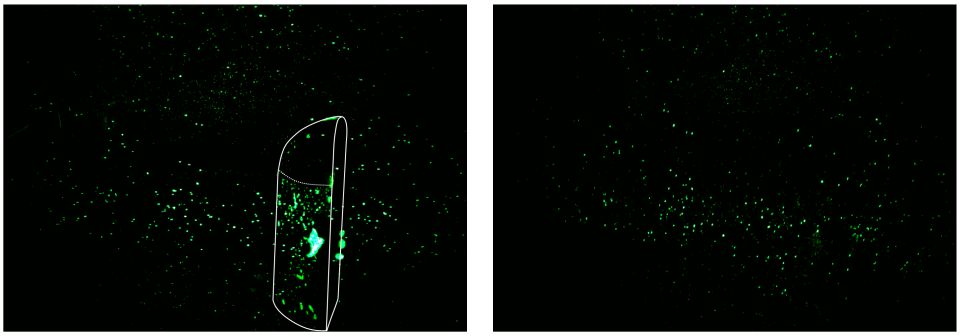

(a) Raw image (b) Pre-processed image

Figure 6.20: Example of particle images, showing triple exposures. Approximate cylinder location indicated by white contour.

cles reconstructed inside the model. It is furthermore observed that the particle concentration is non-uniform due to inhomogeneous HFSB seeding. Differences in local particle concentration are up to one order of magnitude, with the highest concentration exceeding 600 particles/cm^3 (lower, upstream section) and the sparsest regions counting approx. 50 particles/cm^3 (upper section, see Figure 6.21 - III).

The particle distribution shown in Figure 6.21 is analysed using the proposed interface detection routine, including the regression of the centroid shift field on a $5 \times 5 \times 5$ kernel, as discussed in Section 6.2.3. Three different search radii are considered, the smallest being 5 mm, respectively $0.1\,r$, an intermediate search radius of 10 mm ($0.2\,r$), and a coarse search radius of 15 mm ($0.3\,r$). The resulting contours are compared in three selected planes in Figure 6.22. Additionally the positional accuracy of the 3D reconstruction is reported in a mean sense, by evaluation of the root mean square error on the 3D model.

The contours in Figure 6.22 confirm that the proposed method is able to recognize the fluid-solid interface, despite some limitations:

1. Whereas the reconstruction of the planar downstream face closely follows the reference model, sharp features are not represented accurately but are smoothed in the reconstruction. As such, the convex corner on the transition from the cylindrical section to the flat rearward face is eroded, whereas the concave edge on the wall intersection is dilated. The degree of smoothing increases with the search radius.

2. Focusing on the upper, spherical section ($z > 2\,r$), the contours in Figures 6.22(b) and 6.22(c) suggest a light erosion in the interface reconstruction, with the contours lying inside the reference object. The degree of erosion again increases with the search radius. This is in line with the presented 2D curvature analysis in Section 6.1, considering that the ratio of surface curvature to search radius for the experimental case is as small as 3.33 for the largest search radius (respectively 5 and 10 for the smaller search radii).

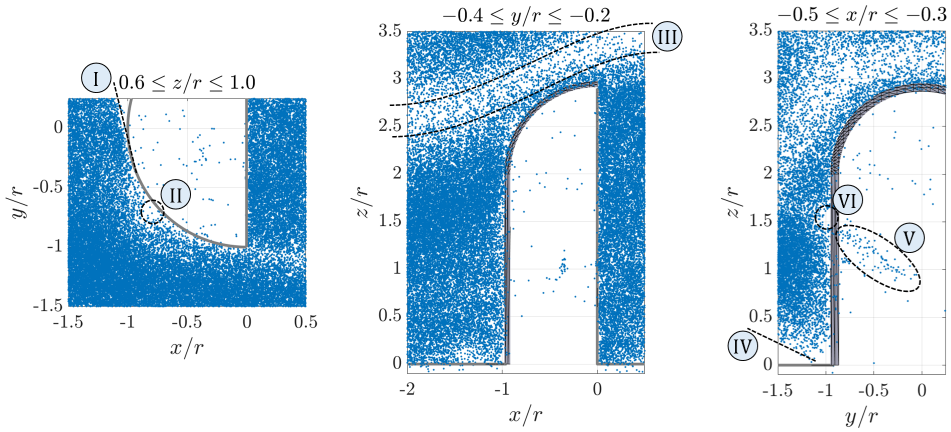

(a) Top view (b) Side view (c) Back view

Figure 6.21: Particle distribution around test model. Data normalized by object radius r. Highlighted features: (I) limit of optical access, (II) local particle void, (III) stream-tube with reduced particle concentration, (IV) illumination limit, (V) ghost particles due to soap contamination on model surface, (VI) local particle void.

3. For the reconstruction on the upstream-facing cylindrical section, it is seen that the detected interface is outside the reference geometry, which is against expectations from the 2D curvature analysis. Therefore, we attribute this mismatch to a lack of tracer particles close to the model in this region, which can also be seen in Figure 6.21(a).

4. Lastly, addressing Figure 6.22(c) it is seen that the reconstruction on the bottom-left corner is off. The contour detected here corresponds to the limit of the measurement domain, rather than a fluid solid interface which becomes clear upon inspection of Figure 6.21 - IV.

5. Instead, the vertical face in Figure 6.22(c) shows a wavy reconstruction pattern around $z = 1.2\,r$. This error is understood upon inspection of the particle distribution in Figure 6.21 - V & VI: a number of ghost particles is located inside the object here, stemming from a soap reflection on the model (see Figure 6.20). The presence of these particles causes a local erosion of the reconstructed interface. Just outside the model, there is a region of low particle concentration in the fluid domain however (Figure 6.21 - VI), which results in a local dilation of the reconstructed interface. In combination, the wavy reconstruction pattern in Figure 6.22(c) is obtained.

To quantify the mean error of the 3D reconstruction, we limit ourselves to the LHS model only ($y < 0$) and isolate the domain of the interface reconstruction where optical access was provided during the measurement. On this domain, the normal distance from each vertex of the reconstructed interface with respect to the refer-

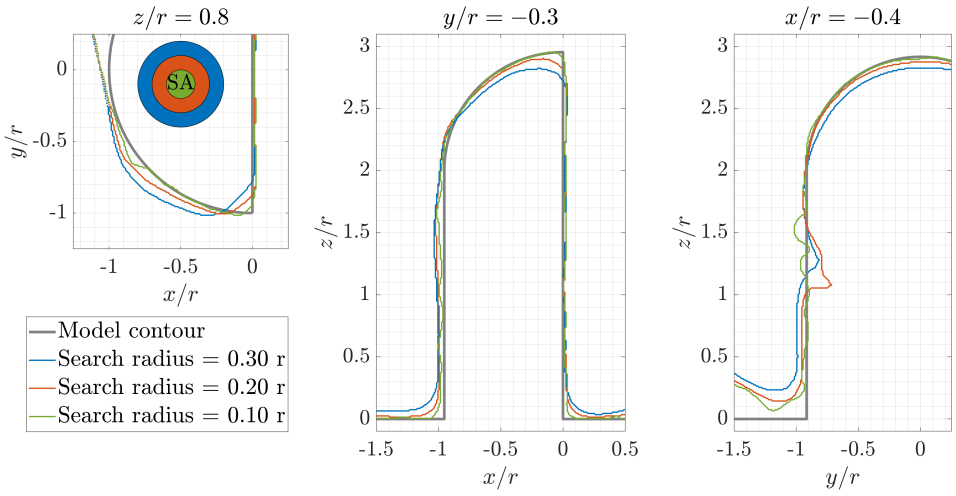

(a) Top view (b) Side view (c) Back view

Figure 6.22: 2D contours of model reconstruction based on experimental data for three different search radii. The corresponding SAs are illustrated in the Top view.

ence model is evaluated, which is illustrated in a contour plot for the intermediate search radius in Figure 6.23.

The contour plot in Figure 6.23 confirms the systematic erosion (dilation) of convex (concave) edges, with the convex edge of the planar rearward face being eroded (blue contour) and the concave edge on the wall interface being dilated (orange/red contour). Furthermore, a hole is visible on the side of the model, caused by the ghost particles reconstructed inside the model. The cylindrical section features a positive error, which is believed to stem from a lack of tracer particles in this region, as discussed previously on the 2D contours in Figure 6.22. Interestingly also the planar rearward face features a systematic positive error, albeit smaller in magnitude. Lastly, the spherical section presents a negative error, corresponding with an erosion of the solid model.

The mean positional error is summarized in Table 6.1, considering three metrics:

1. The root-mean-square error for the full reconstruction, referred to as ϵ_{total}.

2. The same error is computed, excluding the hole that is reconstructed due to the presence of ghost particles ϵ_{sub}.

3. The error on the inner part of the planar rearward face is evaluated separately, thereby excluding effects of surface curvature. For this last analysis on the planar face, the mean (β_{rwd}) and standard deviation (σ_{rwd}) are reported, rather than the root mean square error, in order to distinguish systematic and random error contributions.

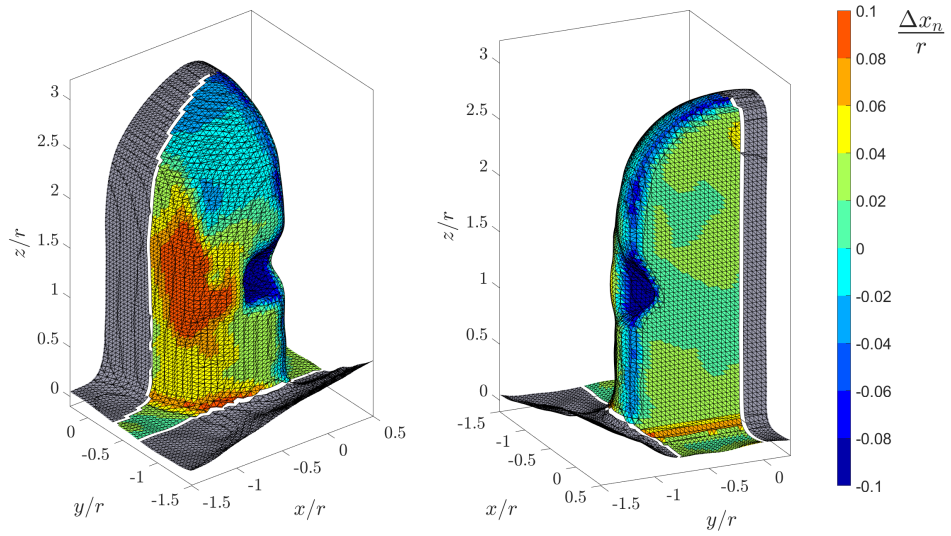

(a) Upstream view (b) Downstream view

Figure 6.23: Reconstructed fluid-solid interface for a search radius of 10 mm ($0.2\,r$) coloured by positional reconstruction error, indicating normal distance of reconstruction to reference model. Only the coloured part is considered in the quantitative error analysis.

Table 6.1: Experimental error analysis, side-mirror reconstruction.

Search radius R	ϵ_{total}	ϵ_{sub}	β_{rwd}	σ_{rwd}
I: $0.3\,r$ (15 mm)	$0.12\,r$ (6.02 mm)	$0.08\,r$ (3.80 mm)	$0.02\,r$ (1.07 mm)	$0.01\,r$ (0.53 mm)
II: $0.2\,r$ (10 mm)	$0.09\,r$ (4.73 mm)	$0.05\,r$ (2.51 mm)	$0.02\,r$ (1.11 mm)	$0.01\,r$ (0.38 mm)
III: $0.1\,r$ (5 mm)	$0.11\,r$ (5.40 mm)	$0.04\,r$ (1.76 mm)	$0.02\,r$ (1.01 mm)	$0.01\,r$ (0.58 mm)

The mean error based on the full reconstruction (ϵ_{total}) does not vary significantly with spatial resolution, respectively the search radius. Excluding the erroneous reconstruction due to ghost particle presence, the error is reduced by approximately a factor two, while additionally showing a clear trend that the error magnitude reduces as the spatial resolution increases. Analysing solely the planar rearward face, a bias error of approx. 1 mm is identified.

A source of this bias error is recognized upon inspection of the tracer particles' concentration gradient in the wall normal direction: the mean concentration obtained in thin slices of 0.5 mm thickness, parallel to the planar downstream interface is shown in Figure 6.24. The data suggests that within 3 mm from the model surface, the concentration drops from about 300 particles/cm^3 far from the model, to zero particles at the interface, possibly due to some tracers impacting at the model surface. Thus, the assumption of a uniform particle distribution is not sat-

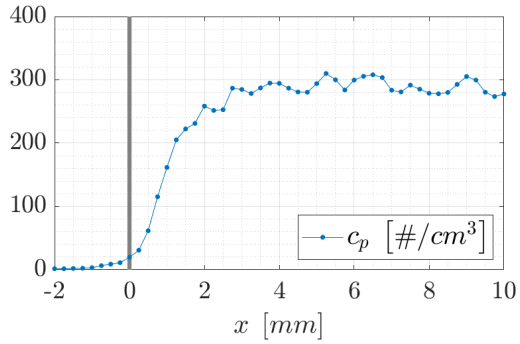

Figure 6.24: Tracer particle concentration downstream of the side-mirror model.

isfied close to the model interface. The observed gradient supports the positive bias error reported above, as the centroid shift magnitude $|\mathbf{x}_n|$ will be amplified for assessment points that are affected by the local concentration gradient.

Besides the observed bias, a random error (σ_{rwd}) is observed, that is on the order of half a millimetre. The magnitude of the random error on the planar rearward face corresponds well with the mean HFSB tracer particle diameter, which is expected to be around 0.5 mm (Faleiros et al., 2018; Scarano et al., 2015). Considering the typical spatial resolution of velocity field measurements acquired by a CVV system as studied here, we find that the mean flow field is typically ensemble averaged in sub-volumes (bins) of the order of $1\,\mathrm{cm}^3$, yielding a vector spacing of approximately 5 mm if assuming cubical bins at $50\,\%$ overlap (Kim et al., 2020; Saredi et al., 2020; Schneiders et al., 2018, among others). The positional reconstruction error observed in the analysis presented here is therefore within the expected vector pitch of the flow measurement, in particular when excluding the error due to ghost particle presence. The latter is to be avoided for a reliable interface reconstruction.

6.5. Conclusion

A method for detection of fluid-solid interfaces in PTV measurements around immersed objects is proposed. The analysis is solely based on the spatial distribution of particle tracers in the fluid domain, assuming the interface between the seeded fluid flow and the void solid region is a valid representation of the object silhouette. The local distribution characteristic is assessed in a search area (volume) of radius R. The theoretical background is developed for the 2D case on a planar interface, whereas the proposed principle is first illustrated on the synthetic particle distribution surrounding a cambered airfoil.

The airfoil case exposes two limitations of the proposed method: first, surface curvature is not accounted for, yielding an erosion of convex and a dilation of concave interfaces. Such error is significant when the radius of curvature is of the same order of magnitude as the search radius R. Second, thin objects present a chal-

lenge for reconstruction: features with thickness between the search radius R, and the search diameter ($2R$) cause the reconstruction of a secondary interface inside the object, whereas elements with a thickness smaller than the search radius R might not be identified at all. The latter justifies that the maximum reconstruction error in the airfoil case correlates with the search radius R. Therefore, R is to be minimized while maintaining a statistically significant sample size inside the search area (volume).

The method is subsequently adapted to the 3D case and applied to the experimental PIV data recorded by a coaxial volumetric velocimeter around a simplified car's side-mirror model mounted on a flat plate. The experimental assessment shows that the object shape is retrieved within the expected resolution of the surrounding flow measurement, if the absence of ghost particles inside the solid object can be guaranteed.

Part II

Applications in Sports Engineering

7

Full-scale cyclist

Life is like riding a bicycle.
In order to keep your balance, you must keep moving.

Albert Einstein

Road cycling pairs speed with endurance. At the highest level, let us take the Tour de France as an example, the winning margin after racing about 3500 *km in* 21 *stages may just be a matter of seconds: recall the 1989 edition, where Greg LeMond regained the race lead from Laurent Fignon by just* 8 *seconds through a time trial victory on the final day? Whereas LeMond raced with a time-trial specific, aerodynamic handlebar; a streamlined, tear-drop helmet; and a disc wheel in the rear, Fignon chose only for the aerodynamic disc wheel, and standard gear otherwise. LeMond averaged* 54.5 *km/h on that day. At such speed, aerodynamic drag contributes to* 90 *% of a rider's total resistance, and thus, it is fair to claim that LeMond won the stage, as well as the general classification because he was aware of the impact of aerodynamics in cycling and used it to his advantage.*

Nowadays it is common to see athletes, and bicycle equipment manufacturers optimizing aerodynamic performance in wind tunnel testing. Since most of these works quantify resistive forces only, comparably little knowledge is available on the flow topology. The latter, however, is crucial in a performance optimization process. To this end, the robotic volumetric PIV system presented in Chapter 3 is used to study the flow around a full-scale cyclist mannequin in time-trial position. The apparatus is introduced in Section 7.1, followed by a discussion of the velocimetry results in Section 7.2.

Jux C, Sciacchitano A, Schneiders JFG and Scarano F. Robotic volumetric PIV of a full-scale cyclist, *Exp. Fluids* **59**, 74 (2018)

Jux C, Sciacchitano A and Scarano F. Flow pressure evaluation on generic surfaces by robotic volumetric PTV, *Meas. Sci. Technol.* **31**, 104001 (2020)

Aerodynamics in competitive cycling remains a vividly discussed topic, which is studied by means of experimental and computational fluid dynamics (CFD) nowadays. A topical review is presented by Crouch et al. (2017), which is complemented by the recent review articles by Malizia and Blocken (2020a, 2021). The relevance of cycling aerodynamics is understood when realizing that at typical racing speeds of 40 km/h and beyond, the aerodynamic drag causes about 90 % of a rider's total resistance. Maximizing aerodynamic performance is consequently one key to success in competitive cycling.

The scientific community aids the aerodynamic optimization process by providing insight into the flow topology on a cycling athlete. Examples of CFD studies indicate interest in the overall flow topology, as well as the pressure distribution on the athlete and his/her equipment (Beaumont et al., 2018; Blocken et al., 2013, among others). Works in the experimental domain are often addressing the wake flow topology, see e.g. the studies of Terra et al. (2019) and Spoelstra et al. (2019) which have benefited from the use of large-scale PIV. Crouch et al. (2014) instead used multi-hole pressure probes to capture the cyclist's wake flow topology, whereas surface pressure readings are obtained through orifices integrated into the mannequin's back. The latter work is the only example known to the author that incorporates the experimental study of the surface pressure on a cyclist model.

In this context, the flow analysis through robotic volumetric PIV as described in Part I provides a suitable tool to study the near flow topology as well as the surface pressure on an athlete model experimentally. The study presented in this chapter utilizes robotic volumetric PIV to analyse the flow field past a full-scale mannequin.

7

7.1. Experimental apparatus and procedures

Wind tunnel measurements are conducted at the Open Jet Facility (OJF) of TU Delft, where the flow behaviour around the full-scale replica of the professional cyclist Tom Dumoulin (Terra et al., 2016) is studied by means of robotic volumetric PIV. Experiments are carried out at a Reynolds number of 5.5×10^5, based on the cyclist's torso length of 600 mm.

The Open Jet Facility is, as previously discussed, an atmospheric, closed-loop, open jet wind tunnel with a contraction ratio of $3:1$ and an octagonal exit section of $2.85 \times 2.85\,\mathrm{m}^2$. During the measurements, the wind speed is held constant at 14 m/s. A heat exchanger downstream of the test section maintains a constant air temperature independent of the flow speed. The turbulence intensity of the free stream is reported to be 0.5 % (Lignarolo et al., 2014). The latter does not include the aerodynamic effects of the seeding generator upstream of the cyclist, which raises the turbulence intensity. This aspect is addressed later in this section.

The need to achieve test repeatability and to cope with potential risks of laser illumination motivates wind tunnel testing with replica models rather than human athletes. To maintain a steady position of the athlete for the complete measurement duration, an additively manufactured full-scale replica of the time trialling athlete (van Tubergen et al., 2017) is installed in the test section, see Figure 7.1. The static mannequin obeys a fixed crank angle of $75°$ as detailed in Table 7.1 which summarizes the characteristic model dimensions. As discussed in Crouch et al.

(a) Athlete 3D scan

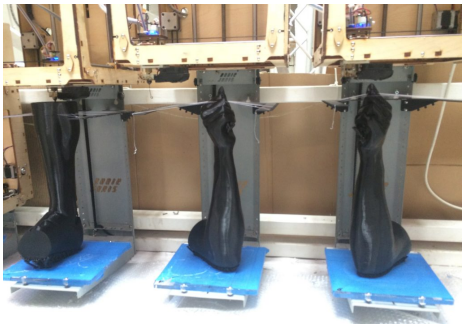

(b) 3D printing of legs and arms

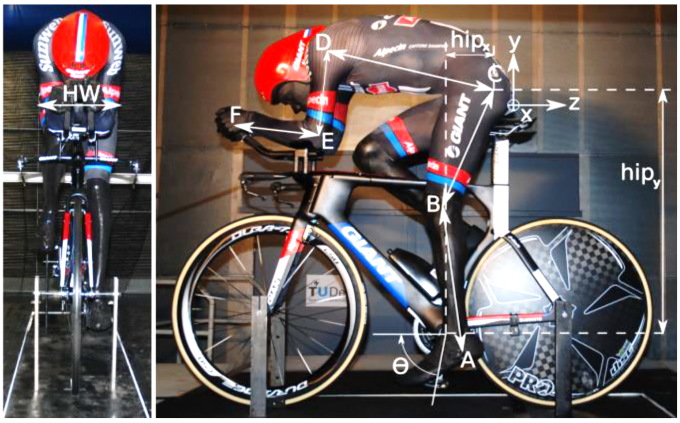

(c) Cyclist model and bike with characteristic dimensions. Reproduced from (Terra et al., 2016).

Figure 7.1: Full-scale cyclist model from 3D scan to ready wind tunnel mannequin.

(2016), the use of a static model yields a wake flow that is highly representative of the phased-averaged flow field of a pedalling athlete, while greatly simplifying the experimental setup.

The cyclist wears a long sleeve *Etxeondo* time trial suit along with a *Giant* time trial helmet, as used by *Team Giant Alpecin* (currently known as *Team DSM*) during the 2016 season. The rider is placed on a *Giant Trinity Advanced Pro* frame equipped with a *Shimano DuraAce C75* front and a *Pro Textreme* disc rear wheel, both fitted with 25 mm tubular *Vittoria Corsa* tires. In this study, the wheels are kept stationary. Rigid supports at front and rear axle connect the bike to a 4.9 m long and 3.0 m wide wooden table, placed 0.2 m above the lowest point of the wind tunnel nozzle exit. The front wheel centre line is located 2.1 m downstream of the contraction exit.

The robotic PIV system, as presented in Chapter 3, comprises three major components: the HFSB seeding generator, the coaxial volumetric velocimeter including the illumination unit, and further the robotic arm. Neutrally buoyant HFSB with

Table 7.1: Characteristic mannequin dimensions (Terra et al., 2016).

Name	Symbol	Dimension	Unit
Crank angle	θ	75	[°]
Hip width	HW	365	[mm]
Shoulder width	SW	380	[mm]
Hip location, x	HIP_x	180	[mm]
Hip location, y	HIP_y	850	[mm]
Lower leg length	$A-B$	475	[mm]
Upper leg length	$B-C$	460	[mm]
Torso length	$C-D$	600	[mm]
Upper arm length	$D-E$	326	[mm]
Lower arm length	$E-F$	290	[mm]

$400\,\mu$m mean diameter are employed as flow tracers. A four-wing seeding rake comprising 80 HFSB generators is installed on a two-axis traversing system at the exit of the wind tunnel contraction. The pitch between generators is 5 cm and 2.5 cm across and along the wings, respectively. The system delivers approximately 2×10^6 tracers per second, distributed over a cross section of $15\times48\,\text{cm}^2$. The seeding generator is controlled through a *LaVision* fluid supply unit.

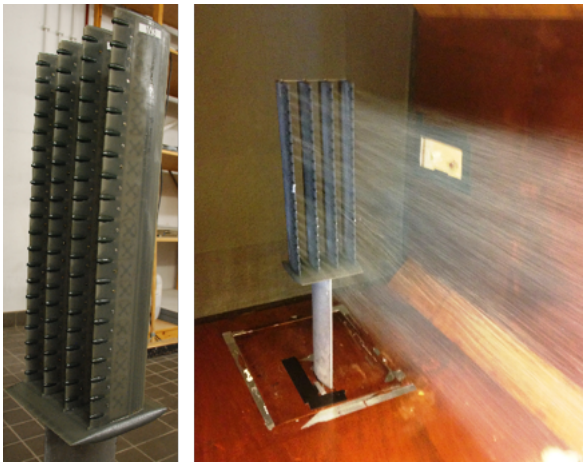

Figure 7.2: HFSB seeding system (left) and the seeded stream-tube (right).

In the assumption of straight flow through the seeding generator, each nozzle seeds a cross section of $12.5\,\text{cm}^2$ based on the nozzle pitch. At a freestream velocity of 14.0 m/s the seeding concentration of the undisturbed flow (C_{HFSB}) is estimated as (Caridi et al., 2016):

$$C_{HFSB} = \frac{\dot{N}}{\dot{V}} = \frac{25,000}{17,500}\frac{\frac{tracers}{s}}{\frac{cm^3}{s}} = 1.43\frac{tracers}{cm^3} \tag{7.1}$$

where $\dot{N}$ is the production rate of an individual generator and $\dot{V}$ is the volume flow

rate across the area delimited by neighbouring generators. The aerodynamic invasiveness of the seeding generator is studied by means of a freestream measurement 2 m downstream of the contraction exit using the robotic PIV system. A turbulence intensity of 1.9 % is measured in the wake of the rake of wings hosting the generators; conversely, it has been observed that the seeding rake does not affect the mean velocity to a measurable extent. It is noted that the freestream turbulence can be reduced below 1 % by placing the seeding rake more upstream inside the wind tunnel's settling chamber. The effect of the supporting strut is neglected, given that its wake region is not included in the PIV measurements.

The CVV probe used in the cyclist study is the *LaVision MiniShaker S* which was introduced in Chapter 3 (Table 3.1). Images of 640×476 px^2 are acquired at a frequency of 758 Hz. Illumination is provided by a *Quantronix Darwin Duo* Nd:YLF laser, coupled with a spherical, converging 20 mm lens to direct the light beam into a 4 m long optical fibre. Another 4 mm spherical, diverging lens is attached at the fibre end to obtain the desired light spreading angle.

The velocimeter's position and orientation is controlled by a collaborative robotic arm (*Universal Robots UR5*). The position and direction of the CVV probe is set by moving the robot manually aiming at a target point specified on a digital display. The position repeatability is reported as ± 0.1 mm from the manufacturer (Universal Robots, A/S, 2017). The robot is installed in two symmetric base positions, each at a height of 65 cm, 90 cm lateral distance to the wheel line and 30 cm downstream of the front wheel centre line. The overall experimental arrangement is illustrated in Figure 7.3.

For particle image recording the probe is placed in a chosen position. To cover the flow around the full cyclist mannequin, measurements are gathered from a total of 450 different positions of the CVV probe. At each position, $5,000$ images are recorded. The system is operated in manual mode by a single-user, where each measurement region requires approximately 2 minutes. A limiting factor is the user interaction time needed to verify the good positioning of the probe. Additional factors affecting the measurement time are the start-up period of the seeding generator and the data storage time.

The raw particle image recordings are pre-processed with a temporal high-pass filter (Sciacchitano and Scarano, 2014), which eliminates most background illumination, see Figure 7.4. The pre-processed images are analysed with the Shake-The-Box algorithm (Schanz et al., 2016), yielding particle tracks with instantaneous velocity vectors at the scattered particle locations.

A total of approximately $10,000$ particles is captured in each recording, corresponding to a tracers concentration of 1 particle/cm^3 and a particle image density of 0.01 particles per pixel. The actual concentration of tracers can vary in the measurement domain and it is typically below the nominal value established in Equation (7.1). About one tenth of the detected particles are tracked continuously along at least four recordings, yielding around $1,000$ particle tracks in each recording.

The scattered velocity data obtained at each measurement position is visualized by particle trajectories sampled over a discrete set of time instants (tracks). For sake of example, Figure 7.5 visualizes the cloud of measured data in a region where

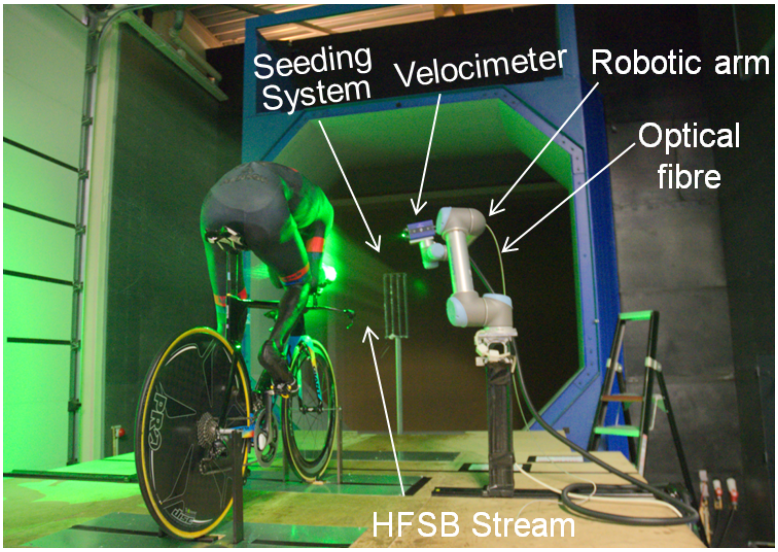

Figure 7.3: Experimental setup in OJF with cyclist, seeding generator, and robotic PIV system.

the optical access is constrained by the mannequin geometry (region between the rider's face and his arms). The CVV position can be inferred from the pyramidal shape of the measured region.

The overall experiment is composed of 450 likewise measurements where the CVV is pointed around the cyclist mannequin to map the entire flow field in its vicinity. The total number of particle tracking velocity measurements is approximately 1.3×10^9, which is then ensemble averaged to return the time-averaged velocity vector field. The volume scanning process is illustrated graphically in Figure 7.6.

The measurements spanning a domain of $2,000 \times 1,600 \times 700\,\mathrm{mm}^3$ are distributed on a Cartesian grid, where the velocity is described by $400 \times 320 \times 140$

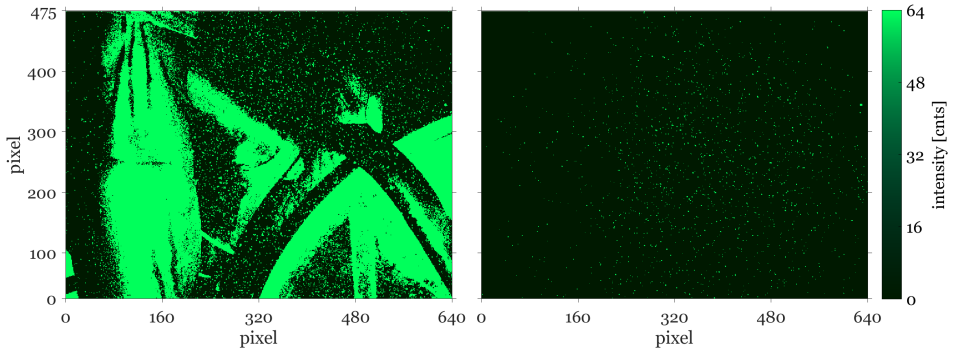

Figure 7.4: Illustration of a recording with the CVV system. Left: instantaneous raw image. Right: image after pre-processing with a high-pass frequency filter.

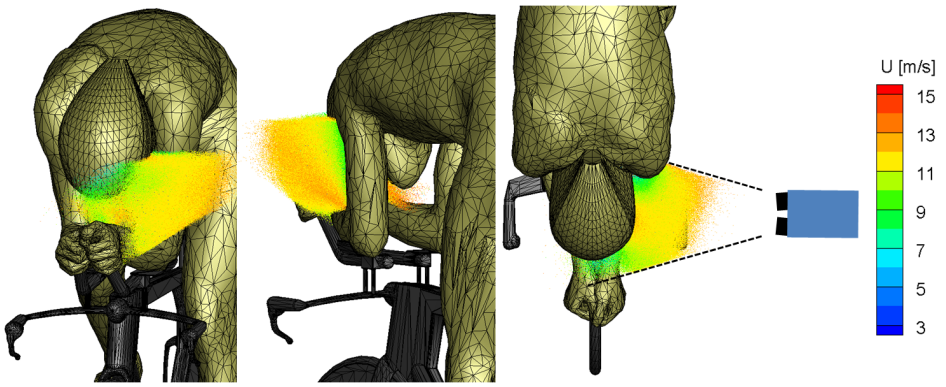

Figure 7.5: Scattered particle data color-coded by streamwise velocity component. The ensemble is obtained from $1,000$ recordings taken from a single position of the robot hand (right).

points, using cubical ensemble averaging cells of 20 mm linear size, with 75 % overlap, resulting in a 5 mm vector spacing. The cell size is determined with the criterion that at least ten valid data should be comprised in the ensemble ($N_{min} = 10$). The minimum cell size is limited by the lower seeding concentration in the separated flow behind the bluff regions of the athlete. Overall, each bin contains on the order of 100 particles on average. For the given settings, a measurement spatial dynamic range $DSR = 100$ is attained as the ratio between domain size $L_G = 2,000$ mm and cell size $l_V = 20$ mm.

For the velocity dynamic range ($\overline{DVR}$) a value of 100 is estimated, based on the average number of particles per bin and assuming turbulent fluctuations of 10 % amplitude relative to the free stream velocity. The data in the overlapping region of adjacent volumes is used to quantify the measurement uncertainty. The discrepancies on the mean velocity are of the order of 2 % for the x- and $y-$velocity components and 4 % for the z-velocity component.

7.2. Results and discussion

The discussion of the velocimetry results on the cyclist mannequin is split into three sections: first, Section 7.2.1 addresses the time-average velocity field; the analysis of the surface pressure distribution is discussed in Section 7.2.2; and lastly, the uncertainty of the pressure measurement is evaluated in Section 7.2.3.

7.2.1. Time-average velocity field

The time-average velocity field of the flow around the cyclist is illustrated in Figure 7.7. The velocity contours in the median xy-plane reveal the velocity pattern at largest scale. The first stagnation region is at the rider's helmet. The flow accelerates along the upper curved back, reaching a maximum at approximately half the torso length. Further downstream, the flow decelerates due to the adverse pressure gradient. The unstable boundary layer undergoes separation at the lower

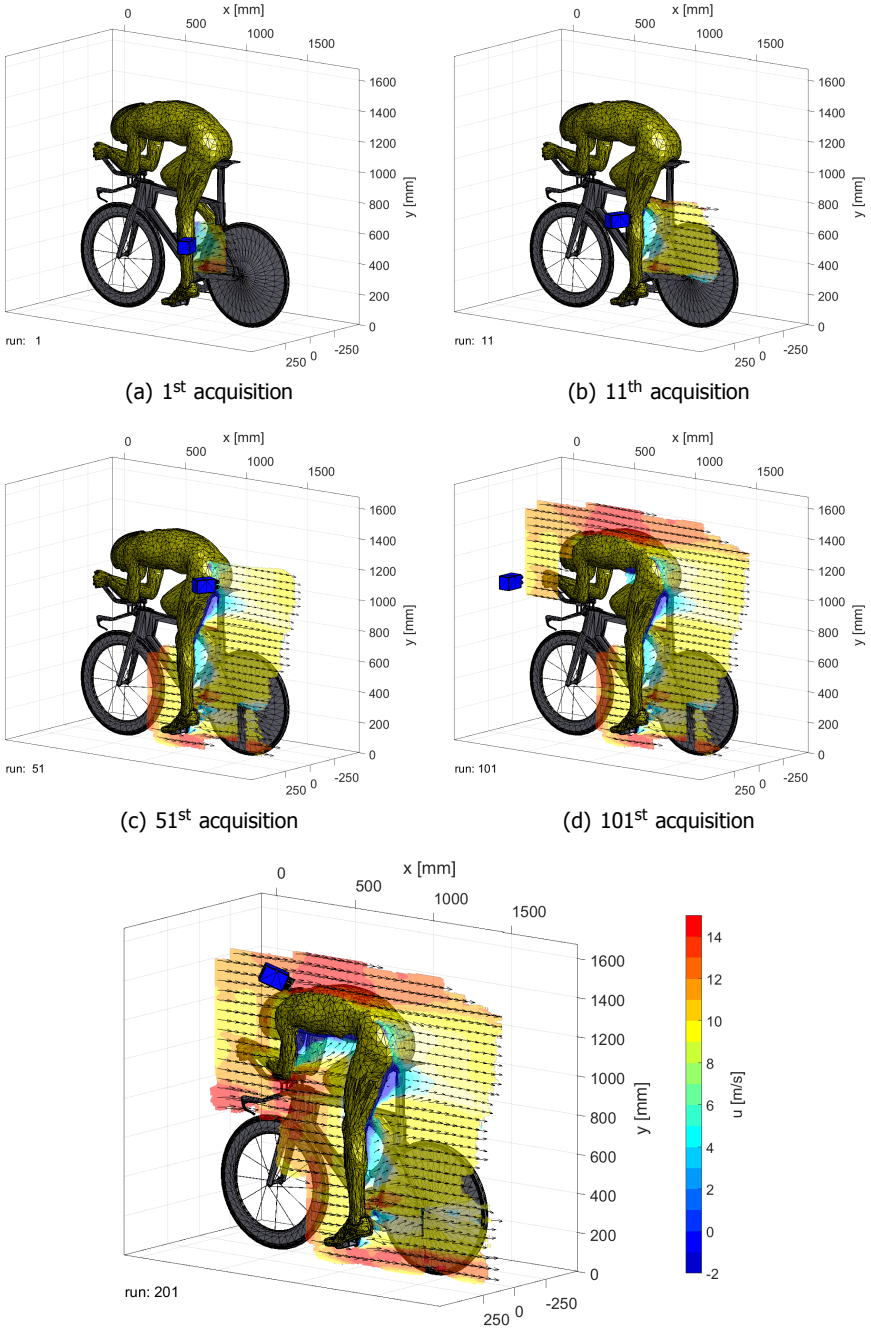

(a) 1st acquisition

(b) 11th acquisition

(c) 51st acquisition

(d) 101st acquisition

(e) 201st acquisition

Figure 7.6: Illustration of the volume scanning process by robotic volumetric PIV, by means of the velocity field in a xy-plane through the mannequin's leg. Animation available online.

back. The separated region has a relatively small extent and is terminated by a saddle point where streamlines converge right below the bicycle saddle. A secondary stagnation at the front of the rider is identified in the hands region, which have a relatively close position in the tested time-trial position. After stagnating, the flow accelerates around the arms and in the structure between the steering and the upper edge of the fork.

The analysis of velocity contours and streamlines in the median plane does not allow the evaluation of three-dimensional structures and features away from the plane. For this purpose the 3D iso-surface of streamwise velocity $u = 7$ m/s $(0.5u_\infty)$ is meant to identify the regions where the momentum deficit is most pronounced. The caveat is that flow deceleration around forward stagnation is not considered as it is not relevant to the process of pressure losses by flow separation. Regions where forward stagnation is observed are the front side of the helmet, the upper arms, the entire upper (extended) leg and part of the lower legs.

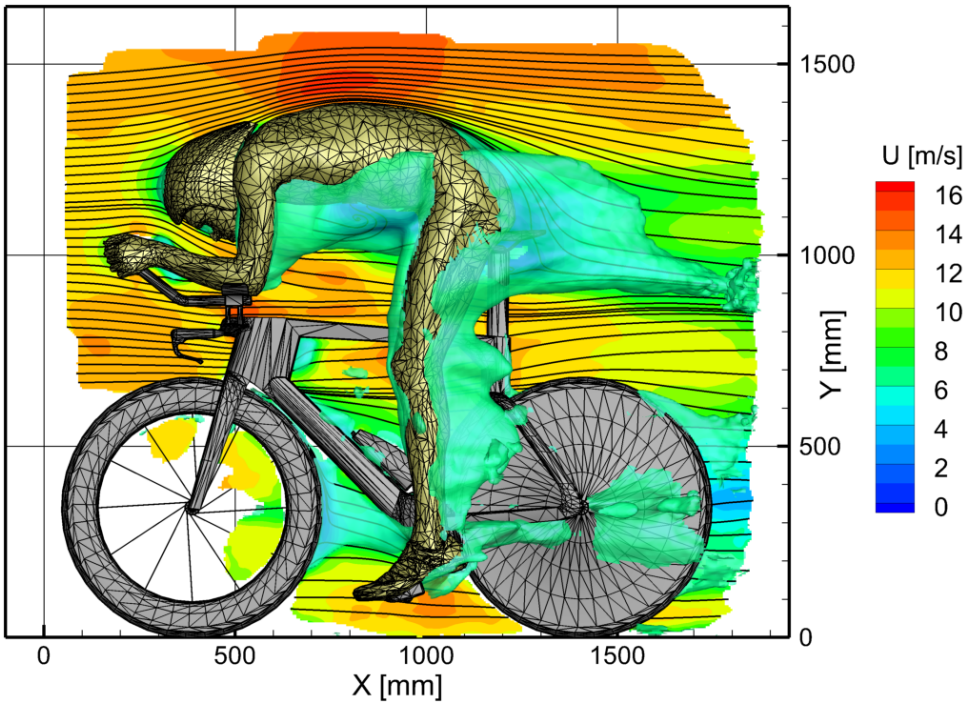

Figure 7.7: Time-averaged velocity field at $u_\infty = 14$ m/s visualized by a contour of streamwise velocity u in the centre plane ($z = 0$ mm) including surface streamlines, together with an iso-surface of $u = 7$ m/s.

The two most extended regions exhibiting velocity deficit are a large part of the decelerated flow comprised between the chest, the elbows, and the pelvis; and the separated flow at the lower back of the cyclist. The flow decelerating around the pelvis develops sidewise enveloping the hip of the stretched leg. The wake from the leg connects in a three-dimensional topology to the separated region at the rider's

low back. The wake region of the latter contracts slightly approaching the knee and becomes again more prominent in the calf region and past the foot. Finally, some more pronounced region of velocity deficit with streamwise elongation are observed at the left heel, signalling the presence of streamwise vortices. The visible deceleration closer to the back wheel may be partly accentuated by the presence of the necessary structure to support the model in the wind tunnel. The (non-rotating) wheels exhibit a similar wake. The front wheel has its wake centred at the most downstream point, whereas the back wheel has its wake in a slightly upper position.

Surface-flow

The availability of velocity data around and in the vicinity of the cyclist body surface is used to estimate the topology of skin friction lines. The latter are notably of difficult detection with PIV over curved surfaces due to the challenge of following the surface contour in 3D with the illumination. An excellent example is given in the work of Depardon et al. (2005), where planar PIV measurements 0.5 mm close to the wall have been used to estimate the detailed topology of skin friction lines around a cubic obstacle mounted on a flat plate. The same technique could not be used in this case, due to the complex 3D geometry under consideration. Typically the distance of the closest vector from the surface is approximately 10 mm, half the size of a measurement cell. The velocity at approximately 5 mm from the wall (dilated surface) is estimated by interpolation. The 3D streamlines pattern on the dilated surface is inspected to reveal the relevant topological features at the surface. The velocity magnitude along the streamlines provides additional information on the flow. The near-surface friction lines are shown in Figure 7.8.

The flow on the rider's back appears to separate only at the sides of the low back region. The air captured in the chest region exits sideways along the lower torso and streams towards the centre of the lower back. On the straight leg side, the separation occurs only at the gluteus as indicated by the interruption of skin friction lines from the side of the upper leg. Separation past both arms on their upper side is also evident with the sudden drop in velocity and the interruption of the streamlines. A long separation line is drawn along the upper leg and the calf region also with the presence of two foci at the lower gluteus and in the middle of the calf respectively. No apparent separation is detected on the lower leg towards the ankle. On the right side the flow passes the bent leg with no distinct separation in the rear of the inclined upper leg[1]. At the right lower back flow separation is indicated by a strong velocity deficit and the interruption of streamlines. Another separation region is visible in the right knee pit and the upper calf region of the right leg. The extent of the velocity deficit on the inclined leg appears smaller as compared to the straight left leg suggesting a condition of maximum aerodynamic resistance for the latter, corresponding with the findings of Crouch et al. (2014).

[1] digital flow visualizations are accessible online at Exp. Fluids

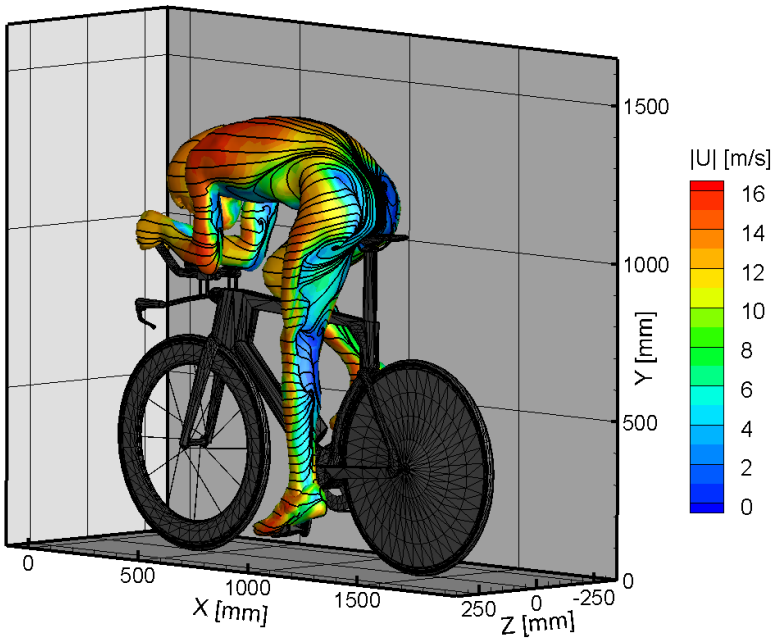

Figure 7.8: Velocity magnitude contour at 5 mm distance to cyclist's body and estimation of skin friction lines over the dilated surface.

Vorticity

The analysis of vorticity is focussed on flow structures oriented along the streamwise direction. Iso-surfaces of streamwise vorticity at ± 100 Hz are illustrated in Figure 7.9(a). Regions with anticlockwise rotation are depicted in red (positive vorticity) and clockwise in blue. The first main feature is a clockwise rotating (blue) vortex originating from the right arm and developing along the upper right leg. A pair of vortices is observed trailing from the right foot, whereas another pair of vortices is formed at the foot tip. The whole system features a vorticity quadrupole. The smallest size of the vortices that are detected is approximately 4 cm.

Wake flow topology

Previous works have characterised the near and far wake of cyclists and inferred from a cross section in the wake that the vortex structures dominate the flow development. Here, a plane is selected in the near wake at $x = 1,500$ mm (300 mm downstream of the lower back of the cyclist).

The velocity contour in Figure 7.10 shows the detailed boundary of the wake region developed downstream of the rider. The momentum deficit is larger on the stretched-leg side, which is consistent with the thin-volume PTV measurements of Terra et al. (2016). A strong downwash is produced by the curved back of the rider, as also found by Crouch et al. (2014) via multi-hole pressure probe measurements. The wake consists of a complex system of vortices, of which many are present below

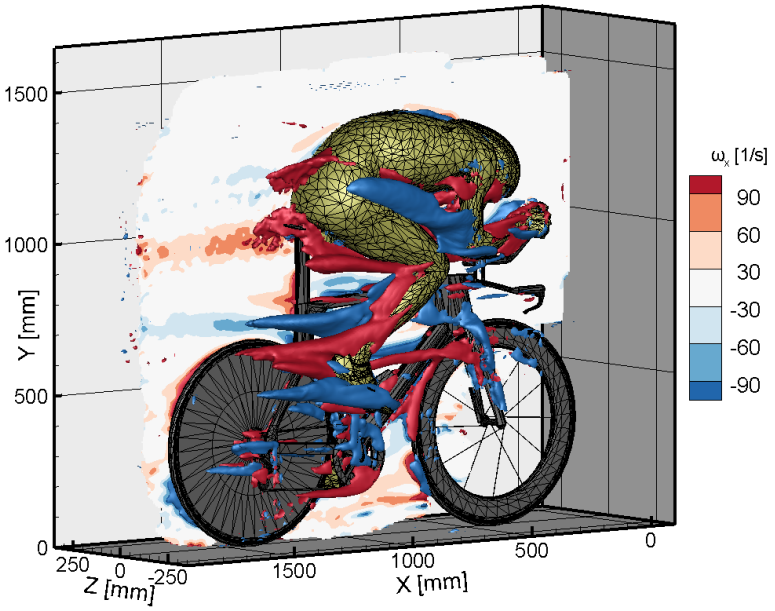

(a) Contour plane of streamwise vorticity ω_x at $z = 10\,\text{mm}$, together with iso-surfaces of $\omega_x = \pm 100\,\text{Hz}$.

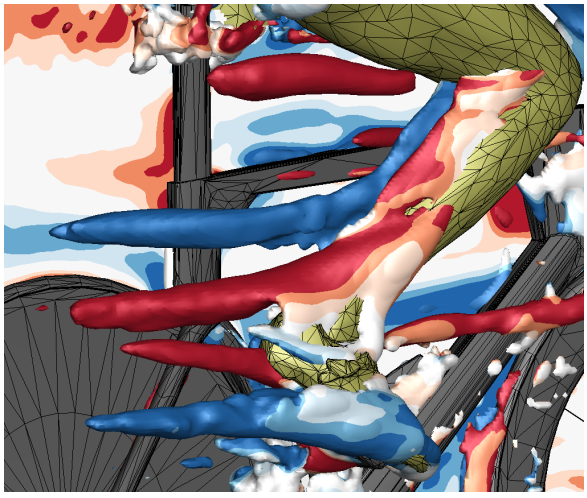

(b) Zoom onto right leg with iso-surfaces of Q-criterion coloured by ω_x.

Figure 7.9: Flow topology visualization by vorticity and Q-criterion.

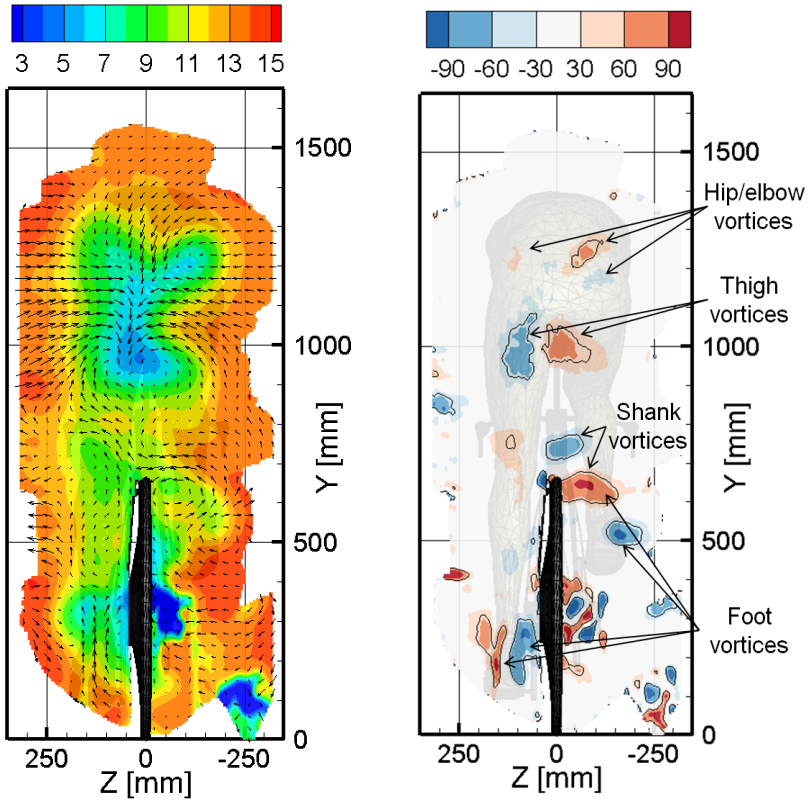

(a) Streamwise velocity u in m/s including in-plane velocity vectors.

(b) Streamwise vorticity ω_x in Hz with black contour lines of $\omega_x = 50$ Hz.

Figure 7.10: Cyclist's wake flow topology, by contour planes at $x = 1,500$ mm.

the rider's torso. Two counter-rotating vortices emanate from the inner thighs and contribute to the downwash in between them, as also reported by Crouch et al. (2014) and Terra et al. (2016). A pair of counter-rotating vortices is produced also by the foot of the stretched leg, which agrees well with the RANS simulations of Griffith et al. (2014) at 75° crank angle. As seen in Figure 7.9(b) and reported by Terra et al. (2016), further streamwise vortices emanate from the foot and the shank of the bent leg. Weaker and smaller vortices are present in the upper part of the model, which are ascribed to the interaction of the upcoming flow with the rider's hip and elbows.

7.2.2. Surface pressure distribution

Based on the full-scale velocimetry data above, the surface pressure on the athlete's body is evaluated following the strategy presented in Chapter 5.

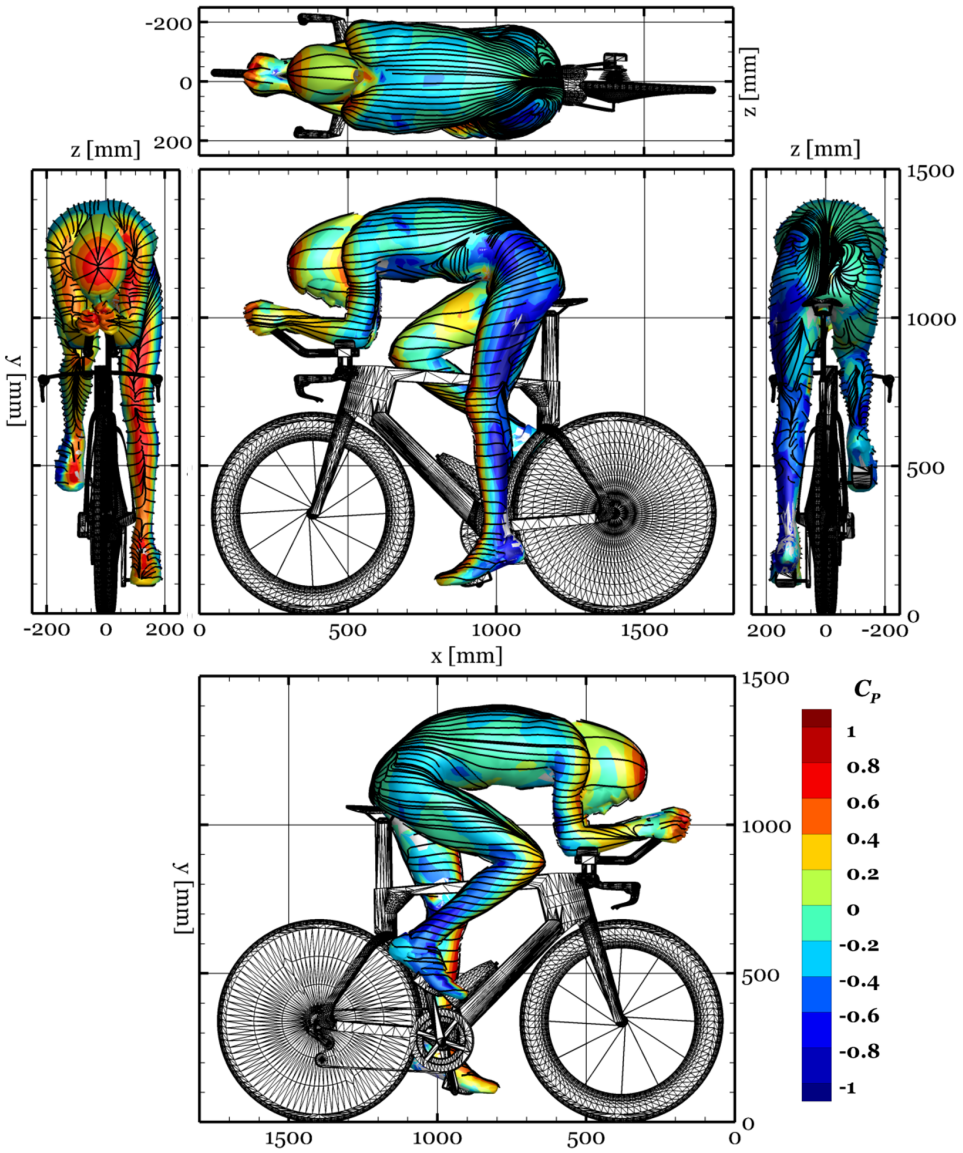

Figure 7.11: Surface pressure coefficient distribution on the full-scale cyclist model. Orthogonal views from front, back, sides and top of the athlete.

Global view

A global view of the pressure distribution on the mannequin is presented here by orthogonal views along the principal axes (Figure 7.11), while the supplementary material[2] contains further views.

Regions of high pressure are clearly identified Figure 7.11 (front-view) on the forward sections of the helmet, the rider's hands and fingers, the upper arms, as well as the extended leg and the right knee where the flow is stagnating. A slightly asymmetric pressure distribution is observed on the two arms, which is less easily explained than that occurring on the legs, where the stretched left leg faces the flow more bluntly as compared to the flexed right leg. Regions of low pressure are observed on the sides of the legs (Figure 7.11 - lateral views), feet and arms as a result of the flow acceleration past these body parts. Similarly, over the curved shoulders, the back and the left hip, low pressure areas are identified in Figure 7.11 (top-view). The former areas are likely due to the curvature of the back inducing local flow acceleration, whereas around the hip (Figure 7.11 - left view), a significant upward flow component causes a local region of suction.

Local view

Three distinct regions are addressed in more detail in the following with the purpose to understand the level of detail that can be represented with the present measurements: the athlete's face, his lower right leg, and the lower back. The face and head region presents a geometry with limited optical access. The right ankle-foot region features the source of a number of vortices, which dominate the local flow topology. Lastly, at the lower back a region of flow separation is expected.

Figure 7.12 displays the pressure distribution in the athlete's head and face region. Areas of high pressure are prominent on the forward facing fingers, the centre of the helmet and the biceps. Here, a stagnation line can be identified which divides the flow into portions passing on the inside and outside of the upper arm respectively. On the helmet instead, there is a stagnation point from which streamlines emanate radially. As the flow passes the athlete, the static pressure reduces towards the widest sections of hands, helmet and upper arm. On the side of the helmet, the pressure reduction is followed by a rapid pressure increase (adverse pressure gradient) due to the flow decelerating in front of the biceps and shoulder. Negative pressure coefficients, indicating local suction, are visible on the outside of the elbow, and past the shoulder onto the curved upper back.

The foot-ankle region is shown in Figure 7.13. On the upstream section displayed in Figure 7.13 (left), the highest pressure is observed at the knee and the forward facing instep of the shoe. A significant pressure reduction is seen on the outside of the shoe, while around the inclined shin, the pressure gradient is less steep. The strong pressure variation on the foot can be linked to the presence of a number of (counter-rotating) vortices originating from the shoe and the ankle region as indicated in Figure 7.13 (centre). Viewing from downstream (Figure 7.13 – right) there is a minimum pressure region just above the ankle, separating two moderate

[2] further surface pressure observations are accessible at Meas. Sci. Technol., and in the digital appendix to this thesis

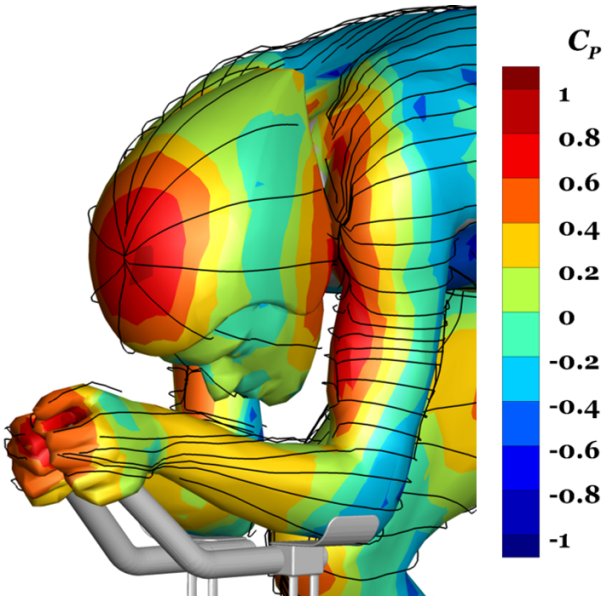

Figure 7.12: Surface pressure coefficient distribution on athlete's head and arms. Surface streamlines are evaluated at 5 mm distance to the body surface.

pressure regions on the heel and the calf. The low pressure region corresponds to the location where the two shear layers from the lower leg roll up into two streamwise, counter-rotating vortices, causing a local pressure reduction.

When discussing the surface flow topology on the athlete's extremities, a word of caution is appropriate: for the surface pressure evaluation we assume a known geometry of the model. In the case of the cyclist this is the surface model employed to manufacture the mannequin by 3D printing (van Tubergen et al., 2017). While the manufacturing process can be regarded accurate, with the layer-resolution in Fused Deposition Modelling (FDM) typically being below 1 mm (e.g., Ultimaker BV, 2019), model deviations can be introduced when installing the mannequin on the bike. In the specific case of the legs, a small degree of bending may occur when the feet are fixed to the pedals, which can result in a displacement of several millimetres compared to the reference geometry. An additional source of uncertainty is therefore introduced in the evaluation of surface flow properties, which has not been considered yet. This type of uncertainty can be alleviated if the final model geometry is determined experimentally, e.g. by means of photogrammetry, 3D-scanning procedures, or directly from the flow measurement as proposed in Chapter 6; but such approach has not been considered at the time of the measurement.

Lastly, Figure 7.14 features the static pressure distribution on the athlete's lower back. Furthermore, an iso-surface of $u = 0.1 \cdot u_\infty$ is plotted as an indicator for quasi stagnant flow. The near-surface streamlines indicate a complex flow pattern: the flow over the hips contains a clear upward component, resulting into an in-wash motion over the lower back. Both hip regions feature low static pressure, especially

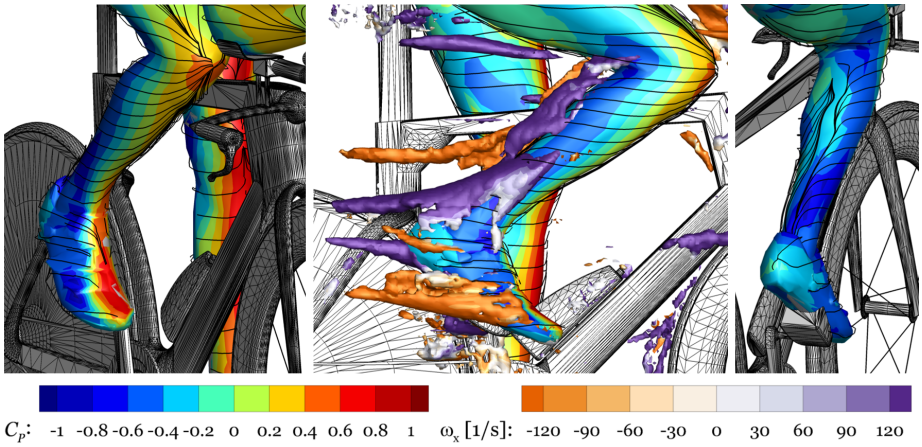

Figure 7.13: Surface pressure coefficient distribution in the foot-ankle region, along with iso-contours of Q-criterion coloured by streamwise vorticity ω_x.

on the left-side of the stretched leg. The streamlines entering the lower back region past the hips are drawn into rotational flow patterns on either side of the back, see Figure 7.14 (a) which are linked to the so-called hip-vortices as first reported by Crouch et al. (2014). The two hip-vortices can also be seen as a driver for the in-wash over the athlete's back and the down-wash in his wake. Below the right hip-vortex core, indicated by point (c) in Figure 7.14, the streamlines feature a source-pattern point, which should correspond to the separated flow moving towards the surface. The left and right sides of the velocity iso-contour highlight the lines of flow separation with a U-shaped region of flow detachment, see Figure 7.14 (b).

7.2.3. Surface pressure uncertainty estimate

The uncertainty for the pressure distribution presented above is estimated by extending the uncertainty analysis performed for the sphere-flow discussed in Chapter 5. Comparing the experimental parameters for sphere and cyclist in Table 7.2, indicates that there are no fundamental differences between the two studies.

Both experiments are carried out in the low-speed, incompressible flow regime, with the Reynolds number in the order of $Re = 10^5$, depending on the length scale which is considered in case of the cyclist. The estimated uncertainty level for the mean velocity compares well. A clear difference is observed in the variability of the free-stream pressure ($\sigma_{C_{P,tot}}$), which is approximately three times higher for the cyclist case. This is attributed to the fact that the seeding generator in the cyclist study is placed downstream of the wind-tunnel contraction rather than inside the settling chamber as in the sphere case, justifying an increased turbulence level in the free-stream. This translates into a higher bias error resulting from the domain partitioning described in Section 5.2, adding a bias error of $2.7\,\%$ in total pressure coefficient, over the $1.5\,\%$ for the case of the sphere.

A clear difference is recognized in the variety of length scales between the two

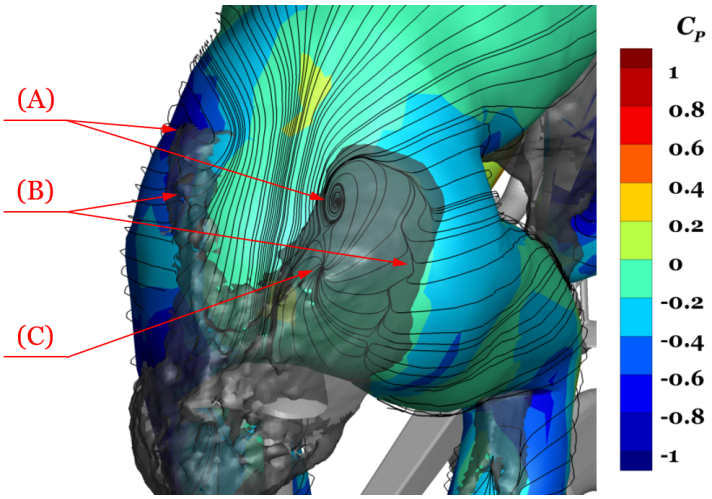

Figure 7.14: Surface pressure coefficient distribution on the athlete's back. Surface streamlines on a 5 mm dilated surface. Transparent grey iso-surface corresponding to $u = 10\,\%$ free-stream velocity. Labels added for (a) hip vortices; (b) separation lines; and (c) source-pattern point.

Table 7.2: Characteristic parameters for sphere- and cyclist-experiment, both conducted at the TU Delft Open Jet Facility.

Paramter	Symbol	Sphere	Cyclist	Unit
Free-stream velocity	u_∞	10	14	m/s
Reynolds number	Re	9.9×10^4	Torso, 5.5×10^5	–
Acquisition frequency	f_{aq}	821	758	Hz
Linear bin-size	l_v	10, 30, 50	20	mm
Mean-velocity uncertainty	$\epsilon_{\bar{u}}$	2	$2-4$	%
Characteristic length scale	L	Radius, R: 75	Torso length: 600 Upper leg, R: 70 Arms, R: 40 Ankle, R: 35 Face details: $\mathcal{O}(10)$	mm
Estimated free-stream pressure variability	$\sigma_{C_{P,tot}}$	0.5	1.4	%

cases: the sphere is uniquely characterized by its radius, whereas the athlete model features a range of scales as indicated in Table 7.2. In the analysis of the sphere data in Section 5.4 it was concluded that spatial resolution effects are not observed however, as long as the linear bin-size l_v remains smaller than half the local radius of curvature R. Assuming the same scaling holds for the cyclist, it is seen that the ratio of l_v over R is below 0.5 for the majority of the athlete model (legs, shoulders, arms, helmet, torso) and only locally, e.g. at the ankles, the fingers, or the facial details, the ratio exceeds the critical value of 0.5. Therefore, it is assumed that, with exception of the aforementioned regions, the confidence in the surface pressure on the athlete model compares well to the sphere-case, where an uncertainty level of

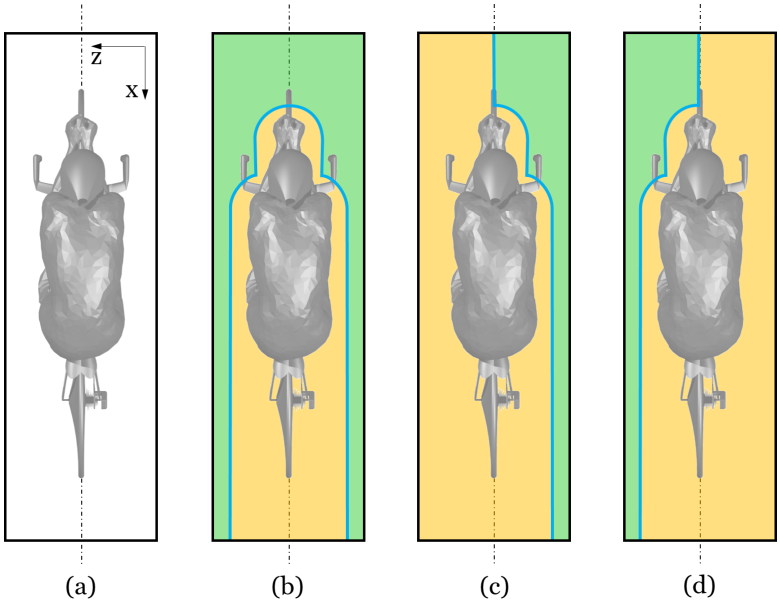

Figure 7.15: Schematic illustration of variations in domain partitioning applied for the a-posteriori uncertainty analysis. (a) indicates the measurement domain, (b) visualizes the partitioning proposed in Section 5.2 where the green region represents the domain of constant total pressure and the yellow part requires integration of the pressure gradient. (c) and (d) show the modified partitions considered for the uncertainty analysis.

$0.15\,C_P$ (9 Pa) has been established. Accounting for the above-mentioned bias due to the pressure-variability in the free-stream it is expected that the surface pressure distribution on the athlete model is accurate to within $0.2\,C_P$ (approx. 24 Pa, based on the free-stream dynamic pressure $q_\infty = 0.5\rho u_\infty^2$).

An alternative *a-posteriori* estimate for the uncertainty of the surface pressure measurement on the cyclist is obtained by evaluating the pressure variability resulting from different integration paths. To this end, the measurement domain which is schematically illustrated in a top-view in Figure 7.15 (a), is partitioned following the procedure detailed in Section 5.2, resulting in a two-part domain as shown in Figure 7.15 (b). Evaluation of the pressure based on the theory outlined in Section 5.3 yields the results presented in Section 7.2.2, which are herein used as the reference.

Secondly, the domain interface shown in Figure 7.15 (b) is split along the median plane ($z = 0$ mm), yielding the partitions illustrated in Figure 7.15 (c & d), where the irrotational flow assumption is only applied on one side of the measurement domain, and the opposite side is instead spatially integrated. In this way, the extent of spatial integration is significantly increased, whereas the Dirichlet boundary condition for the integration process in cases (c) and (d) are independent of each other. In a third and final step, the surface pressure obtained on the athlete's left-hand side (LHS, $z > 0$ mm) for case (c) and his right-hand-side (RHS, $z < 0$ mm) for case

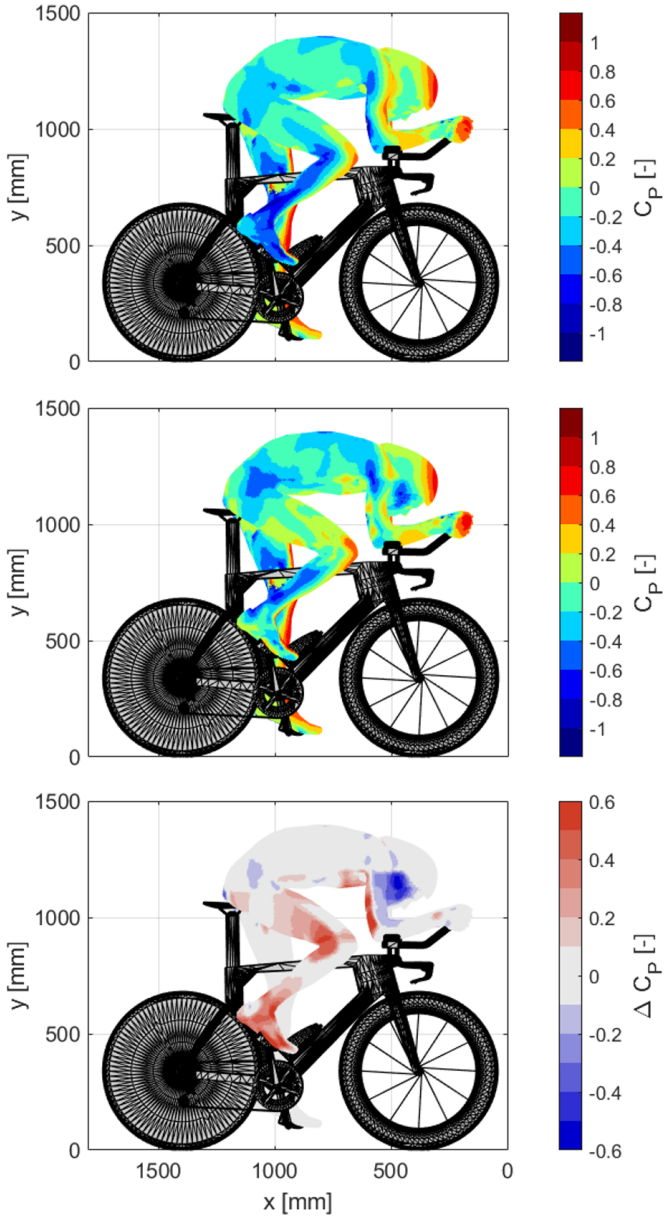

Figure 7.16: Comparison of surface pressure coefficient on the athlete's RHS. (Top) features the results presented in Section 7.2.2. (Mid) shows pressure distribution obtained with full integration of the RHS, as illustrated in Figure 7.15 (d). (Bottom) visualizes the pressure difference $\Delta C_P = C_P(d) - C_P(b)$.

(d) are compared to the reference result, indicating the variability of the resulting surface pressure with the applied change in boundary condition. The results are graphically compared for case (d) in Figure 7.16.

Pressure differences are predominant only on the far-side with respect to the side where pressure integration is started (RHS for case (d); and LHS for case (c)), as the integration path to reach the far-side is significantly longer compared to the reference case. As such, the pressure differences on the extremities (legs and arms) are larger as compared to the athlete's back or helmet, which are closer to the median plane. Furthermore, it is seen that there is no clear bias, but both, higher pressure (red) is observed on the right leg and the downstream facing side of the upper arm, and lower (blue) surface pressures are seen on the right hip, the upstream facing upper arm and the right-hand-side of the face and helmet. Lastly, the statistical distributions from both cases (LHS case (c) and RHS case (d)) are combined in a histogram of the pressure variation $\Delta C_P = C_{P_i} - C_{P_{ref}}$ in Figure 7.17.

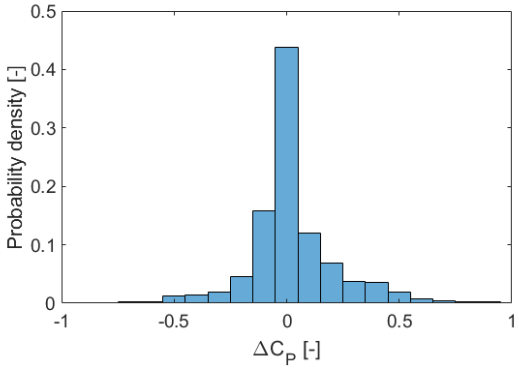

Figure 7.17: Histogram of pressure differences, taking into account the LHS variations for the case shown in Figure 7.15 (c) and the RHS for the case shown in Figure 7.15 (d).

The data in Figure 7.17 reveals a mean delta of $3\,\%$ in C_P, with a root-mean-square value of $23\,\%$, which corresponds approximately with the hypothesized uncertainty of $0.2C_P$ following the scaling between sphere and cyclist-experiment as shown in Table 7.2, thereby confirming the *a-priori* uncertainty estimate above.

7.3. Conclusion

The robotic volumetric PIV system introduced in this thesis (Chapter 3) is applied in a full-scale, volumetric velocimetry study of a time-trialling cyclist mannequin. An unprecedented ensemble of 450 time-resolved volumetric PIV acquisitions composes the time-averaged velocity field on a $2\,\mathrm{m}^3$ domain around the cyclist replica. The observed flow topology compares well to available literature and adds information in the regions near the athlete's body, where the effect of changing posture or specific garments are more pronounced.

Subsequently, the obtained velocimetry data is utilized to evaluate the pressure

distribution on the athlete's body, following the methodology introduced in Chapter 5. The pressure evaluation by robotic volumetric PIV is particularly well suited to such applications, given the model complexity and the use of a mannequin wearing sports garment. The 3D surface pressure data complements the velocimetry data, to further understand the flow behaviour, and to pinpoint areas of high pressure loads. The uncertainty analysis of the surface pressure distribution indicates that the results are accurate within $0.2\,C_P$.

8

Sailing in cycling: bicycle wheel aerodynamics

Cycling is not rocket science.

Jens Voigt

The importance of aerodynamics in competitive cycling is indisputable and has been introduced in Chapter 7. Whereas the athlete presents the dominant source of aerodynamic resistance, the wheels contribute to approximately 10 % of the total aerodynamic drag at road racing speeds. Logically, state-of-the-art bicycle wheels are aerodynamically optimized, and scientists and manufactures have been quantifying the forces on bicycle wheels in various wind tunnel campaigns. The flow topology around a bicycle wheel, however, is largely undocumented in literature, especially if considering experimental studies only.

In this chapter the robotic volumetric PIV system is utilised to study the flow near an isolated cycling wheel in crosswind. The velocimetry data is scrutinized to estimate the pressure distribution on the wheel's rim and tire. Such pressure evaluations on spinning wheels are practically infeasible using classical instrumentation. As such, the application to a bicycle wheel presented here, demonstrates the potential of the proposed technique also for other applications containing spinning objects. Additionally, high-resolution planar PIV data is acquired. Correlating balance and velocimetry data confirms that a bicycle wheel in crosswind behaves similar to an airfoil at incidence, meaning that the wheel can —similar to a sail —actively reduce the aerodynamic resistance.

Jux C, Sciacchitano A and Scarano F. Aerodynamics of a cycling wheel in crosswind by coaxial volumetric velocimetry, *14th International Symposium on PIV*, Illinois, USA, August 1-4 (2021)

Jux C, Sciacchitano A and Scarano F. Tire dependence for the aerodynamics of yawed bicycle wheels, (submitted to) *Journal of Wind Engineering and Industrial Aerodynamics*.

The significance of aerodynamics in cycling has been discussed in Chapter 7. The bicycle wheels contribute to about 10% of the total aerodynamic drag (Greenwell et al., 1995), making them a crucial item in any cycling-performance optimization.

Focusing on road cycling, a rider is exposed to a variety of wind conditions, affecting the perceived yaw angle. The concept of wind-averaged drag (WAD, Cooper, 2003) accounts for the statistically anticipated yaw-angle distribution experienced by a ground vehicle. The higher the vehicle velocity, the smaller the maximum yaw angle perceived for a given wind speed. For professional road cycling speeds, the probability of exceeding 20° yaw angle is reported to be less than 10% (Barry, 2018; Brownlie et al., 2010). Vice versa, a rider spends 90% of the time at yaw angles below 20°.

Aerodynamically designed wheels used in road racing (thus, excluding time-trial and triathlon specific multi-spoke and disc wheels) are characterized by a 40-80 mm deep rim section, that connects via a multitude of thin spokes to a cylindrical hub. In comparison to classical, shallow rim profiles, the deep-section rim fulfills two functions: on one hand, it streamlines the tire shape, effectively reducing the tire-rim drag coefficient. On the other hand, it generates —similar to a sail —a side force perpendicular to the relative wind direction. A component of this force points in the riding direction, effectively "pulling" the wheel forwards for non-zero yaw angles. The latter effect is known as the *sail-effect* in literature, and it can result in a negative net resistive force for wheels at high yaw angles (Barry et al., 2012; Lukes et al., 2005; Malizia and Blocken, 2020a).

Designing a wheel for optimal performance is, however, not solely about minimizing (wind-averaged) drag. As Barry et al. (2012) point out, large side forces on wheels yield strong steering moments and can be a concern of maneuverability. Similar concerns can be expressed when discussing the stall behavior for wheels at large yaw angles.

In addition to the rim-geometry, the aerodynamic characteristics of a wheel depend on the interaction of rim and tire. Crane and Morton (2018) investigate this interaction with specific attention to tire width relative to the rim. While focusing on tire width, Crane and Morton (2018) already speculate that "leading edge geometry", i.e. tire geometry, alters the stall angle of a given wheel. The hypothesis is supported by data from wheel manufacturers, claiming that the tire's surface texture conditions the boundary layer development for the flow over the wheel, and that forcing laminar-to-turbulent boundary layer transition on the tire is essential for drag minimization of bicycle wheels at large yaw angles (Cant, 2014).

To test the above hypothesis, this chapter presents wind tunnel force and velocimetry measurements on a state-of-the-art bicycle wheel, comparing its aerodynamic characteristics when fitted with a regular, lightly textured tire; a smooth tire; and a smooth tire with a tripping element on its tread.

In the discussion of cycling wheel aerodynamics it is common practice to study wheels in isolation. Experimental studies in the field focus predominantly on balance measurements (e.g. Greenwell et al., 1995; Tew and Sayers, 1999; Zdravkovich, 1992), whereas flow topology data remains undocumented to the best of the author's knowledge. Such data is readily available from computational fluid dynamics

(CFD) analysis, which presents an active line of research in the context of cycling wheel aerodynamics (Godo et al., 2010; Malizia and Blocken, 2020b; Malizia et al., 2019). Authors developing numerical tools for the aerodynamic analysis of cycling wheels, however, have to rely on the experimentally documented force data for validation of their simulations. This practice becomes problematic when reported drag measurements for the same wheel show variations of up to 300%, as observed by Godo et al. (2010). The large force sensitivity is ascribed to variations in the experimental setup, including tire choice, free-stream turbulence, wheel support design and wind tunnel blockage.

In view of the gaps and discrepancies in literature, the present work provides an experimental analysis of the flow topology on a state-of-the-art bicycle wheel in crosswind and its dependence on tire surface properties. The change in flow topology with yaw angle and tire selection is documented. The acquired data is then used to scrutinize the hypothesized sail-effect theory.

8.1. Reference frames and terminology

Prior to presentation of the experimental apparatus and procedures in the subsequent section, definitions of the relevant variables and coordinate systems are provided. The given definitions largely follow the work of Tew and Sayers (1999).

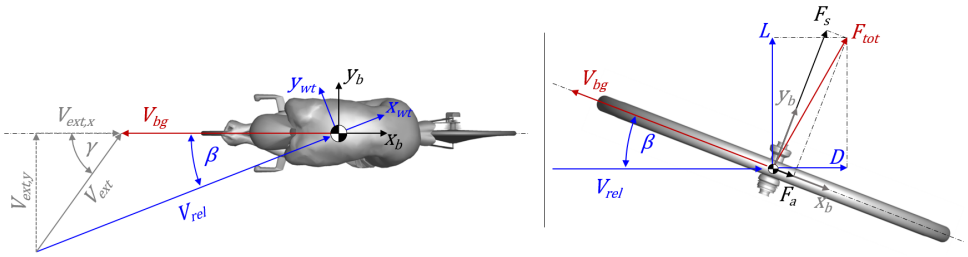

Figure 8.1: Definition of axes systems, flow angles and velocities for a cyclist moving at a velocity V_{bg} relative to the ground (left). Relation of forces in wind and bike reference frames, illustrated on a bicycle wheel in top view (right).

Figure 8.1 (left) shows a cyclist moving at a velocity V_{bg} relative to the ground. The direction of travel defines the main reference frame $\mathbf{X}_b$, pertaining to the bicycle, with the x-axis pointing opposite to the motion direction. In an external environment, the wind velocity V_{ext} and its direction (γ, the crosswind angle) relative to the cyclist's direction of motion are relevant for the definition of the aerodynamic problem. The vector difference of external wind V_{ext} and bicycle ground velocity V_{bg} determines the relative wind velocity V_{rel} experienced by the cyclist. The angle between the cyclist's motion axis and the relative wind velocity defines the yaw angle β. Let us define a second coordinate system $\mathbf{X}_{wt}$ whose x-axis is aligned with V_{rel}. The subscript *wt* signals that this reference frame pertains to the wind-tunnel when testing in a laboratory environment, where the x-axis is always aligned with the relative wind direction.

Figure 8.1 (right) illustrates the resistive and lateral forces acting on a bicycle

wheel. Classically, the drag force D acts parallel to the free-stream direction defined by V_{rel}, whereas the lift force L points perpendicular to it, combining to the resultant force F_{tot}. More relevant for a cyclist, however, are the force components in the reference frame $\mathbf{x}_b$ connected to the direction of motion. The side force F_s and the axial force F_a are expressed as geometrical projections of L and D:

$$F_a = D\cos(\beta) - L\sin(\beta) \tag{8.1a}$$

$$F_s = D\sin(\beta) + L\cos(\beta) \tag{8.1b}$$

It follows that a situation can arise in which $L\sin(\beta) > D\cos(\beta)$, resulting in a thrusting force which supports the cyclist's motion —the sail effect. In the remainder of this work, forces are always provided and discussed in the bicycle reference frame.

8.2. Experimental apparatus and procedures

Wind tunnel measurements are conducted at TU Delft's Open Jet Facility, similar to the cyclist study presented in Chapter 7. All measurements are executed at a freestream velocity of 12.5 m/s (45 km/h). The turbulence intensity in the test section, with a large-scale PIV seeding system installed in the settling chamber, is reported with 0.8% by Giaquinta (2018). An overview of the test setup is provided in Figure 8.2.

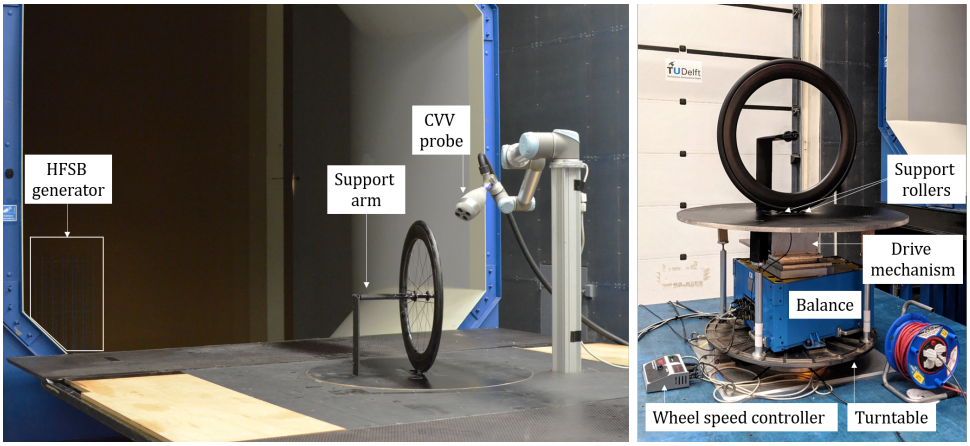

Figure 8.2: Experimental setup in the Open Jet Facility (left). Details of the mechanical systems installed in the wind tunnel, with surrounding floor plates removed (right).

8.2.1. Wheel model and mechanical setup

A *DT Swiss ARC 1100 Dicut DB 62* front wheel is installed in the test section. The 28" (700 mm diameter with tire fitted) wheel features a 62 mm deep and 27 mm wide carbon rim. While the wheel is designed to run with disc brakes, no brake discs were installed during the wind tunnel test. The clincher rim is fitted with a 25 mm

tire, inflated at 7 bar. A *Continental GP 5000* tire featuring a mild periodic surface pattern is chosen as a baseline tire, which is compared to a slick tire, a *Continental GP TT*. The difference in tire profile is shown in Figure 8.3. The grooved texture element on the baseline tire is approximately 35 mm long, and 12 mm wide, with a 35 mm gap along the circumference between two subsequent elements.

Because new tires were fitted for the measurements, the tires had a small production-seam in the tread centre, as indicated in Figure 8.3(b). This seam did not wear off during the wind tunnel test, and therefore, the aerodynamic effect of the seam was assessed separately on the slick (GP TT) tire. For this assessment, the balance and planar PIV measurements are repeated after sanding the seam down. This means, that the volumetric PIV data presented in Section 8.3 includes the aerodynamic effect of the seam, however. Because the production seam is hypothesized to function as a tripping element, triggering laminar-to-turbulent boundary layer transition, it is also referred to as tripping element in the remainder.

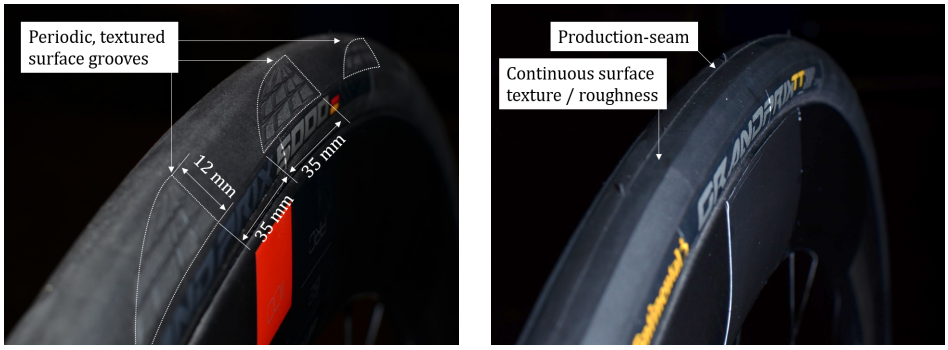

(a) Baseline tire, Continental GP 5000, with approximate indication of texture element size.

(b) Option tire, Continental GP TT

Figure 8.3: Photographs of the tested tires mounted on the wheel.

The wheel is connected to the support structure using a standard 12×100 mm through axle. The single-sided support holding the wheel from the left hand side is designed to enhance optical access for the velocimetry measurements.

The tire rests on two 70 mm diameter (60 mm width) rollers embedded in the wooden ground plate. The rearward roller is driven by a variable speed DC motor to control wheel rotation. The wheel rotational speed is kept constant at 348 rpm, matching a ground velocity (V_{bg}) of 12.5 m/s equal to the freestream velocity. Wheel rotational speed and freestream velocity are both maintained constant at all times, and only the yaw angle is adjusted during the measurements.

For the volumetric PIV campaign, the wheel branding is covered by black adhesive foil to limit background reflections in the PIV acquisition. A few circular (2 mm diameter) targets on the rim serve as reference markers to locate the model in the PIV data, as well as a means to verify the wheel rotational speed. For the planar PIV measurements, the rim is painted matt black.

8.2.2. Force measurement system

The wheel model including the mechanical support and drive mechanism is installed on a 6-axis force balance situated underneath the ground plate. The balance acquires data at a frequency of 2 kHz, and its accuracy is reported with 0.06% (0.15 N) of its full 250 N load capacity (Alons, 2008). Force data is acquired and averaged over 20 s. The balance is placed on a turntable that controls the yaw angle. As such, the force measurements delivered by the balance system pertain to the bicycle wheel reference frame ($\mathbf{x}_b$). The yaw angle is varied in a range of β between -24° and +24° in steps of 2°. The arrangement of the components is illustrated in Figure 8.2 (right).

Prior to force measurements on the wheel, the forces on the isolated support are recorded for all yaw angles of interest. This data is subsequently subtracted from the measurements with the wheel installed to identify the forces generated by the wheel only.

8.2.3. Velocimetry systems

The 3D and 2D PIV systems are introduced here, respectively.

Volumetric PIV

Three-dimensional particle image velocimetry data is acquired by a *LaVision MiniShaker Aero* CVV probe, recording image quadruples of 640×476 px^2 at a frequency of 821 Hz. 16,400 images are acquired for each yaw angle, equaling an acquisition period of 20 s. The velocimeter is mounted on a *Universal Robots UR5* robotic arm, allowing to keep a similar imaging position and distance relative to the wheel for all yaw angles.

Neutrally-buoyant helium filled soap bubbles (HFSB, Scarano et al., 2015) of 300 - 500 μm diameter serve as tracer particles, which are provided by a 0.6×0.8 m^2 seeding rake installed in the wind tunnel settling chamber. The measurement domain spans a 30×20×20 cm^3 volume near the most upstream section of the wheel. Data is acquired on the leeward, respectively, the suction-side of the rim.

The wheel rotation results in unsteady reflections which are filtered from the particle images by means of a Butterworth frequency filter (Sciacchitano and Scarano, 2014), followed by a directional minimum filter on a local 5×5 px^2 kernel. Preprocessed images are analyzed by the 3D Lagrangian particle tracking algorithm Shake-The-Box (STB, Schanz et al., 2016) as implemented in Davis 10.1. The scattered STB tracks are subsequently ensemble averaged by a linear fit of the velocity data in ellipsoidal cells of 6×6×30 mm^3 ($x \times y \times z$), as detailed in Chapter 2. Anisotropic cells are selected to enhance spatial resolution in the horizontal directions, where velocity gradients are anticipated to be stronger as compared to the vertical direction, for the section of the wheel imaged by the velocimetry system. The grid spacing is maintained constant at 1.5 mm in all axes.

Based on the time-averaged velocity data, the static pressure is evaluated following the dual-model approach presented in Chapter 5. In the region of irrotational flow, Bernoulli's equation provides the local pressure and the necessary Dirichlet condition for the subsequent spatial integration of the pressure gradient in the ro-

tational flow domain. Lastly, the static pressure in the flow is mapped onto rim and tire surface, using the local pressure gradient information.

Planar PIV

Planar (2D-2C) PIV data is acquired in a horizontal plane at hub-height, imaging a 20×17 cm^2 field of view. The images capture the most upstream section of the wheel, and the flow over the leeward side of tire and rim. The PIV camera, a LaVision sCMOS 16-bit camera with a $2,560 \times 2,160$ px^2 sensor and a 35 mm lens, is installed on the turntable, imaging the flow past the wheel through a Plexiglas window in the floor. Therefore, the camera is at all times aligned with the wheel's riding direction. A top view showing the relative position of wheel and camera is provided in Figure 8.4.

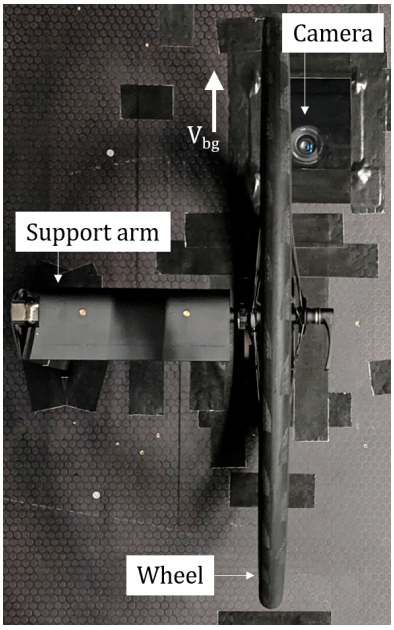

Figure 8.4: Wheel in top-view with PIV camera visible through window on the top right.

At each yaw angle, 300 image pairs are acquired at a frequency of 15 Hz, with a time separation of 70 μs between two frames. Illumination is provided by a Quantel Evergreen 200 Nd:YAG laser (532 nm wavelength, 200 mJ maximum pulse energy). A Safex fog generator seeds the flow with water-based micron sized droplets of approximately 1 μm diameter. The combination of a 5 Mpx camera with micron sized particles allows to study the flow field in the selected plane with enhanced spatial resolution compared to the volumetric setup above.

Raw PIV images are pre-processed using an anisotropic diffusion filter (Adatrao and Sciacchitano, 2019), which effectively filters the continuous light reflection on tire and rim surface, as well as the occasional sharp reflection resulting from a spoke

passing the laser sheet. An example of a raw and processed image is provided in Figure 8.5.

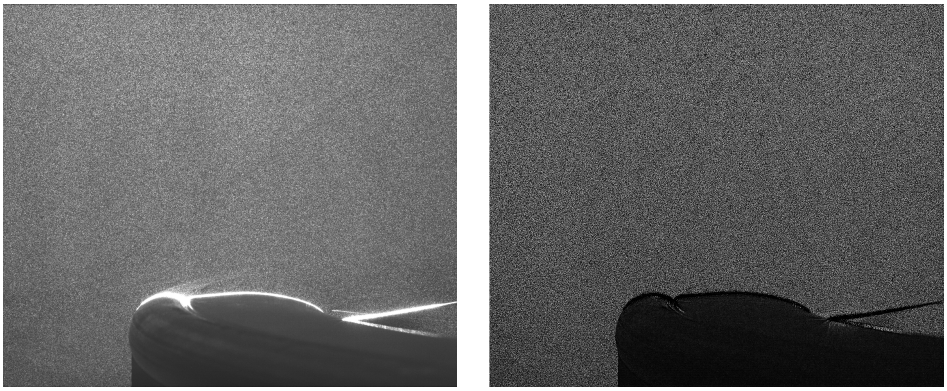

(a) Raw (b) Pre-processed

Figure 8.5: Example of planar PIV image, taken through a window in the floor.

8.3. Results and discussion

The analysis of the measurement data starts with the force measurements. Subsequently, the velocimetry data is analysed, leading to the discussion of the pressure distribution.

8.3.1. Force measurement

Figure 8.6 displays the force measurements versus yaw angle in the bicycle reference frame for the three tested tire options.

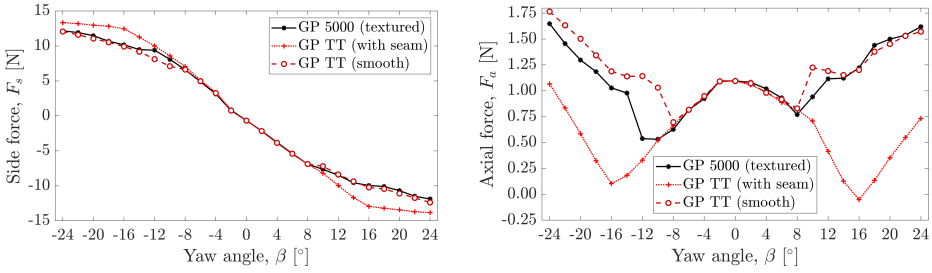

(a) Lateral force (b) Axial force

Figure 8.6: Force measurements on the isolated wheel versus yaw angle.

For moderate yaw angles within $\beta \leq 8°$ the recorded forces are equivalent for all tested tires. In this range, the lateral force reduces by approximately $0.85\,\mathrm{N/^{\circ}}$.

Interestingly, the angle of zero side force is slightly negative at about $-0.8°$. It is noted, however, that neither the wheel nor the support design are fully symmetric, giving rise to a non-zero lateral force in straight ahead conditions.

For yaw angles exceeding $8°$ magnitude, the linear behaviour in the lateral force is only continued for the smooth tire with the production seam, i.e. the tire with the tripping element. For this wheel-tire combination, the linear behaviour continues until $16°$ yaw, where the slope tapers off. For the tires without the production seam, the lateral force magnitude increases at a significantly reduced rate for yaw angles in excess of $8°$.

The differences observed in the lateral force translate also into the axial force readings. For moderate yaw angles within $8°$, the tires behave similarly, showing maximum resistance at (near) zero yaw angle. For small non-zero yaw angles the aerodynamic resistance decreases. For yaw angles in excess of $8°$, the resistive force keeps decreasing only for the slick tire with the production seem, i.e. the tire with the tripping element. The smallest resistive force for this tire is recorded at 16° yaw, where a resistance of -0.05 N is measured. Beyond $16°$ a steep increase in axial resistance is observed. Such increase in axial force, along with a stagnating lateral force is signifying that the flow over the wheel is separated, which is confirmed later by the velocimetry data.

If the production seam is removed from the slick tire, the axial force reduction stops already at $8°$, indicating that flow separation occurs as much as $8°$ earlier when comparing to the tire with the tripping element. The textured tire behaves similar to the slick tire. Only for negative yaw angles the increase in resistive force is observed below $-12°$ for the textured tire, as compared to $-8°$ for the slick tire.

The above force data confirms the sail-effect hypothesis: at high yaw angles, the wheel is able to generate a thrusting force, albeit small in magnitude. Importantly, the extent of the resistance reduction is observed to be strongly dependent on the tire surface characteristics. For a better understanding of the tire dependence, the velocimetry data is compared in the following.

8.3.2. Time-average velocity field

The flow topology analysis is started by the planar PIV data, displaying the flow field in a horizontal plane at hub-height. The data shown in Figure 8.7 contains the velocity field upstream and past the leeward (suction) side of the rim. The velocity contours show the normalized axial velocity component in the bicycle wheel reference frame $\mathbf{x}_b$,

$$u_b^* = \frac{u_b}{u_{b_\infty}} = \frac{u_b}{u_{wt_\infty} \cos(\beta)} \tag{8.2}$$

where the subscript '∞' indicates free-stream conditions upstream of the wheel. The velocity contours are complemented by streamlines in the 2D planes.

At $0°$ yaw the three tire options behave equivalently: the flow stagnates on the tread centre, followed by an acceleration on the side of the tire and the rim. The region of accelerated flow is characterized by two local maxima; one on the side of the tire and a second one near the thickest point of the rim. Thus, a local region

of adverse pressure gradient must be anticipated close to the rim-tire junction. Downstream of the rim a region of reverse flow is observed.

At 8° yaw the three tire options still behave similarly. The stagnation point has rotated towards the windward side. The region of accelerated flow is larger and more intense. Compared to straight ahead conditions with two local velocity maxima, only one region of maximum velocity is visible, which is located near the tire-rim junction. The recirculating flow in the rim's wake is slightly more pronounced, and similar to the other features is rotated counter-clockwise as compared to the 0° case.

The first substantial difference between the tires is observed at 12° yaw, where the flow past the wheel with the smooth tire is fully separated, compared to the same tire with the tripping element where the flow is mostly attached. The flow over the wheel with the textured tire is also separated, however, the separation zone is smaller when compared to the fully smooth tire. Considering the velocity fluctuations (u'_{rms}) for this yaw angle (shown in Figure 8.8), one finds that the velocity variation near the rim-tire junction is stronger and distributed over a larger area for the textured tire, as compared to the smooth tire which features a confined region of peak velocity fluctuation near the widest section of the tire. This suggests that the smooth tire features a well-defined flow separation point, whereas the textured tire features a varying point of separation that oscillates approximately between the widest points of rim and tire. The smooth tire with the tripping element on its tread shows an elongated zone of high velocity fluctuations in vicinity of the rim, suggesting the presence of a thick, turbulent boundary layer. Based on this observation, it is concluded that,

1. The production seam on the smooth tire does indeed trigger the laminar-to-turbulent boundary layer transition. The turbulent boundary layer remains attached to the rim-tire profile.

2. Without the production seam, the smooth tire features a laminar boundary layer, that separates from the tire at its widest section.

3. The grooved elements on the textured tire yield an oscillating separation point. It is therefore speculated that the roughness elements on the textured tire, similar to the tripping element on the smooth tire, trigger local boundary layer transition and thereby, push the flow separation point further downstream. Between the periodic roughness elements the tire behaves similar to the smooth tire, featuring a "leading-edge" separation. This hypothesis can be confirmed by acquiring time-resolved velocimetry data with a high-speed PIV system.

The observed flow field correlates well with the force data in Section 8.3.1, where at 12° it was found that the smooth tire with tripping element features by far the lowest resistance, followed by the textured tire, and lastly the fully smooth option.

At 16° yaw, the smooth and textured tire behave equivalently, with both options featuring a large zone of recirculating flow, starting upstream of the tire-rim-junction. The u'_{rms} contours for the two tires are now also similar, indicating that

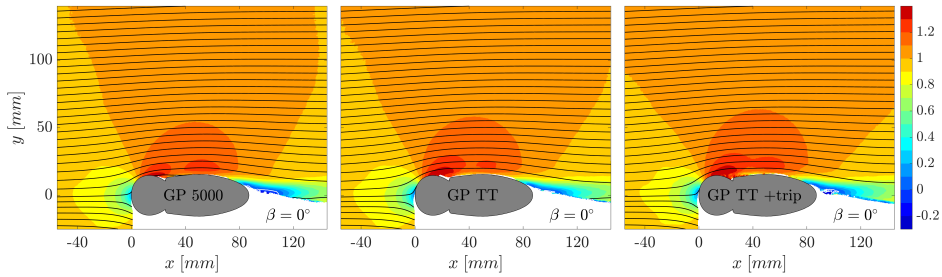

(a) β = 0°

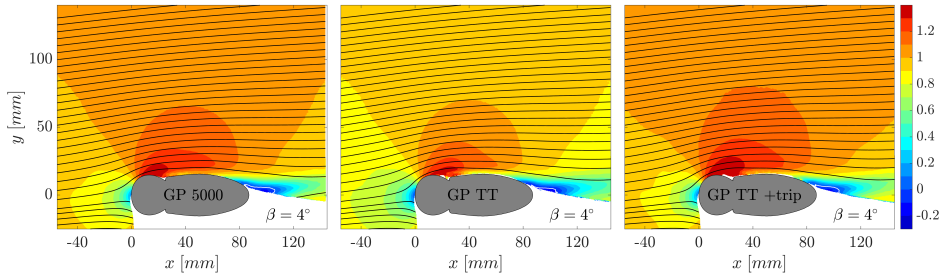

(b) β = 4°

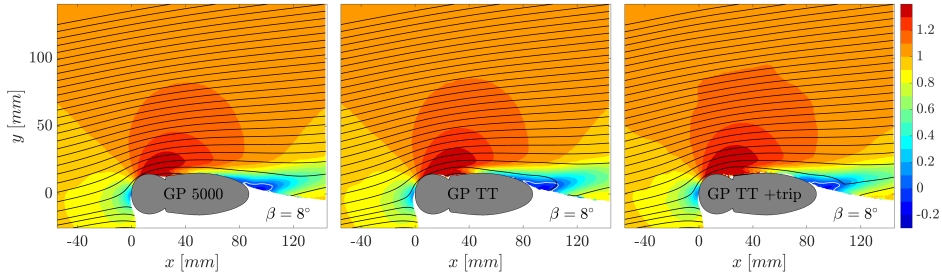

(c) β = 8°

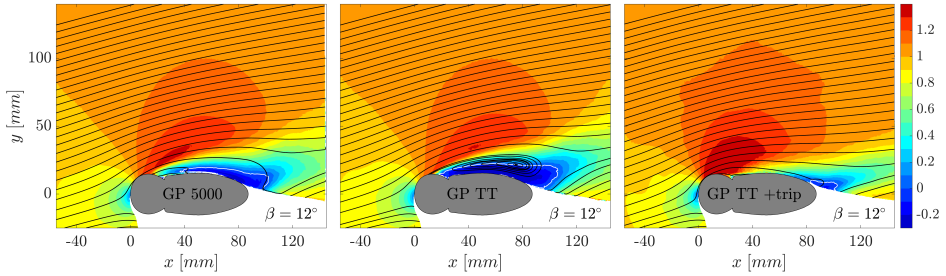

(d) β = 12°

Figure 8.7: Time-average velocity contours in xy-planes at hub height (z = 342.5 mm), along with 2D surface streamlines. Velocity contours show the normalized axial velocity component in the bicycle wheel reference frame. (Left) Baseline tire, GP 5000. (Centre) Option tire, GP TT. (Right) Option tire including tripping element (GP TT with production seam). (*Continues on next page*)

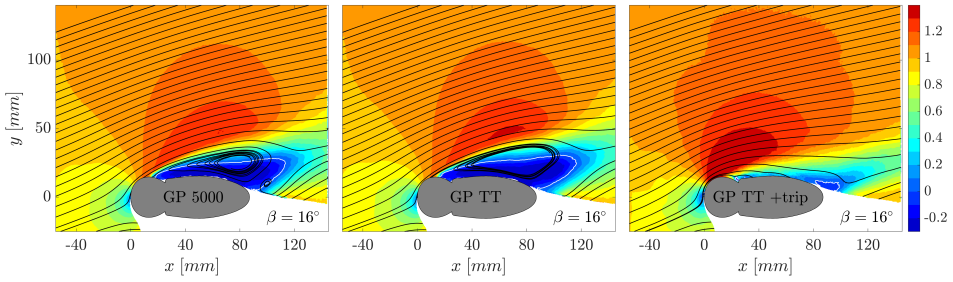

(e) β = 16°

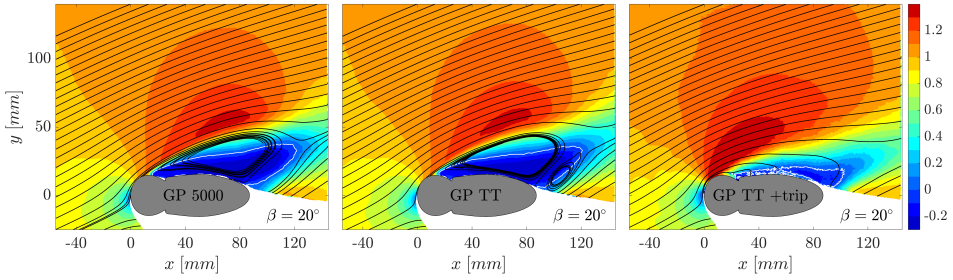

(f) β = 20°

Figure 8.7: *(Continued)* Time-average velocity contours in xy-planes at hub height (z = 342.5 mm), along with 2D surface streamlines. Velocity contours show the normalized axial velocity component in the bicycle wheel reference frame. (Left) Baseline tire, GP 5000. (Centre) Option tire, GP TT. (Right) Option tire including tripping element (GP TT with production seam).

both tires feature a well-defined flow separation point. The smooth tire with tripping element, instead, features an attached flow over the tire and rim.

At the largest considered yaw angle of $20°$ all three tire options show a clear flow separation. The separated zone on the smooth tire with tripping element is still significantly smaller compared to the other two options.

8.3.3. Pressure data

Following the analysis of the velocity data, we briefly investigate the pressure distribution over tire and rim profile. This analysis is based on the volumetric PIV data, that allows evaluating the 3D pressure gradient, unlike the planar PIV data which cannot be used to evaluate the velocity (gradients) in the out-of-plane direction appearing in the pressure gradient. The analysis is limited to the slick tire including the production seam (tripping element), which was seen to benefit most from the indicated sail-effect compared to the other tires. Similar to the previous assessment, the analysis is initially carried out in a horizontal xy-plane at hub height.

Figure 8.9 shows the pressure profiles on the leeward side of the wheel for β = [0, 8, 16]°. The pressure profiles are characterized by a steep pressure reduction over the upstream tire section. As the yaw angle increases, the pressure reduction

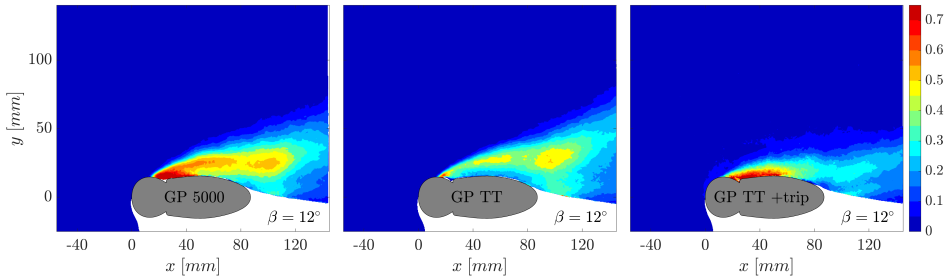

(a) β = 8°

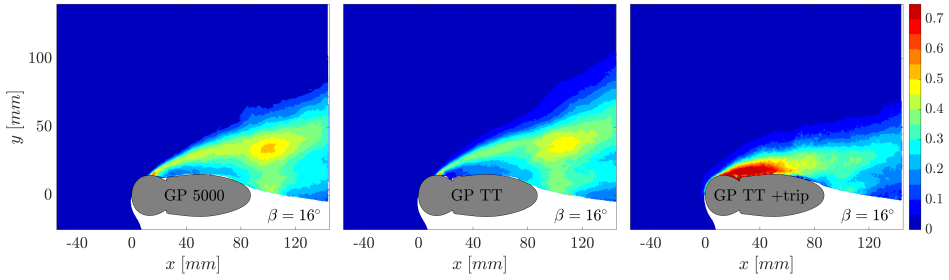

(b) β = 12°

Figure 8.8: Statistical velocity fluctuations u'_{rms} in xy-planes at hub height (z = 342.5 mm). Contours are normalized by the axial freestream velocity component in the bicycle wheel reference frame. (Left) Baseline tire, GP 5000. (Centre) Option tire, GP TT. (Right) Option tire including tripping element (GP TT with production seam).

gains in magnitude, signifying greater suction with increasing yaw angle. The location of minimum C_P moves downstream as the yaw angle grows. At 0° yaw the minimum pressure of C_P = -0.7 is recorded at x/c = 0.06, before approaching an approximately constant value of C_P = -0.5 further downstream. At 8° yaw instead, the minimum pressure coefficient exceeds a value of -1, and it is obtained slightly further downstream (x/c = 0.13). Increasing the yaw angle further to 16°, the pressure coefficient drops to a minimum of C_P = -1.75 at x/c = 0.26, followed by an adverse pressure gradient approaching C_P = -0.5 at x/c = 0.6.

Complementing the above pressure profiles in the wheel center plane, 3D iso-surfaces of pressure coefficient are shown for the three selected cases in Figure 8.10, along with axial velocity contours on the upper and lower boundary of the measurement volume. For each case, two iso-surfaces are plotted: the first, at C_P = 0.35 (red) indicates the volume of increased pressure resulting from the flow deceleration upstream of the wheel. The second, at C_P = -0.6 (blue) is selected to visualize the volume of reduced pressure induced by the flow acceleration alongside the wheel. Comparing the latter iso-surface for the three yaw angles confirms the growth of the low-pressure region with increasing yaw angle, signaling a likewise increase in side force.

The observed trend is qualitatively in line with the force data presented in Sec-

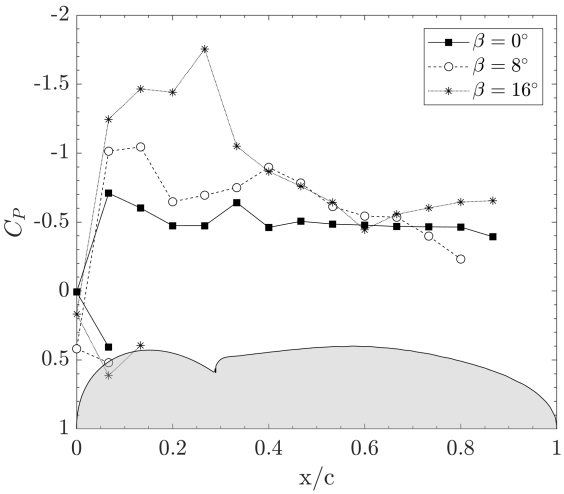

Figure 8.9: C_P profiles over the tire-rim surface at hub-height (z = 342.5 mm) for the option tire (GP TT) with tripping element (production seam).

tion 8.3.1 which indicated a monotonically increasing side force magnitude with increasing yaw angle in this range. It further supports the theory that the tire-rim profile indeed behaves like an airfoil at incidence, thereby making the wheel work like a sail.

8.3.4. Practical implications

The force-, velocimetry-, and pressure-data analysis has confirmed that the tire surface structure is an important design parameter when attempting to minimize the aerodynamic drag of a road bicycle wheel. The production seam on the tread of the smooth tire worked as an effective element to trigger laminar-to-turbulent boundary layer transition. The latter is found to be essential for maintaining attached flow over the tire-rim section at yaw angles exceeding $8°$.

It is clear that the production seam cannot function as a boundary layer tripping device in real cycling conditions, given that it rapidly wears off when ridden on tarmac under a rider's load. The observations highlight that appropriate modelling of the tire characteristics is essential for obtaining realistic results when studying bicycle wheel performance through computational fluid dynamic (CFD) simulations. In the wind-tunnel environment it is shown that the potential gain that can be realized when tripping the boundary layer on the tire is large: the stall angle is increased as much as $8°$, reducing the wind averaged drag (Barry, 2018) by 33 % when considering a mean wind-speed of 3 m/s that follows a Weibull distribution ($k = 2$), and a riding velocity of 12.5 m/s. The texture of the baseline tire still yields a 8 % drag reduction relative to the fully smooth tire.

The flow topology comparison of smooth and textured tire at moderate yaw angle ($12°$) indicates that the grooved elements on the textured tire bear the potential

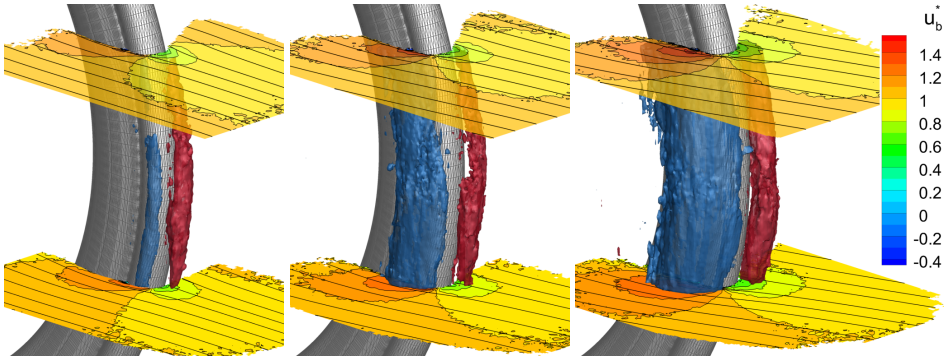

(a) β = 0° (b) β = 8° (c) β = 16°

Figure 8.10: Axial velocity contours in horizontal planes at z = [242.5, 442.5] mm along with 3D pressure iso-surfaces of C_P = 0.35 (red) and -0.6 (blue). Data shown for wheel fitted with option tire and production seam.

of delaying flow separation locally. Optimization of the texture elements for aerodynamic performance is therefore deemed to be essential, and should be considered by both, tire and wheel manufacturers. Likewise, reporting force measurements on a road bicycle wheel is only meaningful if the tire specifications are also provided.

8.4. Conclusion

The aerodynamic characteristics of a state-of-the-art road cycling wheel in cross wind have been assessed experimentally by means of force measurements, coaxial volumetric velocimetry and planar PIV. Specific attention is paid to the interaction of rim and tire, by comparing the wheel's behavior with changing tire surface texture. The resistive force on the isolated wheel is highest in straight ahead conditions ($\beta = 0°$). The aerodynamic resistance of the wheel is reduced as the yaw angle magnitude increases. Analysis of the velocimetry data confirms that the reduction in resistance measured by the force balance is indeed a consequence of the sail-effect, resulting from a substantial side-force on the wheel at yaw incidence. The benefit of this effect is limited by the stall angle of the tire-rim combination, which is found to depend significantly on the tire choice. A greater stall angle is obtained if the tire triggers laminar-to-turbulent boundary layer transition. For the tested tires differences of up to $8°$ in stall angle are obtained, that ultimately result in a 33 % difference in wind averaged drag for the considered 62 mm deep wheel.

9

Swimming hydrodynamics

I think goals should never be easy,
they should force you to work,
even if they are uncomfortable at the time.

Michael Phelps

Swimming is a fascinating sport for anyone who is excited by fluid dynamics. It is one of the few disciplines where the athlete's propulsive force is generated by the direct interaction of the human body with the surrounding fluid. Similar to professional cycling (Chapters 7 and 8), winning margins in professional swimming are slim: consider e.g., the recent men's 800 m freestyle final at the Tokyo 2020 (+1) Olympics where the four fastest finishers were separated by less than one second after more than 7 minutes of swimming. Minor improvements in swimming efficiency can consequently have a significant impact on the race result.

This chapter focuses on the propulsive force generated by a swimmer's hand, and its dependence on the thumb position. The study is carried out in a wind tunnel on a full-scale model of a swimmer's arm, using the robotic volumetric PIV system introduced in Chapter 3. Details on the experimental setup are presented in Section 9.1, followed by a discussion of the 3D flow topology in Section 9.2.

van den Berg J, Jux C, Sciacchitano A, van de Water W and Westerweel J. Robotic Volumetric PIV measurements of a full-scale swimmer's hand, *13th International Symposium on Particle Image Velocimetry*, Munich, Germany, July 22-24 (2019)

van den Berg J, Bazuin R, Jux C, Sciacchitano A, Westerweel J. and van de Water W, The effect of hand posture on swimming efficiency, *Exp. Fluids* **62**, 245 (2021)

First force measurements in terms of lift and drag on a swimmer's hand and arm have been reported over four decades ago already by Schleihauf (1979). Progress in numerical and experimental techniques has advanced the understanding of the propulsive force generation in swimming, and its dependence on hand orientation and configuration. Recent reviews by Takagi et al. (2016) and van Houwelingen et al. (2017a) acknowledge, nonetheless, that fully resolved flow simulations on a swimmer's hand will aid a further optimization of the propulsive force. Despite the capabilities of state-of-the-art computational fluid dynamics codes, such simulations require validation by experiments.

Selected experimental studies (e.g., Matsuuchi et al., 2009; Takagi et al., 2014) capture quantitative flow information by means of PIV, albeit mostly limited to 2D measurement planes. The geometric complexity of the human hand and its surrounding flow topology in swimming, however, demand a fully three dimensional flow analysis. The latter is challenged by the large range of spatial scales in the flow, encompassing the full hand and arm, as well as the flow through small gaps between the fingers, for instance. Resolving such small-scale details is vital, however, since maintaining a small finger spread is believed to yield noticeable improvement in propulsive force (Marinho et al., 2010; Minetti et al., 2009; Sidelnik and Young, 2006; van Houwelingen et al., 2017b, among others).

Focussing on finger posture, the thumb takes a special role. Takagi et al. (2001) demonstrate that a *closed* (adducted) thumb position provides a greater propulsive force as compared to an *open* (abducted) thumb posture. It remains unclear, however, how the thumb position affects the flow topology surrounding the hand.

In this chapter, the robotic volumetric PIV system introduced in Chapter 3 is used to investigate the influence of thumb position on the (time average) fluid mechanics around a swimmer's hand. While similar submersible PIV systems are available by now (Roettig et al., 2019), the measurements presented in this chapter were conducted in air, matching the Reynolds number anticipated in water by increasing the free-stream velocity. Adequately resolving the small-scale flow features poses a particular challenge for the robotic volumetric PIV system.

9.1. Experimental setup and procedures

Wind tunnel experiments are conducted at TU Delft's Open Jet Facility (OJF) which has, as previously introduced (Sections 3.3.1 and 7.1), a $2.85 \times 2.85\,\mathrm{m}^2$ exit cross-section. Measurements are carried out at $15\,\mathrm{m/s}$ in $20^\circ\mathrm{C}$ air, which in terms of Reynolds number, is equivalent to a velocity of about $1\,\mathrm{m/s}$ in water.

The hand model is a custom designed, additively manufactured (SLS, selective laser sintering) model, consisting of a fixed forearm that can be combined with different hand shapes. The hand and arm surfaces are designed using the open source *MakeHuman* software. The base-shape of the hand is equivalent to earlier studies on finger spreading by van Houwelingen et al. (2017b). The thumb position is subsequently altered using the *Blender* CAD software. Lastly, 16 pressure orifices are integrated into each hand model, enabling local surface pressure measurements.

Two hand models are compared: the first model features a thumb stretched away from the index finger. This model is referred to as the *abducted*, and *open*

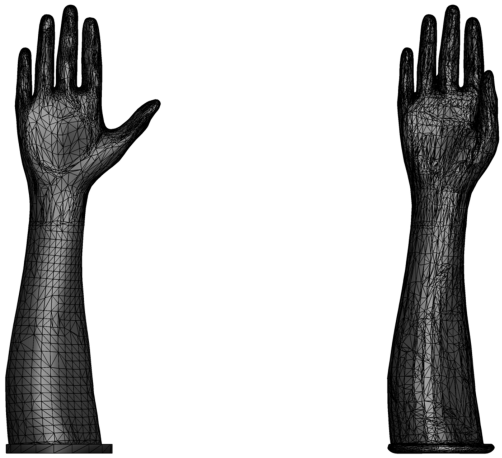

(a) Open (abducted) thumb. (b) Closed (adducted) thumb.

Figure 9.1: CAD geometry of the swimmer's arm and hand. Models measure 50 cm in height.

thumb. The second model features a thumb closed on the index finger, herein referred to as the *adducted*, or *closed* thumb model. The arm models are representative of a full-scale, male athlete, measuring 50 cm from elbow to finger-tip, with a 10 cm wide palm. The Reynolds number based on the palm width equals 10^5. Each hand model is studied at multiple yaw angles within a range of $\pm 40°$, where $0°$ corresponds to the hand's palm facing perpendicular to the free-stream. In this chapter, only the measurements at $0°$ yaw are considered.

The robotic volumetric PIV system is identical to the one described in Section 3.3.1, consisting of a *MiniShaker Aero CVV* probe, mounted on a *Universal Robots - UR5* robotic arm. Illumination is provided by a *Quantronix Darwin Duo* laser. Tracer particles are provided by a 10-wing, 200-nozzle HFSB seeding system installed in the wind tunnel settling chamber. The robot base is positioned at a lateral distance of 75 cm and 25 cm downstream of the hand, approximately 50 cm above the ground plate. This configuration allows for taking measurements from the top of the hand, thereby also imaging the space between individual fingers.

Images are recorded at a resolution of 640×476 px^2, at a rate of 821 Hz. $10,000$ images are taken per view, equivalent to an observation period of approx. 12 s. The full measurement domain is composed by 15 views for each orientation of the hand model, resulting in a total measurement volume of about 120 L. On average, 700 particles are tracked in each image by the Shake-The-Box (STB) algorithm.

Particle tracks are ensemble averaged using a first order polynomial fit inside cubical cells. Prior to averaging the velocity track data, outliers are removed by a two-stage, standard deviation based filter: in the first loop, any data deviating more than 7.5 m/s from the cell median is removed. Subsequently, all data beyond $2\sigma_u$ from the cell mean are also excluded. The linear bin size is varied between 5 and 40 mm, keeping a constant overlap of 75 %.

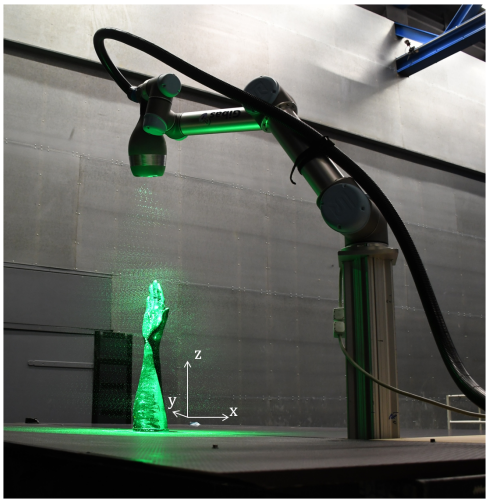

Figure 9.2: Experimental setup of the swimmer's hand measurements in OJF, with indication of coordinate axes.

9.2. Results and discussion

Identifying the "optimal" thumb position for swimming translates to the task of finding the hand posture that maximizes the swimmer's propulsive force. This problem can be solved by trial-and-error, measuring the aerodynamic loads on a variety of hand configurations. Knowledge of the flow topology, as accessible through PIV measurements for instance, enables to make an informed choice on a potentially improved hand posture. Prior to comparison of the two hand models, Section 9.2.1 addresses aspects of the measurement spatial resolution. Subsequently, the time-average flow topology is presented in Section 9.2.2 which leads to the comparison of the two thumb postures in Section 9.2.3.

9.2.1. Measurement spatial resolution

As indicated in the introduction to this chapter, the measurement spatial resolution takes a key role in this study, given that relevant geometrical features such as the finger spacing are on the order of a millimetre. The spatial resolution, herein quantified by the linear bin size of the ensemble averaging cell, is limited by the available number of samples. In the following the effect of the linear bin size on the mean velocity measurement is addressed on the open thumb model at $0°$ yaw.

Figure 9.3 illustrates the streamwise velocity distribution in a horizontal plane at mid-thumb height for a linear bin size of 20 mm. Extracting a velocity profile in the near wake ($x = 40$ mm) yields the distribution shown in Figure 9.3(b). The latter features two distinct velocity deficit regions: a large wake pertaining to the fingers, and a small wake downstream of the thumb. Comparing this velocity profile for linear bin sizes of 5, 10, 20 and 40 mm captures effects of random- and truncation-error that are associated with the spatio-temporal ensemble averaging process. For

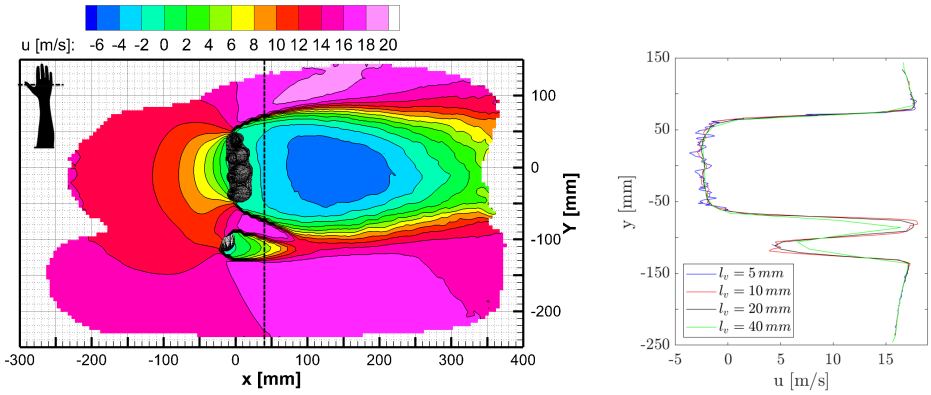

(a) xy-plane at $z = 390$ mm, bin size $l_v = 20$ mm. (b) u-profiles at $x = 40$ mm.

Figure 9.3: Effect of spatial resolution on the time-average streamwise velocity measurement u for the open-thumb hand model at $0°$ yaw.

the finest resolution of 5 mm the velocity measurement shows random fluctuations which are particularly well visible in the wake of the fingers. Such fluctuations point to a lack of statistical convergence. The latter is even more problematic in the thumb wake, where an insufficient number of tracers is recorded to compute the ensemble average for the 5 mm cell. The thumb wake further illustrates the effect of spatial modulation, where it is seen that the modulation of the velocity deficit is increasing with bin size. Comparing the minimum velocity in the thumb wake, one finds a velocity of 4.5 m/s considering a bin size of 10 mm which increases to 6.6 m/s upon lifting the bin size to 40 mm.

Similar to the above analysis, another velocity profile is extracted in the streamwise direction near the finger tips, following a path between the middle and the ring finger ($y = 0$ mm). The corresponding velocity distribution is shown in Figure 9.4. Basic fluid dynamic considerations (mass conservation) require that a fluid element passing between the fingers accelerates with respect to the inflow velocity. The velocity profiles in Figure 9.4(b) indicate that such acceleration is only partially resolved for a linear bin size of 10 mm and below. For larger bins, the mean velocity is modulated, and biased by the low velocity in the nearby finger wakes. Nonetheless, a bin-size of 20 mm is selected for the remaining analysis to ensure a statistically significant number of tracers is captured inside each averaging cell.

9.2.2. Time-average flow topology

This section illustrates the global flow features around the swimmer's arm on the open-thumb model at $0°$ yaw. The time-average, 3D streamlines near the hand are shown in Figure 9.5, where two large recirculation regions are identified: on the upper end, the flow downstream of the fingers and palm is recirculating; and likewise on the lower end the arm's wake shows a similar recirculating region. The flow to the side of these regions is characterised by an increased velocity.

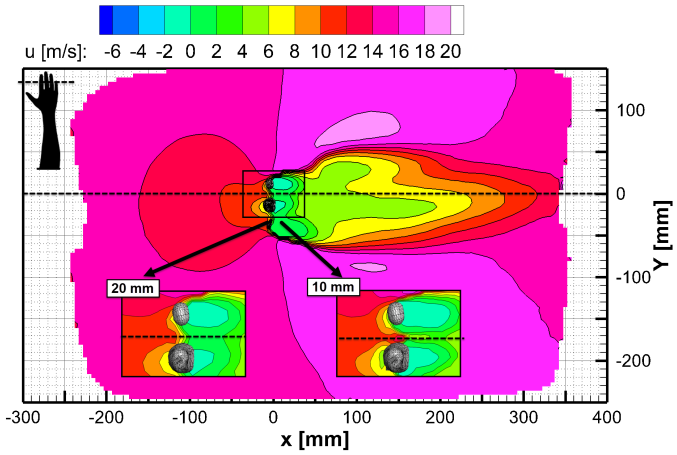

(a) xy-plane at $z = 470$ mm, bin size $l_v = 20$ mm.

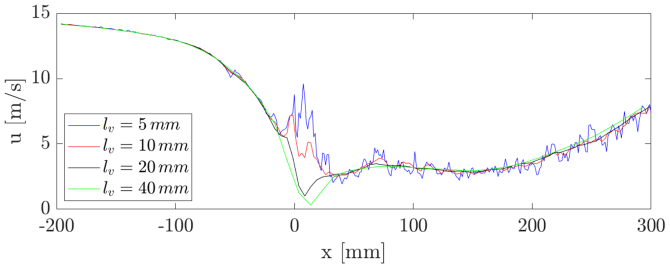

(b) Profiles at $y = 0$ mm.

Figure 9.4: Effect of spatial resolution on the time-average streamwise velocity measurement u for the open-thumb hand model at 0° yaw.

To compare the two recirculating zones, a vertical slice in the median plane ($y = 0$ mm) is extracted and the distribution of mean streamwise velocity u and the corresponding fluctuations u'_{rms} are plotted in Figures 9.6(a) and 9.6(b), respectively.

The recirculation zone in the hand's wake shows a clear rolling motion (over the y-axis), with a peak reverse velocity of -7 m/s at $y = 350$ mm. The lower arm's wake appears less structured, with a weaker recirculation, but higher velocity fluctuation magnitude as can be seen in Figure 9.6(b). It seems that the flow through the fingers feeds the hand's recirculation zone, resulting in a rather steady flow rotation; whereas the arm experiences a more unsteady wake similar to the wake of a cylinder.

Repeating a similar analysis in a horizontal plane at $z = 390$ mm yields the distributions shown in Figures 9.6(c) and 9.6(d). Hand and thumb wake are separated by an accelerated flow region. While flow stagnation on the thumb's upstream face is not resolved, Figure 9.6(c) features an asymmetric zone of decelerated flow

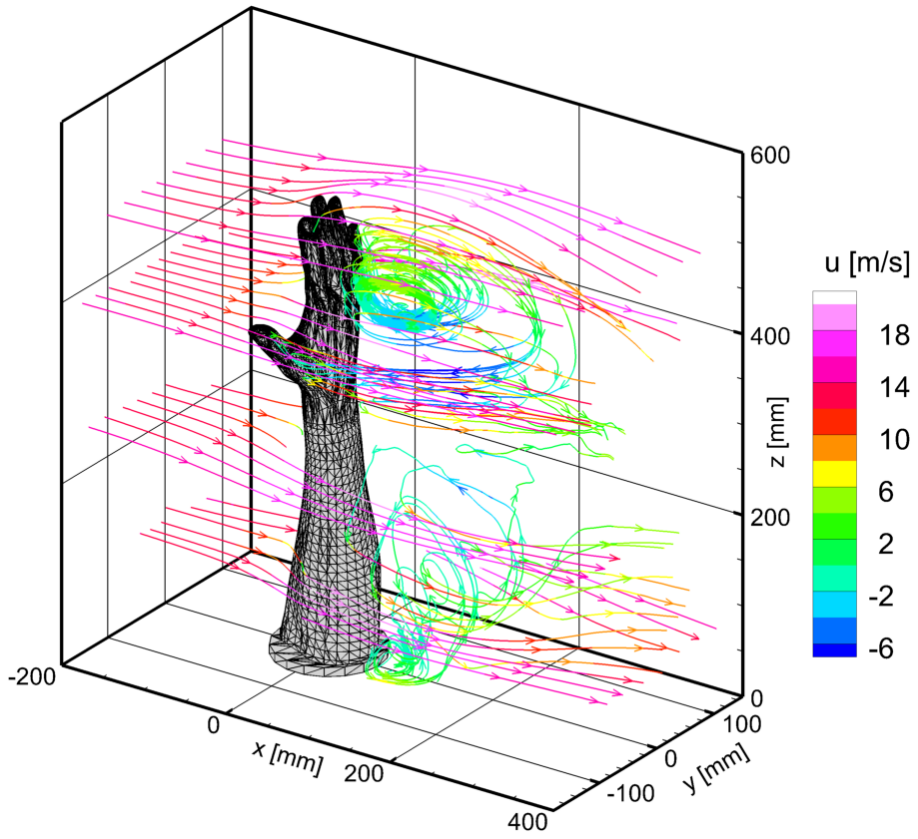

Figure 9.5: Time-average 3D flow topology visualization on the open-thumb hand model at $0°$ yaw, by means of streamlines colored by streamwise velocity u.

upstream of the hand, due to the increased gap between the thumb and the remaining fingers. Downstream, the shear layers of thumb and hand wake interact. Streamwise velocity fluctuations in this region reach a maximum approx. 90 mm downstream of the hand, where the streamwise fluctuation field suggests that the wakes are merged (Figure 9.6(d)).

While the above analysis considers the time-average flow field, the reader is reminded that the swimming stroke is a dynamic process which may affect the interaction of thumb and hand wake. The force study of Gomes and Loss (2015), for instance, suggests that there is a significant variation of forces when switching from steady to unsteady conditions.

9.2.3. Comparison of open- and closed-thumb model

Time-average streamlines on the open- and closed-thumb hand at $0°$ yaw are illustrated in Figure 9.8. On the closed-thumb hand, the flow that was previously seen to pass between thumb and index finger (see Section 9.2.2) has to pass around the

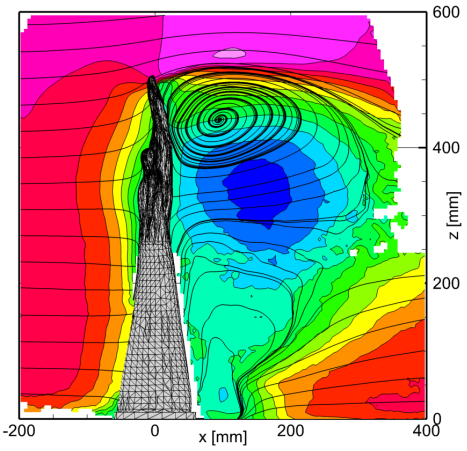

(a) Streamwise velocity u ($y = 0$ mm)

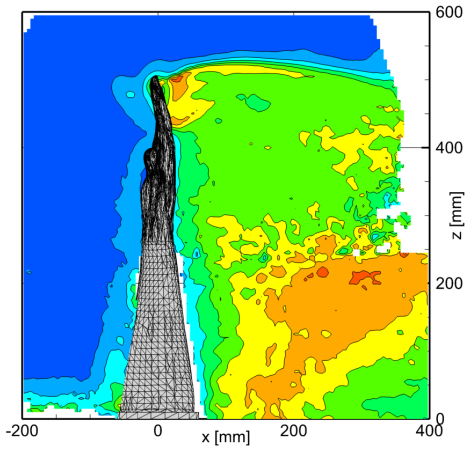

(b) Streamwise velocity fluctuations u'_{rms} ($y = 0$ mm)

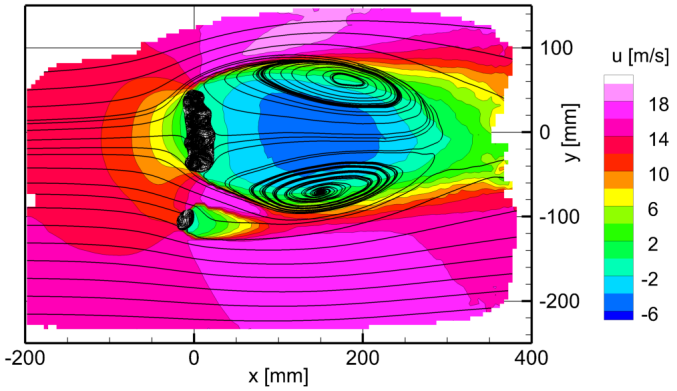

(c) Streamwise u ($z = 390$ mm)

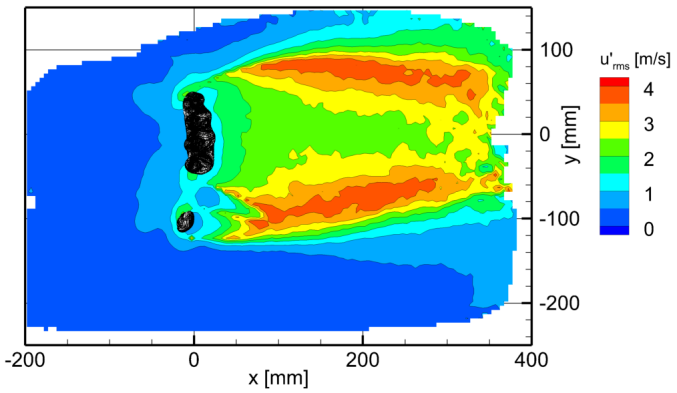

(d) Streamwise velocity fluctuations u'_{rms} ($z = 390$ mm)

Figure 9.6: Mean streamwise velocity and fluctuations for the open-thumb hand model at 0° yaw.

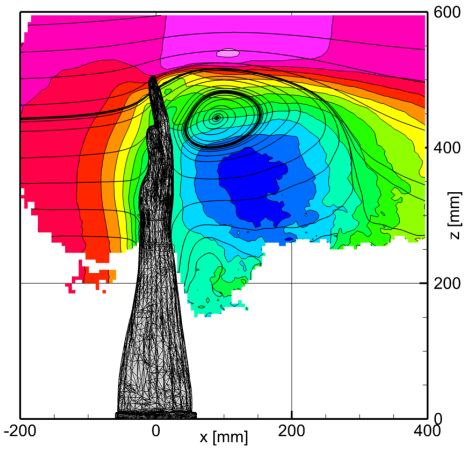

(a) Streamwise velocity u ($y = 0$ mm)

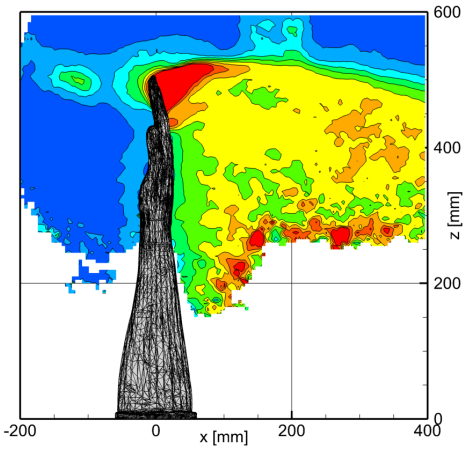

(b) Streamwise velocity fluctuations u'_{rms} ($y = 0$ mm)

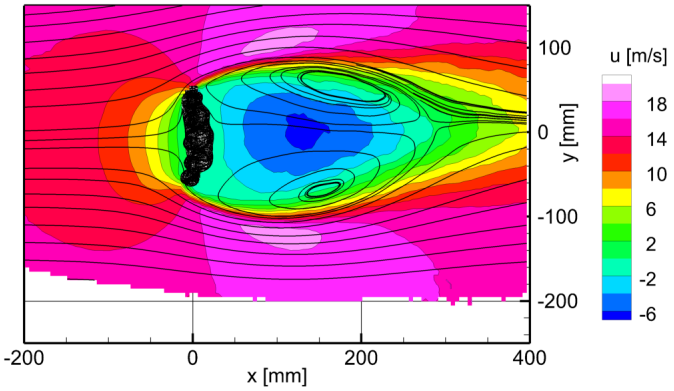

(c) Streamwise velocity u ($z = 390$ mm)

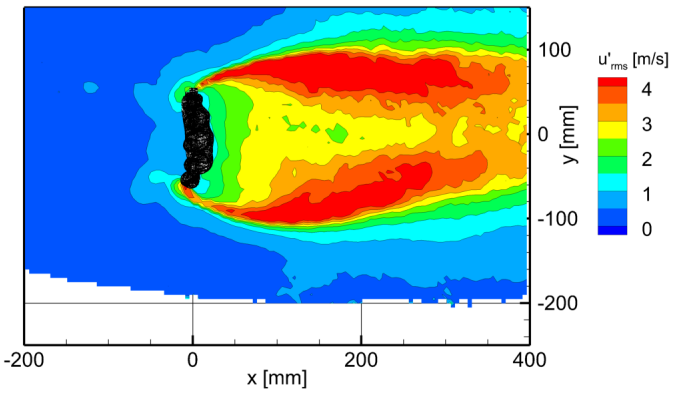

(d) Streamwise velocity fluctuations u'_{rms} ($z = 390$ mm)

Figure 9.7: Mean streamwise velocity and fluctuations for the closed-thumb hand model at $0°$ yaw.

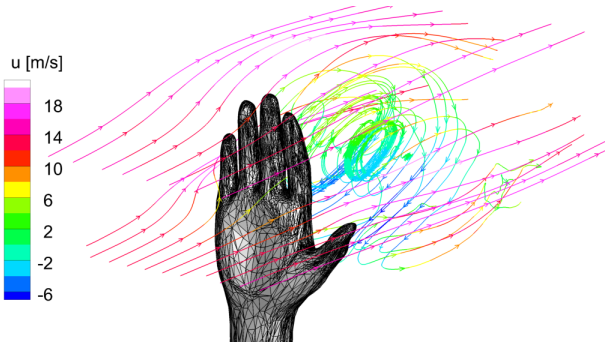

(a) Open hand.

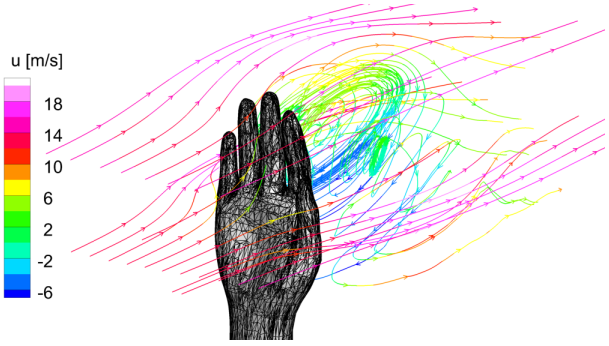

(b) Closed hand.

Figure 9.8: Time-average 3D streamlines, coloured by streamwise velocity on open- and closed-hand model at $0°$ yaw.

thumb now. The flow on the closed hand thus, needs to curve stronger to pass the model. Downstream of the hand, the closed hand features one large recirculation zone, whereas on the open hand a large vortex behind the palm and fingers is distinguishable from a small vortical structure in the thumb's wake.

Figures 9.6 and 9.7 compare the streamwise velocity and fluctuation distribution in a horizontal plane at mid-thumb-height ($y = 390\,\text{mm}$), and the median vertical plane ($y = 0\,\text{mm}$). Comparing the mean velocity distribution in Figures 9.6(c) and 9.7(c) shows the change in the shape of the decelerated flow upstream of the hand, which is more compact and symmetric for the closed hand; as well as the different wake structure downstream with one big separated zone for the closed hand, compared to the two distinct recirculation zones of fingers and thumb on the open hand. The wakes are further distinguished by the maximum reverse velocity, which is seen to be higher for the closed thumb configuration, indicating a stronger recirculation.

The streamwise velocity fluctuations in Figures 9.6(d) and 9.7(d) reveal further differences between the hand models. The fluctuations in the shear layers appear

stronger for the closed thumb model. On the open thumb model the fluctuation magnitude in the shear layers is slightly reduced. Whereas the fluctuations in the shear layers are stronger downstream of the closed thumb model, the wake contracts slightly faster with streamwise distance from the hand, suggesting that the wake behind the closed thumb model is more confined in the streamwise direction.

For a direct quantitative comparison velocity profiles are extracted along three x-, and three z-stations downstream of the hand models. These profiles are plotted in Figure 9.9. Immediately downstream of the hand, the closed hand shows a marginally larger velocity deficit over the open hand. To use the velocity deficit as a drag-indicator, the profiles further downstream are more suitable however, given that the pressure-term contribution to the drag is less significant further downstream (compare e.g. Terra et al., 2017). Interestingly, at the most downstream profile ($x = 300$ mm) in the two lower planes ($z = 300$ and 400 mm) the open hand shows a more pronounced velocity deficit, suggesting a greater drag magnitude. Since the trend is again opposed at the upper plane, no clear conclusion on the drag force can be made from the shown velocity measurements. The measurements were, however, also not designed for such drag analysis, and therefore, further conclusions on this are prohibited.

An alternative option to infer the drag force from the PIV measurement, in the assumption that the total drag is dominated by pressure drag rather than friction drag, is the evaluation of the pressure distribution on the hand models, following the methodology proposed in Chapter 5, which is illustrated in the subsequent section.

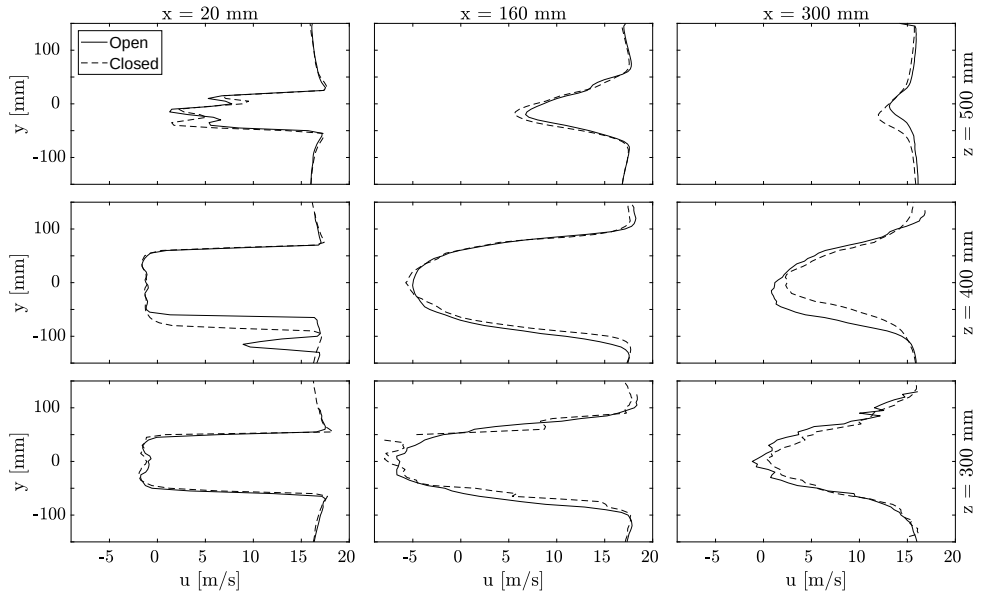

Figure 9.9: Comparison of streamwise velocity profiles in the wake of closed- and open-thumb hand at 0° yaw, 20, 100, 200 and 300 mm downstream of the hand at three heights ($z = 300$, 400, and 500 mm).

9.2.4. Surface pressure distribution

The above analysis has shown that the swimmer's hand posture affects the flow topology up- and downstream of the hand model. Similarly, it is expected each hand posture features a unique surface pressure distribution. Applying the approach introduced in Chapter 5, the pressure distributions on the hand models are evaluated. The results are illustrated and compared to local transducer measurements in Figure 9.10.

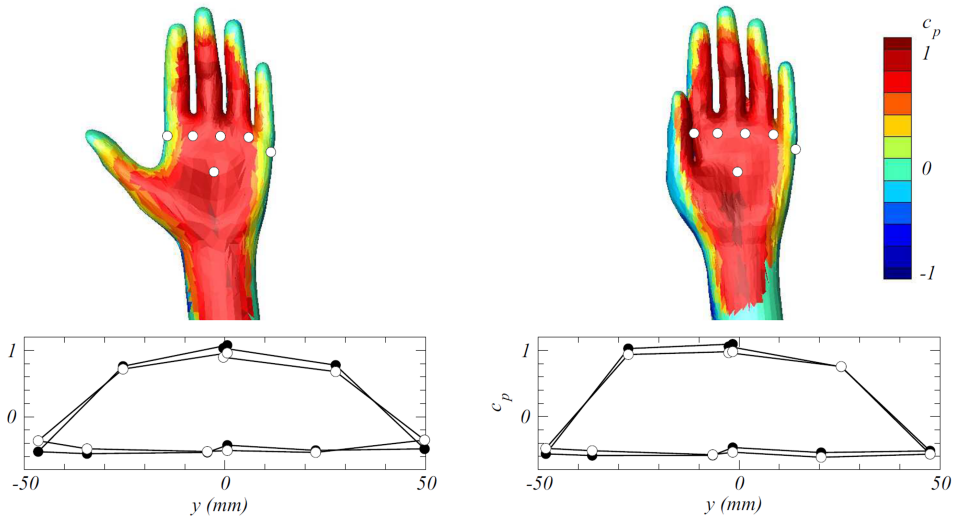

(a) Open hand (b) Closed hand

Figure 9.10: Top: Time-average static pressure distribution on open- and closed-hand model at 0° yaw with indication of pressure tap locations. Bottom: Comparison of PIV-based pressure values (open circles) against transducer readings (solid dots). Figure reproduced from van den Berg et al. (2021).

The comparison to the pressure tap readings on the hand's palm area indicates an agreement of the pressure distribution to within 10 %, corresponding well with the uncertainty analysis presented in Chapter 5. On the fingers, the uncertainty is found to be larger as a consequence of spatial resolution effects. Therefore, the pressure map shown in Figure 9.10 provides a quantitative indication of the pressure distribution on the hand model, but its accuracy is not sufficient to derive a drag measurement from integration of the surface pressure.

Comparing open and closed thumb hand, it is seen in Figure 9.10 that closing the thumb raises the pressure at the base of the index finger. Such pressure increase is indicative for higher drag, unless it is compensated for by an increased pressure difference across the (open thumb) hand model.

9.3. Conclusion

The robotic volumetric PIV system introduced in this thesis (Chapter 3) is applied in a full-scale, volumetric velocimetry study of two swimmer's hand models. The effect of abducted (open) and adducted (closed) thumb position on the time-average flow topology and pressure distribution is investigated.

While the CVV probe provides optical access for measurements between individual fingers, spatial resolution of the time-average velocity measurement is limited by the available data density: below a cell volume of 1 cm^3 the ensemble averaged velocity field shows local gaps and lacking convergence.

The swimmer's arm wake is characterized by two dominant recirculation zones: a first recirculating structure forms downstream of the hand. The fluid flow between the fingers feeds into this flow structure, resulting in a consistent rolling motion. A second area of reverse flow forms in the arm's wake. The arm's wake is more chaotic in nature, which is attributed to the arm's cylindrical shape. For the abducted (open) thumb model, a third, small recirculation zone is observed downstream of the thumb. The latter merges with the hand's wake at approximately one hand width downstream of the hand.

Evaluation of the surface pressure distribution shows that closing the thumb on the index finger raises the pressure on the index finger base, indicative for a higher (pressure) drag contribution. For a conclusive statement on the pressure drag of the two hand models, however, the flow near the fingers must be measured with increased spatial resolution.

Epilogue

10

Impact of robotic volumetric PIV in aerodynamic research

It always seems impossible until it's done.

Nelson Mandela

In this thesis, the concept of robotic volumetric PIV has been introduced (Chapter 3) and applied in selected disciplines in sport aerodynamics (Part II). Despite my passion for sports, it would be a pity if robotic volumetric PIV was limited to research in sport aerodynamics only. Gratefully, this is not the case. Since its first public presentation at the ISPIV conference 2017 in Busan (South Korea), robotic volumetric PIV has already made an impact through several aerodynamic studies to date. This chapter provides an overview of such investigations, aiming to illustrate its wide range of applications, and inspire fellow researches to consider robotic volumetric PIV in their upcoming studies.

Irrespective of its young age robotic volumetric PIV has already found its way into engineering applications. In the following, examples in the field of aeronautics (Section 10.1), fluid-structure-interaction (FSI, Section 10.2), and ground vehicles (Section 10.3) are illustrated. Further cases including research relating to wind engineering and water flows are presented in Section 10.4. An overview of the referenced studies is given in Table 10.1.

Table 10.1: Experiments conducted with robotic volumetric PIV by fellow researchers and engineers.

	Research application & group	Facility	Flow velocity	Domain size
Airborne Vehicles	Turboprop aircraft model Sciacchitano et al. (2018)	LST, DNW Marknesse	8 & 50 m/s	150 L
	Flapping-wing MAV Gallar et al. (2020)	OJF, TU Delft	≤ 2 m/s phase-averaged	60 L
Fluid-Structure Interaction	Pitching airfoil Mertens et al. (2021b)	OJF, TU Delft	5.6 m/s LED illumination	32 L
	Gust-loaded plate Mitrotta et al. (2019)	OJF, TU Delft	12 m/s	150 L
	Gust-loaded wing Mertens et al. (2021a)	OJF, TU Delft	14 m/s	15 L
Ground Vehicles	Ahmed body Sciacchitano et al. (2019)	OJF, TU Delft	12 m/s	130 L
	Platooning truck models van Tilborg et al. (2019)	OJF, TU Delft	15 m/s	NA
	Car-mirror models Kim et al. (2020)	W-Tunnel TU Delft	13 m/s	$\mathcal{O}$ (10 L)
	Juncture flow Saredi et al. (2021)	W-Tunnel TU Delft	12 m/s	40 L
	Cyclist mannequin Terra et al. (2020)	OJF, TU Delft	5 – 25 m/s	(5×) $\mathcal{O}$ (300 L)
Wind & Water	Vertical axis wind turbine Huang et al. (2020)	W-Tunnel TU Delft	5 m/s	$\mathcal{O}$ (300 L)
	Ship propeller model Roettig et al. (2019)	ISMT, University of Duisburg-Essen	1 m/s water	(2×) 10 L

10.1. Airborne vehicles

The versatility of airborne vehicles in terms of size, speed and range is huge, ranging from micro air vehicles (MAV) to airliners and transport aircraft. The two examples in this section demonstrate that robotic volumetric PIV can be useful at both ends of this scale. The first example by Sciacchitano et al. (2018) features the study of a 1:12 scale turboprop aircraft model in the Low Speed Tunnel (LST) at the German-Dutch Wind Tunnels (DNW). The second example by Gallar et al. (2020), instead, investigates the wake flow of a flapping MAV at TU Delft's Open Jet Facility.

The turboprop measurements focus on a 150 L volume near the aircraft's wing and propeller, as illustrated in Figure 10.1. Flow measurements are acquired at 8 m/s in time-resolved mode, and at a speed of 50 m/s in double frame mode. For the measurement at 50 m/s the authors adapt the recent multi-Δt approach

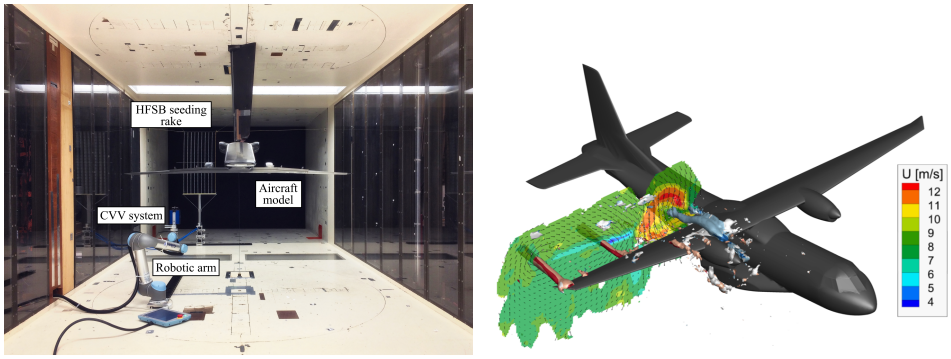

(a) Experimental setup (b) Flow visualization

Figure 10.1: Measurements on a turboprob aircraft model at the German-Dutch Windtunnels (DNW). Figures reproduced from Sciacchitano et al. (2018).

by Saredi et al. (2020) in which data is acquired at a successively increasing time separation (Δt) of the image frames. Key flow topology features, such as vortices emanating from wing tip and flap edge, are identified in both acquisition modes. A more detailed comparison of the cases shows that the time-resolved data is superior in terms of accuracy and spatial resolution, and thus, time-resolved acquisitions should be aimed at when affordable.

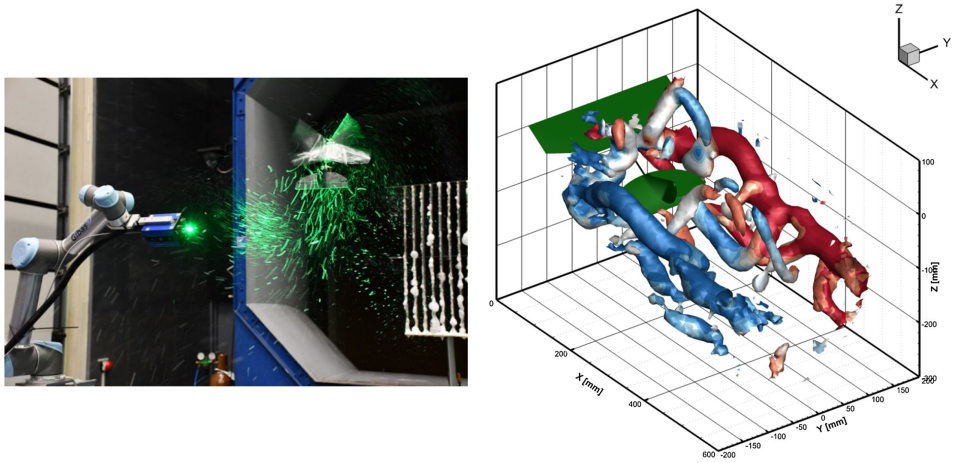

(a) Experimental setup (b) Flow visualization

Figure 10.2: Flow analysis on the Delfly MAV in TU Delft's Open Jet Facility. Figures reproduced from Gallar et al. (2020).

The study by Gallar et al. (2020) addresses the aerodynamics of a micro air vehicle (MAV) in free-flight. The researchers focus on the wake flow of the Delfly, a flapping wing MAV. The work investigates different phases of the periodic flapping cycle by means of phase-locked analysis of the 3D PIV data. A photograph of the MAV flying in the HFSB stream in the open jet wind tunnel is shown in Figure 10.2 along with an illustration of the 3D vortex structures in the MAV's wake. The robotic volumetric PIV measurements assisted the authors in analysing the change in wake flow topology as a function of the reduced flapping frequency.

10.2. Fluid structure interaction

The separate, experimental study of fluid flows and structural mechanics is already challenging. To complicate the matter, a fluid flow affects the structural response of an immersed object, and vice versa, the structural deformation of an object affects the surrounding fluid flow topology. In engineering problems where the interaction of fluid and structure is crucial, the experimentalist needs to analyse the two simultaneously.

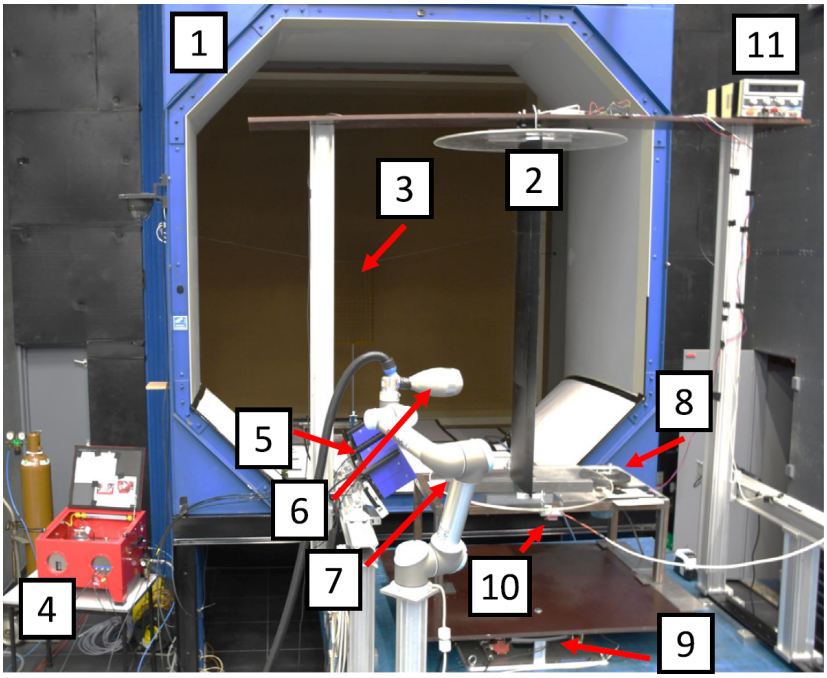

Figure 10.3: Robotic volumetric PIV setup with external LED illumination on a pitching airfoil model in OJF. Labelled items: (1) Wind tunnel nozzle exit, (2) Airfoil model, (3) HFSB seeding rake, (4) HFSB controller, (5) LED arrays, (6) CVV probe, (7) robotic arm, (8) pitch mechanism, (9) turntable, (10) flap actuation servo, (11) servomotor power supply. Figure reproduced from Mertens et al. (2021b).

A practical approach to this problem is the synchronisation of fluid- and structure specific measurement instruments. Optical techniques such as PIV, instead allow

for the simultaneous study of fluid and structure, by segmentation of the images. The three examples in this section illustrate, how the robotic volumetric PIV system may be used for such FSI studies.

The first example by Mertens et al. (2021b) addresses the dynamics of a pitching airfoil model with an actively controlled trailing edge flap. The setup, which makes use of external LED illumination is shown in Figure 10.3. The CVV cameras simultaneously track the HFSB flow tracer particles along with fiducial markers on the airfoil. In this way, the authors demonstrate that the system can be used to determine the unsteady aerodynamic load from the flow field measurements, as well as the unsteady flap position of the trailing edge flap.

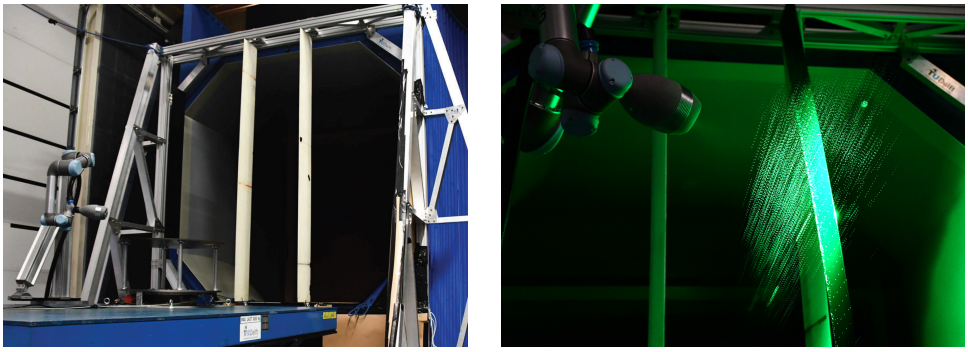

(a) Setup overview by Mitrotta et al. (2019)

(b) Robotic PIV during acquisition. Image reproduced from Mitrotta (2020).

Figure 10.4: Experimental setup for the FSI study of a slender plate under gust loading in OJF.

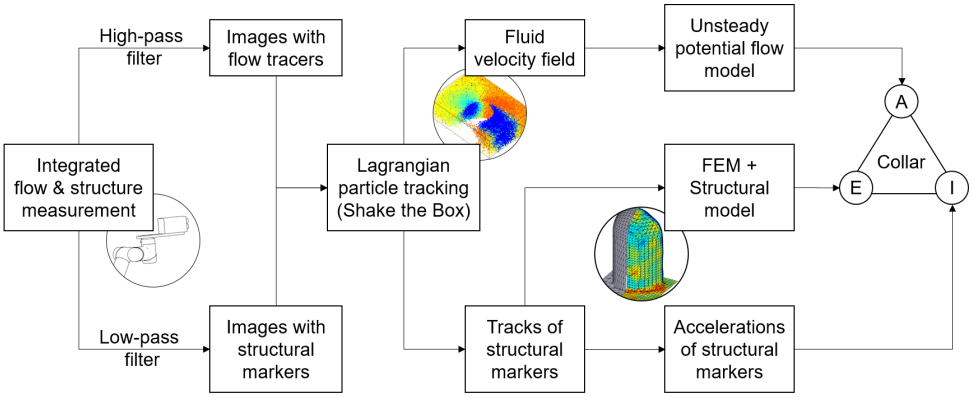

Figure 10.5: Working principle of the simultaneous fluid- and structure-analysis by means of robotic volumetric PIV. Figure adapted from Mertens et al. (2021a).

The second example by Mitrotta et al. (2019) uses a likewise approach to study the structural and aerodynamic response of a flat plate under periodic gust load-

ing. The robotic volumetric PIV system is shown to be suitable for a simultaneous, phase-averaged analysis of the plate response and the flow topology. A photograph of the experimental setup is presented in Figure 10.4.

More recently the group of Mertens et al. (2021a) studied a 1.75 m span airfoil under periodic inflow conditions using a similar setup to the one shown by Mitrotta et al. (2019). The authors show the ability to record aerodynamic, elastic, and inertial forces by means of robotic volumetric PIV measurements. Consequently, the three forces of the well known *Collar's triangle* are evaluated experimentally with a single instrument. The principle by which Mertens et al. (2021a) distinguish the three forces is summarized in Figure 10.5.

10.3. Ground vehicles

The previous examples in this chapter were all closely connected to flying vehicles where aerodynamics are essential. Similarly, aerodynamic performance of ground vehicles is key. The following studies exemplify how robotic volumetric PIV may be used to enhance the aerodynamic understanding of typical flows in ground vehicle applications.

A greatly simplified, standardized car model for aerodynamic investigations is the so called *Ahmed body*. Studies on such simplified models allows for better comparison and data validation across different research groups. In the case shown here, Sciacchitano and Giaquinta (2019) employed the robotic volumetric PIV system to analyse the 3D flow topology near the Ahmed body in straight ahead and cross-wind conditions. The vortex dominated flow topology at 8° yaw angle is illustrated in Figure 10.6.

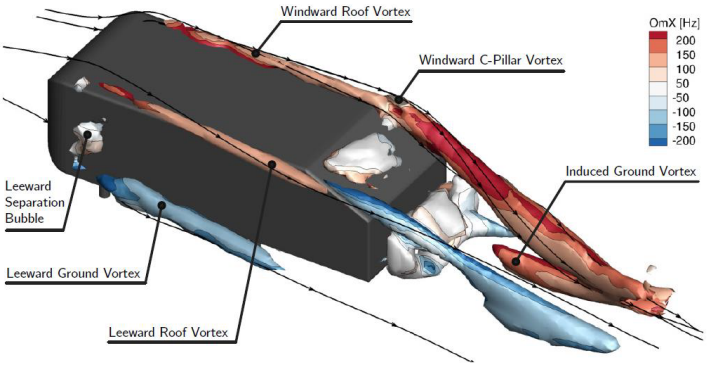

Figure 10.6: Flow topology of the Ahmed body at 8° yaw angle, and 12 m/s freestream velocity. Vortices illustrated by iso-surfaces of Q-criterion ($4000\,s^{-2}$), colour-coded by streamwise vorticity. Figure reproduced from Sciacchitano and Giaquinta (2019).

The study by van Tilborg et al. (2019) makes use of generic truck models, similar to the Ahmed model presented above. The investigation focuses on the platooning effect between two trucks following each other. The optical access provided by the CVV probe, allows for 3D flow measurements in between the two truck models.

Like the study on the Ahmed body, the experiments by van Tilborg et al. (2019) are carried out at TU Delft's Open Jet Facility. An illustration of the setup and an example of the flow measurements are presented in Figure 10.7.

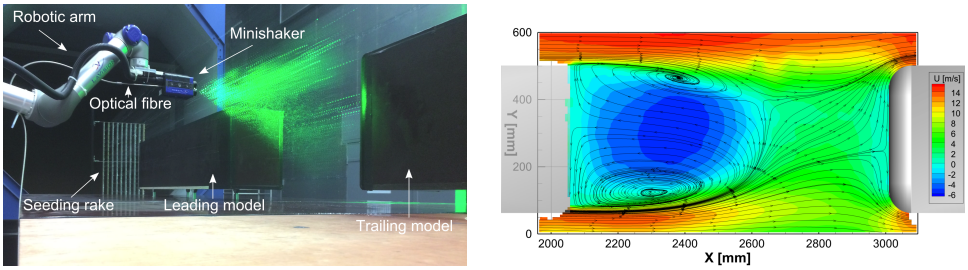

(a) Experimental setup (b) Flow visualization

Figure 10.7: Robotic volumetric PIV on platooning truck models in OJF. Study conducted by van Tilborg et al. (2019), figures reproduced from van Tilborg (2018).

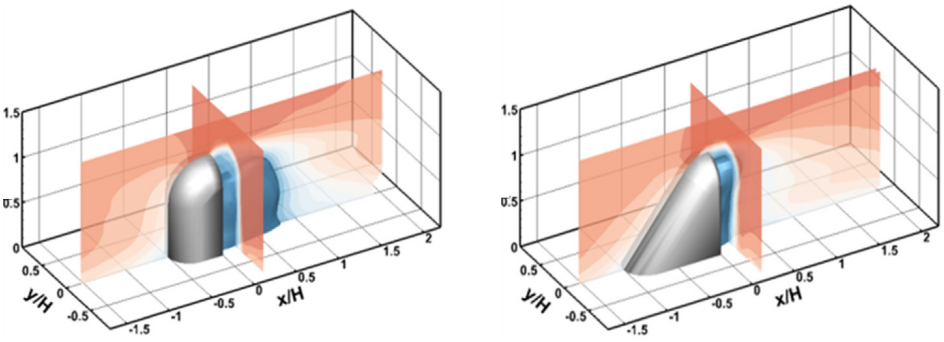

(a) Cylindrical model (b) Wedge-like model

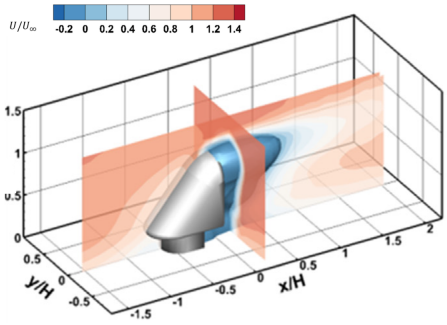

(c) Undercut model

Figure 10.8: Mean flow visualisations by robotic volumetric PIV on simplified car-side-mirror models. Figures reproduced from Kim et al. (2020).

The third and fourth example in this section focus on a specific component, namely a car's side mirror. The study by Kim et al. (2020) compares three simplified side mirror shapes, as illustrated in Figure 10.8. The 3D PIV data provides insight on the wake flow topology, which is observed to be vortex dominated.

The study by Saredi et al. (2021) focuses on a similar juncture flow as presented by Kim et al. (2020). Saredi et al. (2021) present a state observer data assimilation approach for Reynolds averaged Navier Stokes (RANS) models, in which the experimental velocimetry data is leveraged to enhance a numerical simulation. In fact, the data presented in this work has already been used in Chapter 6 for demonstration of the tracer based geometry reconstruction approach. For convenience the experimental setup along with an exemplary flow measurement is shown in Figure 10.9. The authors demonstrate that the time-average 3D velocity data is suitable to enhance the accuracy of the numerical simulation.

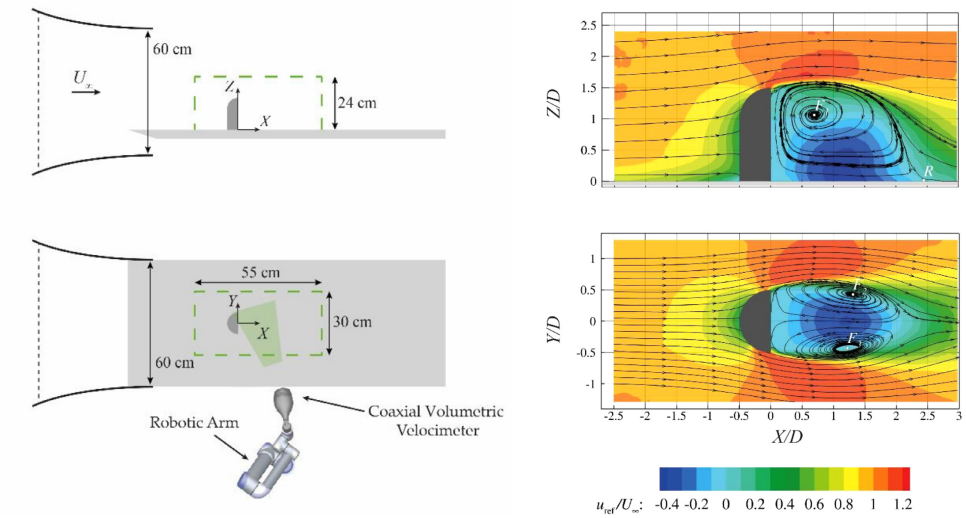

(a) Experimental setup (b) Flow visualization

Figure 10.9: Robotic PIV on a wall-mounted cylinder. Figures reproduced from Saredi et al. (2021).

Part II of this thesis has shown that robotic volumetric PIV has great potential for aerodynamic research in sports, and in cycling specifically. This is underlined by the study of Terra et al. (2020), who investigate Reynolds number effects on a cyclist's arm- and leg-wake. The study considers a full-scale cyclist replica, at free-stream velocities between 5 and 25 m/s. Details on the leg wake are illustrated in Figure 10.10. The robotic volumetric PIV setup enabled the researchers to rapidly repeat fully 3D wake measurements at increasing speed, and hence increasing Reynolds number.

The authors find that the momentum deficit in the athlete's wake is highly dependent on the Reynolds number. This knowledge aids e.g., in the design of sports garment, where roughness elements are utilized to trigger boundary layer transi-

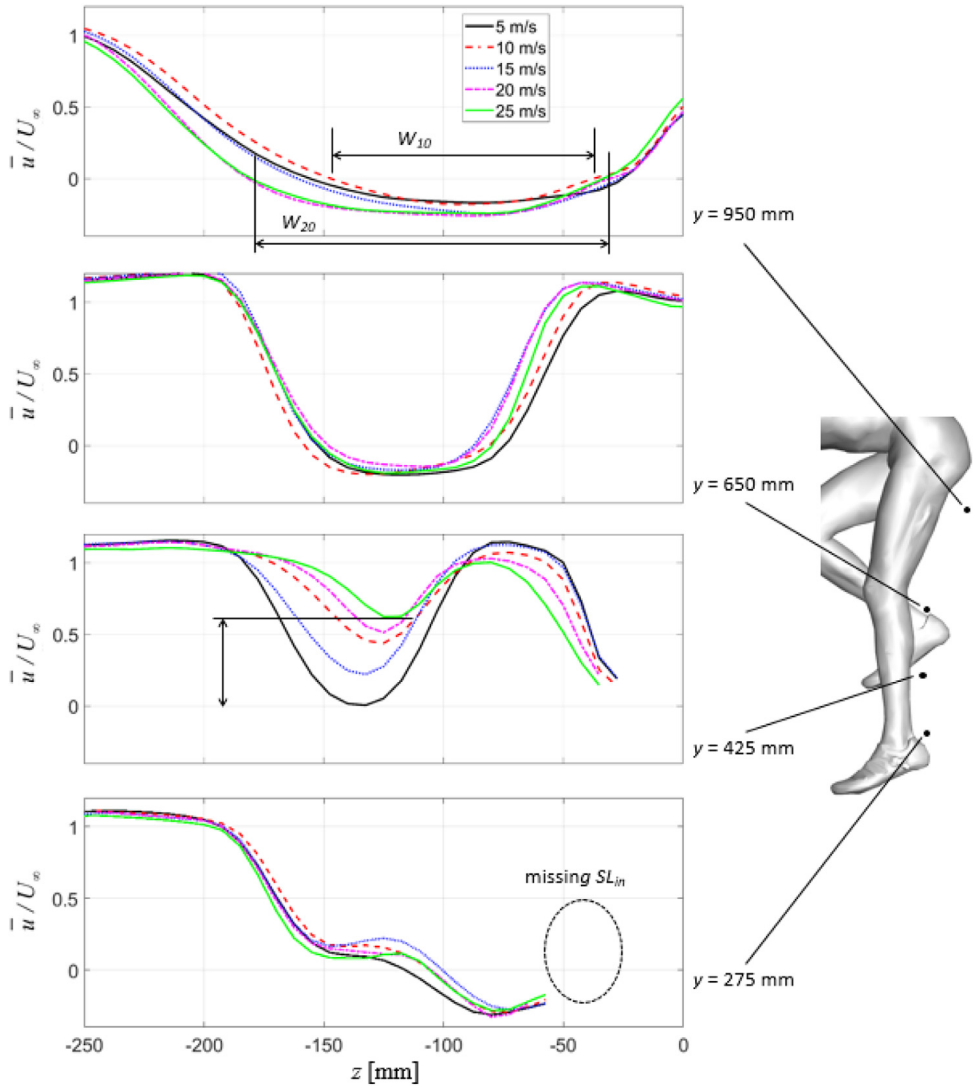

Figure 10.10: Velocity (deficit) profiles in a cyclist's leg wake for varying Reynolds number. Figure reproduced from Terra et al. (2020).

tion on body segments where the local Reynolds number is nominally sub-critical. The study of Terra et al. (2020) reveals in which areas, depending on the athlete's anticipated speed, such roughness elements can return a noticeable drag reduction.

10.4. Wind and water

This last section contains two more examples: the study of a vertical axis wind turbine, followed by the analysis of a ship propeller.

Load estimations for conventional horizontal axis wind turbines (HAWT) can be achieved by a range of aerodynamic models. A simple, yet popular model is the actuator disc model in which the blade-plane is modelled by an actuator surface. The available models are, however, less suitable for vertical axis wind turbines (VAWT). The work of Huang et al. (2020) therefore compares the 3D wake topology of a VAWT with that of planar actuator surfaces. Details of the model, and an exemplary wake measurement are provided in Figure 10.11.

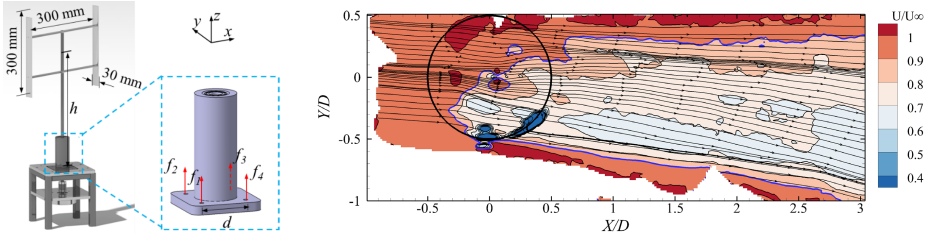

(a) Experimental setup (b) Wake flow visualization

Figure 10.11: Robotic volumetric PIV on a VAWT model. Figures reproduced from Huang et al. (2020).

Comparison of the wind turbine wake with that of the actuator surfaces indicates that the porous actuator surface needs to be yawed by $15°$ to produce a wake similar to that of the turbine model. Such insight is valuable in the design of load estimation models for VAWTs.

The developments presented in this dissertation are targeted to an audience in experimental aerodynamics. Chapter 9 has already shown, however, that the disciplines of aero- and fluid-dynamics are closely related. It shall therefore be no surprise, that the robotic volumetric PIV approach has already been adapted for measurements in water. An example thereof is the work of Roettig et al. (2019), who conducted flow measurements in the wake of a ducted ship propeller model, as illustrated in Figure 10.12.

An interesting observation from this study, is that the cameras are arranged in-line, as compared to the square (and diamond) arrangement of the CVV probes used in this thesis. A potential benefit of such configuration is a greater tomographic aperture angle between the outer cameras, giving rise to a reduced positional uncertainty of the 3D particle reconstruction along the median viewing direction.

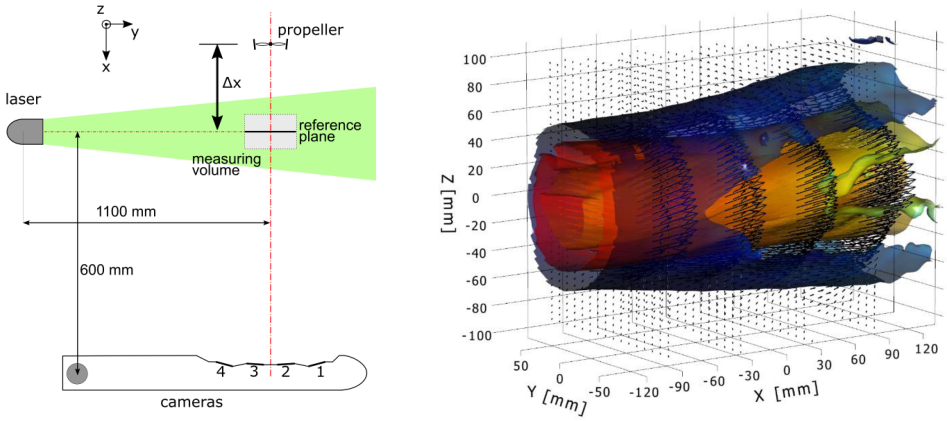

(a) Experimental setup (b) Flow visualization

Figure 10.12: Robotic volumetric PIV on a ducted ship propeller model. Figures reproduced from Roettig et al. (2019).

10.5. Conclusion

The overview of applications presented in this chapter shows that to date robotic volumetric PIV has already made an impact in multiple engineering disciplines. It is fair to assume that more examples are available in the industrial environment, but have not been published for the scientific community. For most studies flow velocities remain below $20\,\mathrm{m/s}$, and acquisitions are carried out in time-resolved mode. The works by Sciacchitano et al. (2018) and Terra et al. (2020) address higher flow velocities, acquiring images in double-frame mode. To maintain a high dynamic velocity range in the two latter studies, the authors adopt the multi-Δt technique presented by Saredi et al. (2020), in which double-frame acquisitions are repeated with increasing time-separation (Δt) between two frames. Extending the velocity range of robotic volumetric PIV further into the compressible flow regime will demand further research in seeding technology and data acquisition strategies.

11

Conclusions and perspectives

Change is never easy, but always possible.

Barack Obama

This chapter summarizes the key conclusions of this dissertation. Similar to the main body of the thesis, conclusions are divided into two parts: the advancements in measurement technology and instrumentation in Section 11.1; and their application in the domain of sport aerodynamics in Section 11.2. Subsequently, Section 11.3 highlights the potential as well as the current limitations of the proposed tools. Finally, aiming to mitigate the identified challenges, Section 11.4 provides directions for future research.

11.1. Measurement technology

Part I addressed three fundamental measurement challenges: firstly, the 3D PIV data acquisition at large scale; secondly, the pressure analysis based on such measurement data; and thirdly, the identification of the test model surface based on flow data.

11.1.1. 3D flow measurement at the cubic-meter scale

In an attempt to facilitate a greater dissemination of PIV technology in industrial applications, a novel approach for measuring large-scale and complex aerodynamic flows has been proposed —robotic volumetric PIV. The approach is based on the combination of coaxial volumetric velocimetry and robotics, while also drawing advantage from recent progress in tracer particle technology and 3D Lagrangian particle tracking algorithms. The overall system complexity is reduced by the compact CVV technology, which furthermore enhances optical access and eliminates the need for re-calibration following a probe movement. Especially, the latter reduces the required user experience when employing the system, as the CVV probe only demands a "once-in-a-lifetime" calibration. The combination with a collaborative robot arm yields the capability to rapidly partition a large fluid domain into multiple adjacent sub-volume measurements.

Measurement volumes of up to 20 L are obtained in a single CVV measurement. The volume is rapidly enlarged when scanning the domain of interest with assistance of a robotic arm. A proof of concept application yields the time-average flow measurement in a 50 L volume surrounding a 15 cm diameter sphere. Subsequent studies confirm that the measurement volume can be lifted beyond a cubic meter.

The alignment of imaging and illumination axes allows to capture the near-surface flow around the convex sphere model from a small number of view points, reducing precious acquisition time. The flip side of the enhanced optical access, is the increased positional uncertainty of the tracer particle reconstructions along the viewing direction. The latter is alleviated by data regularization of the temporally coherent Lagrangian particle tracks, as well as the ensemble averaging procedure to retrieve the mean flow velocity. In the proof of concept experiment a dynamic spatial range of 50, and a dynamic velocity range of 100 is obtained for the time-average velocity measurement.

11.1.2. Pressure analysis

Two aspects of the proposed robotic volumetric PIV concept make the system particularly interesting for aerodynamic pressure analysis: the ability to capture relevantly large volumes, and the superior optical access. The former promises time-savings compared to wake scanning approaches by traversing of pressure probes. The latter gives rise to PIV based surface pressure evaluations on complex 3D geometry.

Total pressure wake rake

The study in Chapter 4 demonstrates the use of robotic volumetric PIV to obtain time-average total pressure estimates in a 3D domain at a relatively large scale, similar to those otherwise obtained by intrusive pressure probes. The case study

of the flow past a truncated cylinder compares the data gathered with a Kiel probe with those inferred from PIV. Discrepancies do not exceed $0.125\,C_P$ (7.5 Pa). The PIV analysis excels in the near wake close to the cylinder, where the results are not affected by flow reversal. As such, the PIV wake survey offers a complementary approach if not alternative to classical wake surveys by total pressure probes.

Static surface pressure

Whereas the wake-pressure evaluation solves the pressure Poisson equation in a box-shaped domain, such approach is found to be less suitable in the context of PIV based surface pressure measurements. The issue stems from the difficulty to prescribe accurate boundary conditions on the 3D model. Therefore, a novel pressure-evaluation approach is presented, that circumvents the specification of boundary conditions on the immersed object. The pressure field is retrieved in a dual-model approach, exploiting Bernoulli's equation in the region of constant total pressure, and integrating the mean pressure gradient elsewhere. In this way the domain where spatial integration is to be carried out is maintained at a minimum.

The method is benchmarked on a sphere-flow test case, where good agreement with measurements from pressure orifices in the model surface is obtained. Differences remain within $0.15\,C_P$ in the region of maximum pressure gradient and in the separated wake. To preserve this level of accuracy the spatial resolution of the ensemble averaged velocity field, quantified in terms of the linear averaging cell size, must remain below half the object's local radius of curvature.

11.1.3. Tracer-based geometry reconstruction

Evaluation of quantities such as surface pressure is only achievable if the object geometry, position, and orientation are known. Knowledge of the test geometry can not be taken for granted, however. This inspired the development of a method for detection of fluid-solid interfaces in PIV measurements. The analysis is solely based on the spatial distribution of particle tracers in the fluid domain, assuming the interface between the seeded fluid flow and the void solid region is a valid representation of the object silhouette.

The method assesses the spatial distribution of tracer particles in isotropic search volumes of radius R. Geometrical features smaller than the search diameter ($2R$) may therefore not be correctly detected. Above this scale, the method is found to reconstruct the model surface well within the resolution of the flow measurement, provided the absence of ghost particles inside the solid model.

The proposed method avoids the necessity to invest in a second measurement device for reconstruction and tracking of the model surface, while eliminating error sources from mismatched reference frames if operating two independent systems for fluid and structure measurement.

11.2. Application to sports aerodynamics

Part II leveraged the technological advancements detailed in the first part of this thesis, by applying the proposed measurement technology in the field of sport aerodynamics. Fluid flow around the human body, and sport equipment is characterized

by its large scale, low speed, and high geometric complexity; serving as an engaging technology demonstrator. Two disciplines were addressed: propulsive force generation in swimming; and cycling aerodynamics at athlete and equipment level.

11.2.1. Swimming

Swimming is one of the few disciplines where the athlete's propulsive force is generated by the direct interaction of the human body with the surrounding fluid. The robotic volumetric PIV system is applied in a full-scale, volumetric velocimetry study of two swimmer's hand models. The effect of thumb position on the time-average flow topology and pressure distribution is investigated.

The superior optical access provided by the CVV probe gives rise to velocimetry measurements between individual fingers, which are otherwise challenging to realise, thereby providing a more complete flow field as could be obtained with other instruments. At the same time, spatial resolution of the time-average velocity measurement is found to be limited by the available data density: the minimum attainable cell size is $1\,\mathrm{cm}^3$ for the ensemble averaged velocity field. Given the fingers diameter of $\mathcal{O}\,(1\,\mathrm{cm})$, higher spatial resolution must be achieved for a detailed analysis of the flow through and around the fingers.

The flow measurements in a $120\,\mathrm{L}$ domain show that the swimmer's arm wake is characterized by two dominant recirculation zones: a rolling vortex structure forms downstream of the hand and it is fed by the fluid flow between the fingers. The lower arm's wake is, instead, comparable to that of a cylinder. Upon stretching the thumb away from the index finger, a third recirculation zone is observed downstream of the thumb which merges with the hand's wake at approximately one hand width downstream of the hand.

Evaluation of the surface pressure distribution shows that closing the thumb on the index finger raises the pressure on the index finger base, indicative for a higher (pressure) drag contribution. For a conclusive statement on the pressure drag of the two hand models, however, the flow near the fingers must be measured with increased spatial resolution. Doing so can lead to new insight for propulsive force maximization in swimming.

11.2.2. Cycling

The dominant share of Part II focused on cycling aerodynamics. The flow topology study on the full scale mannequin of a time-trialling cyclist highlights the potential of robotic volumetric PIV for velocimetry and pressure measurements on large and complex test models. The investigation on the aerodynamics of a cycling wheel included the additional challenge of a rotating test model which makes the surface pressure measurement with traditional instruments ever harder.

Full-scale cyclist

An unprecedented ensemble of 450 time-resolved volumetric PIV acquisitions composes the time-averaged velocity field on a $2\,\mathrm{m}^3$ domain around the cyclist replica. To date, this remains the largest measurement volume acquired with robotic volumetric PIV, to the best of the author's knowledge. The observed flow topology

compares well to wake data in the available literature, and it adds information in the regions near the athlete's body, where the effect of changing posture or specific garments are more pronounced.

The 3D velocimetry data is subsequently utilized to evaluate the pressure distribution on the athlete's body using the dual-model strategy introduced in this thesis. Given the model complexity, the speed regime and the use of a mannequin wearing sports garment, it is tough to imagine likewise pressure measurements with classical pressure sensors. The 3D surface pressure data complements the velocimetry data, to further understand the flow behaviour, and to pinpoint areas of high pressure loads. The uncertainty analysis of the surface pressure distribution indicates that the results are accurate within $0.2\,C_P$.

Beyond the measurements presented in this thesis, the robotic volumetric PIV system was used to study the dependence of the cyclist's flow topology on Reynolds number (see Chapter 10; Terra et al., 2020). The repeated scans of the cyclist's arm and leg wake at increasing air speed, are challenging to obtain in a timely manner with alternative 3D velocimetry systems, that cannot be easily re-positioned without the demand for re-calibration.

Wheel aerodynamics

The aerodynamic characteristics of a state-of-the-art road cycling wheel in cross wind have been assessed experimentally by means of force measurement, a 3D velocimetry investigation as well as high-resolution planar PIV analysis. Additionally, the interaction of rim and tire is studied by comparison of a textured and a slick tire.

The resistive force on the isolated wheel peaks in straight ahead conditions. The aerodynamic resistance of the wheel is reduced as the yaw angle magnitude increases. Analysis of the velocimetry data confirms that the reduction in resistance measured by a force balance is indeed a consequence of the sail-effect, resulting from a substantial side-force on the wheel at yaw incidence; which indeed compares well to an airfoil, respectively, a sail at incidence. The benefit of this effect is limited by the stall angle of the tire-rim combination, which is found to be dependent on the tire choice. The tire dependence is confirmed by the robotic volumetric PIV measurements, but demanded an analysis of the local flow topology at higher resolution. The latter was provided by planar PIV measurements in vicinity of tire and rim. The planar PIV data underlines that the sail-effect is maximized when the tire profile triggers boundary layer transition, thereby allowing the flow to remain attached to the rim for a greater yaw angle range.

11.3. Measurement potential and challenges

Combining the above observations it is concluded that the developed PIV system and analysis methods merge to a unique solution for integrated aerodynamic analysis at large scale. Using a single instrument, the experimentalist has access to 3D velocimetry data, pressure distribution in the fluid and on an immersed object's surface, as well as the ability to retrieve the object shape and position through the flow measurement. These capabilities unite to a great potential for aerodynamic

studies in various engineering disciples. Suitable applications include, but are not limited to, studies in aerospace, automotive and wind engineering as demonstrated in Chapter 10.

Irrespective of the strengths and opportunities, the proposed technology faces a number of challenges that cannot be overlooked. System specific limitations include the positional accuracy along the coaxial viewing direction for 3D particle reconstructions. For low speed flows the uncertainty is alleviated by the temporal coherence of the particle track data. Because current commercially available CVV probes feature cameras that remain within a 1 kHz frame rate at a reasonable sensor size, temporally resolved image acquisition becomes inaccessible at velocities exceeding approximately 20 m/s. The analysis of faster flows remains accessible with double-frame recordings, albeit at the cost of a reduced dynamic velocity range. Methods enhancing the DVR in double-frame mode are available, e.g. by successively increasing the time separation between an image pair (Δt) as demonstrated by Saredi et al. (2020). A comparison of the multi-Δt approach by Saredi et al. (2020) to time-resolved and conventional double-frame data is provided in Figure 11.1, by illustration of vorticity iso-contours in the wake of an Ahmed body.

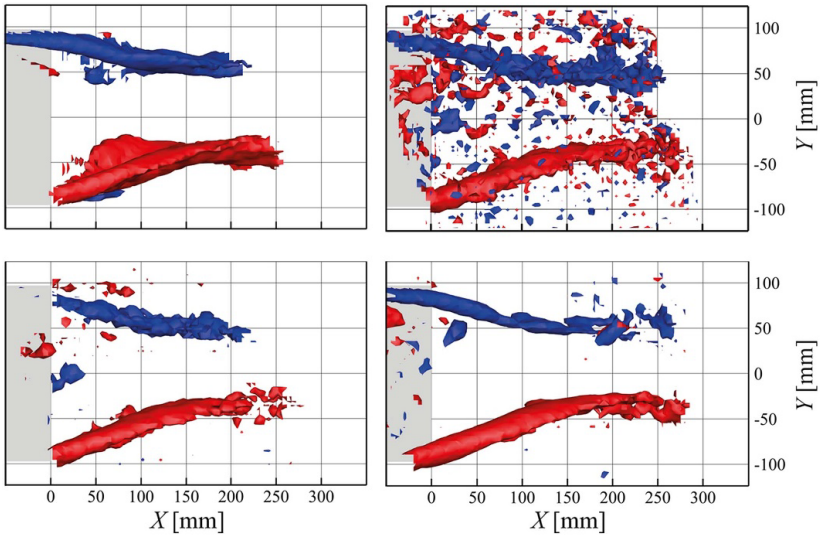

Figure 11.1: Comparison of acquisition modes in the wake of an Ahmed body, based on vorticity iso-contours. Time-resolved data processed with Shake-The-Box (top-left) serves as reference. Conventional double-frame recording with fixed Δt_0 (top-right); Multi-step double-frame acquisition with $\Delta t_2 = \Delta t_0$ (bottom-left); and multi-step double-frame data with increasing time separation $\Delta t_2 = 10 \cdot \Delta t_0$ (bottom-right). Image reproduced from Saredi et al. (2020).

11

If instead of increasing the measurable flow velocities, one is interested in a further increase of the measurement volume, the system presented in this thesis has reached its volume limit during the measurement of the full-scale cyclist. Extending the measurement domain is not as simple as acquiring a robot arm with a bigger workspace, as this will result in a more intrusive system that interferes

with the fluid flow. Handling and integration of larger manipulators in a wind tunnel becomes increasingly difficult as footprint and weight of the machines increase rapidly. Robots suitable for PIV with a reach of up to $\mathcal{O}(2\,\mathrm{m})$ have been identified in the work of Michaux et al. (2018). Besides the scaling aspects of the manipulator, care must be taken to ensure sufficient tracer particle seeding over the full domain of interest. Simultaneously, data readout and processing times will scale up.

Transitioning from system- to processing specific challenges, the spatial resolution of the time-average 3D velocity measurement demands attention. Clear spatial resolution requirements are formulated for the proposed PIV based surface pressure evaluation: the linear bin size shall be no larger than half the object's radius of curvature. Available studies approach a minimum bin size of approximately $1\,\mathrm{cm}^3$. For selected studies, consider the swimmer's hand example, higher spatial resolution is desirable. The latter can be realized through improvements in hardware and processing algorithms as indicated in the subsequent section.

The tracer-based object reconstruction also features its own spatial resolution limitations. Thin, and sharp features are smoothed by the reconstruction algorithm. The issue relates to the isotropic shape of the search volumes, and the finite tracer particle concentration. For a more generic object reconstruction, that can also handle edges and thin details, the current approach is to be extended.

Considering the strengths and weaknesses summarized above, the developed measurement system and technology carries a great potential for integrated aerodynamic analysis at large scale. Nonetheless, several aspects demand further advancements to yield more robust and versatile measurement data. The following section details the elements that deserve attention, providing directions and perspectives for future research.

11.4. Perspectives and recommendations

The proposed systems and methods have already made an impact in aerodynamic research, and likely there will be more examples in future. To enhance the measurement capabilities of the developed technology further, several elements deserve consideration. The most relevant items, from an author's and user's perspective, are listed and discussed here:

1. *Maximum permissible flow velocity*

   Currently available coaxial volumetric velocimeters record images in the $1\,\mathrm{kHz}$ range. For time-resolved data acquisition at velocities in excess of $20\,\mathrm{m/s}$ higher frame rates are needed, given that a switch to double-frame (single-exposure) recordings degrades the velocity measurement uncertainty, especially along the coaxial direction. Mitigation approaches to enhance the DVR in double frame recordings are available, e.g. by successively increasing the time separation between frames (Saredi et al., 2020), or through multi-exposure strategies as demonstrated by Novara et al. (2019).
   A second limitation for measurements at higher velocities stems from the tracer particles. Measurements utilizing helium filled soap bubbles have been demonstrated for flow velocities up to $70\,\mathrm{m/s}$ (Faleiros et al., 2021), whereas

the applicability of HFSB in the compressible flow regime remains to be seen. Further research in bubble seeding technology and image acquisition strategies will be instrumental for extending the measurable flow velocity range of robotic volumetric PIV.

2. *Uncertainty along the coaxial axis direction*

   The reconstruction uncertainty along the coaxial direction is one order of magnitude higher than the corresponding in-plane uncertainty, which is partially alleviated by the temporal coherence of the particle track data. A further uncertainty reduction benefits the overall data quality, and may simultaneously make double-frame (single exposure) recordings more feasible. Algorithmic enhancements are difficult to foresee. On the system side a larger tomographic aperture angle will be beneficial, e.g. through an in-line arrangement of the cameras. Consequences on aerodynamic intrusiveness and optical access are to be evaluated and traded-off based on the intended application.

3. *Aerodynamic intrusiveness assessment and reduction*

   The aerodynamic assessment presented in Chapter 3 considers a simple potential flow model. For applications where the robotic volumetric PIV system is immersed in the flow, its aerodynamic impact on the flow through the measurement domain shall be re-assessed using a higher fidelity model and accounting for the presence of the robot arm.
   When scanning big domains that require a large share of the robot's movement range, it will be instructive to install the robot arm on a linear traverse. In this way, the user will be able to maintain the robot base and arm downstream of the current measurement volume, reducing the aerodynamic interaction between the robot and the flow inside the measurement region. Such integration will demand a re-assessment of the combined (robot arm and traverse) positional accuracy, which is critical for the volume scanning process and deserves scrutiny for any chosen robot arm. If successful, the integration of a traverse increases the accessible measurement volume, and it simultaneously simplifies the robot operation. Ultimately, positioning of the robot and CVV probe may be automated for minimum intrusiveness based on a targeted measurement volume and inflow condition.

4. *Absolute positioning accuracy assessment*

   The robotic volumetric PIV system presented in Chapter 3 relied on the accurate manipulation of the velocimeter through a collaborative robotic arm. The positioning uncertainty was based on the repeatability of the robotic arm, and a first order assessment based on the reconstruction of fixed reference markers imaged from different robot arm positions. To quantify and possibly improve the positioning accuracy of a robotic volumetric PIV system, it will be instructive to assess the absolute positioning accuracy of the robot through an independent instrument. For instance, a camera based motion tracking system can be used to track the absolute robot position independently.

5. *Localised tracer particle seeding*

   The volume scanning approach enables the assembly of large measurement domains through multiple sub-volume measurements. Strategies for tracer particle seeding can be split into full-volume seeding by a large seeding system, and partial volume seeding by traversing of a smaller seeding generator. One of the biggest seeding systems for large-scale PIV measurements by HFSB was recently realised by Faleiros (2021). The 400-nozzle system shown in Figure 11.2 seeds a cross-section of $9\,\mathrm{m}^2$.
   For a sustainable use of tracer particles, it is ideal if the domain of interest can be seeded locally, such that only the currently measured sub-volume is seeded; compared to full seeding of the final measurement domain. In this way excessive tracer particles appearing in the particle images, and tracers possibly impacting and contaminating the camera lenses are also avoided. Such localized seeding is only effective, however, if the seeded volume can be adjusted rapidly and ideally automatically, e.g. by a traversable seeder or a system that allows (de-)activating individual bubble generators.

6. *Ensemble averaging & tracer distribution analysis*

   The ensemble averaging schemes employed in the data analysis of this thesis are rather simple, considering only uniform Cartesian grids and low order polynomial regression models. While more advanced models exist and have been pointed out (adaptive, functional binning), data analysis on an object-compliant grid, similar to CFD-type meshes, will be instructive. A compliant mesh is expected to positively impact the PIV-based pressure analysis, e.g. by enabling a robust specification of boundary conditions on the object surface. The presented tracer-based fluid-solid interface detection provides a starting point for development of object compliant ensemble averaging schemes.
   The spatio-temporal ensemble averaging process relies on a random dispersion of tracer particles. In selected experiments the observed distribution of tracer particles was biased (see e.g. Section 6.4). It will be insightful to study the significance of such a potentially systematic seeding bias. If the bias is found to be significant, its effect on the ensemble average must be analysed, and possibly remedied by means of a normalization strategy. The recent work by Martins et al. (2021) quantifies the effect of intermittent seeding for the correlation-based PIV analysis.

7. *Iterative object surface reconstruction*

   The proposed object surface reconstruction works solely on the tracer particle positions in 3D space, analysing the tracers distribution in isotropic search volumes. Upon a first approximation of the model shape, a second iteration using knowledge of the identified model shape (interface location and wall-normal direction) is foreseen to improve the resulting shape reconstruction. Feature detection approaches may then also allow the correct identification of sharp geometry features.

(a) 400-nozzle, $3 \times 3\,\mathrm{m}^2$ HFSB seeding generator

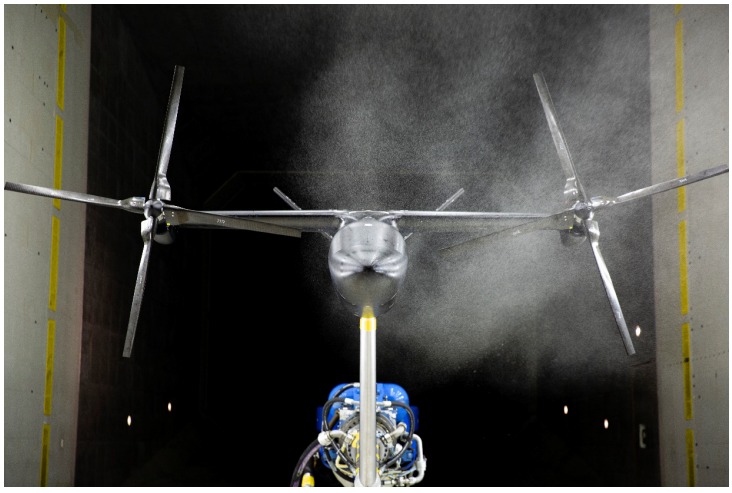

(b) HFSB streamtube on a tiltrotor aircraft model

Figure 11.2: Large-scale HFSB seeding system at the Royal Netherlands Aerospace Centre (NLR). Images reproduced from Faleiros (2021).

Additionally, the velocity and particle track information can provide valuable input if this data is connected to physical boundary conditions, e.g. the no-slip condition. In the assumption that the flow near the wall is parallel to the object surface, the scalar product of local flow velocity and wall-normal direction shall be zero. Such condition can be used to eliminate incorrectly detected surfaces, e.g. due to the presence of ghost particles.

8. *Dynamic flow analysis*

   The fluid flow analyses presented in this thesis focused exclusively on the time-averaged velocity data. In selected cases, consider e.g. the swimming stroke in Chapter 9 or the wake flow analysis of the flapping micro air vehicle by Gallar et al. (2020) illustrated in Chapter 10, extracting information on the flow dynamics is desirable. The question arises if there is a way to study the dynamic flow characteristics of a volume-scanned, 3D PIV data set; i.e. a partitioned measurement volume with its sections acquired at uncorrelated time instances? Such capability will make robotic volumetric PIV relevant for further applications.

9. *Autonomous volume scanning*

   The robotic arm in the proposed volumetric PIV concept serves two main purposes: it provides accurate knowledge of the velocimeter's position and orientation; and it provides a controlled means to rapidly move the velocimeter in space. Selecting appropriate positions to scan a volume of interest remains a user's task. Determining a suitable set of views for a given measurement domain, however, presents a typical problem for artificial intelligence applications. Developing a tool for automated volume scanning by robotic volumetric PIV will likely result in more efficient data acquisition while simultaneously reducing the required user expertise.

The above recommendations conclude this thesis. While the list may seem extensive, it shall not obscure the advancements that have been achieved to date. On the contrary, it will be great to see if any of the provided directions inspire fellow researches and engineers to follow up some of the ideas.

References

Achenbach, E. (1972). Experiments on the flow past spheres at very high Reynolds numbers. *Journal of Fluid Mechanics*, 54(3):565–575.

Acher, G., Thomas, L., Tremblais, B., Gomit, G., Chatellier, L., and David, L. (2019). Simultaneous measurements of flow velocity using Tomo-PIV and deformation of a flexible wing. In *13th International Symposium on Particle Image Velocimetry – ISPIV 2019*, Munich, Germany.

Adatrao, S. and Sciacchitano, A. (2019). Elimination of unsteady background reflections in PIV images by anisotropic diffusion. *Measurement Science and Technology*, 30(3):035204.

Adhikari, D. and Longmire, E. K. (2012). Visual hull method for tomographic PIV measurement of flow around moving objects. *Experiments in Fluids*, 53(4):943–964.

Adrian, R. J. (1984). Scattering particle characteristics and their effect on pulsed laser measurements of fluid flow: speckle velocimetry vs particle image velocimetry. *Applied Optics*, 23(11):1690–1691.

Adrian, R. J. (1997). Dynamic ranges of velocity and spatial resolution of particle image velocimetry. *Measurement Science and Technology*, 8(12):1393.

Adrian, R. J. and Westerweel, J. (2011). *Particle Image Velocimetry*. Cambridge University Press, Cambridge, New York.

Agüera, N., Cafiero, G., Astarita, T., and Discetti, S. (2016). Ensemble 3D PTV for high resolution turbulent statistics. *Measurement Science and Technology*, 27(12):124011.

Agüí, J. C. and Jimenez, J. (1987). On the performance of particle tracking. *Journal of Fluid Mechanics*, 185:447–468.

Alons, H. J. (2008). OJF External Balance. Report NLR-CR-2008-695, Nederlands Lucht- en Ruimtevaartcentrum (National Aerospace Laboratory, NLR).

Anderson, J. D. (2011). *Fundamentals of Aerodynamics*. McGraw-Hill, 3rd edition.

Arroyo, M. and Greated, C. (1991). Stereoscopic particle image velocimetry. *Measurement Science and Technology*, 2(12):1181.

Bansal, P. and Ardell, A. (1972). Average nearest-neighbor distances between uniformly distributed finite particles. *Metallography*, 5(2):97–111.

Barry, N. (2018). A New Method for Analysing the Effect of Environmental Wind on Real World Aerodynamic Performance in Cycling. In *12th Conference of the International Sports Engineering Association*, volume 2, page 211.

Barry, N., Burton, D., Crouch, T., Sheridan, J., and Luescher, R. (2012). Effect of crosswinds and wheel selection on the aerodynamic behavior of a cyclist. In *Engineering of Sport Conference 2012*, volume 34, pages 20–25.

Beaumont, F., Taiar, R., Polidori, G., Trenchard, H., and Grappe, F. (2018). Aerodynamic study of time-trial helmets in cycling racing using CFD analysis. *Journal of Biomechanics*, 67:1–8.

Bitter, M., Hara, T., Hain, R., Yorita, D., Asai, K., and Kähler, C. J. (2012). Characterization of pressure dynamics in an axisymmetric separating/reattaching flow using fast-responding pressure-sensitive paint. *Experiments in Fluids*, 53(6):1737–1749.

Blocken, B., Defraeye, T., Koninckx, E., Carmeliet, J., and Hespel, P. (2013). CFD simulations of the aerodynamic drag of two drafting cyclists. *Computers & Fluids*, 71:435–445.

Bosbach, J., Kühn, M., and Wagner, C. (2009). Large scale particle image velocimetry with helium filled soap bubbles. *Experiments in Fluids*, 46(3):539–547.

Brownlie, L., Ostafichuk, P., Tews, E., Muller, H., Briggs, E., and Franks, K. (2010). The wind-averaged aerodynamic drag of competitive time trial cycling helmets. *Procedia Engineering*, 2(2):2419–2424.

Brücker, C. (1995). Digital-particle-image-velocimetry (DPIV) in a scanning light-sheet: 3D starting flow around a short cylinder. *Experiments in Fluids*, 19(4):255–263.

Brune, G. (1994). Quantitative low-speed wake surveys. *Journal of Aircraft*, 31(2):249–255.

Burgmann, S., Brücker, C., and Schröder, W. (2006). Scanning PIV measurements of a laminar separation bubble. *Experiments in Fluids*, 41(2):319–326.

Canny, J. (1986). A Computational Approach to Edge Detection. *IEEE Transactions on Pattern Analysis and Machine Intelligence*, PAMI-8(6):679–698.

Cant, G. (2014). Back to the wind tunnel. www.swissside.com/blogs/news/back-to-the-wind-tunnel Accessed on 17.05.2021.

Cardano, D., Carlino, G., and Cogotti, A. (2008). *PIV in the Car Industry: State-of-the-Art and Future Perspectives*, pages 363–376. Springer Berlin Heidelberg, Berlin, Heidelberg.

Caridi, G. C. A. (2018). Development and application of helium-filled soap bubbles. Doctoral Thesis, TU Delft.

Caridi, G. C. A., Ragni, D., Sciacchitano, A., and Scarano, F. (2016). HFSB-seeding for large-scale tomographic PIV in wind tunnels. *Experiments in Fluids*, 57(12):190.

Casa, L. and Krueger, P. (2013). Radial basis function interpolation of unstructured, three-dimensional, volumetric particle tracking velocimetry data. *Measurement Science and Technology*, 24(6):065304.

Casper, M., Lemke, C., and Dierksheide, U. (2016). PIV in large wind tunnel by HFSB and STB.

Coleman, H. W. and Steele, W. G. (2009). *Experimentation, Validation, and Uncertainty Analysis for Engineers*. John Wiley & Sons, 3rd edition.

Colgate, J. E., Edward, J., Peshkin, M. A., and Wannasuphoprasit, W. (1996). Cobots: Robots for collaboration with human operators. In *International Mechanical Engineering Congress and Exhibition, Atlanta, GA*, pages 433–439.

Cooper, K. R. (2003). Truck aerodynamics reborn-lessons from the past. *SAE transactions*, 112:132–142.

Coustols, E., Jacquin, L., Moëns, F., and Molton, P. (2004). Status of ONERA research on wake vortex in the framework of national activities and European collaboration. *Tiré à part- Office national d'études et de recherches aerospatiales*.

Crane, R. and Morton, C. (2018). Drag and Side Force Analysis on Bicycle Wheel-Tire Combinations. *Journal of Fluids Engineering-Transactions of the ASME*, 140(6).

Crouch, T., Burton, D., Brown, N., Thompson, M., and Sheridan, J. (2014). Flow topology in the wake of a cyclist and its effect on aerodynamic drag. *Journal of Fluid Mechanics*, 748:5–35.

Crouch, T. N., Burton, D., LaBry, Z. A., and Blair, K. B. (2017). Riding against the wind: a review of competition cycling aerodynamics. *Sports Engineering*, 20(2):81–110.

Crouch, T. N., Burton, D., Thompson, M. C., Brown, N. A., and Sheridan, J. (2016). Dynamic leg-motion and its effect on the aerodynamic performance of cyclists. *Journal of Fluids and Structures*, 65:121–137.

Dabiri, J. O., Bose, S., Gemmell, B. J., Colin, S. P., and Costello, J. H. (2014). An algorithm to estimate unsteady and quasi-steady pressure fields from velocity field measurements. *Journal of Experimental Biology*, 217(3):331–336.

de Kat, R. and van Oudheusden, B. (2012). Instantaneous planar pressure determination from PIV in turbulent flow. *Experiments in Fluids*, 52(5):1089–1106.

Depardon, S., Lasserre, J., Boueilh, J., Brizzi, L., and Borée, J. (2005). Skin friction pattern analysis using near-wall PIV. *Experiments in Fluids*, 39(5):805–818.

Di Felice, F. and Pereira, F. (2007). Developments and applications of PIV in naval hydrodynamics. In *Particle image velocimetry*, pages 475–503. Springer.

Discetti, S. and Coletti, F. (2018). Volumetric velocimetry for fluid flows. *Measurement Science and Technology*, 29(4):042001.

Duda, R. O., Hart, P. E., and Stork, D. G. (1973). *Pattern classification and scene analysis*, volume 3. Wiley New York.

Ebi, D. and Clemens, N. T. (2016). Simultaneous high-speed 3D flame front detection and tomographic PIV. *Measurement Science and Technology*, 27(3):035303.

Elsinga, G. E., Scarano, F., Wieneke, B., and van Oudheusden, B. W. (2006). Tomographic particle image velocimetry. *Experiments in Fluids*, 41(6):933–947.

Falchi, M., Felli, M., Grizzi, S., Aloisio, G., Broglia, R., and Stern, F. (2014). SPIV measurements around the DELFT 372 catamaran in steady drift. *Experiments in Fluids*, 55(11):1–20.

Faleiros, D. E. (2021). Soap bubbles for large-scale PIV: Generation, control and tracing accuracy. Doctoral Thesis, TU Delft.

Faleiros, D. E., Tuinstra, M., Sciacchitano, A., and Scarano, F. (2018). Helium-filled soap bubbles tracing fidelity in wall-bounded turbulence. *Experiments in Fluids*, 59(3):56.

Faleiros, D. E., Tuinstra, M., Sciacchitano, A., and Scarano, F. (2019). Generation and control of helium-filled soap bubbles for PIV. *Experiments in Fluids*, 60(3):1–17.

Faleiros, D. E., Tuinstra, M., Sciacchitano, A., and Scarano, F. (2021). The slip velocity of nearly neutrally buoyant tracers for large-scale PIV. *Experiments in Fluids*, 62(9):1–24.

Gallar, B. M., van Oudheusden, B., Sciacchitano, A., and Karásek, M. (2020). Large-scale volumetric flow visualization of the unsteady wake of a flapping-wing micro air vehicle. *Experiments in Fluids*, 61(1):16.

Gesemann, S., Huhn, F., Schanz, D., and Schröder, A. (2016). From noisy particle tracks to velocity, acceleration and pressure fields using B-splines and penalties. In *18th International Symposium on Applications of Laser and Imaging Techniques to Fluid Mechanics, Lisbon, Portugal*, pages 4–7.

Ghaemi, S., Ragni, D., and Scarano, F. (2012). PIV-based pressure fluctuations in the turbulent boundary layer. *Experiments in Fluids*, 53(6):1823–1840.

Giaquinta, D. (2018). The Flow Topology of the Ahmed Body in Cross-Wind: An Experimental Investigation by means of Robotic Volumetric PIV. MSc Thesis, TU Delft.

Gibeau, B. and Ghaemi, S. (2018). A modular, 3D-printed helium-filled soap bubble generator for large-scale volumetric flow measurements. *Experiments in Fluids*, 59(12):1–11.

Giovannetti, L. M., Banks, J., Turnock, S., and Boyd, S. (2015). Developing tools for assessing bend-twist coupled foils.

Godbersen, P. and Schröder, A. (2020). Functional binning: improving convergence of Eulerian statistics from Lagrangian particle tracking. *Measurement Science and Technology*, 31(9):095304.

Godo, M., Corson, D., and Legensky, S. (2010). A comparative aerodynamic study of commercial bicycle wheels using CFD. In *48th AIAA Aerospace Sciences Meeting Including the New Horizons Forum and Aerospace Exposition*, page 1431.

Gomes, L. E. and Loss, J. F. (2015). Effects of unsteady conditions on propulsion generated by the hand's motion in swimming: a systematic review. *Journal of Sports Sciences*, 33(16):1641–1648.

Greenway, B. (2000). Robot accuracy. *Industrial Robot: An International Journal*, 27(4):257–265.

Greenwell, D. I., Wood, N. J., Bridge, E. K. L., and Addy, R. J. (1995). Aerodynamic Characteristics of Low-Drag Bicycle Wheels. *Aeronautical Journal*, 99(983):109–120.

Gregory, J., Asai, K., Kameda, M., Liu, T., and Sullivan, J. (2008). A review of pressure-sensitive paint for high-speed and unsteady aerodynamics. *Proceedings of the Institution of Mechanical Engineers, Part G: Journal of Aerospace Engineering*, 222(2):249–290.

Griffith, M. D., Crouch, T., Thompson, M. C., Burton, D., Sheridan, J., and Brown, N. A. (2014). Computational fluid dynamics study of the effect of leg position on cyclist aerodynamic drag. *Journal of Fluids Engineering*, 136(10).

Grizzi, S., Pereira, F., and Di Felice, F. (2010). A simplified, flow-based calibration method for stereoscopic PIV. *Experiments in Fluids*, 48(3):473–486.

Gui, L., Wereley, S., and Kim, Y. (2003). Advances and applications of the digital mask technique in particle image velocimetry experiments. *Measurement Science and Technology*, 14(10):1820.

Gurka, R., Liberzon, A., Hefetz, D., Rubinstein, D., and Shavit, U. (1999). Computation of pressure distribution using PIV velocity data. In *Workshop on particle image velocimetry*, volume 2, pages 1–6.

Hain, R., Kähler, C. J., and Michaelis, D. (2008). Tomographic and time resolved PIV measurements on a finite cylinder mounted on a flat plate. *Experiments in Fluids*, 45(4):715–724.

Hinsch, K. D. (1995). Three-dimensional particle velocimetry. *Measurement Science and Technology*, 6(6):742.

Huang, M., Ferreira, C., Sciacchitano, A., and Scarano, F. (2020). Experimental Comparison of the Wake of a Vertical Axis Wind Turbine and Planar Actuator Surfaces. In *Journal of Physics: Conference Series*, volume 1618, page 052063. IOP Publishing.

Huffaker, R. M., Fuller, C. E., and Lawrence, T. (1969). Application of laser Doppler velocity instrumentation to the measurement of jet turbulence. *SAE Transactions*, pages 1174–1188.

Huhn, F., Schanz, D., Manovski, P., Gesemann, S., and Schröder, A. (2018). Time-resolved large-scale volumetric pressure fields of an impinging jet from dense Lagrangian particle tracking. *Experiments in Fluids*, 59(5):81.

Im, S., Heo, G. E., Jeon, Y. J., Sung, H. J., and Kim, S. K. (2014). Tomographic PIV measurements of flow patterns in a nasal cavity with geometry acquisition. *Experiments in Fluids*, 55(1):1644.

Im, S., Jeon, Y. J., and Sung, H. J. (2015). Tomo-PIV measurement of flow around an arbitrarily moving body with surface reconstruction. *Experiments in Fluids*, 56(2):25.

Jenkins, L. N., Yao, C.-S., Bartram, S. M., Harris, J., Allan, B., Wong, O., and Mace, W. D. (2009). Development of a Large Field-of-View PIV System for Rotorcraft Testing in the 14-x 22-Foot Subsonic Tunnel. In *AHS International 65th Forum and Technology Display*. NASA Langley Research Center, United States.

Jeon, Y., Schneiders, J., Müller, M., Michaelis, D., and Wieneke, B. (2018a). 4D flow field reconstruction from particle tracks by VIC+ with additional constraints and multigrid approximation. In *18th International Symposium on Flow Visualization*. ETH Zurich.

Jeon, Y. J., Gomit, G., Earl, T., Chatellier, L., and David, L. (2018b). Sequential least-square reconstruction of instantaneous pressure field around a body from TR-PIV. *Experiments in Fluids*, 59(2):27.

Jeon, Y. J. and Sung, H. J. (2012). Three-dimensional PIV measurement of flow around an arbitrarily moving body. *Experiments in Fluids*, 53(4):1057–1071.

Jones, B. M. (1936). *The measurement of profile drag by the pitot-traverse method*. HM Stationery Office.

Jux, C., Sciacchitano, A., and Scarano, F. (2019). Aerodynamic pressure reconstruction on generic surfaces from robotic PIV measurements. In *Proceedings of the 13th International Symposium on Particle Image Velocimetry*. Universität der Bundeswehr München.

Kai, C. C., Jacob, G. G., and Mei, T. (1997). Interface between CAD and rapid prototyping systems. Part 1: a study of existing interfaces. *The International Journal of Advanced Manufacturing Technology*, 13(8):566–570.

Khalil, W. and Dombre, E. (2002). Chapter 1 - terminology and general definitions. In Khalil, W. and Dombre, E., editors, *Modeling, Identification and Control of Robots*, pages 1–12. Butterworth-Heinemann, Oxford.

Kim, D., Kim, M., Saredi, E., Scarano, F., and Kim, K. C. (2020). Robotic PTV study of the flow around automotive side-view mirror models. *Experimental Thermal and Fluid Science*, 119:110202.

Klein, C., Engler, R. H., Henne, U., and Sachs, W. E. (2005). Application of pressure-sensitive paint for determination of the pressure field and calculation of the forces and moments of models in a wind tunnel. *Experiments in Fluids*, 39(2):475–483.

Kurtulus, D., Scarano, F., and David, L. (2007). Unsteady aerodynamic forces estimation on a square cylinder by TR-PIV. *Experiments in Fluids*, 42(2):185–196.

Lignarolo, L., Ragni, D., Krishnaswami, C., Chen, Q., Ferreira, C. S., and van Bussel, G. (2014). Experimental analysis of the wake of a horizontal-axis wind-turbine model. *Renewable Energy*, 70:31–46. Special Issue on Aerodynamics of Offshore Wind Energy Systems and Wakes.

Liu, X. and Katz, J. (2006). Instantaneous pressure and material acceleration measurements using a four-exposure PIV system. *Experiments in Fluids*, 41(2):227.

Lukes, R. A., Chin, S. B., and Haake, S. J. (2005). The understanding and development of cycling aerodynamics. *Sports Engineering*, 8(2):59–74.

Maas, H., Gruen, A., and Papantoniou, D. (1993). Particle tracking velocimetry in three-dimensional flows. *Experiments in Fluids*, 15(2):133–146.

Malik, J., Belongie, S., Leung, T., and Shi, J. (2001). Contour and texture analysis for image segmentation. *International Journal of Computer Vision*, 43(1):7–27.

Malizia, F. and Blocken, B. (2020a). Bicycle aerodynamics: History, state-of-the-art and future perspectives. *Journal of Wind Engineering and Industrial Aerodynamics*, 200:104134.

Malizia, F. and Blocken, B. (2020b). CFD simulations of an isolated cycling spoked wheel: The impact of wheel/ground contact modeling in crosswind conditions. *European Journal of Mechanics B-Fluids*, 84:487–495.

Malizia, F. and Blocken, B. (2021). Cyclist aerodynamics through time: Better, faster, stronger. *Journal of Wind Engineering and Industrial Aerodynamics*, 214:104673.

Malizia, F., Montazeri, H., and Blocken, B. (2019). CFD simulations of spoked wheel aerodynamics in cycling: Impact of computational parameters. *Journal of Wind Engineering and Industrial Aerodynamics*, 194:0167–6105.

Marinho, D. A., Barbosa, T. M., Reis, V. M., Kjendlie, P. L., Alves, F. B., Vilas-Boas, J. P., Machado, L., Silva, A. J., and Rouboa, A. I. (2010). Swimming propulsion forces are enhanced by a small finger spread. *Journal of Applied Biomechanics*, 26(1):87–92.

Martins, F. J., Kirchmann, J., Kronenburg, A., and Beyrau, F. (2021). Quantification and Mitigation of PIV Bias Errors Caused by Intermittent Particle Seeding and Particle Lag by Means of Large Eddy Simulations. *Measurement Science and Technology*.

Matsuuchi, K., Miwa, T., Nomura, T., Sakakibara, J., Shintani, H., and Ungerechts, B. (2009). Unsteady flow field around a human hand and propulsive force in swimming. *Journal of Biomechanics*, 42(1):42–47.

McAlister, K., Schuler, C., Branum, L., and Wu, J. (1995). 3-D Wake Measurements Near a Hovering Rotor for Determining Profile and Induced Drag. Technical report, National Aeronatics and Space Administration Moffet Field CA AMES Research.

McLachlan, B. G. and Bell, J. H. (1995). Pressure-sensitive paint in aerodynamic testing. *Experimental Thermal and Fluid Science*, 10(4):470–485.

Mead, C. J., Wrighton, C., and Britchford, K. (2015). An Experimental Study of Coaxial Jets Using Acoustic PIV and LDA Methods (CoJeN). In *21st AIAA/CEAS Aeroacoustics Conference*, page 3122.

Melling, A. (1997). Tracer particles and seeding for particle image velocimetry. *Measurement Science and Technology*, 8(12):1406.

Mercedes-Benz AG (2019). In conversation: Olympic champion Jan Frodeno and Head of Aerodynamics Dr Teddy Woll. https://media.mercedes-benz.com/article/81e9d1f2-27db-47fb-b7f2-297d90f8d410. Press release.

Mertens, C., de Rojas Cordero, T., Sodja, J., Sciacchitano, A., and van Oudheusden, B. W. (2021a). Aeroelastic Characterization of a Flexible Wing Using Particle Tracking Velocimetry Measurements. *AIAA Journal*, pages 1–11.

Mertens, C., Sciacchitano, A., van Oudheusden, B., and Sodja, J. (2021b). An integrated measurement approach for the determination of the aerodynamic loads and structural motion for unsteady airfoils. *Journal of Fluids and Structures*, 103:103293.

Michaux, F., Mattern, P., and Kallweit, S. (2018). RoboPIV: how robotics enable PIV on a large industrial scale. *Measurement Science and Technology*, 29(7):074009.

Minetti, A. E., Machtsiras, G., and Masters, J. C. (2009). The optimum finger spacing in human swimming. *Journal of Biomechanics*, 42(13):2188–2190.

Mitrotta, F. (2020). Experimental Fluid-Structure Interaction of a Flexible Plate Under Gust Excitation: A Wind-tunnel Investigation by Means of Robotic Volumetric PIV. MSc Thesis, TU Delft.

Mitrotta, F. M., Sciacchitano, A., Sodja, J., De, R., and Breuker, B. W. (2019). Experimental investigation of the fluid-structure interaction between a flexible plate and a periodic gust by means of Robotic Volumetric PIV. In *Proceedings of the*

13th International Symposium on Particle Image Velocimetry. Universität der Bundeswehr München.

Nakagawa, M., Michaux, F., Kallweit, S., and Maeda, K. (2015). Unsteady flow measurements in the wake behind a wind-tunnel car model by using high-speed planar PIV. In *11th International Symposium on Particle Image Velocimetry – PIV15, Santa Barbara*.

Noca, F., Shiels, D., and Jeon, D. (1999). A comparison of methods for evaluating time-dependent fluid dynamic forces on bodies, using only velocity fields and their derivatives. *Journal of Fluids and Structures*, 13(5):551–578.

Novara, M. and Scarano, F. (2013). A particle-tracking approach for accurate material derivative measurements with tomographic PIV. *Experiments in Fluids*, 54(8):1–12.

Novara, M., Schanz, D., Geisler, R., Gesemann, S., Voss, C., and Schröder, A. (2019). Multi-exposed recordings for 3D Lagrangian particle tracking with Multi-Pulse Shake-The-Box. *Experiments in Fluids*, 60(3):1–19.

Novara, M., Schanz, D., Geisler, R., and Schröder, A. (2018). Applications of multi-pulse shake-the-box 3D Lagrangian particle tracking to single-and multi-exposed recordings. In *Proceedings 18th International Symposium on Flow Visualization*. ETH Zurich.

Pan, Z., Whitehead, J., Thomson, S., and Truscott, T. (2016). Error propagation dynamics of PIV-based pressure field calculations: How well does the pressure Poisson solver perform inherently? *Measurement Science and Technology*, 27(8):084012.

Pengel, K., Kooi, J., Raffel, M., Willert, C., and Kompenhans, J. (1997). Application of PIV in the large low speed facility of DNW. In *New Results in Numerical and Experimental Fluid Mechanics*, pages 253–258. Springer.

Polidori, G., Legrand, F., Bogard, F., Madaci, F., and Beaumont, F. (2020). Numerical investigation of the impact of Kenenisa Bekele's cooperative drafting strategy on its running power during the 2019 Berlin marathon. *Journal of Biomechanics*, 107:109854.

Raffel, M., Richard, H., Ehrenfried, K., Van der Wall, B., Burley, C., Beaumier, P., McAlister, K., and Pengel, K. (2004). Recording and evaluation methods of PIV investigations on a helicopter rotor model. *Experiments in Fluids*, 36(1):146–156.

Raffel, M., Willert, C. E., Scarano, F., Kähler, C. J., and Wereley, S. (2018). *Particle Image Velocimetry - A Practical Guide*. Springer, 3rd edition.

Ragni, D., Ashok, A., van Oudheusden, B., and Scarano, F. (2009). Surface pressure and aerodynamic loads determination of a transonic airfoil based on particle image velocimetry. *Measurement Science and Technology*, 20(7):074005.

Raiola, M., Lopez-Nuñez, E., Cafiero, G., and Discetti, S. (2020). Adaptive ensemble PTV. *Measurement Science and Technology*, 31(8):085301.

Reuther, N. and Kähler, C. J. (2018). Evaluation of large-scale turbulent/non-turbulent interface detection methods for wall-bounded flows. *Experiments in Fluids*, 59(7):121.

Roettig, F., Wennemar, K., Hoyer, K., Beslac, R., Hesseling, C., Beck, T., and Friedhoff, B. (2019). Volumetric flow measurements in the wake of a ducted propeller. In *The 6th International Conference on Advanced Model Measurement Technology for The Maritime Industry*. Rome, Italy.

Saiz, G. G., Sciacchitano, A., and Scarano, F. (2021). Towards the closure of Collar's triangle by optical diagnostics. In *14th International Symposium on Particle Image Velocimetry*.

Saredi, E., Ramesh, N. T., Sciacchitano, A., and Scarano, F. (2021). State observer data assimilation for RANS with time-averaged 3D-PIV data. *Computers & Fluids*, 218:104827.

Saredi, E., Sciacchitano, A., and Scarano, F. (2020). Multi-Δt 3D-PTV based on Reynolds decomposition. *Measurement Science and Technology*, 31(8):084005.

Scarano, F. (2001). Iterative image deformation methods in PIV. *Measurement Science and Technology*, 13(1):R1.

Scarano, F. (2012). Tomographic PIV: principles and practice. *Measurement Science and Technology*, 24(1):012001.

Scarano, F., Ghaemi, S., Caridi, G. C. A., Bosbach, J., Dierksheide, U., and Sciacchitano, A. (2015). On the use of helium-filled soap bubbles for large-scale tomographic PIV in wind tunnel experiments. *Experiments in Fluids*, 56(2):42.

Schanz, D., Gesemann, S., and Schröder, A. (2016). Shake-The-Box: Lagrangian particle tracking at high particle image densities. *Experiments in Fluids*, 57(5):70.

Schanz, D., Gesemann, S., Schröder, A., Wieneke, B., and Novara, M. (2012). Non-uniform optical transfer functions in particle imaging: calibration and application to tomographic reconstruction. *Measurement Science and Technology*, 24(2):024009.

Schleihauf, R. E. (1979). A hydrodynamic analysis of swimming propulsion. In *Swimming III. Proceedings of the Third International Symposium of Biomechanics in Swimming*. University of Alberta, Edmonton, Canada, Baltimore University Park Press.

Schneiders, J. F., Caridi, G. C., Sciacchitano, A., and Scarano, F. (2016). Large-scale volumetric pressure from tomographic PTV with HFSB tracers. *Experiments in Fluids*, 57(11):164.

Schneiders, J. F. and Scarano, F. (2016). Dense velocity reconstruction from tomographic PTV with material derivatives. *Experiments in Fluids*, 57(9):1–22.

Schneiders, J. F. G., Scarano, F., Jux, C., and Sciacchitano, A. (2018). Coaxial volumetric velocimetry. *Measurement Science and Technology*, 29(6):065201.

Schröder, A., Geisler, R., Elsinga, G. E., Scarano, F., and Dierksheide, U. (2008). Investigation of a turbulent spot and a tripped turbulent boundary layer flow using time-resolved tomographic PIV. *Experiments in Fluids*, 44(2):305–316.

Schröder, A., Schanz, D., Bosbach, J., Novara, M., Geisler, R., Agocs, J., and Kohl, A. (2021). Large-scale 3D flow investigations around a cyclically breathing thermal manikin in a 12 m^3 room using HFSB and STB. In *14th International Symposium on Particle Image Velocimetry*.

Sciacchitano, A. and Giaquinta, D. (2019). Investigation of the Ahmed body crosswind flow topology by robotic volumetric PIV. In *Proceedings of the 13th International Symposium on Particle Image Velocimetry*. Universität der Bundeswehr München.

Sciacchitano, A., Giaquinta, D., Schneiders, J., Scarano, F., van Rooijen, B., and Funes, D. (2018). Quantitative flow visualization of a turboprop aircraft by robotic volumetric velocimetry. In *Proceedings 18th International Symposium on Flow Visualization*. ETH Zurich.

Sciacchitano, A. and Scarano, F. (2014). Elimination of PIV light reflections via a temporal high pass filter. *Measurement Science and Technology*, 25(8):084009.

Senft, V. and Gillan, M. (2019). Recent advances and test processes in automotive and motorsports aerodynamic development. *Proceedings of the Institution of Mechanical Engineers, Part C: Journal of Mechanical Engineering Science*, 233(23-24):7573–7589.

Sidelnik, N. and Young, B. (2006). Optimising the freestyle swimming stroke: the effect of finger spread. *Sports Engineering*, 9(3):129–135.

Soloff, S. M., Adrian, R. J., and Liu, Z.-C. (1997). Distortion compensation for generalized stereoscopic particle image velocimetry. *Measurement Science and Technology*, 8(12):1441.

Spoelstra, A., de Martino Norante, L., Terra, W., Sciacchitano, A., and Scarano, F. (2019). On-site cycling drag analysis with the Ring of Fire. *Experiments in Fluids*, 60(6):1–16.

Sumner, D. (2013). Flow above the free end of a surface-mounted finite-height circular cylinder: a review. *Journal of Fluids and Structures*, 43:41–63.

Tagliabue, A., Scharnowski, S., and Kähler, C. J. (2017). Surface pressure determination: a comparison between PIV-based methods and PSP measurements. *Journal of Visualization*, 20(3):581–590.

Takagi, H., Nakashima, M., Sato, Y., Matsuuchi, K., and Sanders, R. H. (2016). Numerical and experimental investigations of human swimming motions. *Journal of Sports Sciences*, 34(16):1564–1580.

Takagi, H., Shimada, S., Miwa, T., Kudo, S., Sanders, R., and Matsuuchi, K. (2014). Unsteady hydrodynamic forces acting on a hand and its flow field during sculling motion. *Human Movement Science*, 38:133–142.

Takagi, H., Shimizu, Y., Kurashima, A., and Sanders, R. (2001). Effect of thumb abduction and adduction on hydrodyamic characteristics of a model of the human hand. In *ISBS-Conference Proceedings Archive*.

Terra, W., Sciacchitano, A., and Scarano, F. (2016). Evaluation of aerodynamic drag of a full-scale cyclist model by large-scale tomographic-PIV. In *International workshop on non-intrusive optical flow diagnostics, Delft*, pages 25–26.

Terra, W., Sciacchitano, A., and Scarano, F. (2017). Aerodynamic drag of a transiting sphere by large-scale tomographic-PIV. *Experiments in Fluids*, 58(7):83.

Terra, W., Sciacchitano, A., and Scarano, F. (2020). Cyclist reynolds number effects and drag crisis distribution. *Journal of Wind Engineering and Industrial Aerodynamics*, 200:104143.

Terra, W., Sciacchitano, A., and Shah, Y. (2019). Aerodynamic drag determination of a full-scale cyclist mannequin from large-scale PTV measurements. *Experiments in Fluids*, 60(2):29.

Tescione, G., Ragni, D., He, C., Ferreira, C. S., and Van Bussel, G. (2014). Near wake flow analysis of a vertical axis wind turbine by stereoscopic particle image velocimetry. *Renewable Energy*, 70:47–61.

Tew, G. S. and Sayers, A. T. (1999). Aerodynamics of yawed racing cycle wheels. *Journal of Wind Engineering and Industrial Aerodynamics*, 82:209–222.

Timmer, W. and Van Rooij, R. (2003). Summary of the Delft University wind turbine dedicated airfoils. *Journal of Solar Energy Engineering*, 125(4):488–496.

Toyota Motorsport GmbH (2017). Toyota Motorsport wind tunnel helps automotive engineers design faster high-performance cars with sophisticated built-in PIV system. https://www.toyota-motorsport.com/media/tmg/Tecplot_PIV.pdf Accessed on: 27.04.2017.

Tropea, C., Yarin, A. L., and Foss, J. F. (2007). *Springer handbook of experimental fluid mechanics*. Springer Science & Business Media.

TU Delft (2021). Measuring system using laser beams and helium bubbles helps top skaters go for gold. Web article.

Ultimaker BV (2019). Ultimaker Original+ specifications. https://ultimaker.com/en/products/ultimaker-original/specifications Accessed on 23.09.2019.

Universal Robots, A/S (2017). Technical Specifications - UR5. https://www.universal-robots.com/media/1514597/101081_199901_ur5_technical_details_web_a4_art03_rls_eng.pdf Accessed on 27.03.2017.

van den Berg, J., Bazuin, R., Jux, C., Sciacchitano, A., Westerweel, J., and van de Water, W. (2021). The effect of hand posture on swimming efficiency. *Experiments in Fluids*, 62(245).

van Houwelingen, J., Schreven, S., Smeets, J. B., Clercx, H. J., and Beek, P. J. (2017a). Effective propulsion in swimming: grasping the hydrodynamics of hand and arm movements. *Journal of Applied Biomechanics*, 33(1):87–100.

van Houwelingen, J., Willemsen, D. H., Kunnen, R. P., van Heijst, G. F., Grift, E. J., Breugem, W. P., Delfos, R., Westerweel, J., Clercx, H. J., and van de Water, W. (2017b). The effect of finger spreading on drag of the hand in human swimming. *Journal of Biomechanics*, 63:67–73.

van Oudheusden, B. (2008). Principles and application of velocimetry-based planar pressure imaging in compressible flows with shocks. *Experiments in Fluids*, 45(4):657–674.

van Oudheusden, B., Scarano, F., and Casimiri, E. (2006). Non-intrusive load characterization of an airfoil using PIV. *Experiments in Fluids*, 40(6):988–992.

van Oudheusden, B. W. (2013). PIV-based pressure measurement. *Measurement Science and Technology*, 24(3):032001.

van Oudheusden, B. W., Scarano, F., Roosenboom, E. W., Casimiri, E. W., and Souverein, L. J. (2007). Evaluation of integral forces and pressure fields from planar velocimetry data for incompressible and compressible flows. *Experiments in Fluids*, 43(2-3):153–162.

van Tilborg, F. (2018). Flow analysis between two bluff bodies in a close distance platooning configuration: A Numerical and Experimental Study. MSc Thesis, TU Delft.

van Tilborg, F., van Raemdonck, G., Sciacchitano, A., and Casalino, D. (2019). Flow Analysis between Two Bluff Bodies in a Close Distance Platooning Configuration. *SAE International Journal of Commercial Vehicles*, 12(02-12-03-0015):179–196.

van Tubergen, J., Verlinden, J., Stroober, M., and Baldewsing, R. (2017). Suited for performance: fast full-scale replication of athlete with FDM. In *proceedings of the 1st Annual ACM Symposium on Computational Fabrication*, pages 1–2.

Vedula, P. and Adrian, R. J. (2005). Optimal solenoidal interpolation of turbulent vector fields: application to PTV and super-resolution PIV. *Experiments in Fluids*, 39(2):213–221.

Vennemann, B. and Rösgen, T. (2020). A dynamic masking technique for particle image velocimetry using convolutional autoencoders. *Experiments in Fluids*, 61(7):1–11.

Vogel, A. and Lauterborn, W. (1988). Time Resolved Particle Image Velocimetry. *Optics and Lasers in Engineering*, 9(3-4):277–294.

Wendt, V. and Forll, M. (2001). Flow field measurements around a car using particle image velocimetry. In *4th International Symposium on Particle Image Velocimetry*, pages 1–6.

Wieneke, B. (2008). Volume self-calibration for 3D particle image velocimetry. *Experiments in Fluids*, 45(4):549–556.

Wieneke, B. (2012). Iterative reconstruction of volumetric particle distribution. *Measurement Science and Technology*, 24(2):024008.

Yeh, Y. and Cummins, H. (1964). Localized fluid flow measurements with an He–Ne laser spectrometer. *Applied Physics Letters*, 4(10):176–178.

Zdravkovich, M. (1992). Aerodynamics of bicycle wheel and frame. *Journal of Wind Engineering and Industrial Aerodynamics*, 40(1):55–70.

Zhang, P., Peterson, S. D., and Porfiri, M. (2019). Combined particle image velocimetry/digital image correlation for load estimation. *Experimental Thermal and Fluid Science*, 100:207–221.

Ziou, D., Tabbone, S., et al. (1998). Edge detection techniques-an overview. *Pattern Recognition and Image Analysis C/C of Raspoznavaniye Obrazov I Analiz Izobrazhenii*, 8:537–559.

Curriculum vitæ

Constantin Jux

04-10-1992 Born in Bergisch Gladbach, Germany

Education

2002–2011 Secondary School
Gymnasium Odenthal (GER)

2011–2014 Bachelor of Science, Aerospace Engineering
Delft University of Technology (NED)
Minor: Eidgenössische Technische Hochschule Zürich (SUI) (2013–2014)
Thesis: Printing the Personal Aircraft of Tomorrow

2015–2017 Master of Science, European Wind Energy Master
Delft University of Technology (NED)
Technical University of Denmark (DEN)
Thesis: Robotic Volumetric Particle Tracking Velocimetry by Coaxial Imaging and Illumination

2018–2022 PhD Aerospace Engineering – Aerodynamics
Delft University of Technology (NED)

Professional experience

2014–2015 Industrial Placement, Aerodynamics Engineer
Mercedes-Benz Grand Prix Limited (GBR)

List of publications

Journal publications

8. **Jux C**, Sciacchitano A and Scarano F. Tire dependence for the aerodynamics of yawed bicycle wheels, *submitted to Journal of Wind Engineering and Industrial Aerodynamics*

7. **Jux C**, Ordóñez D, Sciacchitano A and Scarano F. Total-pressure wake survey by robotic volumetric PIV, *in preparation for Exp. Fluids*

6. van den Berg J, Bazuin R, **Jux C**, Sciacchitano A, Westerweel J and van de Water W. The effect of hand posture on swimming efficiency, *Exp. Fluids* **62**, 245 (2021)

5. Scarano F, **Jux C** and Sciacchitano A. Recent advancements towards large-scale flow diagnostics by robotic PIV, *Fluid Dynamics Research* **53**, 1 (2021)

4. **Jux C**, Sciacchitano A and Scarano F. Object surface reconstruction from flow tracers, *Exp. Fluids* **62**, 42 (2021)

3. **Jux C**, Sciacchitano A and Scarano F. Flow pressure evaluation on generic surfaces by robotic volumetric PTV, *Meas. Sci. Technol.* **31**, 104001 (2020)

2. Schneiders JFG, Scarano F, **Jux C** and Sciacchitano A. Coaxial volumetric velocimetry, *Meas. Sci. Technol.* **29**, 065201 (2018)

1. **Jux C**, Sciacchitano A, Schneiders JFG and Scarano F. Robotic volumetric PIV of a full-scale cyclist, *Exp. Fluids* **59**, 74 (2018)

Conference publications and presentations

8. van de Water W, van den Berg J, Bazuin R, **Jux C**, Sciacchitano A and Westerweel J. Shaping your hand for more efficient swimming. *Sports Physics conference*, Lyon, France, December 6-8 (2021)

7. **Jux C**, Sciacchitano A and Scarano F. Aerodynamics of a cycling wheel in crosswind by coaxial volumetric velocimetry, *14th International Symposium on Particle Image Velocimetry*, Illinois, USA, August 1-4 (2021)

6. **Jux C**, Scarano F and Sciacchitano A. Tracer-based 3D surface reconstruction, *14th International Symposium on Particle Image Velocimetry*, Illinois, USA, August 1-4 (2021)

5. van den Berg J, **Jux C**, Sciacchitano A, van de Water W and Westerweel J. Robotic Volumetric PIV measurements of a full-scale swimmer's hand, *13th International Symposium on Particle Image Velocimetry*, Munich, Germany, July 22-24 (2019)

4. **Jux C**, Sciacchitano A and Scarano F. Aerodynamic pressure reconstruction on generic surfaces from robotic PIV measurements, *13th International Symposium on Particle Image Velocimetry*, Munich, Germany, July 22-24 (2019)

3. **Jux C**, Sciacchitano A and Scarano F. Surface pressure visualization by 3D PTV, *18th International Symposium on Flow Visualization*, Zurich, Switzerland, June 26-29 (2018)

2. Schneiders JFG, **Jux C**, Sciacchitano A and Scarano F. Coaxial volumetric velocimetry. *12th International Symposium on Particle Image Velocimetry*, Busan, South Korea, June 18-22 (2017)

1. **Jux C**, Schneiders JFG, Sciacchitano A and Scarano F. Full-scale cyclist aerodynamics by coaxial volumetric velocimetry. *12th International Symposium on Particle Image Velocimetry*, Busan, South Korea, June 18-22 (2017)

Prizes and awards

4. Innovationspreis des Landkreises Göttingen – Sonderpreis Messtechnik (2018), *MiniShaker Robotic - vollautomatische großvolumige Strömungsmessung*, received by LaVision GmbH

3. Gallery of Fluid Motion – Burgers Symposium (2018), *Robotic volumetric PIV of a full-scale cyclist*

2. Best paper award – 12th International Symposium on PIV, Busan, South Korea, June 18-22 (2017), *Coaxial volumetric velocimetry*

1. Nomination for NVvL Hans Wittenbergprice (2017), *Robotic Volumetric Particle Tracking Velocimetry by Coaxial Imaging and Illumination*

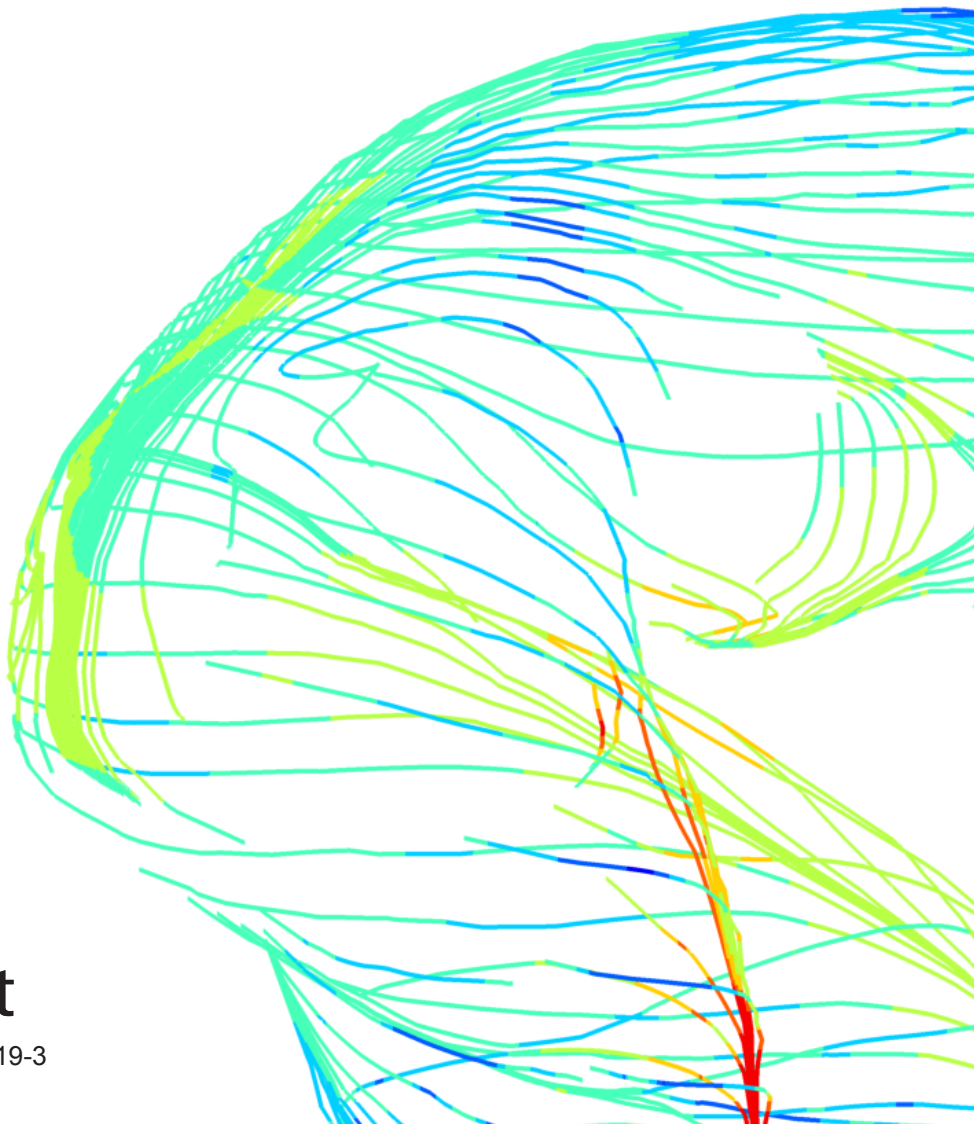

TU Delft

ISBN 978-94-6366-519-3